



**HAL**  
open science

# Use of fiberglass geogrids to the reinforcement of bituminous mixtures layers

Reuber Arrais Freire

► **To cite this version:**

Reuber Arrais Freire. Use of fiberglass geogrids to the reinforcement of bituminous mixtures layers. Structural mechanics [physics.class-ph]. Université de Lyon, 2020. English. NNT : 2020LYSET009 . tel-03249370

**HAL Id: tel-03249370**

**<https://theses.hal.science/tel-03249370>**

Submitted on 4 Jun 2021

**HAL** is a multi-disciplinary open access archive for the deposit and dissemination of scientific research documents, whether they are published or not. The documents may come from teaching and research institutions in France or abroad, or from public or private research centers.

L'archive ouverte pluridisciplinaire **HAL**, est destinée au dépôt et à la diffusion de documents scientifiques de niveau recherche, publiés ou non, émanant des établissements d'enseignement et de recherche français ou étrangers, des laboratoires publics ou privés.



N°d'ordre NNT : 2020LYSET009

**THÈSE DE DOCTORAT DE L'UNIVERSITÉ DE LYON**  
opérée au sein de  
**l'École Nationale des Travaux Publics de l'État**

**École Doctorale N° 162**  
**Mécanique, Energétique, Génie Civil et Acoustique (MEGA)**

**Spécialité / discipline de doctorat : Génie Civil**

Soutenue publiquement le 29/06/2020, par :

**Reuber Arrais Freire**

---

**Utilisation de géogrilles en fibre de verre  
pour le renforcement des couches d'en-  
robé bitumineux**

---

Devant le jury composé de :

DJERAN MAIGRE, Irini	Prof., INSA de Lyon	Présidente
CHAZALLON, Cyrille	Prof., INSA de Strasbourg	Rapporteur
CANESTRARI, Francesco	Prof., Università Politecnica delle Marche	Rapporteur
RIOT, Mathilde	Expert, Afitexinov	Examinatrice
POUGET, Simon	Dr., EIFFAGE Infrastructures	Examineur
DI BENEDETTO, Hervé	Prof., Université de Lyon/ENTPE	Directeur de thèse
SAUZÉAT, Cédric	Prof., Université de Lyon/ENTPE	Co-Directeur de thèse
LESUEUR, Didier	Dr., Afitexinov	Invité
VAN ROMPU, Julien	Dr., EIFFAGE Infrastructures	Invité



N° d'ordre NNT : 2020LYSET009

**DOCTORAL THESIS OF THE UNIVERSITY OF LYON**  
prepared at  
**Ecole Nationale des Travaux Publics de l'Etat**

**Doctoral School N° 162**  
**Mécanique, Energétique, Génie Civil et Acoustique (MEGA)**

**Specialty: Civil Engineering**

Publicly defended the 29<sup>th</sup> of June 2020 by:

**Reuber Arrais Freire**

---

**Use of fiberglass geogrids to the reinforcement of bituminous mixtures layers**

---

before the committee composed of:

DJERAN MAIGRE, Irini	Prof., INSA de Lyon	President
CHAZALLON, Cyrille	Prof., INSA de Strasbourg	Reviewer
CANESTRARI, Francesco	Prof., Università Politecnica delle Marche	Reviewer
RIOT, Mathilde	Expert, Afitexinov	Examiner
POUGET, Simon	Dr., EIFFAGE Infrastructures	Examiner
DI BENEDETTO, Hervé	Prof., Université de Lyon/ENTPE	Advisor
SAUZÉAT, Cédric	Prof., Université de Lyon/ENTPE	Co-advisor
LESUEUR, Didier	Dr., Afitexinov	Invited
VAN ROMPU, Julien	Dr., EIFFAGE Infrastructures	Invited

# TABLE OF CONTENTS

TABLE OF CONTENTS .....	1
ACKNOWLEDGEMENTS.....	6
RÉSUMÉ.....	8
ABSTRACT .....	10
LIST OF TABLES.....	12
LIST OF FIGURES .....	14
MAIN SYMBOLS.....	26
Chapter 1: INTRODUCTION.....	27
Chapter 2: LITERATURE REVIEW.....	31
2.1. Pavement structures .....	32
2.2. Pavements design method.....	33
2.3. Bituminous mixtures.....	36
2.3.1. Composition.....	39
2.3.2. Thermo-mechanical behavior.....	43
2.4. Linear viscoelastic behavior of materials .....	46
2.4.1. Definition.....	46
2.4.2. Creep, Relaxation and Convolution Integral .....	47
2.4.3. Complex modulus and Poisson's ratio .....	49
2.4.4. Time-Temperature Superposition Principle (TTSP) and Master Curves .....	51
2.4.5. Modelling LVE behavior.....	53
2.5. Fatigue in bituminous materials.....	55
2.5.1. Fatigue of bituminous binders, mastics and mixtures .....	55
2.5.2. Experimental observations and failure criteria.....	58
2.6. Cracking in bituminous materials .....	61
2.6.1. Cracking distresses presenting in flexible pavements .....	61
2.6.2. Introduction to Linear Fracture Mechanics (LFM) .....	62
2.6.3. Fracture energy determination.....	64
2.6.4. Crack propagation tests for bituminous mixtures.....	66



2.7.	Overview of geosynthetics for pavements reinforcement .....	68
2.7.1.	Background.....	68
2.7.2.	Types of geosynthetics interlayers .....	71
2.7.3.	Geosynthetic functions and behavior mechanisms.....	73
2.7.4.	Geosynthetics important properties and characterization.....	76
2.7.5.	Reinforcement of unbound layers.....	77
2.7.6.	Reinforcement of bound layers.....	79
<b>Chapter 3: MATERIALS AND EXPERIMENTAL CAMPAIGNS .....</b>		<b>96</b>
3.1.	Materials .....	97
3.1.1.	Bituminous Mixture.....	97
3.1.2.	Geogrid reinforcement.....	98
3.2.	Specimens Preparation.....	100
3.2.1.	Slabs configurations .....	100
3.2.2.	Slabs fabrication .....	101
3.2.3.	Specimens coring and nomenclature .....	103
3.2.4.	Air voids .....	106
3.3.	Experimental campaign overview.....	117
<b>Chapter 4: CYCLIC TENSION-COMPRESSION TEST CAMPAIGN.....</b>		<b>119</b>
4.1.	Introduction.....	120
4.2.	Objectives .....	120
4.3.	Experimental devices and procedures.....	121
4.3.1.	Hydraulic press and instrumentation .....	121
4.3.2.	Complex modulus test protocol.....	123
4.4.	New method to characterize interface behavior.....	127
4.4.1.	Bulk approach using continuum mechanics hypothesis .....	127
4.4.2.	Infinitely thin interface .....	129
4.5.	Tested Specimens.....	129
4.6.	Bituminous mixtures and interfaces results and modeling .....	131

---

4.6.1.	Example of result and modeling for specimens without interface: A1-H3 ..	131
4.6.2.	Example of result and modeling for specimens containing interface.....	137
4.6.2.1.	Specimen type V: C2-V1 (bituminous mixture).....	137
4.6.2.1.	Specimen type V: C2-V1 (interface) .....	140
4.6.2.2.	Specimen type H: C2-H3 .....	143
4.6.3.	Complex modulus test results.....	145
4.6.3.1.	Bituminous mixtures analysis and modelling.....	145
4.6.3.2.	Interfaces analysis and modeling.....	152
4.6.4.	Influence of fiberglass geogrid on H specimen's behavior .....	156
4.7.	Chapter conclusions .....	159
Chapter 5: TENSION TEST CAMPAIGN .....		160
5.1.	Introduction.....	161
5.2.	Objectives .....	161
5.3.	Experimental procedures and devices.....	162
5.3.1.	Hydraulic press and instrumentation .....	162
5.3.2.	Tension test protocol .....	162
5.3.3.	Analysis of interface concerning specimens type V.....	165
5.4.	Tested Specimens.....	166
5.5.	Bituminous mixtures and interfaces results .....	169
5.5.1.	Example of result of specimens without interface: A3-H4, 19°C, 2%/min	169
5.5.2.	Example of result obtained from specimens having interface.....	170
5.5.2.1.	Specimen type V: C2-V5, 19°C, 2%/min (Bituminous Mixture).....	170
5.5.2.2.	Specimen type V: C2-V5, 19°C, 2%/min (Interface).....	171
5.6.	Verification of specimen's diameter size effect for specimens type V .....	173
5.7.	Verification of time-Temperature superposition principle .....	175
5.7.1.	Frequency sweep test results .....	175
5.7.2.	Specimens type H .....	180
5.7.3.	Specimens type V .....	189
5.8.	Fiberglass geogrid contribution to the maximum tensile strength of bituminous mixture.....	199

5.9. Effect of fiberglass geogrid on maximum interface tensile strength .....	203
5.10. Chapter conclusions .....	206
<b>Chapter 6: FATIGUE TEST CAMPAIGN .....</b>	<b>208</b>
6.1. Introduction.....	209
6.2. Objectives .....	209
6.3. Experimental procedures and devices.....	210
6.3.1. Hydraulic press and instrumentation .....	210
6.3.2. Fatigue test protocol .....	211
6.4. Tested specimens .....	213
6.5. Example of fatigue tests results: B3-H4, 90 $\mu$ m/m.....	215
6.6. Classical analysis of fatigue tests in cylindrical samples results .....	219
6.6.1. Influence of strain level on fatigue .....	219
6.6.2. Analysis of fatigue life (number of cycles to failure).....	222
6.6.3. The Wöhler curve and determination of the $\epsilon_6$ value .....	227
6.6.4. Influence of geogrid on fatigue resistance.....	231
6.7. Chapter conclusions .....	233
<b>Chapter 7: CRACK PROPAGATION TEST CAMPAIGN .....</b>	<b>235</b>
7.1. Introduction.....	236
7.2. Objectives .....	237
7.3. Experimental procedures and devices.....	237
7.3.1. Hydraulic press and instrumentation .....	237
7.3.2. Specimens preparation.....	239
7.3.3. Four Points Bending Notched Fracture (FPBNF) test protocol .....	240
7.4. Digital Image Correlation (DIC) analysis.....	241
7.4.1. Procedure of analysis.....	242
7.4.2. Average strain vs beam's height: principle of calculation .....	245
7.5. Tested specimens .....	246
7.6. Example of crack propagation test result: B1-B2 .....	247

7.7. Force evolution with beam's deflection analysis.....	249
7.8. Analysis of crack tip height (a).....	253
7.9. Energy restitution rate ( $G_f$ ) .....	256
7.10. Average and maximum strain images analysis .....	258
7.10.1. Example of specimen without interface: A2-B3 .....	258
7.10.2. Example of unreinforced specimen with interface: B1-B2 .....	260
7.10.3. Example of reinforced specimen: D1-B3 .....	262
7.10.4. Comparison between analysed configurations .....	265
7.11. Chapter conclusions .....	267
Chapter 8: CONCLUSION AND PESPECTIVES .....	270
REFERENCES .....	274

# ACKNOWLEDGEMENTS

After 4 years, I am not able to describe how happy I am about finally finishing this huge step in my life. I always pictured the day I would be done with this project and all the background I would acquire at the end of it. Now I realize that my imagination could not be even closed from what really feels like to be done. This work is by far the biggest and hardest achievement that I had in my entire life so far. Not simply the PhD itself was a challenge, but leaving my country behind without speaking French, as well as having a hard time adjusting, facing a distinctly new culture that I was not used to. All of these things were huge challenges that I had to face by myself. For those reasons, I grew up, and I did as a person, as a professional, and more importantly, as a scientist. However, I understand that this was not a path of a single person only. The interaction with many people had a significant influence on those growing aspects of my life. Not only the friendly interactions but all of them, even the bad ones. For these reasons, I would like to express all my gratitude to all the people, directly and indirectly, involved in my PhD and on the construction of the person I am today.

Firstly, I would like to express my gratitude and esteem to my advisor, Dr. **Hervé Di Benedetto**. The various meetings we had together constructed “brick per brick” my scientific formation. Our exchanges on many subjects related to this thesis taught me to always use detailed and rigorous approaches when it comes to science. Moreover, and not less importantly, I am grateful to my co-advisor Dr. **Cédric Sauzéat** for all his support and advice during the development of this thesis. At the end of four years, I finally could be able to understand his jokes and how good they were. His patience and ideas during hard moments were essential to making me finish this work. Thanks to both of you for making me have the opportunity to work with you, I highly appreciated it.

I also would like to thank all the other members of my PhD defense committee, Dr. **Irini Djeran Maigre**, president of the jury, Dr. **Cyrille Chazallon**, and Dr. **Francesco Canestrari** for reviewing this PhD thesis, Dr. **Simon Pouget** and **Mathilde Riot** for examining this PhD thesis. In addition, thanks to Dr. **Didier Lesueur** and Dr. **Julien Van Rompu** for participating in my defense as invited members. Thank you for the huge contributions given to increase the quality of this work during our periodic meetings.

I cannot forget to thank **Afitexinov** and **EIFFAGE Infrastructure** for the financial and material support of the research project, as well as the aid of the members from both companies such as **Marie** and **Jacques Tankéré**, **Yves Durkheim**, **Gwenael Leguernevel**, **Fraçois Olard**

and **Jean-Paul Desgrange**. Also, thanks to **CNPq** and its Science without Borders (*Ciência sem Fronteiras* - CsF) program for the grant I had within my PhD project. Moreover, I really want to thank to all the **LTDS** colleagues that helped me since the beginning and were responsible for my adaptation in the lab and in France, and rapidly became good friends: **Alvaro, Diego, Lucas, Evelyn, Salvo, Stephano, Andrei, Viet, Thang, Frank, Isa, Mounir, Gabriel, Jean-Claude, Jean-Marie, Yasmina, Thomas**, and lastly **Tanguy** that worked with me during his masters.

Finally, I would like to express all my gratitude to the woman I chose to spend the rest of my life with: **Geórgia**. She was brave and helpful during all the different moments of my PhD studies, including the first year that we spent apart, I was in France and she was in Brazil. Moreover, to my beloved parents: **Ismênia e Roberto**. Especially my father that first gave me the passion for Civil Engineering I have today, but unfortunately, he passed away a few days before my PhD defense and he was not able to see me become a doctor. However, I believe he is happy for my accomplishment wherever he is and **I dedicate this thesis for him**. In addition, to my sister **Roberta** to be always there for me. Lastly, to the many friends I met in Lyon that made my life wonderful during the PhD: **Alejandro, Carlitos, Tiago, João, Sergio, Nicole, Patricia, Felipe, Fabio, Cláudia, Daila, Marcos, Gabi, Juliana, Rodrigo, and Priscila**.

Thank you all.

Reuber Arrais Freire

# RESUME

Cette thèse de doctorat a été développée au Laboratoire de Tribologie et Dynamique des Systèmes (LTDS) de l'École Nationale des Travaux Publics de l'Etat (ENTPE), France. Il faisait partie d'un partenariat entre les sociétés françaises Afitexinov et EIFFAGE Infrastructures. Il a également bénéficié du soutien du programme brésilien de science sans frontières du CNPq. L'objectif de cette étude est de contribuer au développement de nouveaux géosynthétiques structurés pour le renforcement des couches bitumineuses des chaussées, ainsi que de méthodes de dimensionnement transférables vers l'ingénierie. En plus de fournir des informations utiles qui pourraient permettre la proposition d'une nouvelle méthode de conception pour les structures de chaussées renforcées. À cette fin, cinq complexes de plaque ont été conçues, quatre à deux couches et une entière, contenant le même type d'enrobé bitumineux quelle que soit la configuration. À partir des plaques à deux couches, trois ont été renforcées par la combinaison de deux géogrilles en fibre de verre (résistance à la traction maximale de 50 et 100 kN/m) avec deux émulsions comme couche d'accrochage (bitumen pur et modifié par SBS). La dernière plaque bi-couche était non renforcée, ne contenant que du bitume en émulsion pur à son interface. Des échantillons cylindriques et en forme de poutre ont été carottés dans les plaques afin de mener quatre campagnes expérimentales.

La première campagne expérimentale a porté sur la caractérisation du comportement des éprouvettes cylindriques renforcées par une géogrigle en fibre de verre dans le domaine de petites déformations à l'aide de essais cycliques de traction-compression, appelés essais de module complexe. Une nouvelle méthode d'analyse d'interface a été proposée pour les essais de module complexes sur les échantillons renforcés par géogrigle et ayant l'interface orientée perpendiculairement à la direction longitudinale de l'échantillon cylindrique. D'après les résultats des tests, le comportement d'interface obtenu était viscoélastique linéaire (VEL) et il pourrait être modélisé par le modèle 2S2PD. Cependant, un niveau très bas de mobilisation des géogrilles a été observé pendant le test.

La deuxième campagne expérimentale a porté sur la caractérisation à la charge de traction axiale monotone. Trois températures (0, 19 et 40°C) ont été combinées avec deux vitesses de déformation (2 et 0,002%/min) pour la caractérisation. La déformation d'interface a été mesurée et l'interface non renforcée a présenté la résistance à traction plus élevée par rapport les échantillons renforcés puisque la géogrigle diminue la surface de liaison efficace entre les couches

d'enrobé. Encore une fois, la géogridde n'était pas très mobilisée, peut-être à cause du glissement de l'interface.

La troisième campagne expérimentale concernait la caractérisation à la fatigue. Des essais de traction-compression sinusoïdale à 10°C, 10 Hz et à déformation contrôlée à différentes amplitudes (80, 90, 100 et 110  $\mu\text{m/m}$ ) ont été effectués. Les différents complexes présentaient une sensibilité distincte à la variation d'amplitude de déformation des courbes de Wöhler. Pour la méthode de dimensionnement française des chaussées, selon le paramètre  $\varepsilon_6$  obtenu dans ce travail, l'effet de renforcement de la géogridde était négligeable. Cependant, le paramètre de pente de la courbe de Wöhler ( $-1/b$ ) a montré une contribution positive de la géogridde, notamment celui contenant du SBS dans la couche d'accrochage.

La quatrième campagne expérimentale a porté sur la caractérisation sur la résistance à la propagation des fissures. L'essai *four-point bending notched fracture* (FPBNF), développé au LTDS/ENTPE, a été réalisé sur les échantillons prismatiques en forme de poutre. Un dispositif de corrélation d'image numérique (DIC) 3D a été utilisé pour calculer le champ de déformation pendant la propagation de la fissure ainsi que son hauteur. Un plateau de force, proportionnel à la résistance maximale à la traction de la géogridde, a été observé dans les résultats pour les échantillons renforcés liés à la mobilisation de la géogridde lors de l'essai. L'analyse DIC a mis en évidence la propriété de soulagement des contraintes due à la présence de géogriddes.

**Mots clés:** Enrobé bitumineux, géogridde en fibre de verre, module complexe, traction, fatigue, propagation de fissure



# ABSTRACT

This doctoral dissertation was developed at the Laboratory of Tribology and Dynamics of Systems (LTDS – *Laboratoire de Tribologie et Dynamique des Systèmes*) at the *Ecole Nationale des Travaux Publics de l'Etat* (ENTPE), France. It was part of a partnership between the French companies AfiteXinov and EIFFAGE Infrastructures. It also had the support of the Brazilian science without borders program from CNPq. The objective of this study is to contribute to the future development of new geosynthetics optimized to the reinforcement of bituminous mixtures. As well as to provide useful information that could allow the proposition of new design method for reinforced pavement structures. To this end, five slab configuration was conceived, four bi-layered and one whole, containing the same type of bituminous mixture regardless of the configuration. From the bi-layered slabs, three were reinforced with the combination of two fiberglass geogrids (50 and 100kN/m maximum tensile strength) with two emulsions as tack coat (bitumen pure and modified by SBS). The last bi-layered slab was unreinforced, containing only emulsion bitumen pure on its interface.

The first experimental campaign concerned the characterization of the behavior of cylindrical specimens reinforced by fiberglass geogrid at a small strain domain using cyclic tension-compression tests, called complex modulus tests. A new interface analysis method was proposed for complex modulus tests of specimens reinforced by geogrid and having the interface oriented perpendicularly to the longitudinal direction of the cylindrical sample. From test results, the interface behavior obtained was linear viscoelastic (LVE) and it could be modeled by 2S2PD model. However, a considerable low level of geogrid mobilization was observed during the test.

The second experimental campaign concerned characterization at monotonic axial tension loading. Three temperatures (0, 19, and 40°C) were combined with two strain rates of loading (2 and 0.002%/min) to the tension characterization. Interface strain was measured and the unreinforced interface presented the higher tensile strength than the reinforced specimens since the geogrid decreases the effective bonding surface between mixture layers. One more time, the geogrid was not highly mobilized possibly due to the slippage in the interface.

The third experimental campaign concerned fatigue characterization. Sinusoidal tension-compression tests at 10°C, 10Hz, and controlled strain at different amplitudes (80, 90, 100, and 110µm/m) were carried out. The different configurations presented distinct susceptibility to

strain amplitude variation of Wöhler curves. For the French design method for pavements, according to the parameter  $\varepsilon_6$  obtained in this work, the geogrid reinforcement effect was negligible. However, the Wöhler curve slope ( $-1/b$ ) parameter showed a positive contribution by the geogrid, especially containing SBS in the tack coat.

The fourth experimental campaign concerned the crack propagation resistance characterization. Four-point bending notched fracture (FPBNF) test was carried out using specimens in a beam shape. 3D Digital Image Correlation (DIC) device was used to calculate the strain field during the crack propagation as well as its tip. A force plateau, proportional to the geogrid maximum tensile strength, was observed in reinforced results related to the mobilization of the geogrid during the test. The DIC analysis evidenced the stress-relief property due to the geogrid presence.

**Keywords:** Bituminous mixtures, fiberglass geogrid, complex modulus, tension, fatigue resistance, cracking propagation resistance

# LIST OF TABLES

Table 2-1. Boltzmann superposition principle solicitations and responses .....	47
Table 2-2. Creep and relaxation tests equations .....	48
Table 2-3. Geotextile properties and characterization test methods standardized by ASTM (Zornberg and Thompson, 2010) .....	77
Table 2-4. Beams dimensions found in the literature for tests with reinforced specimens .....	84
Table 2-5. Different types of Geosynthetics found in literature and the tack coat information for its installation.....	89
Table 2-6. Information of experimental characterization concerning bituminous mixtures reinforced by geosynthetics in literature .....	92
Table 3-1. Bituminous mixture components information and percentage of use.....	98
Table 3-2. Five different slabs configurations constitution and total of slabs produced for the study .....	101
Table 3-3. Air voids contents, averages and standard deviations of specimens from configuration A slabs .....	108
Table 3-4. Air voids contents, averages and standard deviations of specimens from configuration B slabs.....	110
Table 3-5. Air voids contents, averages and standard deviations of specimens from configuration C slabs.....	113
Table 3-6. Air voids contents, averages and standard deviations of specimens from configuration D slabs .....	115
Table 3-7. Air voids contents, averages and standard deviations of specimens from configuration E slabs.....	116
Table 3-8. Number of specimens necessity in function of each test on experimental campaign for each slab configuration .....	118
Table 4-1. Tested specimens' composition, air voids and instrumentation information	130
Table 4-2. Coefficients of 2S2P1D model calibrated in A1-H3 test results ( $T_{ref} = 15^{\circ}C$ ) .....	137
Table 4-3. Coefficients of 2S2P1D model calibrated for C2-V1 test results concerning the mixture $E_A^*$ .....	140

Table 4-4. Coefficients of 2S2P1D model calibrated for C2-V1 test results concerning the interface .....	141
Table 4-5. Coefficients of 2S2P1D model calibrated for C2-H3 test results ( $T_{ref} = 15^{\circ}C$ ) .....	144
Table 4-6. Coefficients of 2S2P1D model calibrated for mixtures test results .....	146
Table 4-7. Coefficients $v_{00}$ and $v_0$ of 2S2P1D model calibrated for mixtures test results .....	150
Table 4-8. Coefficients of 2S2P1D model calibrated for interface complex modulus ( $K_G^*$ ) .....	153
Table 5-1. Tested specimens' composition, air voids and testing temperatures and strain rates .....	166
Table 5-2. Slow strain rate ( $\epsilon_{slow}$ ) calculated using $a_T$ calculated from WLF model from LVE properties .....	175
Table 5-3. Slow strain rate ( $\epsilon_{slow}$ ) calculated using $a_T$ obtained from frequency sweep tests and used for the tension tests.....	178
Table 6-1. Considered fatigue criteria and graphics to be used.....	212
Table 6-2. Tested specimens' composition, air voids and strain amplitudes .....	213
Table 6-3. Variation between the five different $N_f$ concerning the specimens from configuration A .....	223
Table 6-4. Variation between the five different $N_f$ concerning the specimens from configuration B.....	224
Table 6-5. Variation between the five different $N_f$ concerning the specimens from configuration C.....	225
Table 6-6. Variation between the five different $N_f$ concerning the specimens from configuration D .....	226
Table 6-7. Variation between the five different $N_f$ concerning the specimens from configuration E.....	227
Table 7-1. Tested specimens' composition, air voids in bituminous mixture and temperatures .....	247
Table 7-2. Forces measured at 2mm of deflection on the tested specimens and corresponding pivot height ( $h$ ) .....	253

# LIST OF FIGURES

Figure 2-1. Scheme of a flexible structure and terminology .....	32
Figure 2-2. Scheme of volumetric properties of a bituminous mixture.....	37
Figure 2-3. Crude oil components refining process (Canadian Fuel Association website). .....	39
Figure 2-4. Schematic representation of bitumen type sol (above), type gel (below), and some of its components (Read et al. 2003) .....	40
Figure 2-5. Different gradation curves plotted in x-axis raised to a 0.45 power .....	43
Figure 2-6. Scheme of loading due to traffic and the response on pavement layers (adapted after Di Benedetto, 1998) .....	44
Figure 2-7. Scheme of thermal loading and corresponding pavement response (adapted after Di Benedetto, 1998) .....	45
Figure 2-8. Typical mechanical behavior domains of bituminous mixtures depending on strain amplitude $\varepsilon$ and number of cycles $N$ , for a given temperature (Di Benedetto et al., 2013). .....	46
Figure 2-9. Cancellation tests: strain input (left side) and stress response (right side) ....	47
Figure 2-10. (a) Creep and (b) relaxation tests for a linear viscoelastic material.....	48
Figure 2-11. Example of complex modulus test on a LVE material: sinusoidal signals of axial stress $\sigma(t)$ , axial strain $\varepsilon_1(t)$ and radial strain $\varepsilon_2(t)$ .....	49
Figure 2-12. Example of time-temperature superposition principle verification for linear viscoelasticity of bituminous mixture (Nguyen et al. 2013a). .....	52
Figure 2-13. 2S2P1D model: (a) constants associated with constitutive elements of the model on a general Cole–Cole curve and (b) mechanical analogues.....	54
Figure 2-14. Example of Wöhler curve: loading amplitude versus number of cycles to failure (fatigue life) (Di Benedetto & Corté 2005) and the endurance limit of perpetual pavement of Carpenter et al. (2003).....	56
Figure 2-15. Schematic representation of loading: (a) and (b) strain, or (c) and (d) stress and their respective responses (stress or strain) (Di Benedetto & Corté 2005). .....	58
Figure 2-16. Three phases of fatigue testing evolution in complex modulus (normalized), phase angle and number of cycle axis.....	59

Figure 2-17. Different types of cracks found in flexible pavements (FHWA 2003): (a) Longitudinal Cracks, (b) Fatigue Cracks, (c) Transverse Cracks, (d) Reflective Cracks, (e) Block Cracks, (f) Edge Cracks .....	62
Figure 2-18. Crack representation: perpendicular plane to the crack plane (Di Benedetto & Corté 2005).....	62
Figure 2-19. Fracture failure modes (Bui 1978).....	63
Figure 2-20. Pre-notched four point bending test specimen.....	64
Figure 2-21. Determination of area under the loading curve in the axes force (P) and displacement (u) .....	65
Figure 2-22. Different types of cracking propagation tests in bitumen and bituminous mixtures (Di Benedetto & Corté 2005) .....	67
Figure 2-23. Four-point bending notched fracture (FPBNF) test at ENPTE (Nguyen et al. 2008).....	68
Figure 2-24. Installation of steel mesh for reinforcement of pavements in Michigan/USA (Williams 1953).....	69
Figure 2-25. Construction sites with use of fiberglass geogrid solution to reinforce pavements against reflective cracking in France: (a) Toulouse Blagnac Airport, October 2010 (6D Solution website), (b) Rehabilitation of Charles de Gaulle Airport, Paris 2016 (Colas website). .....	71
Figure 2-26. Construction site with use of fiberglass geogrid solution to reinforce the highway A7 in Montélimar in 2018 by EIFFAGE Infrastructures using the fiberglass geogrid Notex Glass C <sup>®</sup> provided by Afitexinov .....	71
Figure 2-27. Different types of geosynthetic interlayer for pavement reinforcement: (a) Geotextile (MTAG 2009), (b) Paving Mat (MTAG 2009), (c) Geogrid (MTAG 2009), (d) Geocomposite (MTAG 2009), (e) Geomembrane (MTAG 2009), (f) Geocell (Pavco Geosoft <sup>®</sup> ) .....	73
Figure 2-28. Separation function example of a geotextile placed between base aggregate and a soft layer underneath (Zornberg and Thompson, 2010): (a) without geotextile, (b) with geotextile. ....	74
Figure 2-29. Pavement trench drain using a geotextile for filtration (Zornberg and Thompson, 2010) .....	75
Figure 2-30. Scheme of unbound layers reinforcement mechanisms provided by geosynthetics (edited after Zornberg and Thompson, 2010): (a) Lateral restraint, (b) Increased bearing capacity, (c) Membrane type of support.....	78

Figure 2-31. Destructive adhesion test characterization schemes: (a) Leutner Device (Sagnol et al. 2019), (b) Wedge splitting test (Tschegg et al. 2012), (c) Double shear tester (Cho et al. 2016, Safavizadeh and Kim 2014), (d) ASTRA device (Ferrotti et al. 2011), (e) 2T3C Hollow Cylinder Apparatus (Attia et al. 2017) .....	84
Figure 3-1. Bituminous mixture (BBSG 0/10) gradation curve .....	97
Figure 3-2. Fiberglass geogrid Notex Glass® C 50/50-25 and 100/100-25 compositions and coated with bitumen (used in this doctoral thesis) produced by Afitexinov .....	99
Figure 3-3. Force vs elongation characterization of fiberglass geogrid Notex Glass® C in machine direction: (a) 50/50-25 and (b) 100/100-25 .....	100
Figure 3-4. Slab fabrication of reinforced bi-layered bituminous mixture: (a) First layer compaction, (b) Emulsion first application, (c) Fiberglass geogrid placement, (d) Emulsion second application, (e) Upper layer fabrication, and (f) Final compaction.....	103
Figure 3-5. Coring plans in order to obtain three different types of specimen: (a) Plan 1: mix between specimens V and H, (b) Plan 2: specimens H, and (c) Plan 3: mix between specimen H and beams.....	104
Figure 3-6. Additional coring plan for slabs C to allow obtaining specimens with larger diameters (136mm): (a) Plan 1b, and (b) Plan 4 .....	105
Figure 3-7. Coring of 75mm diameter cylindrical specimens from slab: (a) Coring machine, (b) Type H specimen coring, and (c) Types H (left) and V (right) cored specimens before the final trimming.....	105
Figure 3-8. Nomenclature system for bituminous mixtures specimens .....	106
Figure 3-9. Air voids of the specimens cored from the slab A1 .....	107
Figure 3-10. Air voids of the specimens cored from the slab A2.....	107
Figure 3-11. Air voids of the specimens cored from the slab A3.....	107
Figure 3-12. Air voids of the specimens cored from the slab A4.....	108
Figure 3-13. Air voids of the specimens cored from the slab B1 .....	109
Figure 3-14. Air voids of the specimens cored from the slab B2.....	109
Figure 3-15. Air voids of the specimens cored from the slab B3 .....	109
Figure 3-16. Air voids of the specimens cored from the slab C1 .....	111
Figure 3-17. Air voids of the specimens cored from the slab C2.....	111
Figure 3-18. Air voids of the specimens cored from the slab C3.....	111
Figure 3-19. Air Voids of the specimens cored from the slab C4.....	112
Figure 3-20. Air voids of the specimens cored from the slab CE (fabricated with $2 \times 240 \text{g/m}^2$ of residual binder emulsion within the interface).....	112

Figure 3-21. Air voids of the specimens cored from the slab D1 .....	114
Figure 3-22. Air voids of the specimens cored from the slab D2.....	114
Figure 3-23. Air voids of the specimens cored from the slab D3.....	114
Figure 3-24. Air voids of the specimens cored from the slab E1 .....	115
Figure 3-25. Air voids of the specimens cored from the slab E2 .....	116
Figure 3-26. Air voids of the specimens cored from the slab E3 .....	116
Figure 3-27. Testing parameters combination scheme for tension test (temperature and strain loading rate).....	118
Figure 4-1. Hydraulic press INSTRON <sup>®</sup> with thermal chamber B.I.A. Climatic <sup>®</sup> used to carry out the experimental campaign .....	121
Figure 4-2. Picture and scheme presenting the specimen (reinforced type V) set up and instrumentation in the hydraulic press for testing .....	123
Figure 4-3. Complex modulus testing protocol: (a) temperatures, and (b) frequencies for the different temperatures and time for temperature conditioning.....	124
Figure 4-4. Scheme showing the radial measurement regarding the two specimen coring directions (a) type V and (b) type H.....	125
Figure 4-5. Continuous Mechanics interface calculation hypothesis scheme .....	128
Figure 4-6. Results obtained for each tested temperature for A1-H3: (a) Norm of complex modulus, (b) Phase angle, (c) Norm of Poisson's ration and (d) Phase angle of Poisson's ratio .....	132
Figure 4-7. (a) Cole-Cole plot and (b) Black space obtained for specimen A1-H3 .....	132
Figure 4-8. (a) Cole-Cole plot and (b) Black space of Poisson's ratio for A1-H3 .....	133
Figure 4-9. Construction of master curves of (a) norm of complex modulus, (b) phase angle of complex modulus, (c) Poisson's ratio, and (d) phase angle of Poisson's ratio.....	134
Figure 4-10. Shift factor ( $a_T$ ) values in function of testing temperature and WLF fitting for complex modulus test of (a) A1-H3 and (b) All specimens.....	135
Figure 4-11. 2S2P1D model calibrated for A1-H3 testing results: (a) Cole-Cole of $E^*$ , (b) Black space of $E^*$ , (c) Cole-Cole of $\nu^*$ , and (d) Black space of $\nu^*$ .....	136
Figure 4-12. 2S2P1D model calibrated for A1-H3 testing master curves: (a) norm of complex modulus, (b) phase angle of complex modulus, (c) Poisson's ratio, and (d) phase angle of Poisson's ratio.....	137
Figure 4-13. Experimental results ( $E_{l1}$ (25mm) and $E_{l2}$ (90mm)) plotted with calculated bituminous mixture modulus ( $E_A^*$ ) for the specimen C2-V1 in (a) Cole-Cole plan and (b) Black space .....	138



Figure 4-14. Master curves results ( $E_{I1}$  (25mm) and  $E_{I2}$  (90mm)) plotted with calculated bituminous mixture modulus ( $E_A^*$ ) for the specimen C2-V1 for (a) norm of complex modulus and (b) phase angle..... 139

Figure 4-15. Specimen C2-V1 master curves of norm of Poisson’s ration ( $T_{ref} = 15^\circ\text{C}$ ) obtained for the radial directions (a) III and (b) I ..... 139

Figure 4-16. Specimen C2-V1 interface complex modulus considering interface as an equivalent layer for three different thicknesses (1.0, 2.5 and 5.0mm) and considering interface infinitely fine in (a) Cole-Cole, (b) Black space, and (c) master curve of  $|E_G^*|$  or  $|K_G^*|$  ..... 141

Figure 4-17. Interface of C2-V1 normalized complex modulus ( $E_{norm}^*$ ) and complex modulus stiffness ( $K_{norm}^*$ ) (points) and 2S2P1D model (line): (a) Cole-Cole plan, (b) Black space, (c) master curve of norm of complex modulus, and (d) master curve of phase angle 142

Figure 4-18. Experimental results ( $E_{I1}$  (25mm) and  $E_{I2}$  (90mm)) for the specimen C2-H3 in (a) Cole-Cole plan and (b) Black space ..... 143

Figure 4-19. Specimen C2-H3 master curves of the norm of Poisson’s ration ( $T_{ref} = 15^\circ\text{C}$ ) obtained for the radial directions (a) III and (b) II ..... 144

Figure 4-20. Complex modulus test results for type V samples and 2S2P1D model for each test in (a) Cole-Cole plan and (b) Black space..... 145

Figure 4-21. Complex modulus test results for type H samples and 2S2P1D simulations for each test in (a) Cole-Cole plan and (b) Black space..... 146

Figure 4-22. Glassy modulus ( $E_0$ ) against voids content for all tested samples..... 147

Figure 4-23. Complex modulus test results of all specimens in normalized Cole-Cole plan ..... 148

Figure 4-24. Complex modulus test results of all specimens in normalized Black space ..... 148

Figure 4-25. Normalized master curve of the norm of the complex modulus of all specimens ..... 149

Figure 4-26. Normalized master curve of the norm of the phase angle of all specimens ..... 149

Figure 4-27. Normalized master curve of the norm of Poisson’s ratio of all specimens 151

Figure 4-28. Normalized master curve of the norm of complex modulus and Poisson’s ratio of all specimens ..... 151

Figure 4-29. Interface complex modulus ( $K_G^*$ ) test results in Cole-Cole plan ..... 152

Figure 4-30.  $K_{G0}$  obtained for each tested specimen ..... 152

Figure 4-31. Normalized interface complex stiffness ( $K_G^*$ ) test results in Cole-Cole plan .....	154
Figure 4-32. Interface complex modulus ( $E_G^*$ ) test results in Cole-Cole plan fixing $E_0 = 3\text{GPa}$ as reference .....	155
Figure 4-33. Thicknesses to consider to obtain the same $E_G^*$ of the interface using $E_0 = 3\text{GPa}$ as reference .....	155
Figure 4-34. Complex modulus test results in Black space of unreinforced specimens plotted with CE-H4 with different percentages of geogrid mobilization for the definition of the real percentage of mobilization .....	157
Figure 4-35. Complex modulus test in Black space for all type H reinforced specimens considering at the percentage of geogrid mobilization during the test ( $C_{MAX}$ ).....	158
Figure 4-36. Percentage of geogrid mobilization in specimens H during complex modulus test for each slab configuration .....	158
Figure 5-1. Experimental program: combinations between temperatures and strain rates .....	163
Figure 5-2. Example of the tension test for $19^\circ\text{C}$ and $2\%/min$ .....	164
Figure 5-3. Example of slow rate determination in tension test concerning $19^\circ\text{C}$ , fast rate ( $2\%/min$ ) and $0^\circ\text{C}$ , slow rate. ....	164
Figure 5-4. Example of tension test result of specimen A3-H4: (a) axial strain vs testing time for $l_1$ “25mm” (controlling) and $l_2$ “90mm” (measuring), (b) axial stress vs testing time, and (c) classical stress-strain curve for $l_1$ “25mm” (controlling) and $l_2$ “90mm” (measuring). .....	170
Figure 5-5. Example of tension test result of specimen C2-V5: (a) axial strain vs testing time for $l_1$ “25mm”, $l_2$ “90mm”, and bituminous mixture only ( $\epsilon_A$ ), (b) axial stress vs testing time, and (c) classical stress-strain curve for $l_1$ “25mm”, $l_2$ “90mm”, and bituminous mixture only ( $\epsilon_A$ ).....	171
Figure 5-6. Interface strain behavior to tension loading for specimen C2-V5: (a) Stress vs interface strain graphic for the three chosen thicknesses: 1.0, 2.5 and 5.0mm, and (b) Stress vs interface gap ( $\Delta u$ ).....	172
Figure 5-7. Relationship between $\epsilon_A$ (bituminous mixture) and the $\epsilon_G$ (interface) evolution during the tension test, concerning the three chosen thickness (1, 2.5 and 5mm) .....	173
Figure 5-8. Tension test carried out at $40^\circ\text{C}$ and $2\%/min$ in specimens type V with two different diameters (75 and 136mm): (a) stress vs $\epsilon_A$ , and (b) stress vs $\Delta u$ . ....	174

Figure 5-9. Tension test carried out at 19°C and 2%/min in specimens type V with two different diameters (75 and 136mm): (a) stress vs $\epsilon_A$ , and (b) stress vs $\Delta u$ .	174
Figure 5-10. Frequency sweep test shifted curves for configuration A (no interface): (a) test results at 19°C shifted to fit the 2S2P1D curve at $T_{ref}=40^\circ\text{C}$ , and (b) test results at 0°C shifted to fit the 2S2P1D curve at $T_{ref}=19^\circ\text{C}$ .	176
Figure 5-11. Frequency sweep test shifted curves for configuration B (interface containing only emulsion bitumen): (a) test results at 19°C shifted to fit the 2S2P1D curve at $T_{ref}=40^\circ\text{C}$ , and (b) test results at 0°C shifted to fit the 2S2P1D curve at $T_{ref}=19^\circ\text{C}$ .	177
Figure 5-12. Frequency sweep test shifted curves for configuration C (geogrid 100kN/m with emulsion bitumen): (a) test results at 19°C shifted to fit the 2S2P1D curve at $T_{ref}=40^\circ\text{C}$ , and (b) test results at 0°C shifted to fit the 2S2P1D curve at $T_{ref}=19^\circ\text{C}$ .	177
Figure 5-13. Frequency sweep test shifted curves for configuration D (geogrid 50kN/m with emulsion bitumen): (a) test results at 19°C shifted to fit the 2S2P1D curve at $T_{ref}=40^\circ\text{C}$ , and (b) test results at 0°C shifted to fit the 2S2P1D curve at $T_{ref}=19^\circ\text{C}$ .	178
Figure 5-14. Frequency sweep test shifted curves for configuration E (geogrid 50kN/m with emulsion bitumen modified by SBS): (a) test results at 19°C shifted to fit the 2S2P1D curve at $T_{ref}=40^\circ\text{C}$ , and (b) test results at 0°C shifted to fit the 2S2P1D curve at $T_{ref}=19^\circ\text{C}$ .	178
Figure 5-15. Tension test results concerning configuration A, type H, pair 40°C with fast strain rate and 19°C with slow strain rate: (a) stress vs strain, and (b) strain vs equivalent time (test loading input).	181
Figure 5-16. Tension test results concerning configuration A, type H, pair 19°C with fast strain rate and 0°C with slow strain rate: (a) stress vs strain, and (b) strain vs equivalent time (test loading input).	181
Figure 5-17. Tension test results concerning configuration B, type H, pair 40°C with fast strain rate and 19°C with slow strain rate: (a) stress vs strain, and (b) strain vs equivalent time (test loading input).	182
Figure 5-18. Tension test results concerning configuration B, type H, pair 19°C with fast strain rate and 0°C with slow strain rate: (a) stress vs strain, and (b) strain vs equivalent time (test loading input).	183
Figure 5-19. Tension test results concerning configuration C, type H, pair 40°C with fast strain rate and 19°C with slow strain rate: (a) stress vs strain, and (b) strain vs equivalent time (test loading input).	184

Figure 5-20. Tension test results concerning configuration C, type H, pair 19°C with fast strain rate and 0°C with slow strain rate: (a) stress vs strain, and (b) strain vs equivalent time (test loading input) ..... 185

Figure 5-21. Tension test results concerning configuration D, type H, pair 40°C with fast strain rate and 19°C with slow strain rate: (a) stress vs strain, and (b) strain vs equivalent time (test loading input) ..... 186

Figure 5-22. Tension test results concerning configuration D, type H, pair 19°C with fast strain rate and 0°C with slow strain rate: (a) stress vs strain, and (b) strain vs equivalent time (test loading input) ..... 187

Figure 5-23. Tension test results concerning configuration E, type H, pair 40°C with fast strain rate and 19°C with slow strain rate: (a) stress vs strain, and (b) strain vs equivalent time at (test loading input)..... 188

Figure 5-24. Tension test results concerning configuration E, type H, pair 19°C with fast strain rate and 0°C with slow strain rate: (a) stress vs strain, and (b) strain vs equivalent time (test loading input) ..... 188

Figure 5-25. Tension test results concerning configuration A, type V, pair 40°C with fast strain rate and 19°C with slow strain rate: (a) stress vs strain, and (b) strain vs equivalent (test loading input) ..... 190

Figure 5-26. Tension test results concerning configuration A, type V, pair 19°C with fast strain rate and 0°C with slow strain rate: (a) stress vs strain, and (b) strain vs equivalent time (test loading input) ..... 190

Figure 5-27. Tension test results concerning configuration B, type V, pair 40°C with fast strain rate and 19°C with slow strain rate: (a) stress vs  $\epsilon_A$ , (b)  $\epsilon_A$  vs equivalent time (test loading input), (c) stress vs  $\Delta u$ , and (d)  $\Delta u$  vs equivalent time (interface rate of loading) ..... 192

Figure 5-28. Tension test results concerning configuration B, type V, pair 19°C with fast strain rate and 0°C with slow strain rate: (a) stress vs  $\epsilon_A$ , (b)  $\epsilon_A$  vs equivalent time (test loading input), (c) stress vs  $\Delta u$ , and (d)  $\Delta u$  vs equivalent time (interface rate of loading) ..... 193

Figure 5-29. Tension test results concerning configuration C, type V, pair 40°C with fast strain rate and 19°C with slow strain rate: (a) stress vs  $\epsilon_A$ , (b)  $\epsilon_A$  vs equivalent time (test loading input), (c) stress vs  $\Delta u$ , and (d)  $\Delta u$  vs equivalent time (interface rate of loading) ..... 194

Figure 5-30. Tension test results concerning configuration C, type V, pair 19°C with fast strain rate and 0°C with slow strain rate: (a) stress vs  $\epsilon_A$ , (b)  $\epsilon_A$  vs equivalent time (test loading input), (c) stress vs  $\Delta u$ , and (d)  $\Delta u$  vs equivalent time (interface rate of loading) ..... 195

Figure 5-31. Tension test results concerning configuration D , type V, pair 40°C with fast strain rate and 19°C with slow strain rate: (a) stress vs  $\varepsilon_A$ , (b)  $\varepsilon_A$  vs equivalent time (test loading input), (c) stress vs  $\Delta u$ , and (d)  $\Delta u$  vs equivalent time (interface rate of loading) ..... 196

Figure 5-32. Tension test results concerning configuration D, type V, pair 19°C with fast strain rate and 0°C with slow strain rate: (a) stress vs  $\varepsilon_A$ , (b)  $\varepsilon_A$  vs equivalent time (test loading input), (c) stress vs  $\Delta u$ , and (d)  $\Delta u$  vs equivalent time (interface rate of loading) ..... 197

Figure 5-33. Tension test results concerning configuration E, type V, pair 40°C with fast strain rate and 19°C with slow strain rate: (a) stress vs  $\varepsilon_A$ , (b)  $\varepsilon_A$  vs equivalent time (test loading input), (c) stress vs  $\Delta u$ , and (d)  $\Delta u$  vs equivalent time (interface rate of loading) ..... 198

Figure 5-34. Tension test results concerning configuration E, type V, pair 19°C with fast strain rate and 0°C with slow strain rate: (a) stress vs  $\varepsilon_A$ , (b)  $\varepsilon_A$  vs equivalent time (test loading input), (c) stress vs  $\Delta u$ , and (d)  $\Delta u$  vs equivalent time (interface rate of loading) ..... 199

Figure 5-35. Peak points obtained from the tension tests results plotted in stress vs strain, concerning the pair 40°C with fast strain rate and 19°C with slow strain rate, type H specimen: (a) maximum tensile strength ( $\sigma_{peak}$ ) and (b)  $\varepsilon_{peak}$  ..... 200

Figure 5-36. Peak points obtained from the tension tests results plotted in stress vs strain, concerning the pair 19°C with fast strain rate and 0°C with slow strain rate, type H specimen: (a) tensile strength ( $\sigma_{peak}$ ) and (b)  $\varepsilon_{peak}$  ..... 202

Figure 5-37. Maximum tensile strength ( $\sigma_{peak}$ ) of type H specimens tested at 40°C and 19°C and at 2%/min..... 202

Figure 5-38. Peak points obtained from the tension tests results plotted in stress vs strain, concerning the pair 40°C with fast strain rate and 19°C with slow strain rate, type V specimen: (a) maximum tensile strength ( $\sigma_{peak}$ ) and (b)  $\Delta u_{peak}$  ..... 204

Figure 5-39. Peak points obtained from the tension tests results plotted in stress vs strain, concerning the pair 19°C with fast strain rate and 0°C with slow strain rate, type V specimen: (a) maximum tensile strength ( $\sigma_{peak}$ ) and (b)  $\Delta u_{peak}$  ..... 205

Figure 5-40. Interface tensile strength ( $\sigma_{peak}$ ) of type V specimens tested at 40°C and 19°C and at 2%/min..... 206

Figure 6-1. Instrumental setup scheme: extensometers and temperature probe location 210

Figure 6-2. Scheme of recorded cycles during the fatigue test (adapted from Mangiafico, 2014)..... 212

Figure 6-3. Local measurements during fatigue tests, concerning B3-H4: (a) extensometers  $l_1$  (72.5mm) and  $l_2$  (75mm) and their average vs testing number of cycles, (b) divergence of

individual extensometer measurement in relation to the strain average, and (c) divergence of individual extensometer phase angle measurement in relation to the average phase angle...	216
Figure 6-4. Global measurements during fatigue tests, concerning B3-H4: (a) $ E^* $ vs $N$ curve, (b) $ E^* / E^* _0$ vs $N$ curve, (c) Phase angle vs $N$ curve, (d) stress vs $N$ curve, (e) Cole-cole plot, (f) Black diagram, and (g) Temperature vs $N$ curve. ....	218
Figure 6-5. Representation of the different $N_f$ values of the B3-H4 fatigue test according to each failure criterion.....	219
Figure 6-6. Fatigue test results in normalized complex modulus vs number of cycles at different strain levels concerning configuration A.....	220
Figure 6-7. Fatigue test results in normalized complex modulus vs number of cycles at different strain levels concerning configuration B.....	220
Figure 6-8. Fatigue test results in normalized complex modulus vs number of cycles at different strain levels concerning configuration C.....	221
Figure 6-9. Fatigue test results in normalized complex modulus vs number of cycles at different strain levels concerning configuration D.....	221
Figure 6-10. Fatigue test results in normalized complex modulus vs number of cycles at different strain levels concerning configuration E.....	222
Figure 6-11. $N_f$ values obtained from to the five different criteria and their average at different strain levels concerning configuration A.....	222
Figure 6-12. $N_f$ values obtained from to the five different criteria and their average at different strain levels concerning configuration B.....	224
Figure 6-13. $N_f$ values obtained from to the five different criteria and their average at different strain levels concerning configuration C.....	225
Figure 6-14. $N_f$ values obtained from to the five different criteria and their average at different strain levels concerning configuration D.....	226
Figure 6-15. $N_f$ values obtained from to the five different criteria and their average at different strain levels concerning configuration E.....	227
Figure 6-16. Wöhler curve of configuration A and $\varepsilon_6$ estimation.....	228
Figure 6-17. Wöhler curve of configuration B and $\varepsilon_6$ estimation.....	229
Figure 6-18. Wöhler curve of configuration C and $\varepsilon_6$ estimation.....	229
Figure 6-19. Wöhler curve of configuration D and $\varepsilon_6$ estimation.....	230
Figure 6-20. Wöhler curve of configuration E and $\varepsilon_6$ estimation.....	230
Figure 6-21. Fatigue test results in Wöhler curves for all analyzed configurations, reinforced and unreinforced specimens.....	231

Figure 6-22. Analysis of parameter used in the French design methods of pavements: (a) strain amplitude corresponding to one million cycles loading fatigue life ( $\epsilon_6$ ) with its uncertainty ( $\Delta\epsilon_6$ ), and (b) slope of Wöhler curves ( $-1/b$ ) ..... 232

Figure 7-1. Hydraulic press, thermal chamber with extension and cameras used during FPBNF test ..... 238

Figure 7-2. Experimental test device and procedure for FPBNF: scheme of specimen and measurement device location ..... 239

Figure 7-3. Detail of beam specimen obtained from sawing and prepared for testing: (a) position of specimen from the slab, and (b) pre-notch size and interface position in beam height ..... 240

Figure 7-4. Actuator displacement and force versus time during the FPBNF test on specimen A2-B3 ..... 241

Figure 7-5. Pictures of the target with black dots for calibration of stereocorrelation taken at the same time by two different cameras: (a) camera on the left, and (b) camera on the right ..... 242

Figure 7-6. Virtual gauge lines and coordinates origin in the area of interest used in VIC-3D software for DIC analysis ..... 243

Figure 7-7. Horizontal strain curve with color scale obtained from virtual gauge line 7 (14mm of height) in DIC analysis of A2-B3 for: (a) at 0s, (b) at 342s, and (c) at 390s ..... 244

Figure 7-8. Explanation of analysis performed from data obtained with DIC using Vic-3D software ..... 245

Figure 7-9. Explanation of correction performed in the calculation of average strain versus beam height ..... 246

Figure 7-10. FPBNF test results example for specimen B1-B2: (a) force measured in the load cell, (b) force versus actuator displacement (test input), and (c) crack height tip evolution measured from DIC analysis ..... 248

Figure 7-11. Force and crack tip height in function of beam deflection for specimen B1-B2 ..... 249

Figure 7-12. Force versus deflection curve results: (a) unreinforced configurations containing interface (B) and not (A), (b) configuration C (100kN/m), (c) configuration D (50kN/m), and (d) configuration E (100kN/m and SBS) ..... 250

Figure 7-13. Force measured at peak of tested specimens ..... 251

Figure 7-14. Force versus deflection curve results comparative between configurations ..... 251

Figure 7-15. Illustration of four points bending beam pivoting around a hinge, supported only by the geogrid, used to calculate the pivot height ( $h$ ) of the hinge ..... 252

Figure 7-16. Crack tip height versus beam deflection results: (a) unreinforced configurations containing interface (B) and not (A), (b) configuration C (100kN/m) with unreinforced configurations, (c) configuration D (50kN/m) with unreinforced configurations, and (d) configuration E (100kN/m and SBS) with unreinforced configurations ..... 255

Figure 7-17. Treated images of tested specimens at the end of crack propagation: (a) A2-B2, (b) A2-B3, (c) B1-B2, (d) C3-B1, (e) C3-B2, (f) C3-B3, (g) D1-B2, (h) D1-B3, (i) E1-B1, and (j) E1-B2 ..... 256

Figure 7-18. Illustration of area underneath the curve  $P$  versus actuator displacement used to the energy restitution rate ( $G_f$ ) calculation ..... 257

Figure 7-19. Energy restitution rate ( $G_f$ ) obtained for the tested specimens ..... 258

Figure 7-20. Analysis of average and maximum strain versus beam height concerning A2-B3: (a) three analyzed points emphasized in  $P$  versus deflection curve, (b) point 1,  $t = 342s$ , (c) point 2,  $t = 390s$ , and (d) point 3,  $t = 420s$  ..... 260

Figure 7-21. Analysis of average and maximum strain versus beam height concerning B1-B2: (a) three analyzed points emphasized in  $P$  versus deflection curve, (b) point 1,  $t = 306s$ , (c) point 2,  $t = 333s$ , and (d) point 3,  $t = 360s$  ..... 262

Figure 7-22. Analysis of average and maximum strain versus beam height concerning D1-B3: (a) four analyzed points emphasized in  $P$  versus deflection curve, (b) point 1,  $t = 306s$ , (c) point 2,  $t = 348s$ , (d) point 3,  $t = 456s$ , and (e) point 4,  $t = 904s$ ..... 265

Figure 7-23. Average strain versus beam height at the point of force peak for all tested specimens: (a) unreinforced configurations containing interface (B) and not (A), (b) configuration C (100kN/m), (c) configuration D (50kN/m), and (d) configuration E (100kN/m and SBS)..... 266

Figure 7-24. Average strain versus beam height at the point of 1mm of displacement for all tested specimens: (a) unreinforced configurations containing interface (B) and not (A), (b) configuration C (100kN/m), (c) configuration D (50kN/m), and (d) configuration E (100kN/m and SBS)..... 267



# MAIN SYMBOLS

Symbol	Definition
$A_v$	Air voids in bituminous mixture
$\sigma(t)$	Normal stress signal, as a function of time
$\varepsilon_1(t)$	Axial strain signal, as a function of time
$\varepsilon_2(t), \varepsilon_3(t)$	Orthogonal transverse strains with respect to $\varepsilon_1(t)$
$\varepsilon_{0j}, \sigma_0$	Amplitude of a given signal
$f$	Loading frequency
$\omega$	Loading pulsation (angular frequency)
$C_1, C_2$	Williams-Landel-Ferry equation constants
$T$	Temperature
$T_{ref}$	Reference temperature for a mastercurve
$a_T$	Time-shift factor from Time-Temperature Superposition
$E$ and $D$	Elastic Young's modulus and elastic compliance
$\nu$	Elastic Poisson's ratio
$E^*, \nu^*$	Complex modulus, and complex Poisson's ratio
$ E^* ,  \nu^* $	Norm of a given complex property
$\varphi_{E^*}, \varphi_{\nu^*}$	Phase angle of a given complex property
$\varphi$	Phase angle
$E_1 = Real(E^*)$	Real part of complex modulus
$E_2 = Imag(E^*)$	Imaginary part of complex modulus
$E_A^*$	Bituminous mixture complex modulus of reinforced specimen
$E_G^*$	Interface layer complex modulus of reinforced specimen
$K_G^*$	Complex interface stiffness
$\varepsilon_A$	Axial strain of the bituminous mixture
$\varepsilon_G$	Axial strain of the interface layer
$\Delta u$	Interface displacement gap
$N$	Number of applied cycles
$N_f$	Number of cycles at fatigue failure
$\varepsilon_6$	Strain amplitude corresponding to one million cycles loading fatigue life
$a$	Crack tip height during cracking propagation
$G_f$	Fracture energy restitution rate

# Chapter 1: INTRODUCTION

Roadways are one of the most used infrastructure to transport people and goods around the world. Since the beginning of human civilization organization, roads constructions were necessary to allow people's traveling and economic development. Alongside human evolution, the roadways construction were also progressing in terms of technics, materials and performance. In these days, good quality roadways are capable of reducing the travel time between cities and vehicles maintenance costs. From engineering point of view, the roadways are pavement structures composed by multi-layers. Most pavements around the world are flexible, which contains a bituminous mixture in the surface layer.

The rehabilitation and maintenance of flexible pavements are fundamental to assure an optimal state of utilization and safety for the user. In addition, high deterioration level in roadways could lead to their complete loss of serviceability, which justifies the importance of the maintenance. Moreover, to repair deteriorated roadways, the governments shall spend huge amounts of money, meantime the maintenance costs are much smaller and effective to keep the roadway serviceability. Thus, advance and new strategies are necessary in order to avoid early deterioration and extend pavement's life. For this reason, new materials have been proposed to improve the pavements properties. In rehabilitation of pavements, steel meshes were employed in the 1950s and 1960s for the reinforcement of these structures. Evidence showed a reduction in rutting and cracking, as consequence of the reinforcement action (Brown et al. 1985; COST Action 2006). Interlayer reinforcement emerged in the 1930s as a solution to improve pavement structure performance by using woven cotton sheets immersed in liquid bitumen (Beckham and Mills 1935; Beck 1999). In the 1970s when the American Federal Highway Administration (FHWA) instituted the "National Experimental Evaluation Program" to reduce reflective cracking in roadways (FHWA 1974, Carver and Sprague 2000). Many interlayer systems have been analyzed by the pavement community ever since, among the range of available commercialized products, such as, sand asphalt; SAMIs (Stress Absorbing Membrane Interlayers, composed by a blend of bitumen and rubber.); fabrics or geotextiles; grids (steel, fiberglass and polymeric); and composites thereof (Vanelstraete and Franken 1997; COST Action 2006; South Africa 2008).

More recently, the use of fiberglass geogrids placed in bituminous mixtures layers has increased as a technical solution to rehabilitate pavements, extend its service life and reduce maintenance costs (de Bondt 2012). They could be used for both rehabilitation and construction

of new bituminous pavements (GMA 2002; COST Action 2006). The reinforcement by geogrid can be effective to reduce the main distresses in flexible pavements worldwide, rutting and cracking. According to some authors, fiberglass geogrids are preferable for presenting high-tension resistance and flexibility at once (Nguyen et al. 2013b). It is also thermally and chemically stable at mixing temperatures for bituminous mixtures (Darling and Woolstencroft 2004), and easily removable by milling in the case of further pavement maintenances. Many works also indicated that the fiberglass geogrid presents better performance to cracking resistance when compared to the other types of geogrids (Lyton 1988; de Bondt 1999; Brown et al. 2001; Canestrari et al. 2015). Geogrids are also effective on the reinforcement of unbound (granular) layers (Mamatha et al. 2019) and concrete pavements (Al-Hedad and Hadi 2019).

According to Vanelstraete and Franken (1997), two types of tests are majorly found in the literature for the characterization of bituminous mixtures reinforced by geogrids: adhesion tests and cracking resistance tests. Regarding the adhesion characterization, many different tests are found in the literature: Leutner test (Sagnol et al. 2019), Wedge splitting test (Jamek et al. 2012; Tschegg et al. 2012), ASTRA test (Ferrotti et al. 2011; Canestrari et al. 2015; Pasquini et al. 2015; Graziani et al. 2017) and double shear tests (Zamora-Barraza et al. 2010; Cho et al. 2016; Noory et al. 2017). Regarding the cracking resistance tests, some authors used three points bending (3Pb) test (Romeo et al. 2014; Canestrari et al. 2015; Graziani et al. 2016; Zofka et al. 2016), four points bending (4Pb) test (Virgili et al. 2009; Ferrotti et al. 2011; Canestrari et al. 2015; Safavizadeh et al. 2015; Arsenie et al. 2016) and other different bending tests (Komatsu et al. 1998; Khodaii et al. 2009; Millien et al. 2012; Obando-Ante & Palmeira 2015; Gonzalez-Torre et al. 2015; Fallah & Khodaii 2015; Pasquini et al. 2014; Gonzalez-Torre et al. 2016; Nejad et al. 2016). Besides, some authors used in situ experiments by building experimental roads reinforced by geogrids (Hornych et al. 2012; Nguyen et al. 2013b; Graziani et al. 2014; Canestrari et al. 2015). Mentioned works indicated a noticeable improvement in the performance of the bituminous mixtures due to the reinforcement, retarding the cracks initiation and propagation. Moreover, in recent works, Digital Image Correlation (DIC) technique was found to be an advantageous tool allowing the identification of different failure mechanisms during the crack propagation in reinforced beams and showing the stress-relieving capacity of geogrid reinforcements (Romeo et al. 2014; Canestrari et al. 2015). Interlayer reinforcement by geogrids is believed to work as a stress-relieving and crack-bridging component and thus, effective to delay reflective cracking (de Bondt 1999). Some authors present evidences the geogrid reinforcement is also effective to control permanent deformation in pavements (Komatsu et al.

1998; Laurinavicius & Oginskas 2006; Khodaii et al. 2009; Graziani et al. 2014; Guler & Atalay 2016; Mounes et al. 2016; Correia & Zornberg 2018).

Despite the advances recently made concerning adhesion and crack propagation of bituminous mixtures reinforced by fiberglass geogrids, further characterizations still need to be done. Those, from which the mechanical behavior of this interlayer system could be fully understood. Especially those linking with the pavement structures design. In addition, the reinforcement optimal location in bituminous mixtures is still a subject of discussion.

Regarding the presented context, this research's general objective is to contribute to the future development of new geosynthetics optimized to the reinforcement of bituminous mixtures. As well as to provide useful information which could allow the proposition of new design method for reinforced pavement structures. In the dissertation framework, the following specific objectives are:

- To verify the effect of fiberglass geogrid on the behavior of reinforced cylindrical specimens, cored in different slab directions, subjected to cyclic tension-compression tests at small strain loading amplitude. In addition, the effect of maximum geogrids strength and the polymer modification effect on the emulsion used as tack coat.
- To evaluate the LVE behavior and maximum tensile strength of interfaces containing or not fiberglass geogrid, and with pure bitumen or polymer modified emulsion used as tack coat.
- To verify the contribution of the fiberglass geogrid to the tensile strength of reinforced bituminous mixtures. Furthermore, to assess the influence of maximum geogrids strength on the bituminous mixtures tensile strength.
- To evaluate the influence of the presence of fiberglass geogrid and its maximum tensile strength on fatigue life of bituminous mixtures. Moreover, the influence of the type of emulsion tack used as tack coat (pure bitumen or polymer modified) on fatigue life of bituminous mixtures.
- To evaluate the contribution of the fiberglass geogrid reinforcement, and its maximum strength, in bituminous mixtures to the crack propagation on specimens having a beam shape.

This doctoral dissertation was developed at the Laboratory of Tribology and Dynamics of Systems (LTDS – *Laboratoire de Tribologie et Dynamique des Systèmes*) at the *Ecole Nationale des Travaux Publics de l'Etat* (ENTPE), France. It was part of a partnership between the

French companies Afiteixinov and EIFFAGE Infrastructures, and ENTPE. It also had the support of the Brazilian Science without Borders (CsF – *Ciência sem Fronteiras*) programme (PhD grant). In addition to this Introduction (Chapter 1) presenting the context of the study and its objectives, the dissertation comprises experimental and modelling approaches, organised as follows.

- Chapter 2 presents the theoretical background concerning bituminous mixtures, describing its formulation and mechanical behavior, and geosynthetics. It presents the historical used and the state-of-art in geosynthetics reinforcement for flexible pavement structures.
- Chapter 3 describes the materials used, the specimens composition and the four experimental campaigns conducted during the doctoral work.
- Chapter 4 presents the cyclic tension-compression campaign at small strain amplitude. It describes the device and the instrumentation used, presents the experimental results, the proposed methodology for interface analysis and LVE modelling using 2S2P1D model.
- Chapter 5 covers the tension test campaign. It describes the device and the instrumentation used and presents the discussions regarding the contribution of geogrid reinforcement in bituminous mixtures subjected to tensile loading. In addition, the time-temperature superposition principle in tensile loading is verified.
- Chapter 6 treats the fatigue damage performance increase linked to the geogrid reinforcement. Moreover, it presents the discussions regarding the geogrid effect in the fatigue parameters used in the French design method of flexible pavements.
- Chapter 7 presents the crack propagation experimental campaign presenting the four-point bending notched fracture (FPBNF) test used in the characterization. In addition, it presents the 3D Digital Image Correlation (DIC) device used to calculate the strain field during the crack propagation as well as its tip, evaluating the stress-relieving capacity of the fiberglass geogrid reinforcing bituminous mixtures
- Chapter 8 presents the conclusions and perspectives for future work.

# Chapter 2: LITERATURE REVIEW

2.1. Pavement structures .....	32
2.2. Pavements design method .....	33
2.3. Bituminous mixtures.....	36
2.3.1. Composition .....	39
2.3.2. Thermo-mechanical behavior.....	43
2.4. Linear viscoelastic behavior of materials .....	46
2.4.1. Definition .....	46
2.4.2. Creep, Relaxation and Convolution Integral.....	47
2.4.3. Complex modulus and Poisson's ratio .....	49
2.4.4. Time-Temperature Superposition Principle (TTSP) and Master Curves.....	51
2.4.5. Modelling LVE behavior .....	53
2.5. Fatigue in bituminous materials .....	55
2.5.1. Fatigue of bituminous binders, mastics and mixtures .....	55
2.5.2. Experimental observations and failure criteria.....	58
2.6. Cracking in bituminous materials.....	61
2.6.1. Cracking distresses presenting in flexible pavements.....	61
2.6.2. Introduction to Linear Fracture Mechanics (LFM) .....	62
2.6.3. Fracture energy determination .....	64
2.6.4. Crack propagation tests for bituminous mixtures .....	66
2.7. Overview of geosynthetics for pavements reinforcement .....	68
2.7.1. Background .....	68
2.7.2. Types of geosynthetics interlayers .....	71
2.7.3. Geosynthetic functions and behavior mechanisms .....	73
2.7.4. Geosynthetics important properties and characterization .....	76
2.7.5. Reinforcement of unbound layers .....	77
2.7.6. Reinforcement of bound layers .....	79

## 2.1. Pavement structures

A roadway pavement can be defined as a multilayered structure, built on a subgrade, designed to resist the loading from vehicular traffic and climate actions. This should also provide its users good using condition, with an appropriate level of comfort, economy, and safety. In addition, it should be impermeable on its surface, or at least avoid the water passage to the layers underneath. The layers could be bounded (surface course and base) or unbounded (sub-base) to each other. To the bonding of the layers, emulsions made by bitumen are usually used. Both can compose pavement surface course: bituminous mixtures or concrete. The base layer can be composed of bituminous mixtures or granular materials, treated or non-treated by hydraulic binders. Finally, sub-bases are usually composed of granular materials. Figure 2-1 illustrates a typical flexible pavement structure in accordance with FHWA (2006).

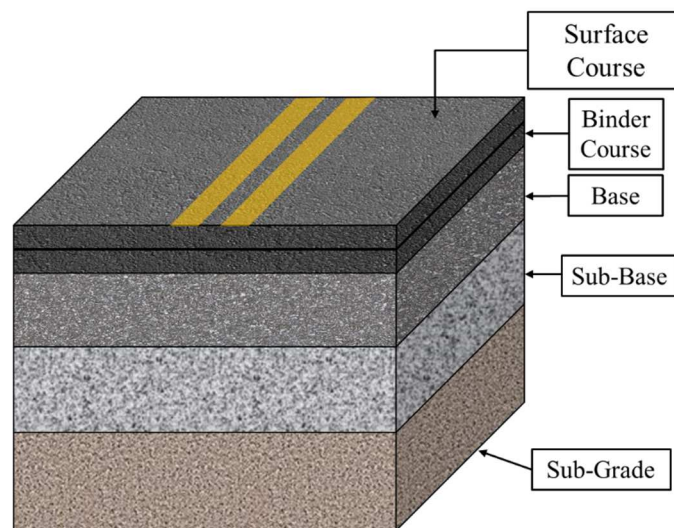


Figure 2-1. Scheme of a flexible structure and terminology

Different types of pavement structures exist in the roadway network in France. According to SETRA-LCPC (1994) there are six families of structures: flexible pavements; thick bituminous layer pavement; semi-rigid pavement; mixed-structure pavement; inverse-structure pavement and rigid pavement.

Flexible pavements are characterized by the presence of a thin bituminous mixture layer in the pavement surface course. The base layer is composed of bituminous mixture with thickness below 15cm over a sub-base layer composed of non-treated granular materials presenting

between 30 and 60cm of the total thickness. Its use is restrained to roadways with low traffic levels (SETRA-LCPC 1994).

Thick bituminous layers pavements are composed of a bituminous mixture surface layer laid over a single or double bituminous mixture layers base. The thickness for the base layer is between 15 and 40cm for this type of pavement structure. In addition, all interface between layers is bounded, and the bounding quality is very important to avoid a loss in structure serviceability.

The employment of materials treated by hydraulic binder as base and sub-base layers characterize the semi-rigid pavements. The thickness of the treated layers is normally between 20 and 50cm according to (SETRA-LCPC 1994). At the same time, it presents a bituminous mixture layer on the surface course.

Mixed-structure pavements are the combination between the bituminous mixture layer and the treated material layer. It has a bituminous mixture on the surface course layer over a bituminous base layer and over a sub-base layer made of materials treated by hydraulic binder. The structure is considered as “mixed” if the ratio between the thicknesses of the bituminous layer with the total pavement thickness is approximately 1/2.

Inverse-structure pavements are composed of bituminous mixture layers of around 15cm total thickness laid over a non-treated granular material (around 12cm). Then, these two layers are laid over a foundation composed of material treated by hydraulic binder. The total structure thickness is between 60 and 80cm.

Lastly, rigid pavements are characterized by the presence of concrete at the surface course layer, reinforced or not. This concrete layer has usually 15 to 40cm of thickness and eventually can be covered by a thin bituminous mixture wearing course layer. The foundation of this type of structure can be composed of a material treated by hydraulic binder, concrete or even non-treated draining layer. The concrete surface layer can be also laid directly over the sub-grade.

## **2.2. Pavements design method**

The concept of design for pavement structures was first developed at the beginning 20th century based on empirical observation of the pavement behavior. The flexible pavement was always constituted by bituminous mixtures on the surface course laid over base and sub-base composed by non-treated granular materials. From this conception, the supporting soil stiffness and moisture sensibility had a great influence on the pavement's life. For this reason, the CBR



(California Bearing Ration) method was developed in the '30s (Porter 1938). This method correlates the observations made on roadways service lives in California accounting soil nature, traffic and pavement thickness with a mechanical penetration test, so-called CBR test (ASTM D1883 2016). However, the CBR method was obsolete when treated bases have arrived for decreasing the loading supported by the sub-grade. In addition, new materials have been introduced as well as new techniques in pavement conception. Thus, the American association of state highway officials (AASHO) road test performed extensive real scale tests in Ottawa-IL from 1957 to 1961 in order to provide data for the pavement design. Then, the AASHTO (American Association of State Highway and Transportation Officials) used the data to propose the first interim guide in 1961 presenting an empirical approach to design pavements based on equations and combined in nomographs years later. From this point, the need for a more mechanistic design method was evidenced and in 2004 the Mechanical-Empirical Pavement Design Guide (MEPDG) was conceived (ARA 2004). This guide started to analyze the pavement as layered elastic structure and considered some materials properties in the calculation. In addition, it predicts the pavement performance concerning the main distresses: fatigue, rutting, and thermal cracking.

In France, the current pavements design method (SETRA-LCPC 1994) has a mechanistic approach elaborated by the *Service d'Etudes sur les Transports, les Routes et leur Aménagements* (SETRA) and the *Laboratoire Central des Ponts et Chaussées* (LCPC). Nowadays, the LCPC makes part of the Institut Français des Sciences et Technologies des Transports, de l'Aménagement et des Réseaux (IFSTTAR). The method is based on the Burminster model (Burminster 1943), which considers the pavement as a multilayer system with the following characteristics: elastic, homogeneous and isotropic, and the support layer is considered as semi-infinity. The interface between layers can be considered as (i) bound, (ii) semi-bound, and (iii) unbound. From the '60s the model has been organized within a software called Alizé developed by LCPC and SETRA. The method can combine a mechanistic analysis of structure, fatigue damage laboratory results, and observation from experiments performed in real scale roadways constructed at the LCPC laboratory (SETRA-LCPC 1994). The design method can be divided into six main steps, which includes the layers efforts calculation, thickness adjustments along with fatigue, rutting and thermal crack verification:

1. Pre-design. This step firstly consists of an initial choice of surface course composition. The chosen material needs to presents some necessary properties. Thus, some characteristics of user's safety and comfort can be highlighted according to (SETRA-LCPC 1994):

- Uniformity;
- Adherence;
- Draining capability;
- Photometric characteristics (color, clarity, luminosity, and reflection); and
- Acoustic.

Secondly, based on comparable situations, a similar structure should be pre-design.

2. Structure calculation. This step consists of the calculation of maximums stresses and strains using the Burminster model. This calculation is performed on the pre-designed structure from the previous step. A reference axle load of 130kN is considered. Each semi-axle presents a single dual-tire configuration, represented by two loading points applying uniform pressure of 0.662MPa. This pressure is divided in two discs with 0.125m radius and 0.375m axis distance between.

3. Structures fatigue and sub-grade strain verification. This step consists of comparing the stresses and strains values obtained in the previous step with the admissible values. Those values are obtained based on:

- Cumulated traffic for the considering period;
- Admissible risk for the period;
- Materials fatigue resistance;
- Thermal effects;
- Observation data of similar pavement behavior.

Finally, an additional calibration coefficient is considered, which allows accounting the effect of all mathematic simplification and biasing effects eventually present in the materials properties characterized in the laboratory.

4. Adjustment of calculated thicknesses. In this step, the initial proposed thickness is adjusted in function of some points:

- Technical constraints of minimal and maximal thickness to reach the objectives of capacity and uniformity;
  - Decrease on risks related to interface bond defects occurred when the number of interfaces are limited;
  - Assure enough protection to layers treated concerning the phenomenon non-accounted in the precedent calculation (particularly the reflective cracking).
5. Verification of thermal effects (cycles of freeze-thaw). This step consists of comparing the reference atmospheric freeze index (IR) with pavement admissible thermal resistance. The reference index is chosen as function of the winter severity to be protected from.
  6. Definition of pavement cross-section. In the last step, the pavement cross-section is designed based on the previous verification applied to the critical lane (most charged), shore side, inside the lateral guide strip. Then, the cross-section thickness is fixed based on traffic, geometric characteristics, surface, and sub-grade slopes.

### **2.3. Bituminous mixtures**

Bituminous mixtures are heterogeneous and impermeable materials presented in surface course layer in flexible pavements and eventually in base layers (c.f. section 0). These materials are composed of a blend of mineral aggregates in different gradations (course, fine and fillers) and bitumen (Corté & Di Benedetto 2005, Di Benedetto & Corté 2005). The bitumen works as a binder and the mineral aggregate is the skeleton of bituminous mixtures. Different aggregates sizes are combined to assure the interlock of particles once mixed with bitumen. The smallest particles from aggregates gradation are the fillers, particles with maximum nominal sizes of 63  $\mu\text{m}$  (EN 13043 2003). The mix between filler and bitumen, called mastic, provides the cohesion of bituminous mixture. Every bituminous mixture presents voids volume, denoted in literature as “air voids” ( $A_v$ ). The  $A_v$  has a direct impact on the mixture performance and behavior, specially concerning to rutting. Figure 2-2 presents a scheme of volumetric properties of a bituminous mixture.

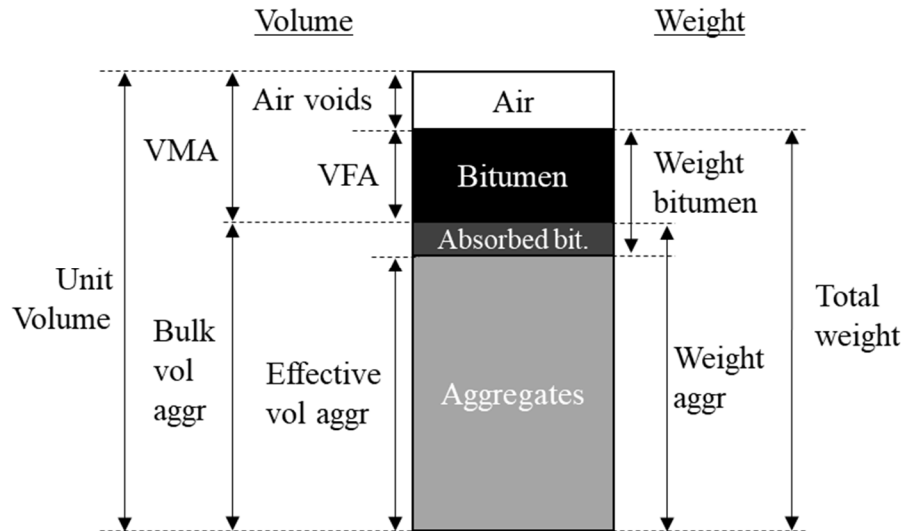


Figure 2-2. Scheme of volumetric properties of a bituminous mixture.

Where *VMA* (Voids in Mineral Aggregate) is the ratio of the total volume of voids between aggregate particles within the compacted mixture, including voids filled with bitumen, with respect to total volume. *VFA* (Voids Filled with Asphalt), corresponds to the part of *VMA* effectively filled with bitumen. From volumetric relations,  $A_v$  is obtained according to Eq. 2-1 (Di Benedetto and Corté, 2005):

$$A_v = 100 \cdot \left(1 - \frac{MVA}{MVR}\right) \quad \text{Eq. 2-1}$$

Where *MVR* is the mixture maximum specific gravity (*masse volumique réelle*, in french), which is calculated by the specimen total weight dividing by the absolute volume (volume of solid matter after excluding volume from all accessible voids). The most common way to obtain this volume is by using a pycnometer according to the French standard NF EN 12697-6 (2012). On the other hand, *MVA* is the mixture bulk specific gravity (*masse volumique apparente*, in french), which is calculated by the total volume of the sample (denoted as unit volume, c.f. Figure 2-2), including air voids. *MVA* can be obtained by three main methods: (i) using a hydrostatic weight balance in sample covered by paraffin; (ii) from measurements of geometric dimensions to calculate the sample volume; and (iii) by measuring the absorption of gamma radiation by the matter.

According to EN 13108-1 (2016), some types of bituminous mixtures are cataloged and used in French pavement structures:

- a) *Béton Bitumineux Semi-Grenu* (BBSG): “Semi-grained bituminous” concrete is considered the reference bituminous mixture because it is used not only in surface courses, but also in parking and sidewalks. It is easily implemented and easily compacted to a thickness that varying from 3 to 9 cm per layer.
- b) *Béton Bitumineux Mince* (BBM): “Thin bituminous concrete” is designed primarily for handily using on construction sites where mechanized implementation is not possible. Its thickness can vary from 2.5 to 5 cm.
- c) *Béton Bitumineux Très Mince* (BBTM): “Very thin bituminous concrete” is known for its excellent durability, aesthetic appearance, and acoustic properties. Used in the surface course with thickness varying from 1.5 to 3 cm.
- d) *Graves Bitumes* (GB): “Gravestone bitumens” are bituminous mixtures with high structural function, used as a base layer for high traffic pavements. High stiffness mixture usually on a thickness that can vary from 6 to 16 cm.
- e) *Enrobé à Module Elevé* (EME): “High modulus mixture” is also a bituminous mixture with high structural function, used as a base layer for high traffic pavements. High stiffness mixture usually on a thickness that can vary from 5 to 15 cm.
- f) *Béton Bitumineux à Module Elevé* (BBME): “High modulus bituminous concrete” is a bituminous mixture with high structural function, used on the surface course layer subjected to high traffic loading (heavy traffic pavement, roundabout). High stiffness mixture having a thickness that can vary from 4 to 9 cm per layer.
- g) *Béton Bitumineux à Froid* (BBF): “Cold bituminous concrete” is a technique used in the maintenance of moderate-traffic pavements requiring the restoration of adhesion properties. The great maneuverability of this product offers great flexibility of his use and allows an easy implementation. The aggregates are mixed with emulsions made from bitumen at ambient temperature. His thickness ranges from 2 to 8 cm.
- h) *Graves Emulsions*: “Gravestone emulsion” responds to the problems of pavement rehabilitation of pavements. It is also used in the new pavement for foundation layers or base layers.
- i) *Béton Bitumineux Aéronautique* (BBA): “Aviation bituminous concrete” is used as a surface course for runways roads at airports and aerodromes. This asphalt can withstand very strong loading and has good performance regarding main airport distresses: rutting, punching, thermal cracking. Its thickness can vary from 3 to 9 cm per layer.

- j) *Béton Bitumineux Colorés* (BBC): “Colored bituminous concrete” is known for its aesthetic appearance and excellent maneuverability, is used as a surface layer for sidewalks, walkways or squares. Its thickness can vary from 2.5 to 6 cm.

More information from the listed bituminous mixtures regarding gradation curves, volumetric information and distresses performance can be found in details at the French standard EN 13108-1, (2007).

### 2.3.1. Composition

#### 2.3.1.1. Bituminous Binder

Bitumen is a material obtained from the petroleum industry composed of carbon and hydrogen (more than 90% by weight), disposed in saturate, cyclic or aromatic structures. According to NF EN 12597 (2014), it is defined as “virtually involatile, adhesive and waterproofing material derived from crude petroleum, or present in natural asphalt, which is completely or nearly completely soluble in toluene, and very viscous or nearly solid at ambient temperatures”. It works as a binder in the mineral aggregates in bituminous mixtures due to its great adhesive power. According to Lesueur (2009), the bitumen found in the market is mainly the result of the crude oil distillation (c.f. Figure 2-3).

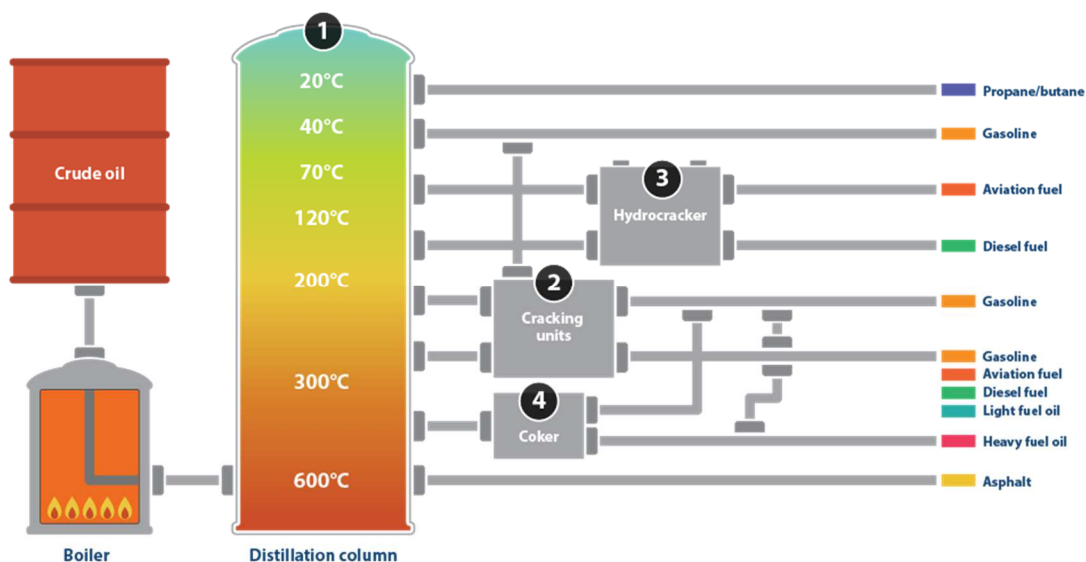


Figure 2-3. Crude oil components refining process (Canadian Fuel Association website).

The bitumen components are traditionally grouped in chemical families: asphaltenes, saturates, aromatics, and resins, determined by a separation method called by the acronym SARA. This method consists first to isolate the asphaltenes using n-heptane, which is the solid phase insoluble. The soluble portion is called maltenes and it is separated into three families: saturates, aromatics and resins, by chromatography in silicone/aluminum gel (Corté & Di Benedetto 2005).

Asphaltene are amorphous solids made of carbon and hydrogen, also containing some nitrogen, sulfur and oxygen atoms. Asphaltene are generally considered to be highly polar and complex aromatic materials. They constitute 5-25% of the total bitumen and have around 2-5nm of particle size. They also have a great influence on bitumen rheological properties. A high quantity of asphaltene leads to an increase in bitumen viscosity. Resins are also solids or semi-solids and highly polar as same as asphaltene. They are responsible for the strong adhesive property of a bitumen. They constitute 13-25% of the total bitumen. Aromatics are viscous liquids composed of carbon and hydrogen, but also a great quantity of sulfur. Non-polar carbon chains where dominate the unsaturated aromatic systems. They constitute 40-65% of the total bitumen. Finally, saturates are constituted by aliphatic hydrocarbons with straight or branched chains. They are viscous nonpolar oils. They constitute 5-20% (Read et al. 2003). The proportions of resin and asphaltene govern the bitumen behavior as solution, “sol” (high proportion of resins) or as gelatinous, “gel” (high proportion of asphaltene).

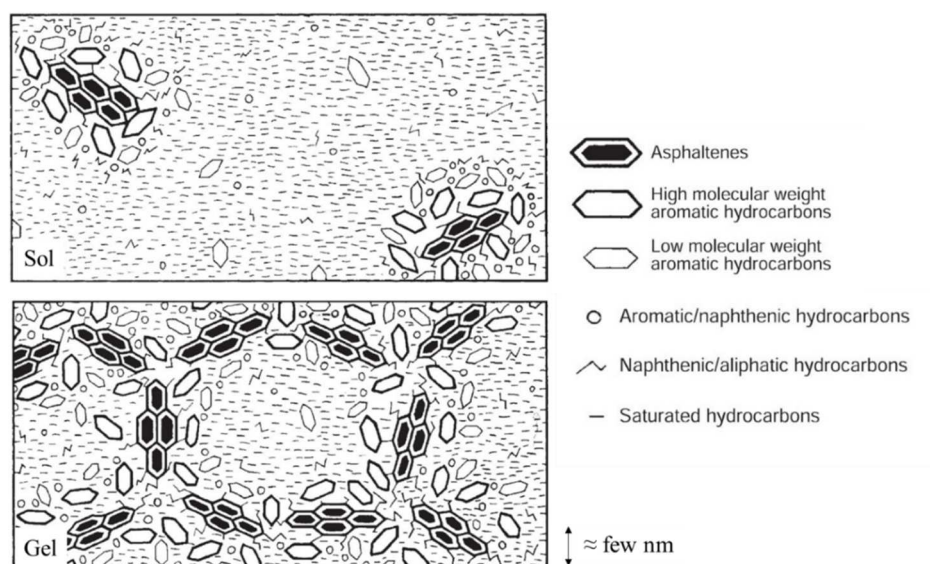


Figure 2-4. Schematic representation of bitumen type sol (above), type gel (below), and some of its components (Read et al. 2003)

The European bitumen classification is based on a penetration test (EN 1426 2007). This test is based on a penetration measurement (in tenths of a millimeter) of a standard needle in a bitumen sample at 25°C for 5 seconds. The load applied by the needle is 100g. Thus, according to the EN 13924-1 (2016) and EN 13924-2 (2016), bitumens having 10/20 and 15/25 of penetration grade are considered "hard" binders. While having 50/70 and 70/100 of penetration grade, bitumens are considered "semi-hard" binders, and a 160/220 bitumen is a "soft" binder. However, this empirical classification only presents information regarding one temperature and is not able to represent the mechanical properties of bitumens.

North America the current bitumen classification was developed in the framework of Strategic Highway Research Program-SHRP (Anderson et al., 1994), part of "Superpave" (Superior Performing Asphalt Pavements). The Performance Grade (PG) classification was created based on the critical temperatures, defining a range of temperatures indicated for its use in the bituminous mixtures fabrication (AASHTO M320, 2009; AASHTO PP6, 1994). The critical temperatures are defined based on mechanical characterization of the bitumen.

#### 2.3.1.2. *Mineral Aggregates*

The mineral aggregates are the bituminous mixtures skeleton and represent approximately 95% of the total mass and 80-85% of the total volume (Corté & Di Benedetto, 2005). They are the result of rock crushing blended with gravels and sand. Other materials can also be used as substitute aggregates: clays, slags, recycled mixtures, etc.

The aggregates' petrographic nature are important to obtain good short-term performance (friability, adhesivity) and long-term performance (polishing, integrity). The rocks could be from nature igneous, metamorphic or sedimentary. Moreover, if there is more than 65% content of SiO<sub>2</sub>, they have acid character, while a content inferior to 55% characterizes a basic character. This nature influences the affinity between bitumen and aggregate. Some geometric characteristics are also important to use for bituminous mixtures. According to Barrett (1980), the shape of an aggregate particle has, in general, three independent properties: form, angularity, and surface texture. The characterization is recently performed using digital image processing (Das 2006, Bessa et al. 2015). Others shape parameters related to the form of aggregates are used to describe it according to Das (2006): elongation and flatness, flakiness, sphericity, shape factor, form factor, roundness, etc. The aggregates form is a direct calculation of the proportions between its dimensions: length, width, and thickness. According to Masad and Button (2000),



angularity quantifies the particle edges and corners, giving general information about its roundness, consequently. Low aggregates angularity in bituminous mixtures could lead to the early appearance of rutting in the roadways pavements (Sanders & Dukatz 1992) caused by the lack of interlocking between particles. Finally, the surface texture is a small property that could not have a big influence on the overall shape (Masad & Button, 2000; Al Rousan, 2004). However, rough-surface aggregates improve particle-to-particle contact and friction resulting in a bituminous mixture more resistant.

The particles sizes distributions of a blend of aggregates are determinant of its classification and its influence in a bituminous mixture. The aggregate gradation has an impact on many mixture properties: stiffness, stability, durability, permeability, workability, fatigue resistance, frictional resistance and moisture susceptibility (Roberts et al. 1996). In France, according to the standard EN 13043 (2015), the gradation classes are quantified by the smaller particle size ( $d$ ) and the higher particle size ( $D$ ) obtained through sieving. For example, a gravel 16/32 contains only particles smaller enough to pass through the sieve with 31.5mm opening mesh, but bigger enough to be retained on the sieve with 16mm opening (Corté & Di Benedetto, 2005). Granular fractions are chosen with  $D/d$  ratio limited to 1.4, for avoiding excessive size dispersion within each fraction. A grading curve is identified by performing a Particle Size Distribution (PSD) analysis. In the 1960s, the FHWA introduced the standard gradation graph used today in North America. This graph raises the sieve sizes to 0.45 power on x-axis. According to Roberts et al. (1996), it is convenient for determining the maximum density line and adjusting gradation. To classify the gradation curves, some terms are used based on the shared common characteristics, as seen in Figure 2-5.

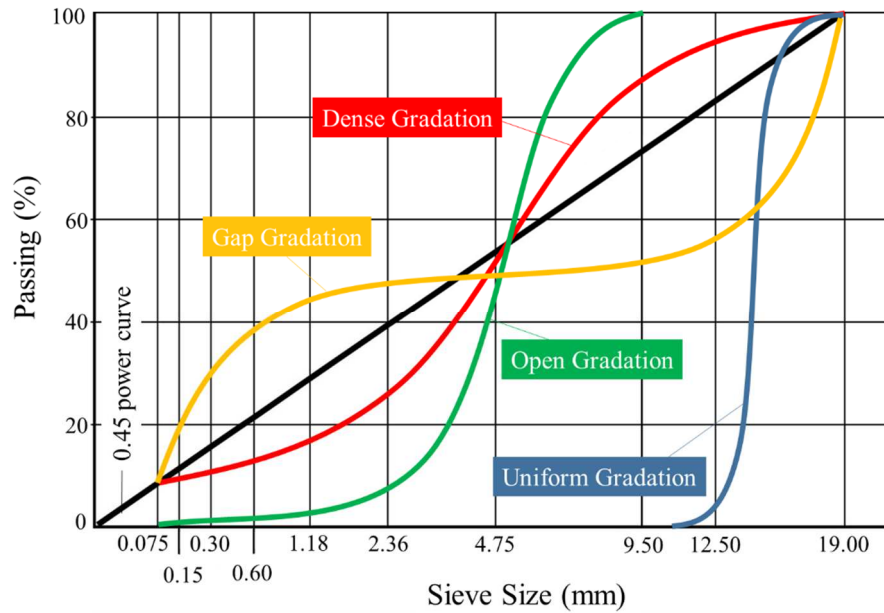


Figure 2-5. Different gradation curves plotted in x-axis raised to a 0.45 power

Dense or Well-Graded are the curves mostly used to design bituminous mixtures. Those curves are closed to the maximum gradation line (c.f. Figure 2-5). However, a dense curve superposed to the maximum gradation line results in an unacceptable low *VMA*. Moreover, the bitumen would be expelled from the mixture. Gap graded curves are characterized by the lack (or few) of mid-size range particles. Despite the fact it could be used for concrete in rigid pavement design, for bituminous mixture, it can be prone to segregation during placement. Open Graded curves contain few quantities of particles in the small range. The lack of enough small particles to fill the voids formed by larger particles results in more air voids in the bituminous mixture. Uniformly Graded curves contain only particles presenting near sizes, which results in a steep curve.

## 2.3.2. Thermo-mechanical behavior

### 2.3.2.1. Loads acting on flexible pavements structure

Pavements structures are multi-layer systems subjected to different types of external loading resulting in complex phenomena (Corté & Di Benedetto, 2005). During the pavement service life, mechanical, thermal, physical and chemical phenomena occur in a combined way. The understanding of the pavement response, when subjected to each effort, could lead to an improvement in pavement design. The pavement structure modeling considers certain numbers

of infinite slabs presenting interfaces varying from fully bonded to completely unbonded compose the road (Corté & Di Benedetto, 2005). Each layer is considered homogenous, isotropic and linear elastic. When the structure is subjected to traffic loading, the local point of loading is induced to a punching, while the layers bend. Considering the bound layers, traffic loading causes horizontal tensile stresses and strains at the bottom and vertical compressive stresses and strains in the bulk section of each layer. The repeated compression leads to rutting, while repeated traction leads to fatigue. Figure 2-6 presents a scheme illustrating the response of traffic loading.

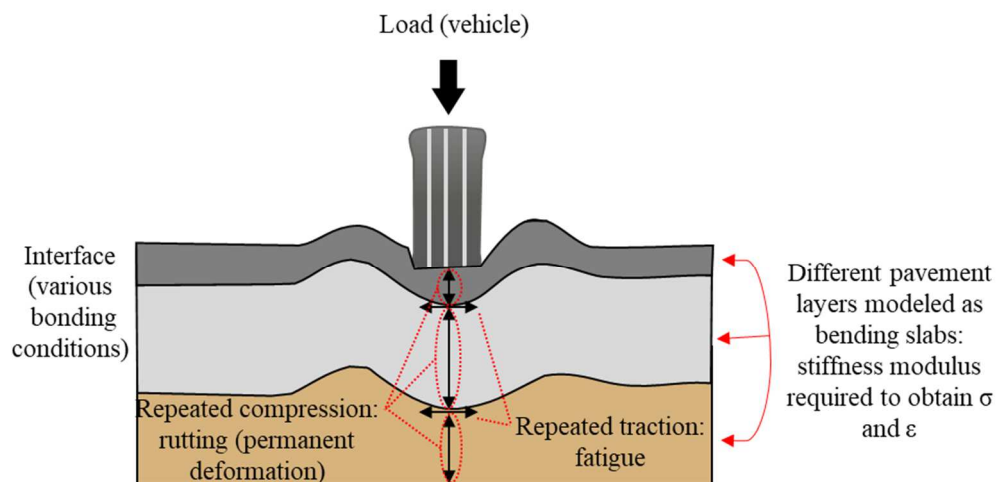


Figure 2-6. Scheme of loading due to traffic and the response on pavement layers  
(adapted after Di Benedetto, 1998)

Climate variation is another source of loading in the pavement structure. The presence of moisture in roadways could increase susceptibility to the cracking (Cardona 2016). Temperature variation is harmful to the pavement in many different aspects. Cycles of freeze-thaw aggravated by insufficient drainage cause progressive degradation of material integrity and performance. Moreover, when the bituminous mixtures are subjected to very low temperatures, a thermal contraction tends to occur, however, it is hindered by friction with other layers in contact. The restrained thermal contraction causes stress in the bituminous mixture, which could lead to so-called "thermal crack". In addition, repeated thermal contraction-expansion cycles may also lead to "thermal fatigue". Another case is in semi-rigid pavements, if there is a crack opening in cement-treated base layer due to shrinkage occurring during hardening, it could lead to a crack propagation throughout the bituminous layer over it. The described phenomenon is

called reflective cracking. Figure 2-6 presents a scheme of thermal loading and possible distresses that could occur in a pavement structure.

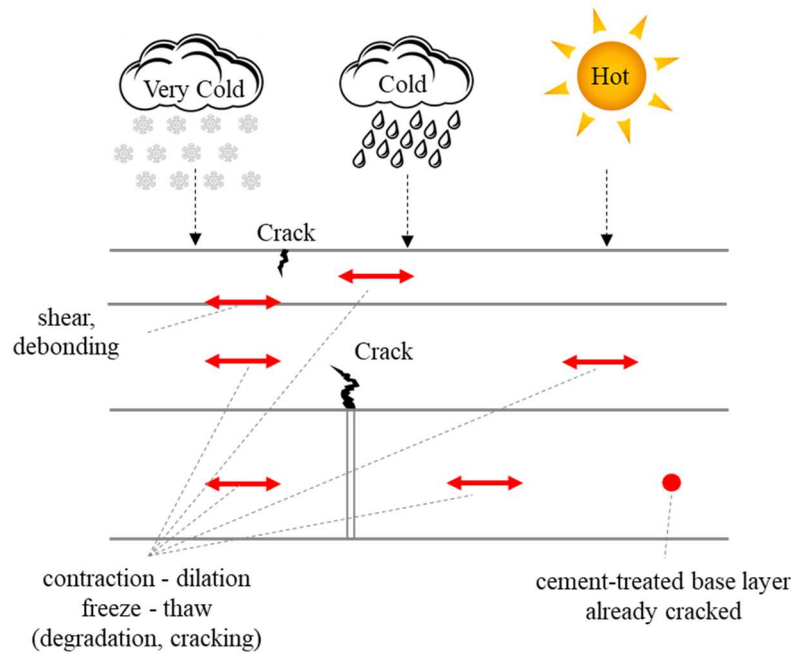


Figure 2-7. Scheme of thermal loading and corresponding pavement response (adapted after Di Benedetto, 1998)

#### 2.3.2.2. Domains of mechanical behavior of bituminous materials

Bituminous materials present a very complex mechanical behavior. However, it is possible to identify four main types of behavior in function of the strain loading amplitude subjected ( $\epsilon$ ) and the number of loading cycles ( $N$ ):

- For few loading cycles amount and strain amplitudes smaller than  $10^{-4}$  m/m, the material behavior is considered in a first approximation as Linear Viscoelastic.
- For few loading cycles amount and strain amplitudes of around  $10^{-2}$  m/m, the material behavior is strongly non-linear. This particular behavior, as well as its threshold is object of research (Doubbaneh 1995, Coutinho et al. 2014, Mangiafico 2014, Babadopulos 2017).
- For high loading cycles amount and small values of strain amplitudes, the material presents fatigue damage.
- Significant irreversible strain occurs for strain amplitudes close to the fracture line. Their accumulation yields in rutting, the last domain indicated in Figure 2-8.

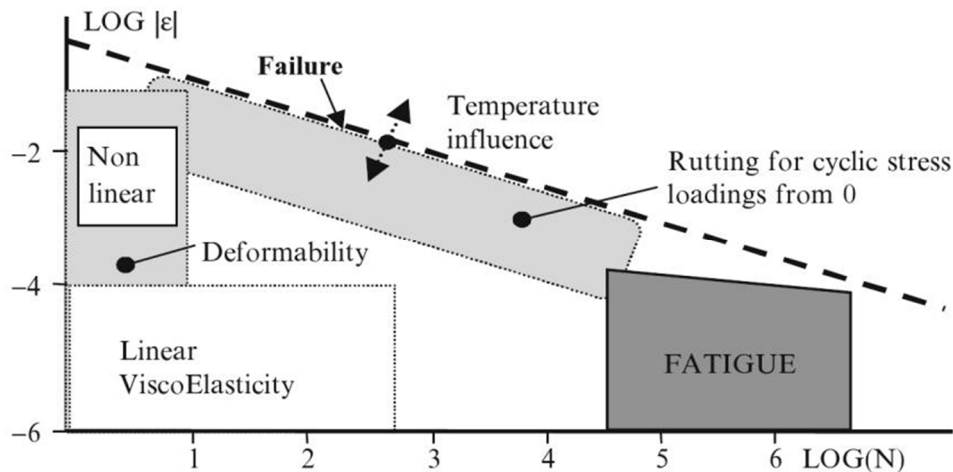


Figure 2-8. Typical mechanical behavior domains of bituminous mixtures depending on strain amplitude  $\varepsilon$  and number of cycles  $N$ , for a given temperature (Di Benedetto et al., 2013).

The temperature affect drastically the bituminous materials behavior, and thus, all the mentioned domains. Threshold values between different domains are shown only as indications of the orders of magnitude.

## 2.4. Linear viscoelastic behavior of materials

### 2.4.1. Definition

Viscoelastic behavior is found in materials that presents elastic and viscous behavior at the same time, depending on the loading conditions (frequency and temperature). When subjected to high frequencies (fast loading) and high temperatures the elastic behavior dominates compared to the viscous. The opposite happens when the viscoelastic materials are subjected to low frequencies (slow loading) and low temperatures.

A unidimensional and non-aged body is considered viscoelastic instead of viscoplastic, if the residual stress  $\sigma_\infty$  at  $t \rightarrow \infty$  is equal to zero when it is subjected to the “cancellation test” (Salençon 2009). This test consists on imposing a strain ( $\varepsilon_0$ ) to an originally undisturbed material at the instant  $t_0$  followed by imposing strain equal to zero (original state), and stress-monitoring as illustrated in Figure 2-9.

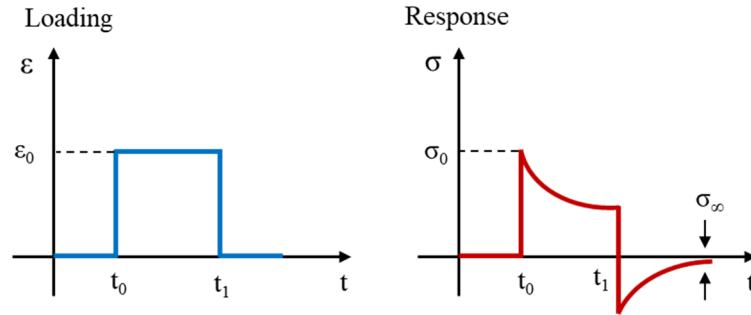


Figure 2-9. Cancellation tests: strain input (left side) and stress response (right side)

A body can be defined as linear viscoelastic (LVE) if the Boltzmann superposition principle is verified (Boltzmann 1876). According to the principle, the response of a material to a solicitation composed of a certain number of elementary solicitations is the sum of the responses to each of these elementary solicitations (Boltzmann 1876, Salençon 2009). Table 2-1 summarizes the Boltzmann superposition principle.

Table 2-1. Boltzmann superposition principle solicitations and responses

Action	Response
$\epsilon_1(t)$	$\sigma_1(t)$
$\epsilon_2(t)$	$\sigma_2(t)$
$\lambda\epsilon_1(t)+\mu\epsilon_2(t)$	$\lambda\sigma_1(t)+\mu\sigma_2(t)$

### 2.4.2. Creep, Relaxation and Convolution Integral

A LVE material behaves particularly when subjected to time-dependent loading. A phenomenon called creep occurs when the material is subjected to a constant stress load, while a relaxation phenomenon occurs when the material is subjected to a constant strain load. For the creep test a given stress  $\sigma_0$  is instantaneously applied to a material at instant  $t_0$  (c.f. Figure 2-10a). The same idea is given for the relaxation test, but at this time it is the inverse of creep, a strain  $\epsilon_0$  is instantaneously applied to a material at instant  $t_0$  (c.f. Figure 2-10b). Table 2-2 summarizes the creep and relaxation tests equations.

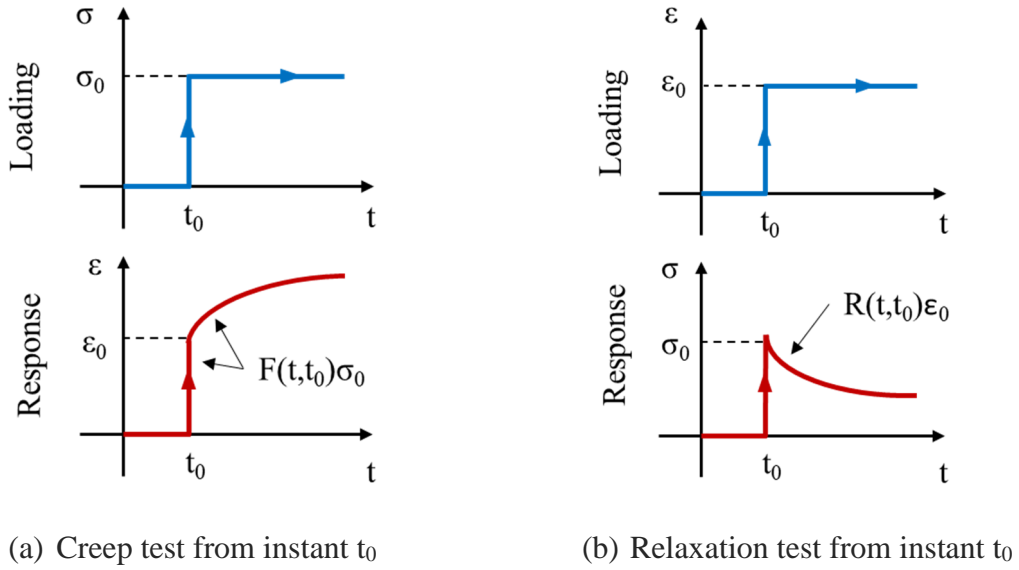


Figure 2-10. (a) Creep and (b) relaxation tests for a linear viscoelastic material

Table 2-2. Creep and relaxation tests equations

	Creep	Relaxation
Solicitation	$\sigma(t) = \sigma_0 H(t - t_0)$	$\varepsilon(t) = \varepsilon_0 H(t - t_0)$
Response	$\varepsilon(t) = F(t, t_0) \sigma_0$	$\sigma(t) = R(t, t_0) \varepsilon_0$
Parameter Definitions	$H(t - t_0) = 0$ for $t < t_0$ $H(t - t_0) = 1$ for $t \geq t_0$ $F(t, t_0) =$ Creep compliance function at any instant $t$ .	$H(t - t_0) = 0$ for $t < t_0$ $H(t - t_0) = 1$ for $t \geq t_0$ $R(t, t_0) =$ Relaxation function at any instant $t$ .

From application of Boltzmann superposition principle, for any stress loading history, total strain response  $\varepsilon(t)$  is equal to the sum of individual responses to each elementary stress variation. Thus, the convolution integral for  $\varepsilon(t)$  can be written according to Eq. 2-2 in function of the material property  $F(t)$ , previously defined. Analogously, for any strain loading history, the same principle can be used to obtain stress response  $\sigma(t)$ . Thus, the convolution integral for  $\sigma(t)$  can be written according to Eq. 2-3 in function of the material property  $R(t)$ , also previously defined.

$$\sigma(t) = \int_0^t R(t - \tau) \frac{\partial \varepsilon}{\partial \tau} d\tau \quad ; \quad t > 0 \quad \text{Eq. 2-2}$$

$$\varepsilon(t) = \int_0^t F(t - \tau) \frac{\partial \sigma}{\partial \tau} d\tau \quad ; \quad t > 0 \quad \text{Eq. 2-3}$$

### 2.4.3. Complex modulus and Poisson's ratio

The LVE properties can be experimentally obtained through cyclic loading characterization in frequency domain. This characterization is performed either sinusoidal strain (with amplitude  $\varepsilon_0$  and frequency  $f$ ) or sinusoidal stress (with amplitude  $\sigma_0$  and frequency  $f$ ) loading application on cylindrical specimens. Figure 2-11 presents an example of complex modulus tests conducted at controlled strain loading and presenting the stress and radial strain response after the steady state. The phase lag between strain and stress signals is the axial phase angle denoted as  $\varphi$ .

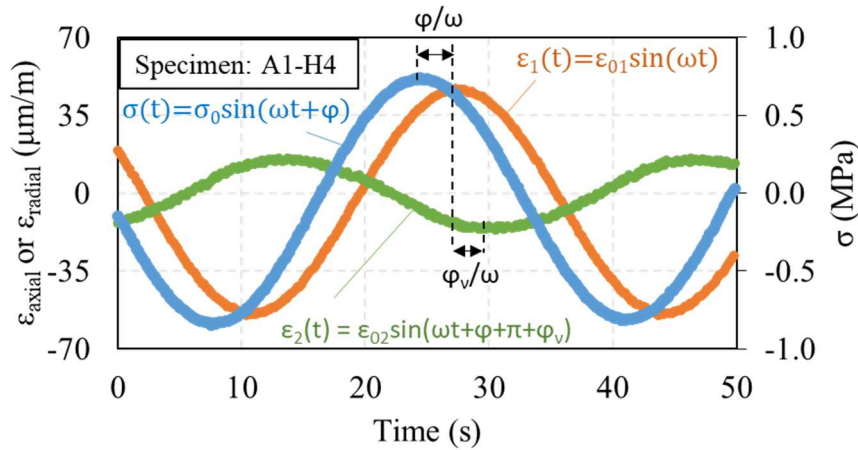


Figure 2-11. Example of complex modulus test on a LVE material: sinusoidal signals of axial stress  $\sigma(t)$ , axial strain  $\varepsilon_1(t)$  and radial strain  $\varepsilon_2(t)$ .

The analysis of the test result can be made in complex notation ( $i^2 = -1$ ). Complex modulus is defined as the ration between the sinusoidal complex stress ( $\sigma^*$ ) and sinusoidal complex strain ( $\varepsilon^*$ ), according to the Eq. 2-4.

$$E^* = \frac{\sigma^*}{\varepsilon^*} = \frac{\sigma_0 e^{i(\omega t + \varphi)}}{\varepsilon_0 e^{i\omega t}} = \frac{\sigma_0}{\varepsilon_0} e^{i\varphi} = |E^*| e^{i\varphi} \quad \text{Eq. 2-4}$$



Where  $\omega=2\pi f$  is known as the pulsation or the angular frequency and the norm of complex modulus ( $|E^*|$ ) is equal to  $\sigma_0/\varepsilon_0$ . Phase angle divides the complex modulus on its real part, also known as storage modulus ( $E_1$ ) and its imaginary part, also known as loss modulus ( $E_2$ ). The real part represents the material elastic properties while the imaginary part represents the material viscoelastic properties (c.f. Eq. 2-5). If  $\varphi = 0$ , the material is perfectly linear elastic. If  $\varphi = 90^\circ$ , the material is purely viscous. For  $\varphi$  varying between 0 and  $90^\circ$ , the material shows LVE behaviour.

$$E^* = E_1 + iE_2 = |E^*| \cos \varphi + i|E^*| \sin \varphi \quad \text{Eq. 2-5}$$

As result axial loading cycles, radial strain is observed due to Poisson's, effect. This radial strain has an additional phase lag in relation to loading signal, denoted as  $\varphi_\nu$ . Moreover, the radial strain is the opposite of axial strain, since when the axial contracts, the radial extends and vice-versa. Thus, the increment  $\pi + \varphi_\nu$  represents signal phase lag for radial strain. Therefore, the complex Poisson's ratio ( $\nu^*$ ) is defined as:

$$\nu^* = -\frac{\varepsilon_2^*}{\varepsilon_1^*} = -\frac{\varepsilon_{02} e^{i(\omega t + \pi + \varphi_\nu)}}{\varepsilon_{01} e^{i\omega t}} = \frac{\varepsilon_{02}}{\varepsilon_{01}} e^{i\varphi_\nu} \quad \text{Eq. 2-6}$$

The representation of complex modulus  $|E^*|$ , and its components  $E_1$ ,  $E_2$  and  $\varphi$  obtained experimentally is done using different graphs. The most frequently used are:

- Isothermal curves: consists of plotting complex modulus results  $|E^*|$  against corresponding test frequencies in logarithmic scale. Can be also done for phase angle.
- Isochronal curves: complementary to the isothermal curves, consists of plotting complex modulus results  $|E^*|$  against test temperatures for each frequency in semi-logarithmic scale.
- Cole-Cole plots: diagrams plotting the imaginary part ( $E_2$ ) in function of real part ( $E_1$ ). This graph highlight the behavior of bituminous materials at low temperature/high frequency. It can be used to verify the validity of the Time-Temperature Superposition Principle (TTSP) for the LVE behavior.
- Black Diagram: so-called “black space”, it plots the  $|E^*|$  values against corresponding  $\varphi$  on a semi-logarithmic scale ( $\log |E^*|$  versus  $\varphi$ ). It is particularly useful

to analyze the behavior of bituminous materials at high temperatures/low frequencies. It can also be used to verify the validity of the TTSP for the LVE behavior.

All these graphs can be also plotted for  $v^*$ .

#### ***2.4.4. Time-Temperature Superposition Principle (TTSP) and Master Curves***

Bituminous materials have a thermoviscoelastic behavior, which means their mechanical behavior depends on frequency, load, and temperature. The material behavior is highly dependent on the testing temperature (e.g. presenting high stiffness at low temperatures and low stiffness at high temperatures). However, the effect on its behavior due to the temperature variation is equivalent to the effect caused by frequency variation, according to Ferry (1980) in the time-temperature superposition principle (TTSP). This principle is only valid if Cole-Cole or Black diagrams tend to form a unique curve, independently of test temperature and frequency. In this case, the material can be considered as thermorheologically simple (Corté & Di Benedetto 2005). Figure 2-12(e) presents an example of unique curve obtained in Black diagram from Nguyen et al. (2013a).

If TTSP is valid for the analyzed material, it is possible to obtain a unique  $|E^*|$  curve for an arbitrarily chosen temperature of reference by applying shift factors ( $a_T(T)$ ) on the isothermal curves, called master curve. To construct this curve, one temperature has to be chosen as the temperature of reference ( $T_{ref}$ ), and then the temperature data above the reference are shifted forward and the temperature data below the reference are shifted backward using the same shift factor for each case. Figure 2-12(a) presents the described methodology to construct the master curve of norm of complex modulus, Figure 2-12(b) for phase angle, Figure 2-12(c) for norm of Poisson's ratio and Figure 2-12(d) for Poisson's ratio phase angle from Nguyen et al. (2013a).

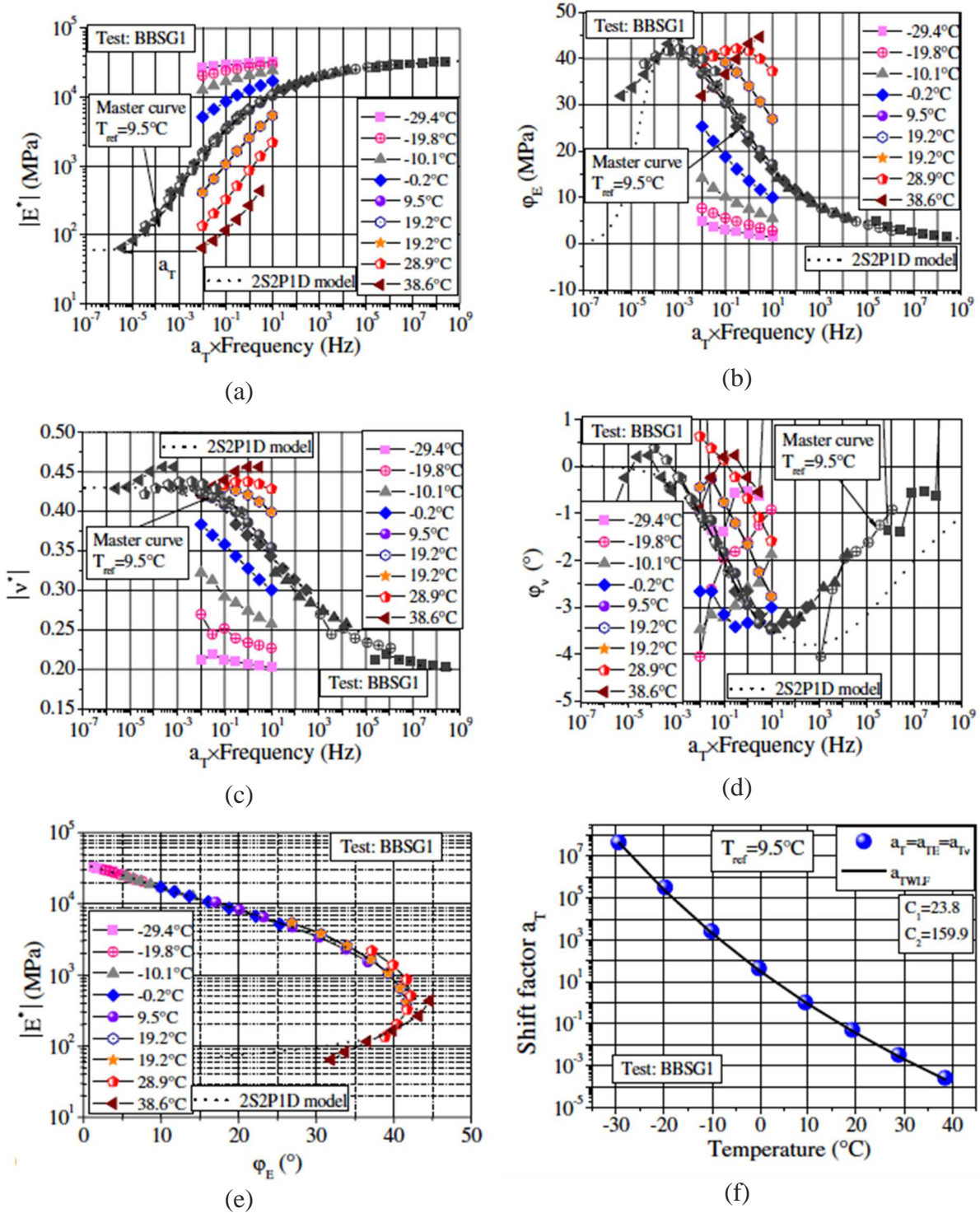


Figure 2-12. Example of time-temperature superposition principle verification for linear viscoelasticity of bituminous mixture (Nguyen et al. 2013a).

Master curves are a significant tool, since it contains information in a range that would be impossible to access experimentally. A  $a_T$  value for each temperature is chosen, with the  $a_T(T_{ref})$  equal to 1. Figure 2-12Figure 2-5(f) presents the different  $a_T$  values obtained for master curves

construction conducted by (Nguyen et al. 2013a). Some equations from literature can be used to fit values of  $a_T$  as a function of temperature. The first one is Arrhenius law written in Eq. 2-7 (Arrhenius 1889):

$$\log(a_T) = \frac{\delta H}{R} \left( \frac{1}{T} - \frac{1}{T_{ref}} \right) \quad \text{Eq. 2-7}$$

Where  $R$  is the ideal gas constant ( $8.314 \text{ J mol}^{-1} \text{ K}^{-1}$ ) and  $\delta H$  is the activation energy of the material. The second one is the Williams-Landel-Ferry (WLF) equation (Williams, Landel, & Ferry 1955), used to fit in Figure 2-12(f) by (Nguyen et al. 2013a). The WLF equation is written as follows (Eq. 2-8):

$$\log(a_T) = \frac{-C_1(T - T_{ref})}{C_2 + (T - T_{ref})} \quad \text{Eq. 2-8}$$

Where  $C_1$  and  $C_2$  are constants, varying with the material and  $T_{ref}$ .

#### **2.4.5. Modelling LVE behavior**

Some LVE models are available in the literature and they are based on combinations of mechanical analogues. The models can be divided into two types: based on mechanical analogues presenting discrete spectra as springs (representing the elastic behavior) and dashpots (representing Newtonian viscous behavior), and based on mechanical analogues presenting continuum spectra. The two simplest models used to describe LVE behavior are Maxwell and Kelvin-Voigt models (Corté & Di Benedetto 2005). However, both the Maxwell and the Kelvin-Voigt models are too simple to describe the viscoelastic behavior of bituminous mixtures. Thus, the combination elements from each models can be done to model more accurately the LVE behavior of materials. The Generalized Maxwell-Wiechert (GMW) model consists in the association in parallel of spring-dashpot pairs linked in series. The continuum spectrum models share the presence of a parabolic element on its combination of elements. Parabolic elements are characterized by a continuous relaxation spectrum but have a finite number of elements. The Huet (Huet 1963), the Huet-Sayegh (Sayegh 1965) and the 2 Springs 2 Parabolic elements and 1 Dashpot (2S2P1D) are examples of continuum spectrum models. The fully description of those models can be found in Corté & Di Benedetto (2005) and Di Benedetto et al. (2007).

## 2.4.5.1. Model 2 Springs 2 Parabolic elements and 1 Dashpot (2S2P1D)

2S2P1D rheological model, developed at the University of Lyon/ENTPE. The model consists of 2 springs (elastic elements), 2 parabolic creep elements and 1 dashpot (purely viscous) (Di Benedetto et al. 2007, Olard & Di Benedetto, 2003) as illustrated in Figure 2-13(a). Seven parameters are used to fit the experimental data (c.f. Figure 2-13(b)) for a general Cole-Cole curve. The value of complex modulus given by the model is calculated by Eq. 2-9.

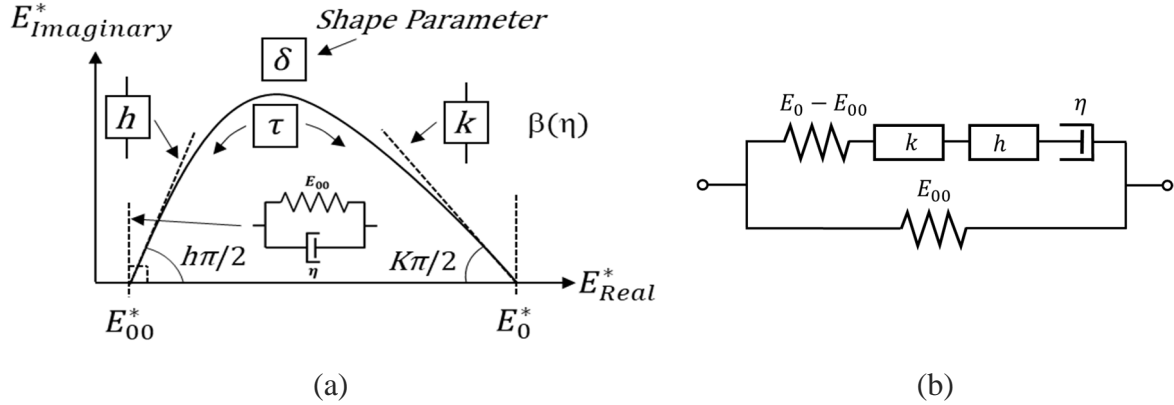


Figure 2-13. 2S2P1D model: (a) constants associated with constitutive elements of the model on a general Cole–Cole curve and (b) mechanical analogues

$$E^*(i\omega\tau) = E_{00} + \frac{E_0 - E_{00}}{1 + \delta(i\omega\tau)^{-k} + (i\omega\tau)^{-h} + (i\omega\beta\tau)^{-1}} \quad \text{Eq. 2-9}$$

Where the pulsation  $\omega = 2\pi f$  with  $f$  the loading frequency.  $E_{00}$  is the static modulus, obtained in the higher temperatures (or lower frequencies), and  $E_0$  the glassy modulus, obtained in the lower temperatures (or higher frequencies). Moreover,  $k$  and  $h$  are dimensionless constants of the two parabolic elements and  $\delta$  is dimensionless shape factor. They are calibration constants. Finally,  $\tau$  is the characteristic time and depends on the temperature, and  $\beta$  is a constant that depends on the dashpot viscosity ( $\eta = (E_0 - E_{00})\beta\tau$ ). The 2S2P1D model can be used for modelling bitumen, mastic and bituminous mixtures linear viscoelastic behaviours (Delaporte et al. 2007, Olard & Di Benedetto 2003, Di Benedetto et al. 2004a). The model can be also extended to 3D (Di Benedetto et al. 2007), to this end, two additional parameters are introduced: static ( $\nu_{00}$ ) and glassy ( $\nu_0$ ) values of Poisson's ratio.

$$v^*(\omega) = v_{00} + (v_0 - v_{00}) \frac{E^*(\omega) - E_{00}}{E_0 - E_{00}} \quad \text{Eq. 2-10}$$

The characteristic time  $\tau$  is the only parameter depending on temperature. It can be obtained at any temperature using shift factors through TTSP discussed in section 2.4.4. Therefore, WLF equation can be used to model material's temperature susceptibility. It is done by using  $\tau_0$  at a temperature of reference and the time-temperature shift factor at the new desired temperature ( $a_T(T)$ ) in Eq. 2-11.

$$\tau(T) = a_T(T)\tau_0 \quad \text{Eq. 2-11}$$

Bituminous mixtures LVE behavior are intimately related to the linear viscoelastic behavior of the bitumen used in their fabrication (Delaporte et al. 2007, Di Benedetto et al. 2007, Di Benedetto et al. 2004a, Olard & Di Benedetto, 2003). For this reason, some authors performed a normalization procedure according to Eq. 2-12. This procedure resulted in a unique curve for all bituminous mixtures produced from the same bitumen (Delaporte et al. 2007, Di Benedetto et al. 2004a, Pouget et al., 2012a and b, Pham et al. 2015).

$$E_{norm}^* = \frac{E^* - E_{00}}{E_0 - E_{00}} = \frac{1}{1 + \delta(i\omega\tau)^{-k} + (i\omega\tau)^{-h} + (i\omega\beta\tau)^{-1}} \quad \text{Eq. 2-12}$$

## 2.5. Fatigue in bituminous materials

### 2.5.1. Fatigue of bituminous binders, mastics and mixtures

The fatigue damage (formation and propagation of micro and macro cracks) is one of the main distresses that occurs in bituminous pavements. This type of damage is caused by the repetitive traffic loading and the change in climatic conditions to which the bituminous mixture is subjected. Fatigue is defined as the weakening of material, by means of stiffness reduction, eventually leading to failure, caused by repeated loading without exceeding material strength (Di Benedetto & Corté 2005). The understanding of the fatigue process in bituminous mixtures is not simple due to the heterogeneity of the material, which is actually composed of aggregate particles with elastic properties and the mastic (filler and asphalt binder) with viscoelastic properties.

The interpretation of the material behavior, during fatigue damage testing, follows two classical approaches: micromechanics, and continuum mechanics. The first captures the phenomena occurring on the scale of microcracks to represent the behavior of the material, considering each crack occurring in the material. This approach is very precise, however it is complex and time consuming. The second one treats the microscale phenomena globally considering the fatigue as loss of resistant cross-section in the material (Kachanov, 1958, 1986; Lemaître & Chaboche, 1990). This loss is obtained with aid of state variables that can be experimentally measurable in laboratory.

Fatigue resistance is highly influenced by the asphalt binder characteristics. For this reason, several authors in the literature characterize the asphalt binder scale trying to upscale these properties to the asphalt mixtures, since it is easier to perform fatigue tests in this mixture constituent. Moreover, testing asphalt mixtures is a complicated and a very time consuming task considering the need to analyze the interaction between the components (Tsai and Monismith, 2005).

Poncelet (1839) was the first one to use the word fatigue to describe this phenomenon. Wöhler (1870) focused on the relationship between the loading amplitude and the number of cycles to failure in metals. This representation yields a linear relation between loading and failure, and despite the fact that it was proposed for metals, it can be used for bituminous materials characterization. Carpenter et al. (2003) introduced the concept of endurance limit of perpetual pavement. For a certain loading level, fatigue life tends to infinite. Thus, the pavements subjected to a loading value underneath this threshold should no present fatigue. Figure 2-14 presents an example of Wöhler curve and endurance limit.

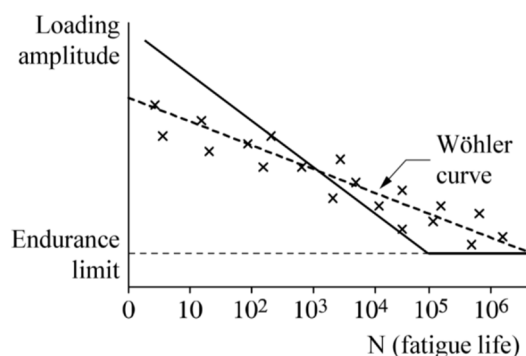


Figure 2-14. Example of Wöhler curve: loading amplitude versus number of cycles to failure (fatigue life) (Di Benedetto & Corté 2005) and the endurance limit of perpetual pavement of Carpenter et al. (2003).

The relation between loading amplitude ( $S$ ) and number of cycles to failure ( $N$ ) can be written according to Eq. 2-13 in logarithmic scale and according to Eq. 2-14 in semi-logarithmic scale:

$$S = aN^{-b} \quad \text{Eq. 2-13}$$

$$S = \alpha - \beta \log N \quad \text{Eq. 2-14}$$

In order to take account the fatigue on the field caused by different loading amplitudes, their combined effect can be estimated by Palmgren-Miner hypothesis (Miner 1945, Palmgren 1924). This hypothesis considers the fatigue life as the accumulation of contribution of each discrete loading.

$$C = \sum_{i=1}^k \frac{n_i}{N_i} \quad \text{Eq. 2-15}$$

Where,  $n_i$  is the number of loading cycles from loading amplitude ( $S_i$ ),  $N_i$  is the fatigue life corresponding to  $S_i$ ,  $k$  is the quantity of different loads applied and  $C$  is a constant obtained experimentally. Miner laws is widely used due to its simplicity, however, it does not take account the loading history, which it highly influence the material's behavior (Mangiafico 2014).

To simulate the fatigue behavior of pavement layer, there are many available approaches on the literature. The characterization can be carried out in full scale using instrumented pavement sections or using accelerated pavement facilities (de la Roche et al. 1994; Highway Research Board, 1961). Another way to characterize the fatigue behavior is simulating its mechanical behavior in laboratory scale. To this end, tests are conducted in bituminous mixtures specimens with repeated loading. Three main type of tests can be found in literature: flexion tests (two, three and four points), traction-compression tests (direct and indirect) and shear tests (Di Benedetto & Corté 2005). The testing type significantly affects the results of fatigue laboratory tests (Di Benedetto et al. 2004b). Homogeneous (strains and stresses are the same in every point of the sample) tension-compression fatigue tests are preferred since they present less dispersion and allow the assessment of the intrinsic fatigue behavior of the material (Olard, 2003).



### 2.5.2. Experimental observations and failure criteria

To perform fatigue tests, the imposed loading can be either in stress controlled or strain controlled mode. When the tests is conducted at stress controlled, the strain resulted from loading decrease along the test. On the contrary, at strain controlled mode, the stress resulted from loading increase along the test. Figure 2-15 represents schematically the different cases of fatigue test cyclic loading.

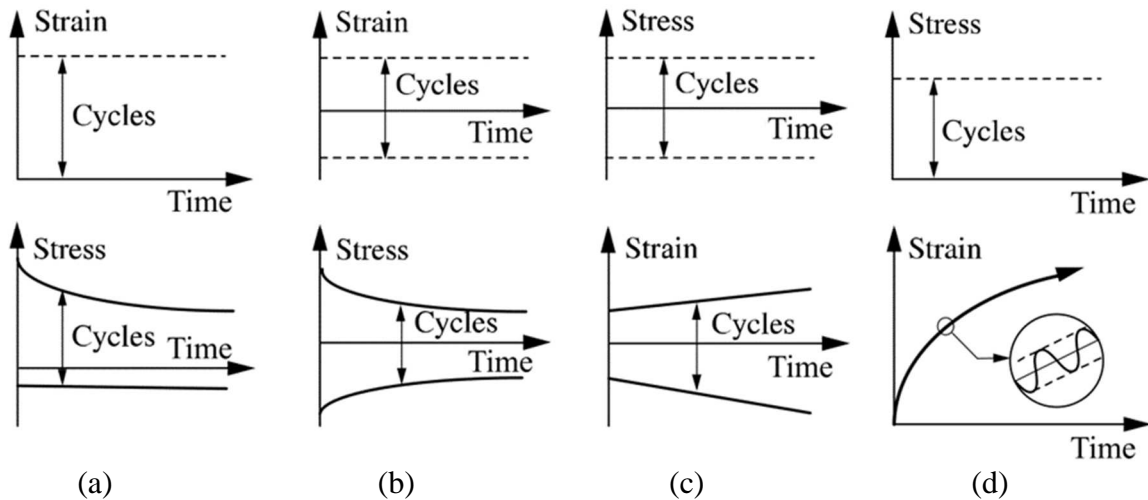


Figure 2-15. Schematic representation of loading: (a) and (b) strain, or (c) and (d) stress and their respective responses (stress or strain) (Di Benedetto & Corté 2005).

An important remark regarding the fatigue test at controlled stress centered in zero (c.f. Figure 2-15d), it leads to an accumulation of permanent deformation along the test that could overcome the fatigue behavior. For this reason, this type of test should not be used for fatigue characterization (Mangiafico 2014).

During the fatigue test, an accumulation of the material deterioration occurs. However, failure occurs before the macroscopic failure of the sample. Generally, complex modulus (stiffness) variation can be monitored as a representation of the deterioration level in the material. Three phases can be identify on the complex modulus decrease due to loading in the fatigue characterization (Piau 1989, Baaj 2002, Di Benedetto et al. 2004b), separated as follows:

- Phase I: is called adaptation phase, characterized by a rapid decrease in complex modulus and increase in phase angle. According to Di Benedetto et al. (2011), Nguyen et al. (2012), Tapsoba et al. (2013), Mangiafico et al. (2015) and further Babadopulos (2017), the first phase can be explained by different effects instead of

fatigue. Biasing effects are responsible for the decrease in the modulus during the cyclic loading, such as non-linearity, self-heating and thyxotropy.

- Phase II: is called quasi-stationary phase, characterized by a quasi-linear decrease in in complex modulus and increase in phase angle. In this phase, fatigue damage is the responsible for the material deterioration.
- Phase III: is the failure phase. In this phase, major cracks are presented in the material, causing a rapid decrease in complex modulus. Continuum mechanics is no longer valid from this point. The threshold between phase II and III is considered the failure point.

Figure 2-16 presents a typical fatigue curve in normalized complex modulus (values divided by the initial modulus obtained) curve and phase angle in function of number of cycles. In addition, the three aforementioned phases are highlighted.

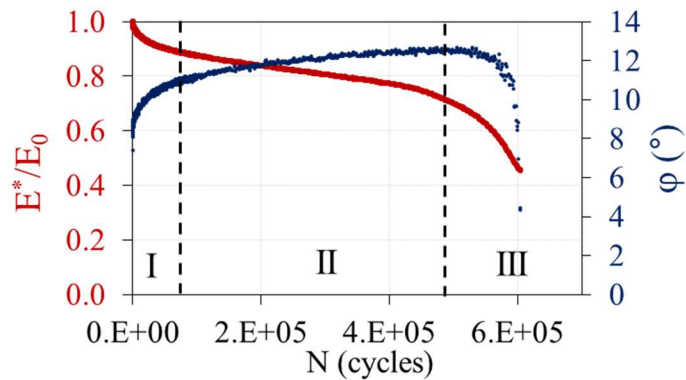


Figure 2-16. Three phases of fatigue testing evolution in complex modulus (normalized), phase angle and number of cycle axis.

One issue highly discussed in the literature by many authors is about the criterion which defines failure in cyclic tests. Some criteria found on literature are based on global measurements during the test, while others are based on local measurements. Criteria based on global measurements are:

- 50% complex modulus loss ( $N_{f-50\%}$ ): When the specimen loses 50% of its complex modulus ( $E^*$ ) it is defined failure. This criterion is used in most fatigue standards (NF EN 12697-24, 2012). Due to the fact that the 50% loss in the stiffness is a good approximation, this criterion has been used for a long time.

However, this is an arbitrary choice and neglects the influence of others phenomena in complex modulus measurements.

- Phase angle behavior ( $N_{f-slope\phi}$ ): A phenomenological failure definition used to define failure is based on phase angle observation. During a cyclic test the phase angle has a trend of increasing, but when the material is not able to resist to additional loading, the phase angle changes its trend abruptly, most of the times decreasing its value.
- Fatigue curve concavity change ( $N_{f-concavity}$ ): This criterion is based on the identification of point that switch from phase II to phase III.
- Energy: The dissipated energy by the material during the fatigue test is another criterion (Hopmann et al. 1989). The parameter DER (Dissipated Energy Ratio) presents an abrupt slope variation when the material reaches to failure. This criterion will be not used in this dissertation.

Local measurements performed individually on each extensometer data can reveal the local behavior of the sample during the test. These criteria is based on the specimens' loss of loading homogeneity during the test caused by the macrocracks appearance. Main local criteria are:

- Strain variation ( $N_{f-\Delta\epsilon_{ax}}$ ): failure is defined when the measured strain variation value ( $\Delta\epsilon_i$ ) of one of the extensometer exceeds 25% (in absolute value) (Soltani 1998, Baaj 2002). Measured strain variation value ( $\Delta\epsilon_i$ ) is calculated according to Eq. 2-16, where  $\epsilon_i$  is the strain amplitude of one extensometer and  $\epsilon_0$  is the average amplitude from the three extensometers.

$$\Delta\epsilon_i = \frac{\epsilon_i - \epsilon_0}{\epsilon_0} \quad \text{Eq. 2-16}$$

- Phase angle variation ( $N_{f-\Delta\phi}$ ): similar to the last one, but based on phase angle variation ( $\Delta\phi_i$ ) individually measured for each extensometer. The failure is defined on the point  $\Delta\phi_i$  exceeds  $5^\circ$  (in absolute value). It is calculated according to Eq. 2-17, where  $\phi_i$  is the phase angle measured in one extensometer and  $\phi$  is the phase angle of the average strain.

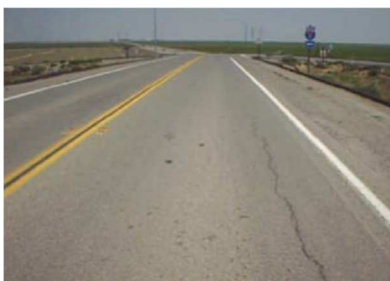
$$\Delta\phi_i = \phi_i - \phi \quad \text{Eq. 2-17}$$

## 2.6. Cracking in bituminous materials

### 2.6.1. Cracking distresses presenting in flexible pavements

LCPC (1998) defines crack as one or many rupture lines appearing on the surface of the roadway. It is the most common distress in roadways around the world. The appearance of crack on the surface of the road can have several origins. It can be resulted from structural deterioration (e.g. deterioration starting in base layer and reflecting to the surface layer), or resulted from superficial deterioration. Typical cracking of (FHWA 2003) are listed as follows:

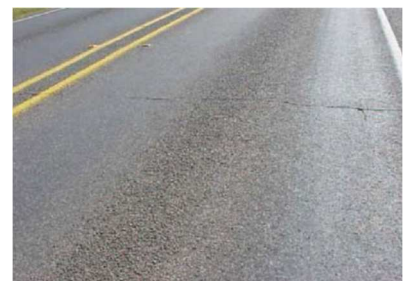
- Longitudinal: cracks parallel to the road painted lines (c.f. Figure 2-17(a)). Normally located within the traffic lane but not in the wheel path. Can be load or non-load related depending on how the crack is positioned on the lane.
- Fatigue: cracks caused by repeated load as discussed in section 2.5. Characterized by the interconnect cracks resembling an alligator skin (c.f. Figure 2-17(b)).
- Transverse: cracks oriented perpendicularly to the road direction (c.f. Figure 2-17(c)). Normally located over Portland cement concrete joints. Could be also caused by the mixture shrinkage due to low temperatures.
- Reflective: crack resulted from deteriorated pavement foundation. Figure 2-17(d) presents an example of this type of crack.
- Block: cracks connected forming rectangular pieces (c.f. Figure 2-17(e)). Normally resulted from freeze-thaw cycles on roadways.
- Edge: group of cracks located near to the pavement edges adjacent to the unpaved shoulder (c.f. Figure 2-17(f)). Could be caused by poor geometry or drainage near the pavement edges.



(a)



(b)



(c)

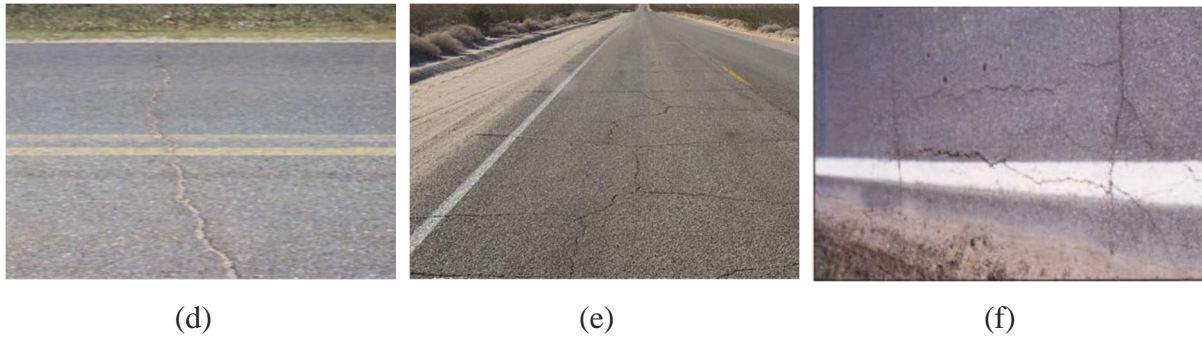


Figure 2-17. Different types of cracks found in flexible pavements (FHWA 2003): (a) Longitudinal Cracks, (b) Fatigue Cracks, (c) Transverse Cracks, (d) Reflective Cracks, (e) Block Cracks, (f) Edge Cracks

### 2.6.2. Introduction to Linear Fracture Mechanics (LFM)

On this section a brief introduction about Linear Fracture Mechanics will be given. The theory in details can be found in Besson (2004), Bui (1978), Fantozzi et al. (1988), Janssen et al. (2002), Leblond (2003) and Miannay (1995). LFM assumes that: (i) the material is non-heterogeneous (continuous media) with elastic, linear and isotropic behavior, and (ii) the crack is flat and has a straight front. These assumptions are schematized in Figure 2-18.

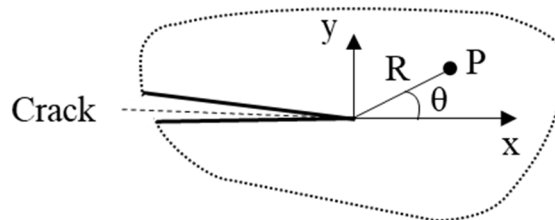


Figure 2-18. Crack representation: perpendicular plane to the crack plane (Di Benedetto & Corté 2005).

Irwin (1957) showed there are three independent kinematic movements relating upper and lower lips from a crack. These are the three main modes of failure (c.f. Figure 2-19) and the mixed mode as follows:

- Mode I: opening mode. The plus frequent in fracture mechanics.
- Mode II: plane shear mode, the shear direction is normal to the front of the crack.
- Mode III: out of shear mode, the shear direction is parallel to the front of the crack.
- Mixed mode: combination of I and either II or III.

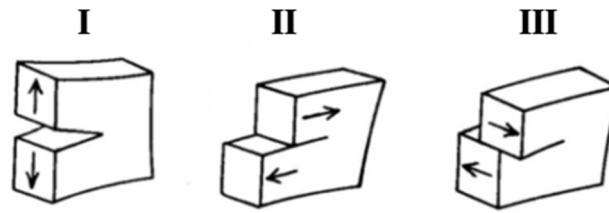


Figure 2-19. Fracture failure modes (Bui 1978)

Using the theory of elasticity, and in the case of plane deformations, Irwin (1957) established the stresses at each point  $P$  (c.f. Figure 2-18) near the crack. Thus, for the zone located at the point of crack, the general form for the stress ( $\sigma_{ij}$ ) is obtaining according to the following equation:

$$\sigma_{ij} = \frac{K_{\alpha}}{\sqrt{2\pi r}} f_{ij}^{\alpha}(\theta) + o[1/(r)^{0.5}] \quad \text{Eq. 2-18}$$

Where:

$\alpha$ : corresponds to indexes I, II or III according to the fracture failure mode considered

$f$ : function of  $\theta$  (c.f. Figure 2-18)

$o(x)$  symbol means that the terms are negligible over  $x$  when  $r$  tends to 0

$K_I, K_{II}, K_{III}$  are the stress intensity factors, corresponding to modes I, II and III respectively

When  $K_{\alpha}$  reaches a critic value  $K_{\alpha c}$ , the crack starts to propagate. Specifically, the critic value in mode I, called fracture toughness ( $K_{IC}$ ), characterize the material resistance to cracking propagation.

Stress intensity factors are determined at boundary conditions. It depends on the applied loading, specimen's geometry, and crack geometry. In cases presenting simple testing configurations (geometry and loading), it is possible to identify the loading stress  $\sigma$  and to express the stress intensity factor in mode I in the form:

$$K_I = f(F, a, Y) \quad \text{Eq. 2-19}$$

Where:

$F$ : applied loading

$a$ : crack height

$Y$ : specimens form factor

Concerning the pre-notched four point bending test specimen (c.f. Figure 2-20), the following analytical equation allows to determine the stress intensity factor in mode I (Fantozzi et al. 1988):

$$K_I = \frac{3P(L-l)}{2BW^2} Y(x) \sqrt{a} \quad \text{Eq. 2-20}$$

Where:

$P$ : force at failure

$L$  and  $l$ : distance between the supports and distance between points of loading, respectively

$B$  and  $W$ : specimens height and width, respectively

$a$ : crack height

$Y(x)$ : form factor (dimensionless)

$x = a/W$ : notch relative depth

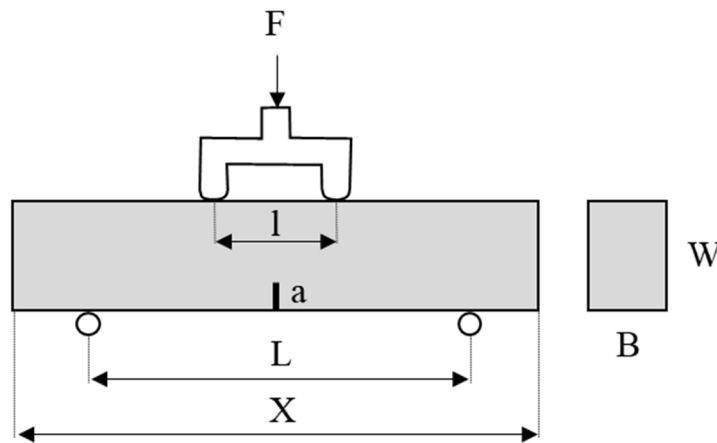


Figure 2-20. Pre-notched four point bending test specimen

### 2.6.3. Fracture energy determination

Bituminous mixtures are considered as semi ductile materials. The energy dissipated during the crack propagation consists in a combination of the dissipated energy due to creep and the dissipated energy due to fracture itself. However, for tests at very low temperatures, the energy dissipated during the test is only due to the fracture (Song et al. 2006). According to Li et al. (2008), the dissipated energy due to creep increases along with the increase in the test temperature. Thus, the fracture characterization should be performed at low temperature in order to avoid the undesired influence of another damage mechanism. In this case, the fracture

energy ( $G_F$ ) corresponds mainly to the dissipated energy due to the failure alone. It is defined as the necessary energy to create a surface unit of a crack. Therefore, fracture energy can be obtained by the area under the full loading curve of a test in the axes Force ( $P$ ) versus displacement ( $u$ ), as showed in Figure 2-21 if viscous dissipated energy can be neglected.

In order to calculate the total fracture energy under the loading curve, Rilem TC-50 FMC (RILEM 1985) recommended the use of Eq. 2-21 for a beam subjected to bending.

$$G_F = \frac{W_0 + mgu_0}{A_{lig}} \quad \text{Eq. 2-21}$$

Where  $W_0$  is the work of fracture, calculated from the area under the  $P$  vs  $u$  curve,  $m$  is the beams weight,  $g$  is the gravitational acceleration ( $9.81 \text{ m/s}^2$ ),  $u_0$  is the displacement corresponding to beam total fracture.  $A_{lig}$  is the area of initially uncracked ligament ( $A_{lig} = B(W-a_0)$ , where  $a_0$  is the notch height. For small specimens, the beams weight is negligible and the second term of Eq. 2-21 ( $mgu_0$ ) could be eliminated. Therefore, the fracture energy becomes:

$$G_F = \frac{W_0}{B(w - a_0)} \quad \text{Eq. 2-22}$$

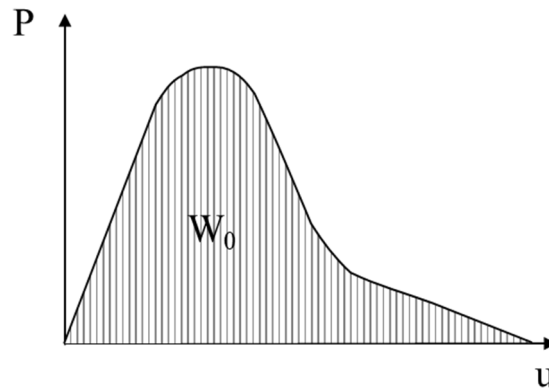


Figure 2-21. Determination of area under the loading curve in the axes force ( $P$ ) and displacement ( $u$ )



### 2.6.4. Crack propagation tests for bituminous mixtures

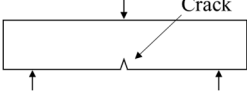
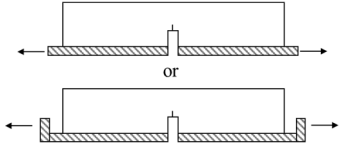
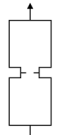

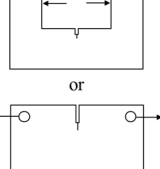
#### 2.6.4.1. Different types of tests found in literature

Fracture mechanics theory have been largely used to study the cracking behavior of bituminous materials. Normally using mode I of fracture (c.f. Figure 2-22). Some studies in monotonous sollicitation have been carried out. However, mostly of studies in literature consider cyclic loading, given the cyclical nature of pavement loads (both climate and traffic related) and apply Paris law (Paris & Erdogan 1963):

$$\frac{dc}{dN} = A(K_I)^n \quad \text{Eq. 2-23}$$

$dc/dN$  is the advancement of the crack in the cycle  $N$ .  $K_I$  is the maximum value reached by the stress intensity factor in the cycle  $N$ .  $A$  and  $n$  are constants of the material.

The cracking studies in mode II concerning bituminous mixes are not very common, however, this type of sollicitation is always present on pavement during the traffic loading. Therefore, further work on shear mode is necessary.

Test Principle	Bitumen (B)/Mix (M) – Monotonic (m)/ cyclic (c)	Mode
	B – m M – c or m	I
	M – c and m	I
	M – c	I
	M – c	I
	M – c or m	I

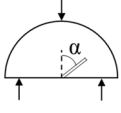
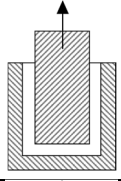
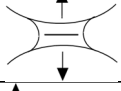
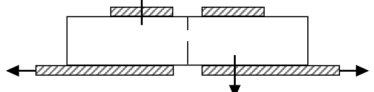
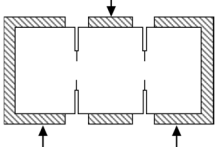
	M – c	I ( $\alpha = 0$ ) II ( $\alpha \neq 0$ )
	B – m	I
	B – m and c	I
	M – c	I and/or II
	M – c	II

Figure 2-22. Different types of cracking propagation tests in bitumen and bituminous mixtures (Di Benedetto & Corté 2005)

#### 2.6.4.2. Four Points Bending Notched Fracture (FPBNF) test

Four-point bending notched fracture (FPBNF) test is designed at the University of Lyon/ENTPE by Nguyen et al. (2008) and further used by Pedraza (2018). Tests are conducted in prismatic beams using a servo-hydraulic press. The specimen is placed over two supports measuring 36cm of distance between each other, and below two points of loading measuring 12cm of distance between each other. Moreover, three Linear Variable Differential Transducers (LVDT) are placed on supports (LVDT 1 and 3) and on beam center (LVDT 2) in order to measure the axial displacement in these three points. Beam's deflection is calculated by the LVDT 2 measure corrected by the punching effect of the lower supports into the beam, obtained from LVDT 1 and 3 measures. Thus, it was calculated according to the following equation:

$$Deflection = LVDT2 - \frac{LVDT1 + LVDT3}{2} \quad \text{Eq. 2-24}$$

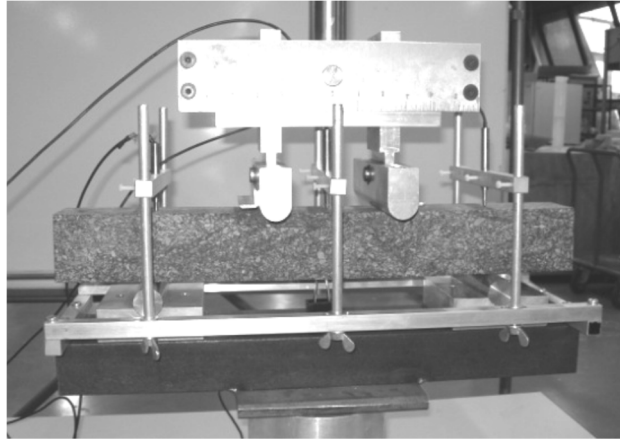


Figure 2-23. Four-point bending notched fracture (FPBNF) test at ENPTE (Nguyen et al. 2008)

## **2.7. Overview of geosynthetics for pavements reinforcement**

### ***2.7.1. Background***

Interlayer reinforcement has recently gained researchers' and constructors' attention due to its capability to enhance flexible pavements performance. The inclusion of a new layer presenting some desired (or designed) characteristics can enhance the performance of the pavement on many levels. COST Action (2006) listed some benefits delivered by interlayer reinforcement:

- Increase pavement fatigue life.
- Minimize differential and total settlement.
- Reduce rutting – surface and subgrade.
- Prohibit or limit reflective cracking.
- Increase resistance to cracking due to frost heave.
- Bridging over voids

Interlayer reinforcement emerged in the 1930s as a solution to improve pavement structure performance by using woven cotton sheets immersed in liquid bitumen (Beckham & Mills 1935, Beck 1999). In 1937 occurred the first attempt to reinforce a deteriorated pavement from reflective cracking by using steel mesh (c.f. Figure 2-24) in Michigan/USA (Williams 1953). In the 50s, great development of airport pavements, and the construction of more than 1 million km of road lane and 140 km<sup>2</sup> of pavement construction occurred (Beck 1999). Moreover, fast

roadways deterioration contributed to more investments in effective rehabilitation methodologies (Barksdale 1991). In the 60s, engineers from the United States, Canada, and Great Britain used wire mesh and expanded metal as reinforcement solutions. Those products returned a reduction in fatigue and cracking on the reinforced roads. However, the good performance was only obtained if the reinforcement was correctly installed, and the products used were very difficult to install (Carver & Sprague 2000). Another drawback was concerning the pavement recycling process.



Figure 2-24. Installation of steel mesh for reinforcement of pavements in Michigan/USA (Williams 1953)

In the 1970s when the American Federal Highway Administration (FHWA) instituted the “National Experimental Evaluation Program” to reduce reflective cracking in roadways (FHWA 1974, Carver and Sprague 2000). In 1972, the California Department of Transportation (Caltrans) quantified the positive effects of nonwovens geotextiles that were later approved by FHWA as an interlayer solution to the reinforcement of roadways (Roschen 1997). Those reinforcements presented beneficial aspects to the pavement, such as stress relieving and waterproofing. However, they were unable to contain the reflective cracking development. Thus, in 80’s, manufacturers began to develop geogrids, and in 1982 they were firstly used for the bituminous mixtures reinforcement in England. Many research efforts have been carried out at the University of Nottingham since 1981 using Tensar AR1 grids, fiberglass and polyester grids. Those studies had as objective to quantify geogrid performance in the rutting and reflective cracking prevention as well as to extend the fatigue life of pavements. Bending tests (Brown et al. 1985, Hughes 1986, Gilchrist & Brown 1988) and field trial in the University of Nottingham’s Pavement Test Facility was carried out (Austin and Gilchrist 1996). From the results was

concluded that the geogrid did not affect the pavement stiffness, the fatigue life was increased by a factor of up to 10, the rutting was reduced by a factor of 3.

In the following years, new products have been developed in the 90s, such as geocomposites coupling geogrid with geotextiles solving some installation issues. New research emerged in order to replicate the theoretical success of the new products and in-field applications. In France, SETRA (1997) and the guide STBA (*Service Technique des Bases Aériennes*) (1999) brought the geocomposites as an effective reinforcement solution to reflective cracking. COST Action 348 (COST Action 2006) was a European research effort to characterize pavements reinforced by steel meshes and geosynthetics. The following countries collaborated in this research effort: Austria, Belgium, Croatia, Czech Republic, Denmark, Finland, France, Germany, Greece, Hungary, Netherlands, Norway, Poland, Portugal, Slovakia, Spain, Sweden, Switzerland and United Kingdom. COST Action (2006) compiled documentation and existing guidelines about the mentioned products, pointed out the best laboratory testing procedure, and reviewed the available design methods. The report concluded that, despite the many benefits observed experimentally, there was no direct link between test results and design procedure. In addition, concerning different loading conditions or pavement performance prediction, there was no validated design method. They finally recommended more effort into creating more user-friendly generic design tools.

Recently, some authors have been preferred fiberglass geogrids to reinforce bituminous mixtures (Nguyen et al. 2013). In France, there are some examples of fiberglass geogrid utilization to combat mainly reflective cracking. Figure 2-25(a) presents the construction site of the rehabilitation made in Toulouse Blagnac Airport occurred in 2010. Figure 2-25(b) presents the construction site of the rehabilitation made in Charles de Gaulle Airport in Paris in 2016 performed by Colas. Figure 2-26 presents one picture of the reinforced pavement execution by EIFFAGE Infrastructures with the fiberglass geogrid Notex Glass C® provided by Afitexinov in Montélimar in 2018.

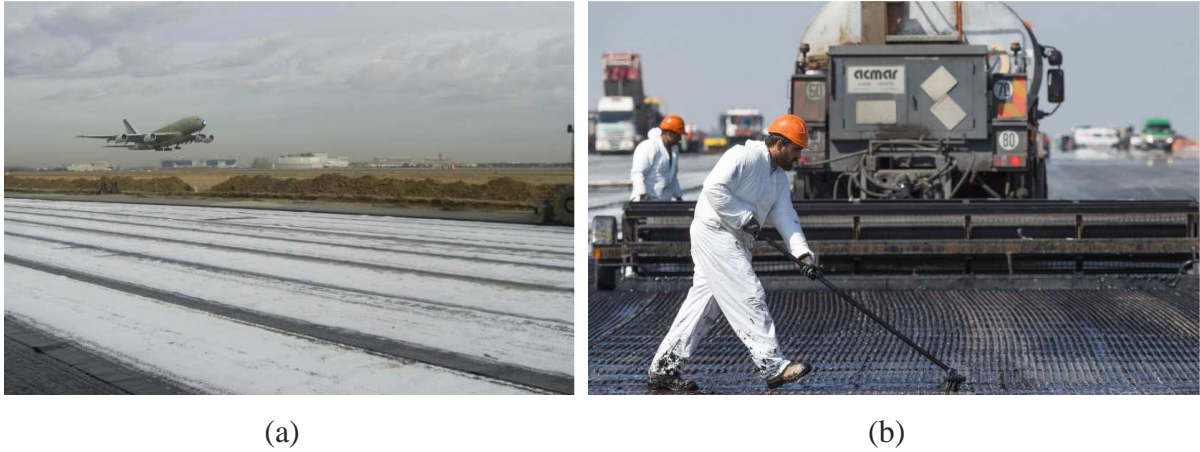


Figure 2-25. Construction sites with use of fiberglass geogrid solution to reinforce pavements against reflective cracking in France: (a) Toulouse Blagnac Airport, October 2010 (6D Solution website), (b) Rehabilitation of Charles de Gaulle Airport, Paris 2016 (Colas website).



Figure 2-26. Construction site with use of fiberglass geogrid solution to reinforce the highway A7 in Montélimar in 2018 by EIFFAGE Infrastructures using the fiberglass geogrid Notex Glass C<sup>®</sup> provided by Afitexinov

### ***2.7.2. Types of geosynthetic interlayers***

Pavement interlayers are defined according to MTAG (2009) as “materials or combinations of materials that can be placed within a pavement system during new construction, rehabilitation or preservation in conjunction with an overlay or surface treatment to extend pavement service life”. Many different types of interlayer products have been suggested from the

60s, however, only geosynthetics interlayers will be discussed due to the scope of this dissertation.

According to Donovan et al. (2000) “geosynthetics” is the group of flexible and synthetic polymer materials, presenting thin thicknesses, used for soils, pavements, and bridge decks reinforcement. For reinforcement purposes of pavements, the following six are commonly suggested (Al-Qadi et al. 2008a, MTAG, 2009):

- Geotextile (or Fabric): most used type of geosynthetics, can be woven or non-woven, permeable synthetic fibers saturated with bitumen forming a porous fabric. Placed with a bituminous mixture overlay or chip seal. Figure 2-27(a) presents an example of geotextile.
- Paving mat: composed by non-woven fiberglass and polyester hybrid material saturated with bitumen. Placed with a bituminous mixture overlay. Figure 2-27(b) presents an example of paving mat.
- Geogrid: is the reinforcement product used in this dissertation, can be composed of high-density materials (polypropylene, polyethylene), fiberglass, carbon fiber, presenting an open mesh structure greater than or equal to ½ inch to allow interlocking with the surrounding bituminous mixture. Coated with polymer or bitumen could be self-adhesive or bounded with bitumen emulsion. Attached with a non-woven (or knitted) material to facilitate the installation. Figure 2-27(c) presents an example of it.
- Geocomposite: composition of two geosynthetics different. Conceived to combine two functions of different geosynthetics (e.g. reinforcement and filtration). Figure 2-27(d) presents an example of it.
- Geomembrane: material very soft, in thin sheets of rubberized and/or polymerized. Also coated with polymer or bitumen could be self-adhesive or bounded with bitumen emulsion. Figure 2-27(e) presents its installation in a construction site.
- Geocells: cubic cells made from slotted aluminum sheets or pre-assembled polymeric frameworks. They are used for soil confinement improving the soil bearing capacity. Figure 2-27(f) presents its installation in a construction site.

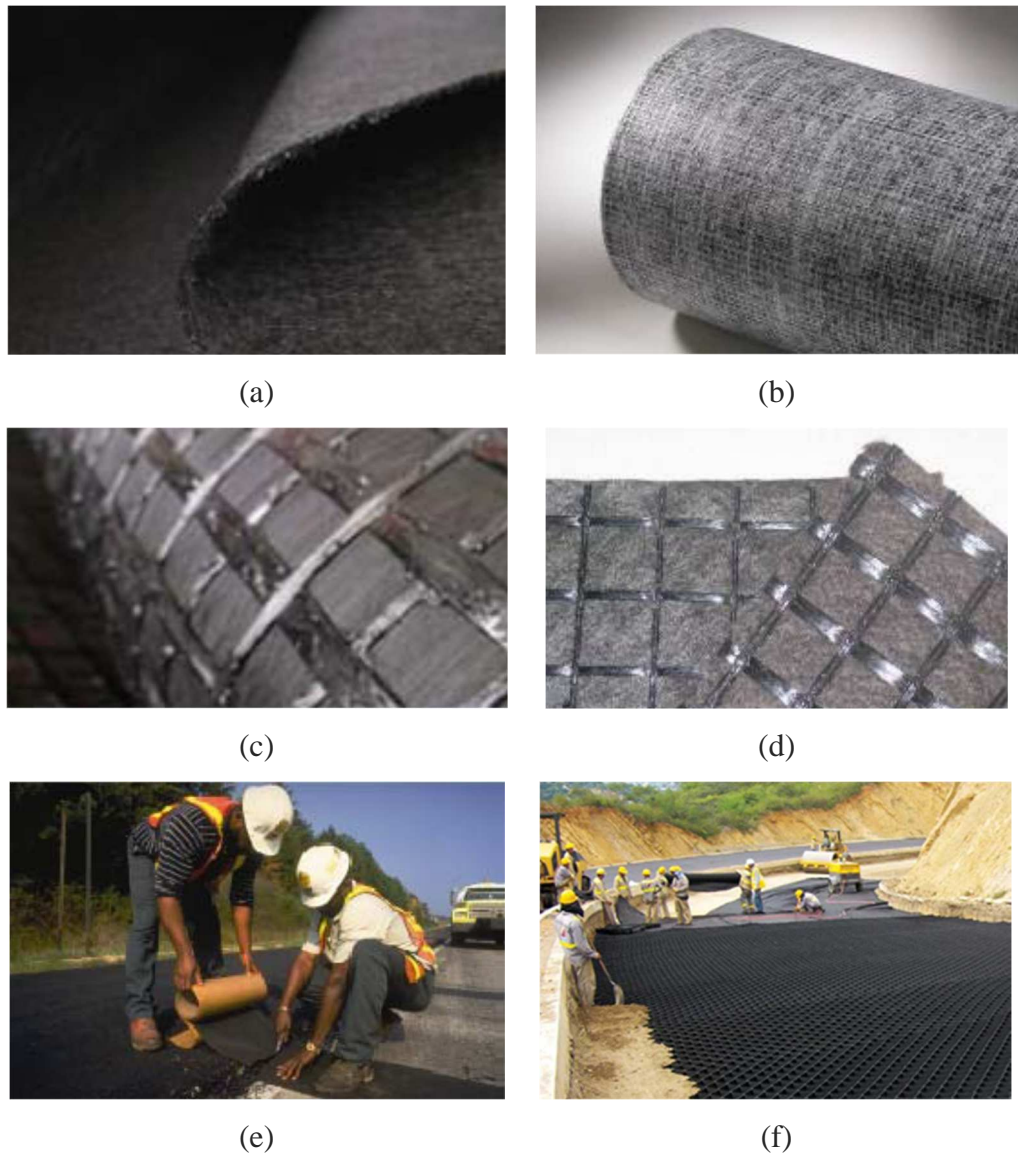


Figure 2-27. Different types of geosynthetic interlayer for pavement reinforcement: (a) Geotextile (MTAG 2009), (b) Paving Mat (MTAG 2009), (c) Geogrid (MTAG 2009), (d) Geocomposite (MTAG 2009), (e) Geomembrane (MTAG 2009), (f) Geocell (Pavco Geosoft®)

### ***2.7.3. Geosynthetic functions and behavior mechanisms***

The primary functions of geosynthetics are separation, filtration, reinforcement of both bound (detailed in section 2.7.6) and unbound layers (detailed in section 2.7.5), drainage (moisture barrier) and stress relief. Different types of geosynthetics are designed to present a combination of these functions or at least one of them. Geogrid, for instance, presents the function of stress relief and reinforcement when used in bituminous mixtures. On the other hand, a geotextile provides the separation of two dissimilar soils used in base layer and subgrade, and also



provide filtration secondarily by relieving the water pore pressure in the soil overhead the geotextile (Zornberg and Thompson, 2010).

- Separation: consists in ensuring the integrity of dissimilar materials so the functioning of both materials remains intact (Koerner 2005). Normally, non-woven porous geotextiles are used to this end. It can avoid the pumping of subgrade fines to the top layer caused by dynamic traffic loading. This case is also effective to avoid the penetration of stone particles into softer layers, which could result in local shear failure. Figure 2-28

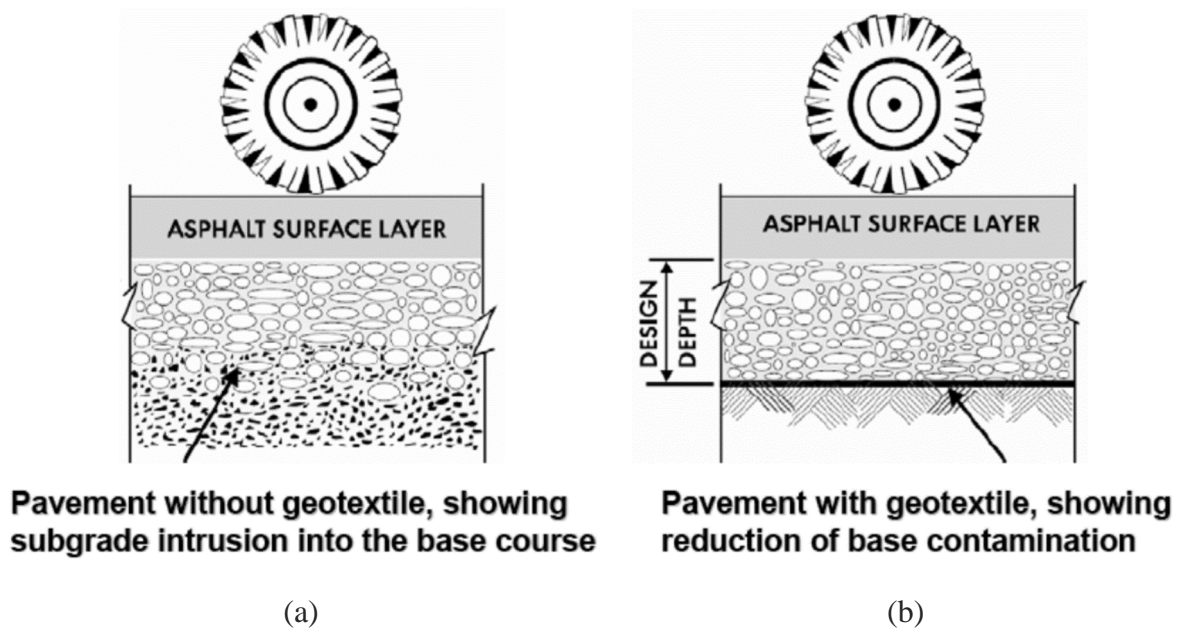


Figure 2-28. Separation function example of a geotextile placed between base aggregate and a soft layer underneath (Zornberg and Thompson, 2010): (a) without geotextile, (b) with geotextile.

- Filtration: defined by Koerner (2005) as “the equilibrium of a geotextile-soil system that allows for adequate liquid flow with limited soil loss across the plane of the geotextile over a service lifetime compatible with the application under consideration”. An example of geotextile to filtration is in a pavement trench drain (c.f. Figure 2-29).

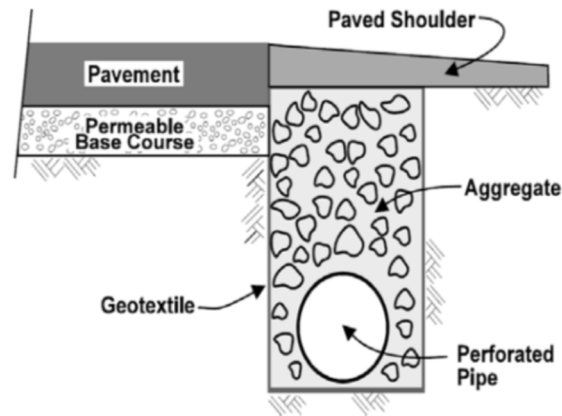


Figure 2-29. Pavement trench drain using a geotextile for filtration (Zornberg and Thompson, 2010)

- Drainage (moisture barrier): moisture arising from rainwater in pavement layers could lead to a faster deterioration. Geotextiles and geomembranes could be employed to avoid the water accumulation forcing the water to flow in the direction to the shoulder drain system. The geosynthetic transmissivity is defined according to Eq. 2-25, where  $\theta$  is the transmissivity,  $k_p$  is the in-plane hydraulic conductivity, and  $t_g$  is the geotextile thickness at a specified normal pressure.

$$\theta = k_p \cdot t_g \quad \text{Eq. 2-25}$$

- Reinforcement: in this case, for both bound and unbound layers, the geosynthetic has a function to provide additional capacity to support loading. Geotextile, geogrid, geocomposites, and geocells are commonly used to this end. More details about geosynthetic reinforcement are discussed in section 2.7.6 for bound layers and in section 2.7.5 for unbound layers.
- Stress relief: consist of the function of dissipation the excess amount of energy due to traffic loading, which would contribute to the crack propagation process (Barksdale, 1991). According to Lytton (1989), the stress relief capacity is responsible for retarding the crack development since when the crack reaches the interlayer it stops propagating due to the lack of energy. Monismith and Coetzee (1980) called a “crack arrest” phenomenon the interlayers’ capacity of redirecting the crack from its original direction to the horizontal plane, due to its stress-relief properties.

#### ***2.7.4. Geosynthetics important properties and characterization***

Some geosynthetic properties are important depending on the engineering condition in which they will be used and designed. These properties are grouped into five categories: physical, mechanical, hydraulic, endurance, and degradation. In addition to those, geosynthetics can be characterized as index or performance (Zornberg and Thompson, 2010). Index test are descendants of testing used for the industrial fabrics decades ago, however, they do not provide much engineering information. Whereas the performance tests were conceived to provide engineering information used to design geosynthetics.

- Physical properties: mostly obtained with index testing, used to characterize in the as-received, manufactured condition. Example of physical properties: specific gravity, mass per unit area, thickness and stiffness. These are properties focused on short-term behavior of geotextiles
- Mechanical properties: compressibility, tensile strength, tear strength, puncture strength, and seam strength. They are geosynthetic behavior when subjected to different types of loading. Some mechanical properties, such as strength value, are very important since they describe geotextile's expected performance in the field. These are properties focused on short-term behavior of geotextiles
- Hydraulic properties: are related to the ability of water to flow through a geosynthetic. They are important depending on the geosynthetic function. Example of hydraulic properties: porosity, percent open area, apparent opening size (AOS), permittivity, and transmissivity. These are properties focused on short-term behavior of geotextiles
- Endurance properties: focused on long-term geosynthetic behavior, these properties are related to the damage during installation. Example of endurance properties: creep response, stress relaxation, long-term clogging, abrasion, and installation damage.
- Degradation properties: also focused on long-term geosynthetic behavior these properties address different mechanisms including ultraviolet light (sunlight), chemical reactions with polymers, and/or thermal degradation.

Table 2-3 summarizes the most important characterization methods for geosynthetics standardized by ASTM.

Table 2-3. Geotextile properties and characterization test methods standardized by ASTM (Zornberg and Thompson, 2010)

Property	Reporting Units	Standard Test Designation
Grab Strength	lbf (kN)	ASTM D 4632
Sewn Seam Strength	lbf (kN)	ASTM D 4632
Tear Strength	lbf (kN)	ASTM D 4533
Puncture Strength	lbf (kN)	ASTM D 6241 / ASTM D 4833
Permittivity	sec <sup>-1</sup>	ASTM D 4491
AOS	US Sieve No. (mm)	ASTM D 4751
Ultraviolet Stability	%	ASTM D 4355

The grab strength test is one of the most important tests since it provides the tensile strength of tested geosynthetic. In France, it is standardized by NF EN ISO 10319 (2015). The test consists of clamping two opposite ends of a specimen in a hydraulic testing press and stretching the specimen until failure occurs. The results are reported in the function of the geosynthetic strain and the force necessary to reaches failure on the specimen. The maximum tensile resistance associated with the specimens' strain at failure is the key parameters to the reinforcement of bituminous pavements.

### ***2.7.5. Reinforcement of unbound layers***

Geotextiles, geogrids and geomembranes are commonly used to reinforced unbound layers. Several studies suggested that geosynthetic reinforces pavement structures when used at subgrade-aggregate base interface (Barksdale et al. 1989, Hass et al. 1987, Webster 1991). In addition, its stiffness is very important to the road reinforcement (Barksdale et al. 1989; Webster 1991). According to Holtz et al (1998), the following three mechanisms the reinforcement are primarily responsible for the reinforcement:

1. Lateral restraint: is the capability of providing tensile resistance to lateral aggregate movement from the friction between the geosynthetic and the particles (Al-Qadi & Bhutta, 1999). Aggregates tend to move laterally when subjected to traffic loading, which could result in rutting. Figure 2-30(a) illustrates this mechanism.

2. Increased bearing capacity: geosynthetic interlayer presents more maximum tensile resistance when comparing to weak soils. Thus, the reinforcement leads to an increase in the bearing capacity. Figure 2-30(b) illustrates this mechanism.
3. Membrane type of support: protects the underneath layer by stress-relief. Figure 2-30(c) illustrates this mechanism.

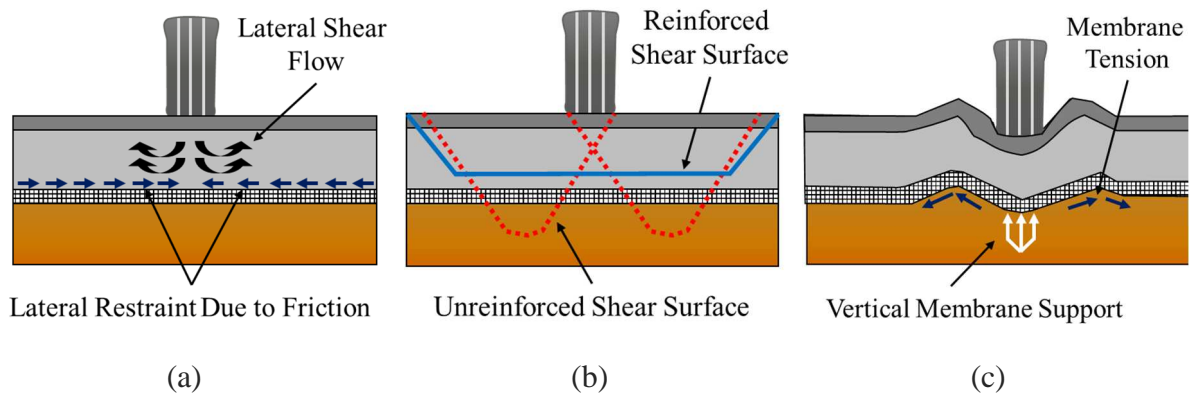


Figure 2-30. Scheme of unbound layers reinforcement mechanisms provided by geosynthetics (edited after Zornberg and Thompson, 2010): (a) Lateral restraint, (b) Increased bearing capacity, (c) Membrane type of support

Several studies have been conducted in the last 40 years, in both, laboratory scale and full-scale field tests (Giroud & Noiray 1981, Al-Qadi et al. 1994, Tang et al. 2008, Mamatha et al. 2019). Those studies have showed benefits concerning reduction in plastic deformation, and relieving stresses at the top of subgrade. Other studies indicated that geosynthetic reinforcement could lead to a reduction in base thickness resulting in substantial reduction in construction costs (Halim et al 1983, Kennepohl et al. 1985, Barksdale et al. 1989, Al-Qadi et al. 1994).

According to Tang and Yang (2013), geogrid/geocell base reinforcement could arrest the degradation that leads to a lack of ability in spreading the traffic load, in the base layer. This was caused by the combination of tensile reinforcement, confinement effects and good interlocking between particles and reinforcement. Concerning geocells, its benefits were only noticeable at higher strain levels (Nair & Madhavi Latha 2014).

Mamatha et al. (2019) focused on the flexural behavior. The author argued that the geosynthetic reinforcement behaves as a flexible layers embedded between layers in pavement structures. Thus, the investigation of its flexural behavior leads to a better comprehension of reinforcing mechanisms. From three-layered beam bending test, the author concluded that the

reinforcement by geogrid/geocell within the granular sub-base significantly improves rutting life (factor of 11.89) and fatigue life (factor of 1.88) of pavement.

### ***2.7.6. Reinforcement of bound layers***

Since the beginning of the utilization of geosynthetic interlayers reinforcement, most of the effort was focused on the unbound layers reinforcement, having its peak around the 80s. However, only recently their true reinforcement potential has been acknowledged that is the utilization in bituminous mixtures (bound layers). Pavement upper layers are critical since they present higher tensile strain than at the subgrade-aggregate interface (Montepara et al. 2012).

From the increase in the funding of road rehabilitation along with the decline of new roads construction, the use of geosynthetic interlayer as a solution to rehabilitate deteriorate roads increase. The existing cracks in a deteriorated road tend to propagate to any new overlay used to rehabilitate due to traffic and thermal loading, this phenomenon is called reflective cracking (Al-Qadi et al. 2008a). Geosynthetics, particularly geogrids, are very efficient in the combat of reflective cracking (Lytton 1988, de Bondt 1999, Brown et al. 2001) and for this reason, they are widely used (Al-Qadi et al. 2008a).

According to Lytton (1989), for every wheel load passing, three critical pulses of stress concentrations occur at the crack tip. First, maximum shear stress occurs, followed by a bending stress and another maximum shear stress. These pulses are responsible for the cracking propagation, which can be further aggravated by temperature variation. Button and Lytton (1987) defined the failure in the reinforcement as follows:

- When the crack reaches the reinforcement layer, if it is stiff enough, the crack moves laterally in the interface direction until its energy is weakened. Button and Lytton (1987) also observed that debond occurs before the specimen failure, confirmed by Al-Qadi et al. (2008b).
- The interlayer stiffness should be sufficiently high than the surrounding materials to occur the reinforcement.
- The reinforcement interface could grant an increase in the structural capacity of the pavement, and then, providing a thickness reduction in the bituminous layer. However, this reduction is based on empirical rules.

To investigate the benefits of geosynthetic reinforcement in bituminous mixtures, damage mechanisms related to shear and bending should be understood. Two types of tests are majorly

found in the literature for the characterization of bituminous mixtures reinforced by geogrids: Interface tests and cracking propagation tests (Vanelstraete and Franken 1997).

#### 2.7.6.1. *Adhesion tests*

The Technical Committee (TC) 237-SIB of the RILEM (International union of laboratories and experts in construction materials, systems, and structures) divided the adhesion test methods into two groups: destructive (torque tests, shear test, etc) and non-destructing (Hammer test, Falling Weight Deflectometer, etc). In this section, some destructive adhesion tests found in the literature used for geosynthetic characterization will be discussed.

The most used test to characterize the interface bonding is the Leutner test (Leutner 1979). This test was developed in Germany by Leutner and consists of a direct application of shear stress. This test can be performed in specimens either fabricated in a laboratory or cored from the field (de Bondt 1999). Figure 2-31(a) presents schematically the device and the specimen positioning during the test. Raab et al. (2010) investigated the interlayer adhesion of several cylindrical specimens in order to evaluate 20 different types of tack coats. Layer-Parallel Direct Shear (LPDS) tester, which is a modification of the Leutner test was used to the bonding strength characterization. The author concluded that this test is a good and effective method for characterizing interlayer bond between bituminous mixtures. Plug and de Bondt (2010) performed modified Leutner tests to characterized the adhesion between fiberglass geogrid and bituminous mixtures. The tests were conducted for evaluating the curing time of emulsion used as a tack coat. The author observed that the shear strength increased for the specimens with longer curing time. Sagnol et al. (2019) performed Leutner tests at monotonic shear loading in bituminous mixtures with and without fiberglass geogrid in the interface. Specimens presented a combination of three types of fiberglass geogrids with non-woven, two types of emulsions (bitumen) as tack coat and different applications of emulsion rate (residual binder) varying from 60 to 1636g/m<sup>2</sup>. The loading was at a shear displacement rate of 50 mm/min until failure. The authors concluded that the presence of geogrid decreased by 60% of the shear strength of the specimens during the tests. Moreover, the emulsion application rate has a great effect on specimens bonding. Greater amounts of emulsion resulted in shear strength closer to the value obtained for unreinforced specimens. Finally, the non-woven presence decreased the shear strength due to the decrease of interlock between the particles on the two layers.

Another test found in the literature used to characterize adhesion of interfaces containing reinforcement by geosynthetics is the Wedge splitting test (c.f. Figure 2-31(b)). This test was

conceived for fracture tests (Tschegg, 1986), but Tschegg et al. (2012) used it to characterize a geotextile and a geogrid reinforcement in bituminous mixtures. Moreover, Jamek et al. (2012) used it to characterize geotextile, geogrid, and geocomposite reinforcement. A wedge splitting test gives an indication of resistance against crack growth. Double shear tests are also found in the literature for this type of characterization. Figure 2-31(c) presents the double shear tester (DST) developed by the North Carolina State University (NCSU) asphalt research team (Safavizadeh & Kim, 2014). However, other similar tests can be found in Zamora-Barraza et al. (2010) and Noory et al. (2017). Zamora-Barraza et al. (2010) used the double shear to characterize the adhesion strength of geosynthetic impregnated with bitumen, between two bituminous mixtures layers. Three geogrids (two polyester and one fiberglass) and two geotextiles were combined with different types of emulsion and application rates were subjected to displacement rate loading of 5 mm/min at 15°C. The authors obtained the highest shear resistance for the lighter geotextile.

Li et al. (2014) conducted research evaluating the effect of grid reinforcement in bituminous mixture performance aiming at reducing the permeability and providing resistance to the cracking caused by low temperatures. The mixtures were reinforced with three different grids made of fiberglass yarns and nonwoven fabrics. Two grids were biaxial (PGM-G100/100 that has three yarns in each direction and PGM-G50/50 that has two yarns in each direction) and the last grid was multi-axial (PGM-G4). The reinforced mixtures were prepared with a PG 64-34 binder as a tack coat in a rate of 1.22l/m<sup>2</sup> for the biaxial grids and 0.86l/m<sup>2</sup> for the multi-axial grid. Moreover, the grids were placed in two different positions, the fiberglass side facing up and down. The authors performed shear strength test at a displacement rate of 12.5mm/min until the specimen was sheared apart. Permeability tests were also performed in the reinforced specimens and in a non-reinforced mixture called control mixture. Finally, indirect tension creep test (IDT) were performed in the reinforced and non-reinforced mixtures at the temperatures of 20, -10 and -30°C and at a constant load level of 12, 1.5 and 0.15kN. From the shear test, the mixtures with the glass side placed facing up presented lower shear resistance (about 35% less), and it should be placed facing down to have better bonding strength. From permeability results, the reinforced mixtures presented coefficients of permeability around 10 times larger than the control mix. Finally, the IDT results showed that the reinforcement with geocomposites reinforcement reduced the temperature sensitivity of the material. In addition, the multi-axial grid (PGM-G4) presented the best overall pavement performance.

Cho et al. (2016) conducted a study to verify the TTSP to the interface shear of specimens reinforced by fiberglass geogrids. Moreover, the effect of grid and tack coat type in the TTSP



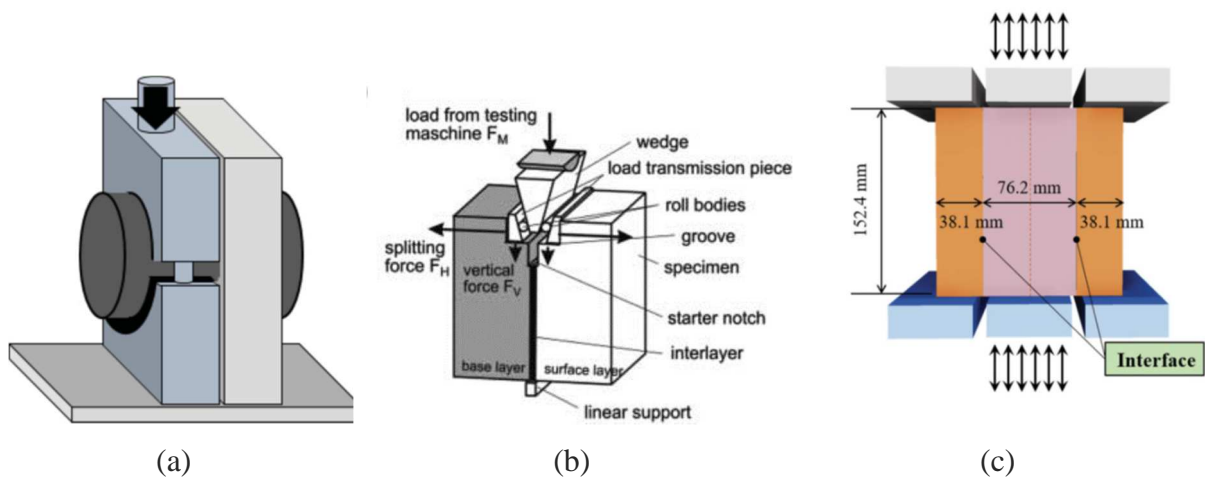
shift factors were analyzed. The grids were impregnated with acrylic polymer resin and differ in the mesh opening (12.5 and 25mm). Two different tack coats were used, PG 64-22 binder for the 12.5mm grid and emulsion bitumen for the 25mm grid, both at a rate of 0.199L/m<sup>2</sup>. DST and Modified Advanced Shear Tester (MAST) were used for the shear test characterization. On MAST tests, a confining loading is applied to the specimens along with shear loading. Constant rate of displacement mode of loading in the MAST device was used to characterize shear bond strength, 0.508 and 5.08 mm/min. Tests were conducted at four different temperatures: 5, 18, 32 and 48°C and normal confining pressure of 275.79 kPa. DST cyclic tests were conducted at frequencies of 0.1, 0.5, 1, 5, 10, and 25 Hz and temperatures of 5°C, 15°C, 25°C, 35°C, and 45°C applying small shear strain to obtain interfaces shear modulus master curve. Interfaces containing geogrid or not were analyzed. Digital Analysis Correlation (DIC) was used to determine interface displacement. The authors concluded that the quality of the tack coat is more important than grid mesh opening to the shear strength. Moreover, the interfaces without geogrid presented the same shift factors than those found for bituminous mixtures complex modulus previously characterized. However, the shift factor for interfaces containing geogrids differed from the others.

Noory et al. (2017) conducted a study in order to characterize shear strength of bituminous mixtures interfaces having geocomposites made of fiberglass geogrids and non-woven filaments, using the DST device. Seven parameter were analysed: tack-coat application rate (0, 0.5, 1, and 1,5kg/m<sup>2</sup>), testing temperature (10, 20, 30 and 40°C), grid mesh opening (22, 33, 67, 111mm), loading frequency (0.25, 1, 3, 5Hz), loading amplitude (2 and 4kN), mean texture depth (0.097 and 0.81mm) and penetration index of bitumen tack coat (76 and 97mm/10). The author monitored the shear stiffness variation in function of loading cycles and they observed three distinct stages in this curve. The first stage was characterized by bitumen action and more than 50% of stiffness was lost during this stage. The second stage was linear and third a rapid stiffness decrease, similar to a fatigue curve behavior. Temperature was the most influent parameter to shear stiffness followed by the tack coat application rate. Grid mesh sizes were the third more influent parameter, but only for when normal confining loading was applied. Bigger grids mesh sizes presented higher shear stiffness because more contact between the two layers increased the interface bonding strength.

In Italy, the Ancona Shear Testing Research and Analysis (ASTRA) was developed for the characterization of shear properties (c.f. Figure 2-31(d)). This device is a direct shear box, very similar to the one used in soil mechanics. Pasquini et al (2015) used it for the evaluation of the shear resistance in the interface of the layers for the specimens cored from the field and also for

the same mixtures reproduced in laboratory. The tests are performed at a temperature of 20°C and at the stress amplitudes of 0.0MPa (laboratory), 0.2MPa (field and laboratory) and 0.4MPa (laboratory). However, the unreinforced section specimens failed during coring operation, and the test could not be performed. From the results obtained in the ASTRA test for the field specimens, the author observed that the elastomeric membrane with 12.5mm mesh presented the best shear interface resistance. It was also observed that the tack coat reduces the adhesion and reduces the shear interface resistance. Finally, the milling process did not have great impact in the shear resistance. Regarding the tests performed in the laboratory specimens, from the ASTRA test, it was confirmed that the presence of the geocomposite reduces the bonding between layers. Moreover, Ferrotti et al. (2011) and Canestrari et al. (2015) used this device to characterize the shear resistance of interfaces containing reinforcement by geogrids.

More recently, Attia et al. (2017) proposed a new apparatus to characterize interfaces between bituminous mixtures called 2T3C Hollow Cylinder (c.f. Figure 2-31(d)). The mentioned author used the device to apply torsion and compression to hollow cylinder specimens at the same time. The interface behavior was obtained using DIC analysis.



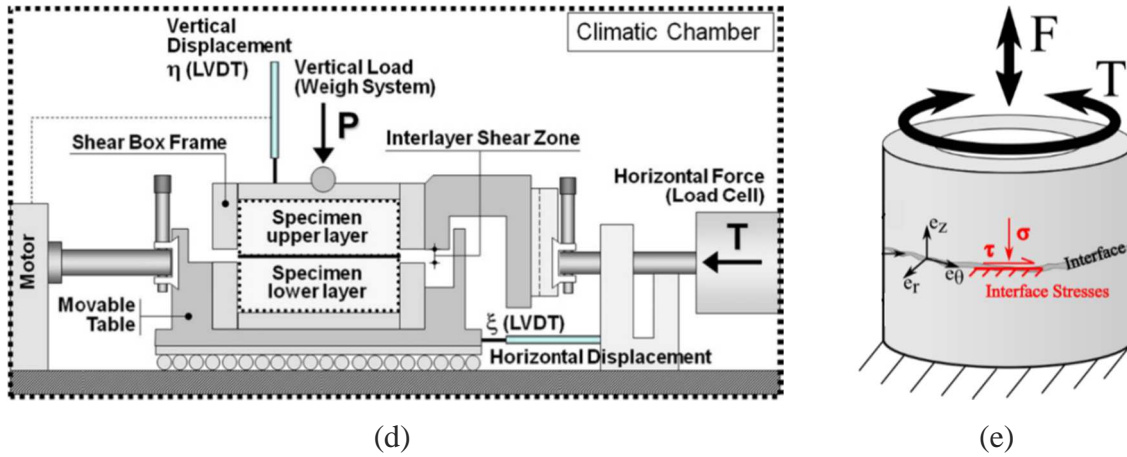


Figure 2-31. Destructive adhesion test characterization schemes: (a) Leutner Device (Sagnol et al. 2019), (b) Wedge splitting test (Tschegg et al. 2012), (c) Double shear tester (Cho et al. 2016, Safavizadeh and Kim 2014), (d) ASTRA device (Ferrotti et al. 2011), (e) 2T3C Hollow Cylinder Apparatus (Attia et al. 2017)

2.7.6.2. Cracking resistance tests

Most of the geosynthetic laboratory and full-scale characterization is aiming at evaluating its performance to combat cracking in road pavements. In laboratory scale, the characterization through reinforced beams bending tests are widely found in literature. Different types of specimens can be found in literature for the bending tests, varying from slabs to beams with different dimensions. Finally, distinct interface positions on reinforced specimen heights are found. Table 2-4 summarizes the constitution of the specimens for bending tests found in the literature.

Table 2-4. Beams dimensions found in the literature for tests with reinforced specimens

Reference	Test type	Specimen dimensions			
		Thickness (mm)		Width (mm)	Length (mm)
		Upper Layer	Lower Layer		
Khodaii et al. (2009)	Slab Bending	75	0	150	380
Virgili et al. (2009)	4Pb	45	30	100	305
Ferrotti et al. (2011)	4Pb	45	30	90	305
Zamora-Barraza et al. (2011)	Anti-reflective cracking test	50	50 (40 notch)	50	305
Millien et al. (2012)	Tensile bending	50	50	110	560

Montepara et al. (2012)	3PB	40	20	100 and 500	400 and 500
Romeo et al. (2014)	3Pb	40	20	100	400
Safavizadeh et al. (2015)	4Pb	36	18	64	400
Canestrari et al. (2015)	3Pb and 4Pb	45	30	90	240
Fallah & Khodaii (2015)	Bending device	50, 70 and 90	70	150	450
Gonzalez-Torre et al. (2015)	Reflective Cracking	50	50	260	410
Obando-Ante & Palmeira (2015)	Bending device	50	50	200	480
Pasquini et al. (2015)	Simulative Re- flective Crack- ing tests	35	45	80	285
Arsenie et al. (2016)	4Pb	25x50x25		100	630
Chantachot et al. (2016)	Bending device	30	30	385	1030
Graziani et al. (2016)	3Pb	45	30	90	240
		50	50	100	400
Nejad et al. (2016)	Bending device	50	70	150	450
Zofka et al. (2016)	3Pb and 4Pb	70	30	200	400

Note: 3Pb, three points bending; and 4Pb, four points bending.

The recent cracking characterization is mainly focused on two types of distresses: mitigation of reflective cracking and increase in the fatigue resistance. Ferrotti et al (2010) conducted 4Pb tests on beams reinforced by fiberglass geogrid at cyclic force controlled (1kN) and constant frequency (1Hz). Four beam configurations were tested, two unreinforced (having interface and not), and two reinforced (emulsions tack coat: bitumen and polymer-modified). The authors observed an increase in the specimen resistance due to geogrid reinforcement: 2.8 times greater for specimen with emulsion bitumen and 4 times greater for specimen with emulsion polymer-modified. However, the reinforced specimens presented higher vertical deformation due to weaker bonding between bituminous mixtures layers.

Millien et al (2012) conducted a work aiming at verifying the reflective cracking performance of two reinforced specimens (Fiberglass geogrid and Carbon fiber) comparing to one unreinforced only presenting an interface bonded by emulsion bitumen. Tensile-bending device

was used to conduct the tests performing tensile loading and bending loading at the same time at temperature of 5°C. Tensile loading represented the thermal effect and was conducted in a displacement rate of 0.01 mm/min. Cyclic-bending loading represented the traffic loading and was conducted in displacement amplitude of 0.2 mm and frequency of 1Hz. From results, authors observed grid interface increased the global strength by a factor of 60%. Moreover, the reinforcement enhance the fatigue resistance of bituminous mixtures.

Arsenie et al. (2012) developed a work aiming at to evaluate and predict of the improvement in the fatigue resistance of bituminous mixtures by the utilization of coated fiberglass geogrid as reinforcement. The authors used the Four Point Bending (4PB) test with the beam geometry of 620x100x90mm. The grid used for reinforcement was fiberglass with resin type SB 383 g/m<sup>2</sup> and fiber of polyester 17g/m<sup>2</sup> with mechanical resistance of 100kN/m at failure, inserted in the height of 60mm from the top of the beam with bituminous emulsion for the adhesion. Four tests were performed, two in bituminous mixtures without reinforcement, one in a mixture with two yarns grid reinforcement and one with three yarns grid reinforcement. The test were performed with controlled strain cyclic mode of loading with an amplitude of 200µm/m, in a temperature of 10°C and frequency of 25Hz. Two failure criterion were used and compared, the criterion I defined as the decrease to half of the initial force value (loss of 50% of specimen stiffness) and the criterion II defined as the decrease to 80% of initial force value (loss of 80% of specimen stiffness). From experimental results, according to criterion I, the mix with 2 yarns reinforcement presented 37% of fatigue life increment, while the mix with 3 yarns reinforcement presented 46% fatigue life increase. From this criterion, the use of 3 warp yarns results in an increment of 9% of fatigue life when compared with the 2 yarns reinforcement. Regarding the criterion II, the 2 yarns mix presented 37% of fatigue life increment again, while the 3 yarns reinforcement presented 68% fatigue life increase. Which means 31% increment compared with the 2 yarns mix. For the modeling of the damage, the authors used the Bondin model implemented in a finite element model. Different strain levels were used in the damage modeling (from 130 to 180µm/m). The results showed an increment in the fatigue life between 33.5% and 45.5% depending of the fiberglass section.

Safavizadeh et al. (2015) conducted research aiming at evaluating different interface conditions in the failure mechanisms in bituminous mixture beams reinforced by fiberglass geogrid using 4PB tests. Two different grids (25.0 and 12.5mm opening) and a beam with no grid were used in the tests prepared with four different tack coats (asphalt binder PG64-22, emulsion cured, uncured, and highly polymer modified) and no tack coat. Double layer slabs were compacted with the fiberglass reinforcement between the layers. The bottom layer was trimmed to

a thickness of 18mm and the upper layer of 36mm. Sinusoidal displacement bending loading was performed in the beams at a frequency of 5Hz, the temperature of 20°C and a displacement level that reaches 900µm/m. In addition, digital image correlation technique was used to measure de strain and displacements around the crack. To the failure definition, two criteria were used: the drop in the curve of stiffness×N (number of cycles) vs N; and the reduction of 50% of specimen's stiffness. From the results, the authors noticed that the polymer-modified tack coat resulted in the best bond quality, and it increases the fatigue life of the beams. However, the uncured emulsion resulted in the weakest bond quality and experienced excessive debonding during the test. This leads the conclusion that relates the direct relates bond quality with cracking mechanisms in 4PB tests. In addition, the 50% stiffness reduction criteria seemed to underestimate the performance of grid-reinforced specimens.

Pasquini et al. (2015) conducted a work using geogrid-reinforced bituminous membranes as a method to prevent the reflexive cracking, and, thus, be an option of pavement rehabilitation. For the development of the research, a field trial was constructed and the specimens were cored from it. The section constructed was divided in an old milled surface and in a totally new surface. For each portion different geocomposites were used, two types of membrane compound (plastomeric and elastomeric) and fiberglass grids with two different square mesh openings (5.0mm and 12.5mm) and two different interface condition (with and without tack coating). Also, an unreinforced section and a geocomposite found in the market were used for comparison purposes. The tests of simulate reflexive cracking (SRC) were performed in prismatic pre-notched specimens (3mm crack tip) produced in laboratory. They were conducted at a temperature of 30°C and at two amplitudes of loading (520 and 615N), with a rate of 21 cycles/min wheel rubber tire passing. A digital camera is also used for recording the crack propagation during the test. However, the SRC tests for the specimens with geocomposite found in the market and unreinforced were only performed for the amplitude of 520N, because the specimens could not reach the higher amplitude. The failure criteria adopted was the position of the crack, and it occurs when the crack reaches the upper surface. From SRC tests, it was noticed that the geocomposites are effective in the anti-reflexive cracking role since their performance was at least five times greater than the unreinforced specimen. Moreover, the 5.0mm and 12.5mm elastomeric geocomposites presented the best performance on the test. Finally, it was concluded that the best reinforcement would be the one with 12.5mm mesh and elastomeric membrane since it combined good anti-reflexive performance with not too bad interface shear resistance (parameters evaluated in the research).

Zofka et al. (2016) performed 3PB and 4PB tests to characterize bituminous mixtures reinforced by fiberglass and carbon fiber geogrids coated with neat bitumen. Tests were conducted using a new universal apparatus, called the AMC (Advanced Material Characteriser) at 13°C. 3PB tests were performed at monotonic loading with a rate of 1 mm/min in displacement control mode. 4PB tests were performed at cyclic loading in a force-controlled mode for fatigue and complex modulus tests. All experimental details are presented in Table 2-6. The authors observed a substantial increase in fatigue resistance due to the reinforcement and concluded that the most effective position to place the geogrid for increase fatigue performance is at 31% height of the beam (measured from the bottom).

In France, located at the IFSTTAR APT facility, there is an outdoor circular carousel dedicated to full-scale pavement experiments. Thus, some work concerning geosynthetics reinforcement has been conducted in this facility. Hornych et al. (2012) constructed four pavement sections, three reinforced by fiberglass geogrid and one without reinforcement. In two reinforced sections, a special designed film was used to replace the tack coat, and the last one was bonded by bitumen as tack coat in an application rate of 300g/m<sup>2</sup>. The same tack coat and rate was used for the unreinforced section. Standard dual wheels applied the load of 65 kN (standard French equivalent axle load) and the loading speed was 6 rounds/minute (43 km/h). The temperatures varied between 20 and 28°C. In crack monitoring results, the reinforced section with the film as tack coat was the first to present cracks (around 600 000 cycles). However, the author reported installation problems that could lead to a debonding in this section. After that, the unreinforced section presented the cracks (around 800 000 cycles). The reinforced section with bitumen tack coat did not present cracks. Nguyen et al. (2013) referring to the full-scale characterization using IFSTTAR APT facility concluded that the fiberglass geogrid, placed near the bottom of the bituminous mixture layer significantly improves the fatigue life. However, the bond quality between the geogrid and the bituminous mixture layers are essential to occur the reinforcement.

### *2.7.6.3. State-of-art summary*

In summary, until the present date, many works evidenced the benefits of geosynthetic reinforcement to bituminous mixtures. These benefits could be related to cracking resistance (Ferrotti et al. 2011, Montepara et al 2012, Millien et al 2012, Walubita et al 2015, Pasquini et al. 2015, Safavizadeh et al 2015, Canestrari et al 2015, Zofka et al. 2016). Moreover to fatigue resistance (Arsenie et al. 2012, de Bondt 2012, Millien et al 2012, Arsenie et al. 2016, Zofka et

al. 2016) and rutting (Khodaii et al 2009, Virgili et al 2009, Guler & Atalay 2016, Mounes et al 2016, Correia and Zornberg 2018). More recently, fiberglass geogrid started to be widely used for bituminous mixtures characterization and the tack coat seems to be very necessary to assure enough bonding. Table 2-5 summarized the geosynthetics characteristics used for bituminous mixtures reinforcement and the tack coat used. Table 2-6 presents the experimental information concerning some works found in literature.

Table 2-5. Different types of Geosynthetics found in literature and the tack coat information for its installation

Reference	Geosynthetic			Tack coat	
	Type(s)	Strength (KN/m)	Mesh (mm)	Type(s)	Rate (g/m <sup>2</sup> )
Austin and Gilchrist (1986)	Polypropylene geogrid (Tensar AR1)	22	65x65	Bitumen Emulsion	1.5 l/m <sup>2</sup>
Nguyen et al. (2013)	Fiber glass grid	100	25x25	Bitumen	500 g/m <sup>2</sup>
Arsenie et al (2016)	Fiber glass grid with nowoven web	100	40x40	65% of residual bitumen	600 g/m <sup>2</sup>
Pasquini et al (2015)	Fiber glass grid with plastomeric and elastomeric compounds	40	5 and 12.5 squares	Emulsion Bitumen	150 g/m <sup>2</sup> (residual binder)
Safavizadeh et al. (2015)	Fiber glass grid	Not given	12.5x12.5	Asphalt binder PG64-22	0.2 l/m <sup>2</sup>
				Emulsion cured	
			50x50	Emulsion uncured	
				Highly polymer modified	0.65 l/m <sup>2</sup>
Obando-Ante and Palmeira (2015)	Geocomposite (polyester)	38	40x40	Cationic RR-1C	Not given
	Wire Mesh (steel)	49	20x20		
	Geogrid (polyester)	128	20x20		
	Geogrid (polyester)	55	20x20		



Canestrari et al. (2013)	Glass/Carbon Fiber geogrid	249	20x20	SBS polymer-modified emulsion	250 g/m <sup>2</sup>
	Glass Fiber Polymer geogrid	211	33x33		
Norambuena-Contreras and Gonzalez-Torre (2016)	Polypropylene non-woven geotextile	Not given		C9 B3 Emulsion (69% residual binder)	Not given
	Polypropylene reinforced with glass fiber filaments		40x40		
	Polyester geogrid with polypropylene geotextile		40x40		
	Polyvinyl alcohol geogrid with polypropylene geotextile		40x40		
	Polypropylene stiff monolithic geogrid with polypropylene/polyester fabric		65x65		
	Fiberglass geogrids with polyester geotextile		40x40		
	Glass-carbon fiber geogrid covered with a bitumen (G8)		20x20		
Chantachot et al. (2016)	Fiberglass geogrid	50	20x20	Emulsion	1100 g/m <sup>2</sup> (450 per contact)
	Polypropylene nonwoven with glass filaments	50	30x30		
Delbono & Giudice (2014)	Polyester fiber + polypropylene geotextile	Not given	40x40	Emulsions	0.9 l/m <sup>2</sup>
Gonzalez-Torre et al. (2015)	Polypropylene geotextile with glass fibre filaments	57	Not given	Emulsion	1100 g/m <sup>2</sup>
Walubita et al. (2015)	Paving mat-fiber-glass/polyester	25	Not given	PG 64-22	Not given

	Paving mat–fiber-glass/polyester (angle 45°)	25			
	Paving mat–fiber-glass/polyester	50			
	Composite grid–fiber-glass grid / polyester	50			
	Composite grid–fiber-glass grid / polypropylene	50			
	Paving mat–fiber-glass/polyester blend	200			
	Paving fabric–nonwoven polypropylene	450			
	Composite grid–polyester	50			
Sobhan & Tandon (2008)	Tensar Biaxial Geogrid (BX 1500) - Polypropylene	20	25x25	Liquid asphalt binder	50 g/m <sup>2</sup>
	Amoco PetroGrid 4582 (polypropylene paving fabric, and glass fiber.	15	30x30		
Komatsu et al (1998)	Polyoxymethylene (POM) fibers (polymeric) - Normal and activated	1.8 and 1.5 (GPa)	5, 10, 20 and 30 squares	Emulsion	300 ml/m <sup>2</sup>
Khodaii et al (2009)	Polyester	50	40x40	Not given	Not given
Virgili et al. (2009)	Fiberglass	100	12.5x12.5	Emulsion	300 g/m <sup>2</sup>
	Polyester	110	30x30		
	Geomembrane	40			
Zamora-Barraza et al (2011)	Polyester, Fiberglass and polypropylene	Not given	Not given	Emulsion bitumen	Not given
Zofka et al (2016)	Fiberglass and carbon fiber	Not given	17.5x19.6	no tack coat used	N/A

Cho et al (2016)	Fiberglass geogrid	Not given	12.5x12.5 and 25x25	PG 64-22 and emulsion	0.199 L/m <sup>2</sup>
Noory et al (2017)	Fiberglass geogrid	100	22, 33, 67, 111, squares	Bitumen	0, 0.5, 1, and 1.5 kg/m <sup>2</sup>
Nejad et al. (2016)	Fiberglass geogrid and Polypropylene	120 and 11	30x30	Bitumen (85/100 penetration)	Not given
Montepara et al (2012)	Fiberglass geogrid	80	12.5x12.5 and 25x25	Bitumen layer	Not given
Millien et al (2012)	Fiberglass and carbon fiber	211 and 249	20x20 and 33x33	Bitumen	210 g/m <sup>2</sup>
Ferrotti et al (2011)	Fiberglass geogrid	211	33x33	Emulsions: bitumen and polymer-modified	0.15 kg/m <sup>2</sup>

N/A: Not applicable

Table 2-6. Information of experimental characterization concerning bituminous mixtures reinforced by geosynthetics in literature

Reference	Testing Parameters				
	Type	Temperature	Controlled INPUT	Amplitude	Frequency/Rate
Austin and Gilchrist (1986)	Wheel loading test	Ambient	Stress	300kPa	N/A
Nguyen et al. (2013)	Accelerated pavement testing (APT)	Variable	Force	65kN	6 rounds/min
Arsenie et al (2016)	Four Point Bending (4PB)	10°C	Strain	200µm/m	25Hz
Pasquini et al (2015)	ASTRA	20°C	Stress	0.0, 0.2 and 0.4MPa	N/A

	Simulate reflexive cracking (SRC)	30°C	Force	520 and 615N	21 cycles/min
Safavizadeh et al. (2015)	Four Point Bending (4PB)	20°C	Strain	900µm/m	5Hz
Obando-Ante and Palmeira (2015)	Beam vertical loading	Ambient	Stress	350KPa, 450KPa, and 560KPa	1Hz
Canestrari et al. (2013)	ASTRA	10, 20 and 30°C	Stress	0.0, 0.2 and 0.4MPa	N/A
	4PB	20°C	Force	1, 1.5 and 2kN	1Hz
	3PB	20°C	Displacement	N/A	50.8mm/min
Chantachot et al. (2016)	Footing load	25°C	Stress	10 to 400kN	0.1333cycles/min
Gonzalez-Torre et al. (2015)	Bending test	20°C	Force	12kN	10; 0.33; 0.005; 0.002 Hz
Walubita et al. (2015)	Overlay Tester	0°C	Monotonic Tensile Loading	N/A	3.375mm/min
Sobhan & Tandon (2008)	Bending test (static and cyclic)	Not given	Force	222, 444, 888, 1110, and 1332 N	2Hz
Komatsu et al (1998)	Wheel tracking testing machine	60°C	Wheel Force	686N	42 revolutions
Khodaii et al (2009)	Cyclic loading in slabs	20 and 60°C	Stress (circular surface)	690 kN/m <sup>2</sup>	10Hz
Virgili et al. (2009)	Beam cyclic compression	20°C	Force	1KN	1Hz

Zamora-Bar-raza et al (2011)	Anti-reflective cracking test	20°C	Wheel pressure	0.65 Mpa	43 times/min
Zofka et al (2016)	3Pb and 4Pb	13°C	Displacement (fracture) and Force (cyclic)	1mm/min and 4kN (fatigue)	1Hz (cyclic)
Nejad et al. (2016)	Bending beam test	0, 20 and 40°C	Force	6.9kN	10Hz
Montepara et al (2012)	3PB (beam and slab)	20°C	Displacement	N/A	0.084mm/s
Millien et al (2012)	Tensile Bending	5°C	Displacement (constant + cyclic)	0.2mm (cyclic)	0.01mm/min and 1Hz
Ferrotti et al (2011)	4PB	20°C	Force	1KN	1Hz

N/A: Not applicable

#### 2.7.6.4. *Fiberglass Geogrids*

Nowadays, fiberglass geogrids are considered one of the best solutions of geosynthetic reinforcement of bituminous mixtures. Those materials presenting high-tension resistance and flexibility at once (Nguyen et al. 2013) and are easily removable by milling in the case of further pavement maintenances. Darling & Woolstencroft (2004) pointed out that one great advantage of fiberglass geogrids is the fact they are thermally and chemically stable at 200°C, temperature easily reached during hot mix fabrication. In addition, de Bondt (1999) stated that fiberglass geogrid provides the necessary stiffness to redirect crack energy.

Fiberglass geogrids are generally impregnated with bitumen or polymer coating. This coating process is useful to increase the compatibility and adhesion with asphalt and protects against chemicals and abrasive materials (Nguyen et al. 2013). Aldea and Darling (2004) give evidence that the used of tack coat enhances the fiberglass geogrid performance regardless of the type of coating (polymeric or bituminous). Moreover, the polymeric tack coat presented the best improvement of fiberglass geogrid performance. Association of fiberglass geogrids with light polyester nonwoven geotextile (about 15-40g/m<sup>2</sup>) is widely done (Nguyen et al. 2013). Firstly, this material contributes to giving protection to the fiberglass yarns during installation, caused by the tires of vehicles. In addition, it helps to distribute better the tack coat and avoid the geogrid

local debond due to lack of tack coat. Furthermore, this geotextile absorbs the tack coat excesses that could lead to problems during construction, according to Vanelstraete and Franken (1997). The geotextile used to this end should be light enough to grant the aggregate particles interlock of the two bituminous layers.

Concerning its performance, many works also indicated that the fiberglass geogrid presents better performance to cracking resistance when compared to the other types of geogrids (Lytton 1988; de Bondt 1999; Brown et al. 2001; Canestrari et al. 2015). Fiberglass geogrids are also effective in the reinforcement of unbound (granular) layers (Mamatha et al. 2019) and concrete pavements (Al-Hedad & Hadi 2019).

Nowadays, there is still the need for the design of pavements structures that take account of the behavior of geosynthetics reinforcement. However, some simplified models and procedures can be found in the literature, mostly based on empirical data, concerning only specific products. COST Action (2006) presents a list of models currently used in practice in Europe, but only two could be used for fiberglass geogrid reinforcement case:

- Anti-Reflective Cracking Design Software (ARCDES0®): developed by Ooms Nederland Holding, finite-element based model created to the rehabilitation of roadways. This software model the crack propagation in the pavement and provides and indicative of the development of reflective cracking.
- University of Nottingham method: reflective cracking prediction tool. The method is based on an estimation of cracking growth induced by traffic load (using OLCRACK software) and by the thermal load (using THERMCR software).

# Chapter 3: MATERIALS AND EXPERIMENTAL CAMPAIGNS

3.1. Materials .....	97
3.1.1. Bituminous Mixture .....	97
3.1.2. Geogrid reinforcement .....	98
3.2. Specimens Preparation .....	100
3.2.1. Slabs configurations .....	100
3.2.2. Slabs fabrication.....	101
3.2.3. Specimens coring and nomenclature.....	103
3.2.4. Air voids.....	106
3.3. Experimental campaign overview .....	117

This chapter aims at describing the bituminous mixture composition, as well as the types of geogrids used for the reinforcement and the emulsions used as tack coat. Moreover, the installation of the geogrids during the slabs fabrication will be presented. Furthermore, the different types and directions of coring will be presented: cylindrical specimens with interface in two different directions, and prismatic (beam shape) specimens. Finally, the experimental campaign will be discussed in terms of the need of each type of specimen to conduct it.

## 3.1. Materials

### 3.1.1. Bituminous Mixture

The same bituminous mixture was used to conduct the entire experimental campaign of this doctoral thesis. According to the European standards (EN 13108-1 2016), the mixture is called *Béton Bitumineux Semi-Grenu* (BBSG) 0/10. This type of mixture was already presented in section 2.3. It is composed by mineral aggregates with nature rhyodactic and rhyolitic, mineral filler of limestone and 20% of recycled asphalt pavement (RAP) resulted from old pavement milling, containing 4.75% of bituminous binder. Figure 3-1 presents the mineral aggregates gradation curve used for the bituminous mixtures fabrication. These aggregates were mixed with 4.40% of bituminous binder classified as 35/50 by its penetration. The total bituminous binder content in the mixture was 5.53%, considering the amount already contained in the RAP. This bitumen is processed at the BP Lavéra INEOS refinery situated in south of France. Table 3-1 presents the bituminous mixture components, producers, nature and percentage of use. The maximum specific gravity (*MVR*) obtained for the bituminous mixture was 2.51 Mg/m<sup>3</sup>.

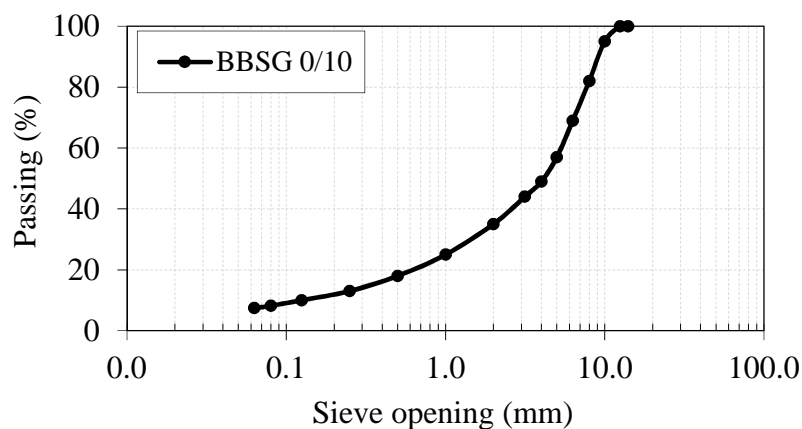


Figure 3-1. Bituminous mixture (BBSG 0/10) gradation curve



Table 3-1. Bituminous mixture components information and percentage of use

<b>Product</b>	<b>Producer</b>	<b>Nature</b>	<b>% use</b>
Gravestone 6/10	CBR Creuzeval quarry	Rhyodactic	28.00
Gravestone 4/6	CBR Creuzeval quarry	Rhyodactic	12.00
Sand 0/4 S	TRMC Igé quarry	Rhyolitic	34.60
Filler	St-Hilaire-de-Brens	Limestone	1.00
RAP	SRE - Belleville Post	Crushed	20.00
Bitumen 35/50	BP Lavéra INEOS refinery	Roadway bitumen	4.40

### ***3.1.2. Geogrid reinforcement***

In order to reinforce the bi-layered bituminous mixtures, two fiberglass geogrid and two emulsions tack coat were used. The geogrids were Notex Glass® fabricated and provided by the French company Afitexinov: the Notex Glass® C50/50-25 and the Notex Glass® C100/100-25. They were composed by fiberglass yarns and polyester knitted veil, both coated with bituminous emulsion. Moreover, both yarns present square mesh opening of 25mm. The letter “C” indicates that the geogrid was previously coated, the numbers “50/50” represent the maximum tensile resistance on each direction in kN, and the last number “25” represents the mesh opening between yarns in millimeters. The polyester veil has the function of increasing the bond between the geogrid and the bituminous mixture, protecting the geogrid during installation and helping to spread homogeneously the emulsion during field application. Figure 3-2 presents pictures of Notex Glass® 50/50-25, Notex Glass® 100/100-25 and Notex Glass® C 100/100-25 (used in this doctoral thesis).

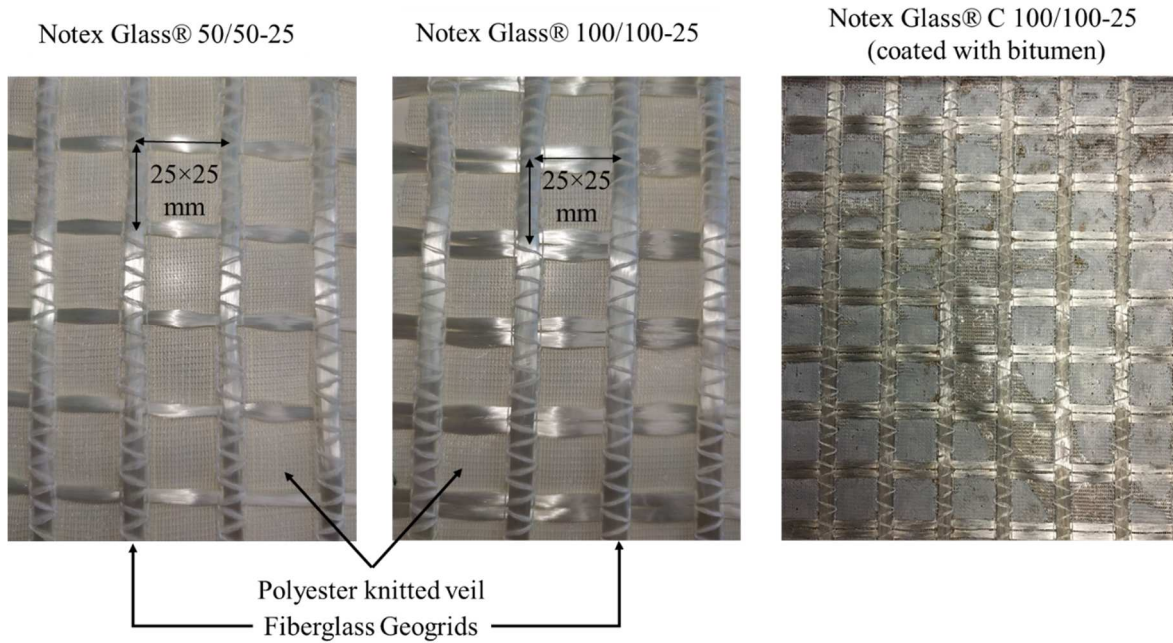


Figure 3-2. Fiberglass geogrid Notex Glass® C 50/50-25 and 100/100-25 compositions and coated with bitumen (used in this doctoral thesis) produced by Afitexinov

EN ISO 10319 (2015) presents the geosynthetics standard tests used to obtain their most relevant characteristics. Notex Glass® geogrids were subjected to tensile test, in order to obtain two important characteristics for the use as reinforcement: maximum tensile strength and elongation value at failure. Notex Glass® C 50/50-25 should provide a minimum 50kN of tensile strength in the two directions and Notex Glass® C 100/100-25 should provide a minimum of 100kN in the two directions, machine and cross machine direction of fabrication. Figure 3-3(a) presents a tensile test in machine direction for Notex Glass® C 50/50-25. Figure 3-3(b) presents a tensile test in machine direction for Notex Glass® C 100/100-25.

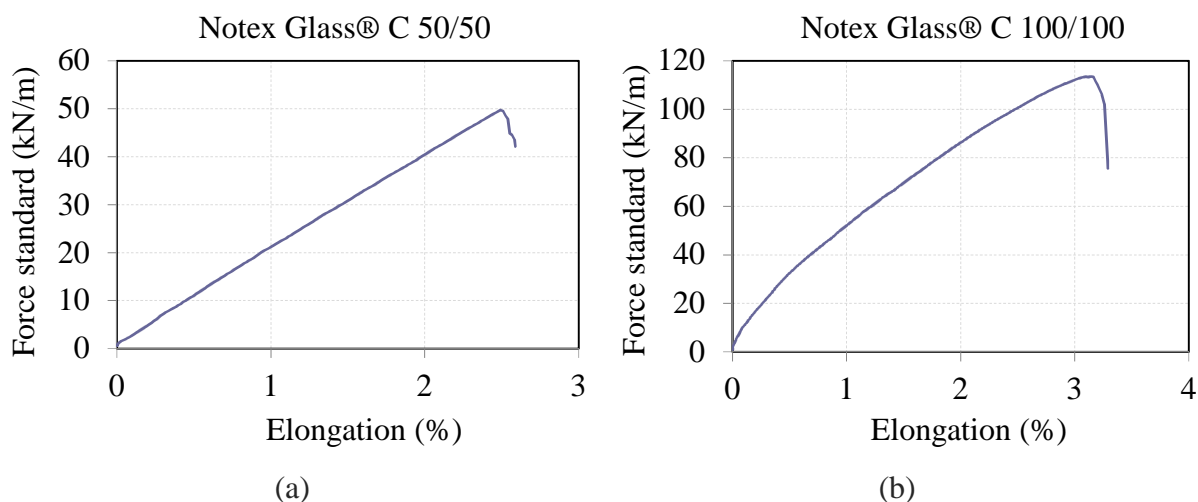


Figure 3-3. Force vs elongation characterization of fiberglass geogrid Notex Glass® C in machine direction: (a) 50/50-25 and (b) 100/100-25

To bond the fiberglass geogrid on the interface of the bi-layered reinforced bituminous mixtures, two emulsions produced by the company EIFFAGE Infrastructure were used. The first one is called Actimul® and is based on bitumen 160/220 penetration grade, diluted in water presenting 65% of residual binder. The second one is called Emulprène® and is based on bitumen 160/220 penetration grade modified with 2.6% of the polymer Styrene-Butadiene-Styrene (SBS). This emulsion was prepared with 64% residual modified binder.

## 3.2. Specimens Preparation

In this section, the specimens used for this research will be detailed. Starting with the explanation about the slabs configuration, fabrication and coring. Lastly, the nomenclature will be presented, as well as the air voids content obtained in the specimens cored from the slabs.

### 3.2.1. Slabs configurations

Five slab configurations were used to conduct this research. They were divided into two groups regarding the presence of interface. Configuration A do not have interface, while B, C, D, and E have interface and are denoted as bi-layered slabs. Concerning the bi-layered slabs, they are also divided into two groups regarding the presence of fiberglass geogrid: unreinforced (configuration B) and reinforced (configurations C, D, and E). As aforementioned, the interfaces were bounded with two types of emulsion bitumen-based. The rate of residual binder in

emulsion was 270g/m<sup>2</sup> for B configuration, and 800g/m<sup>2</sup> divided into two applications of 400g/m<sup>2</sup> of residual binder for C, D and E, as will be discussed in the next section. Table 3-2 summarizes the constitution of each slab configuration, detailing the interfaces and presenting the amount of slabs fabricated to conduct this research. An extra slab of configuration C was fabrication with different emulsion rate in the interface. A total of 540g/m<sup>2</sup> of emulsion Actumul divided in two applications of 270g/m<sup>2</sup> was done, and this slab is denoted in this thesis as “CE”.

Table 3-2. Five different slabs configurations constitution and total of slabs produced for the study

Configuration	Total of slabs	Bituminous Mixture Layers (BBSG 0/10)	Type of geogrid	Interface bound (Emulsion)	
				Type	Residual Binder Rate
A	4	1	No Geogrid	No Interface	
B	3	2	No Geogrid	Bitumen 160/220 (Actimul)	292g/m <sup>2</sup>
C	4	2	Notex Glass® C 100/100-25	Bitumen 160/220 (Actimul)	2×400g/m <sup>2</sup>
D	3	2	Notex Glass® C 50/50-25	Bitumen 160/220 (Actimul)	2×400g/m <sup>2</sup>
E	3	2	Notex Glass® C 100/100-25	Bitumen 160/220 with SBS (Emul-prène)	2×400g/m <sup>2</sup>

### 3.2.2. Slabs fabrication

The 17 slabs having the dimensions of 600×400×150mm were fabricated at the company EIFFAGE Infrastructure at the Research and Innovation Center in Corbas, Rhone department. The slabs were compacted using a French wheel compactor, according to the European standard (EN 12697-33 2019). The slabs of configuration A were prepared in one layer with thickness of 150mm. Concerning the slabs of configuration B, the fabrication was conducted by first compacting half height slab of 75mm (first layer), followed by the application of emulsion tack coat (292g/m<sup>2</sup> of residual binder). The fabrication was concluded by the compaction of the second half height slab of 75mm (second layer). The tack coat rate was chosen based on the

rate regularly used in the field to bound layers in roadways constructions performed by EIFF-AGE Infrastructure.

Regarding the fabrication of reinforced slabs (configurations C, D and E), a similar procedure as for configuration B was adopted, but including the geogrid. The procedure is explained in the five steps as follows:

1. First layer (75mm) slab compaction and cooling (c.f. Figure 3-4(a)).
2. First tack coat application ( $400\text{g/m}^2$ ): conducted with aid of a brush. The emulsion was diluted in 50% more to facilitate de application. Then, the surface of the first layer was divided into four parts, in order to assure an equitable distribution along the entire area. This is step is presented in Figure 3-4(b).
3. Geogrid placement positioning the veil upwards (c.f. Figure 3-4(c)).
4. Second tack coat application ( $400\text{g/m}^2$ ): again conducted with aid of a brush and following the same procedure described in step 2. Figure 3-4(d) presents this step.
5. Second layer (75mm) slab fabrication and compaction over the first already compacted layer after the emulsion break (c.f. Figure 3-4(e) and (f)).

The emulsion rate chosen for the fabrication of reinforced slabs is the recommended value by Afitexinov to Notex Glass® field application. However, for laboratory fabrication it was divided into two applications for technical reasons. The  $800\text{g/m}^2$  of tack coat in only one application led ineffective distribution of emulsion in the interface, which could provide heterogeneous bonding quality at different slab positions within the interface.



(a)



(b)



(c)

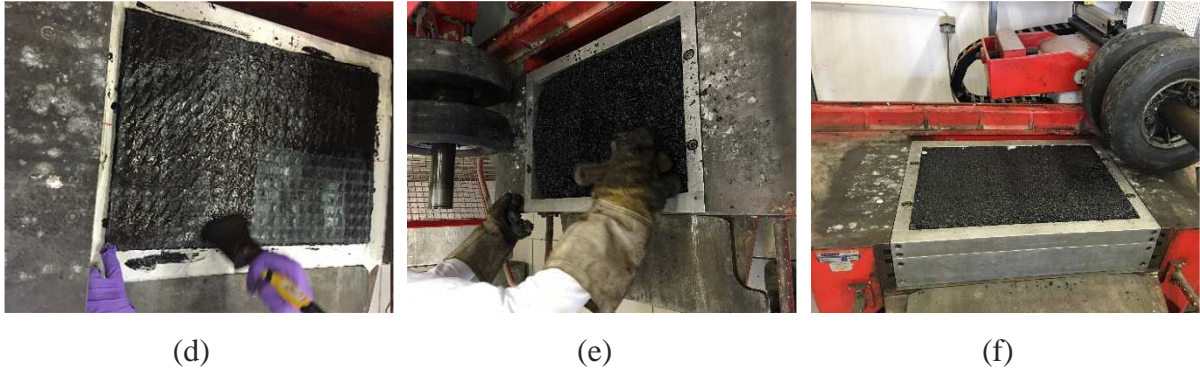


Figure 3-4. Slab fabrication of reinforced bi-layered bituminous mixture: (a) First layer compaction, (b) Emulsion first application, (c) Fiberglass geogrid placement, (d) Emulsion second application, (e) Upper layer fabrication, and (f) Final compaction.

### 3.2.3. Specimens coring and nomenclature

To conduct this research, cylindrical and prismatic specimens were cored from the slabs, at least two weeks after the fabrication. Cylindrical specimens were cored with 75mm diameter and 140mm height, and in two different coring directions. Specimens named H were horizontally cored, in relation to the roller compaction direction, while those named V were vertically cored. Moreover, some cylindrical specimens were cored in a larger diameter (136mm), named specimens type VL (stands for “vertical large”), to verify the size effect influence in experimental results of tension, as will be better discussed in the Chapter 5. Concerning the prismatic specimens, bars in a beam shape, with dimensions 550×70×110mm was sawed from the slabs. Those specimens are named as type B (stands for “beam”) during this thesis.

Three coring plans were proposed to obtain the enough amount of specimen considering each type (V, H or B) for the development of the experimental campaign. Figure 3-5(a) presents the plan 1, Figure 3-5(b) presents the plan 2, and Figure 3-5(c) presents the plan 3. Moreover, the specimens were cored from the most central part of the slabs as possible. Thus, between 30 and 40mm of margins were left in the slab. During wheel compaction, due to the friction between the mold and the material, the borders presents higher voids contents, which make them not representative of the material.



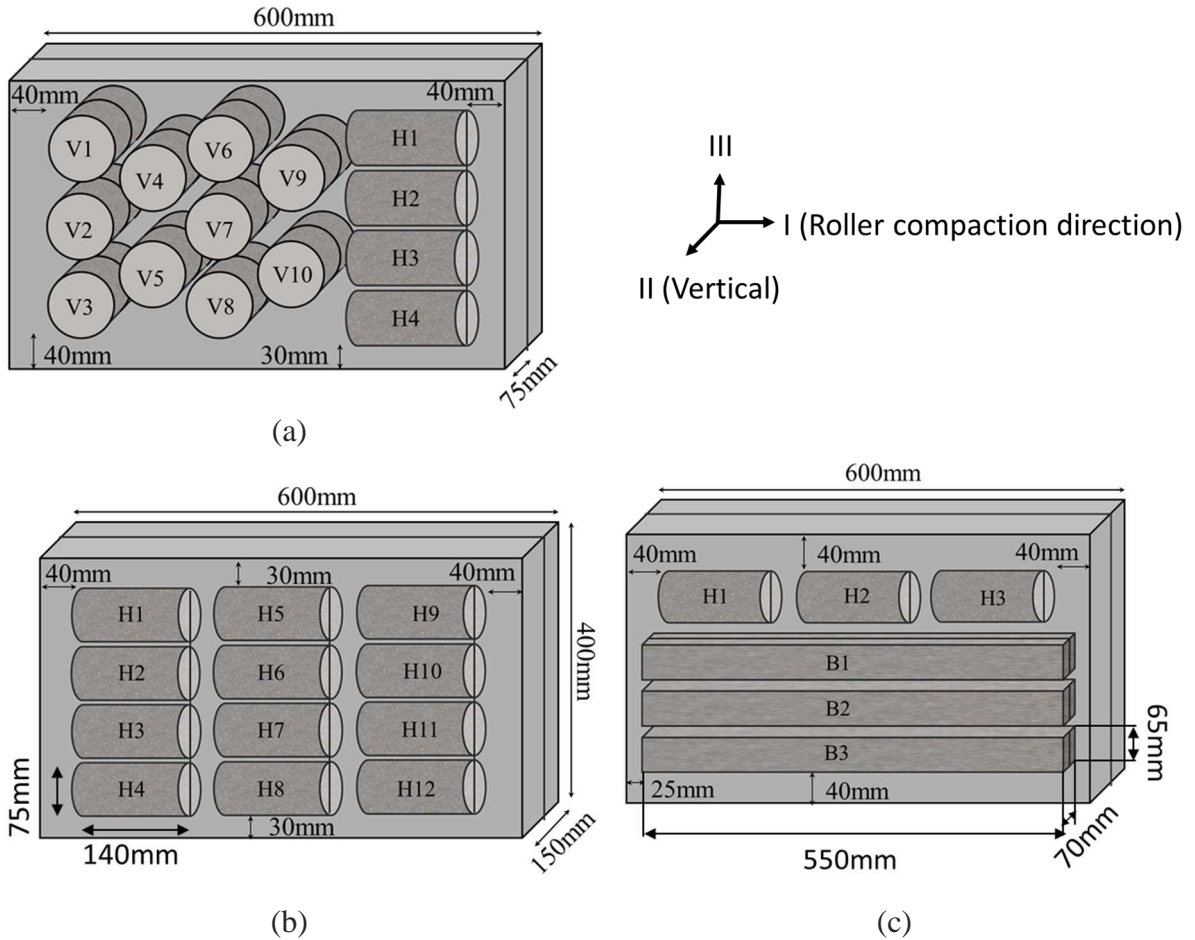


Figure 3-5. Coring plans in order to obtain three different types of specimen: (a) Plan 1: mix between specimens V and H, (b) Plan 2: specimens H, and (c) Plan 3: mix between specimen H and beams.

However, plan 1 (c.f. Figure 3-5(a)) was not used for configuration C. Instead, two other plans were proposed in order to obtain the specimens with a larger diameter (VL). Thus, the plan 1 was replaced by plan 1b (c.f. Figure 3-6(a)) and plan 4 (c.f. Figure 3-6(b)). The coring machine used is shown in Figure 3-7(a), and the drill is coupled with water flow to cool down the drill and slab temperature during the coring. Concerning the coring of specimens type H, the drill is centralized (c.f. Figure 3-7(b)) in relation to the interface position, resulting in interface symmetrically centralized in the specimen. Lastly, the cored specimens (c.f. Figure 3-7(c)) are trimmed on top and bottom using a diamond blade to achieve the desired height, which is around 140mm.

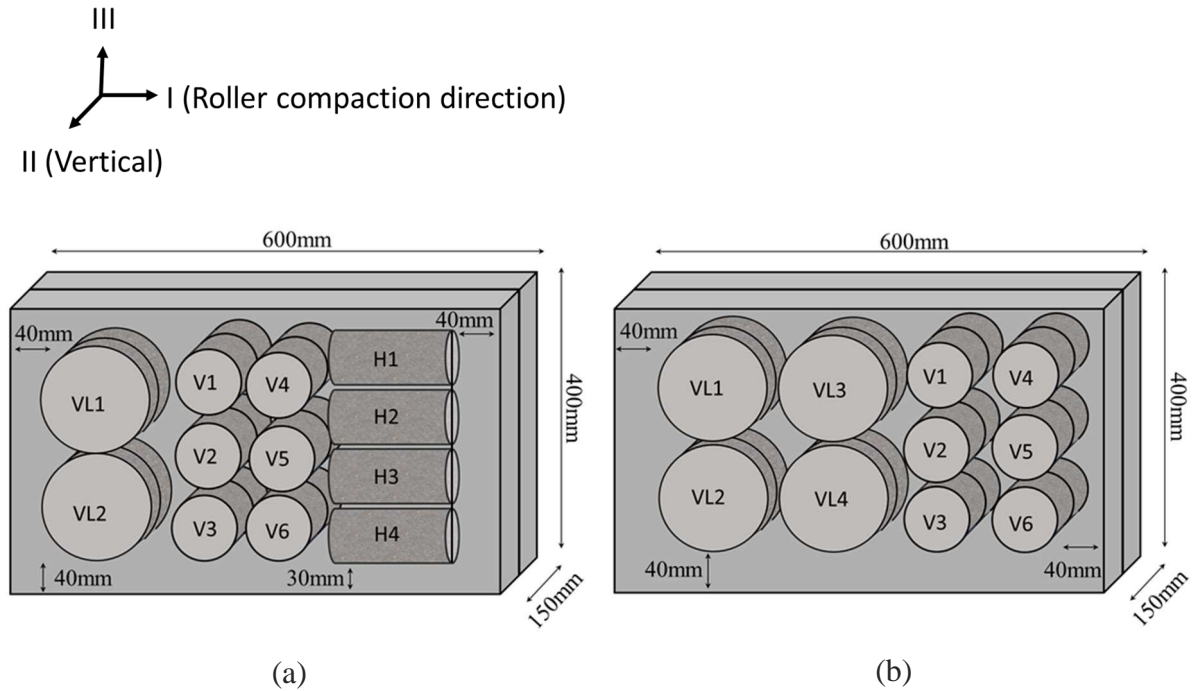


Figure 3-6. Additional coring plan for slabs C to allow obtaining specimens with larger diameters (136mm): (a) Plan 1b, and (b) Plan 4

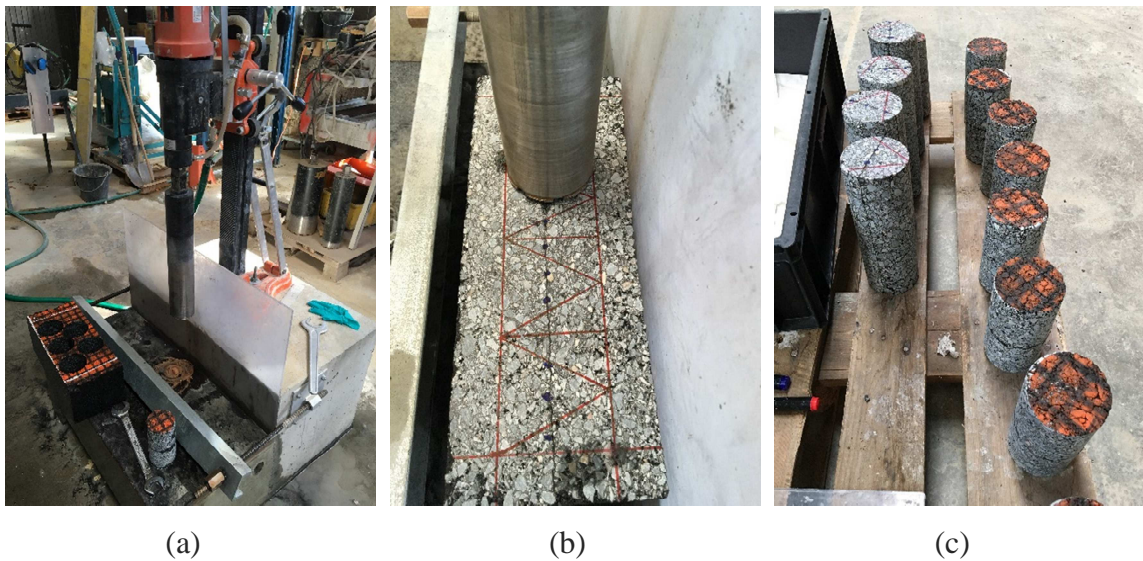


Figure 3-7. Coring of 75mm diameter cylindrical specimens from slab: (a) Coring machine, (b) Type H specimen coring, and (c) Types H (left) and V (right) cored specimens before the final trimming

After a period of two weeks, the specimens dried out and the bulk specific gravity can be measured (*MVA*), in order calculate the air voids content (c.f. Eq. 2-1). Moreover, each specimen is named according to the system presented in Figure 3-8. Slab configurations: A, B, C, D, or E. Specimen type: V (vertically cored), H (horizontally cored), VL (vertically cored large



diameter), or B (beam shape). Test type: E\* (complex modulus), T (traction), F (fatigue), or B (bending).

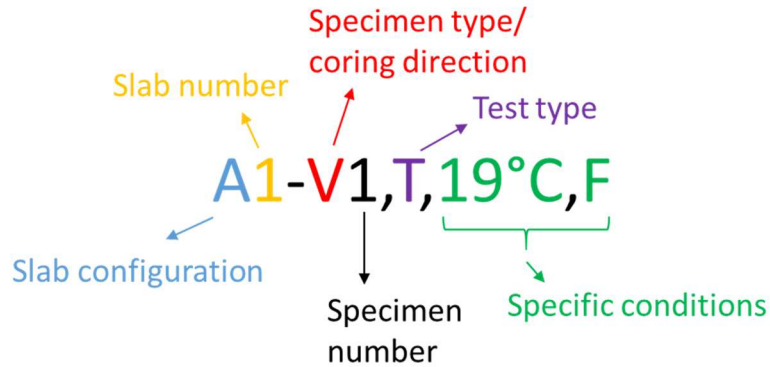


Figure 3-8. Nomenclature system for bituminous mixtures specimens

### 3.2.4. Air voids

The air voids content for each specimen used in this research was calculated according to Eq. 2-1.  $MVA$  is classically obtained by dividing the specimen weight by the volume of a cylinder with the same dimensions as the specimen. This procedure is called geometric in this thesis and is described in Eq. 3-1, where  $h$  is the specimen's height and  $D$  is the diameter. However, concerning the specimens with interface, containing or not geogrid, this calculation should be corrected by the presence of emulsion and geogrid. Thus, for specimens only containing interface, the emulsion weight and volume presented in the interface should be removed from calculation, as shown in Eq. 3-2. Furthermore, for specimens containing both, geogrid and emulsion in the interface, the weights and volumes of emulsion and geogrid should be removed from the calculation, as shown in Eq. 3-3.

$$MVA_1 = \frac{W_{Specimen}}{V_{Cylinder}} = \frac{4 \cdot W_{Cylinder}}{\pi \cdot h \cdot D^2} \quad \text{Eq. 3-1}$$

$$MVA_2 = \frac{W_{Specimen} - W_{Emulsion}}{V_{Cylinder} - V_{Emulsion}} \quad \text{Eq. 3-2}$$

$$MVA_3 = \frac{W_{Specimen} - W_{Emulsion} - W_{Geogrid}}{V_{Cylinder} - V_{Emulsion} - V_{Geogrid}} \quad \text{Eq. 3-3}$$

Figure 3-9 to Figure 3-12 graphically presents the air voids content obtained in specimens from configuration A slabs. For this configuration, the fabrication of a fourth slab was necessary since some specimens were lost during the beginning of the experimental campaign due to test calibrations and adjustments. Table 3-3 presents all air voids contents obtained for configuration A, as well as averages and standard deviations.

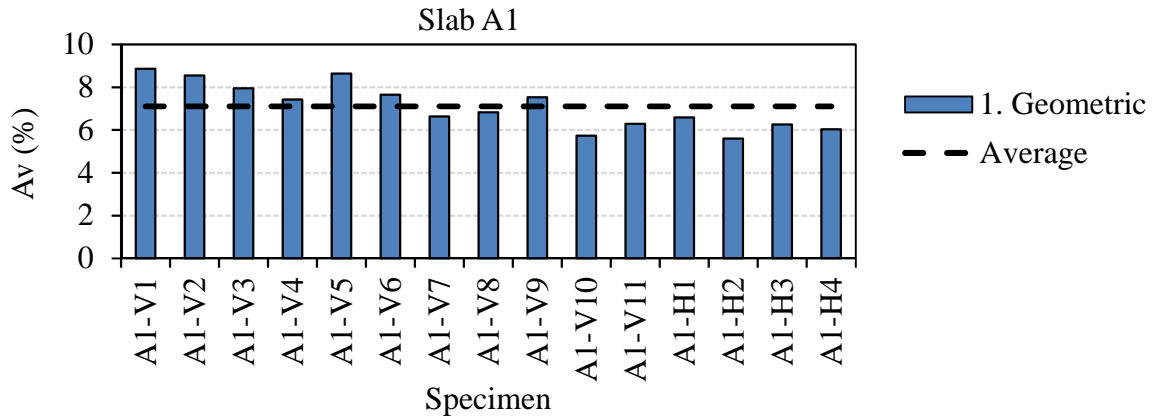


Figure 3-9. Air voids of the specimens cored from the slab A1

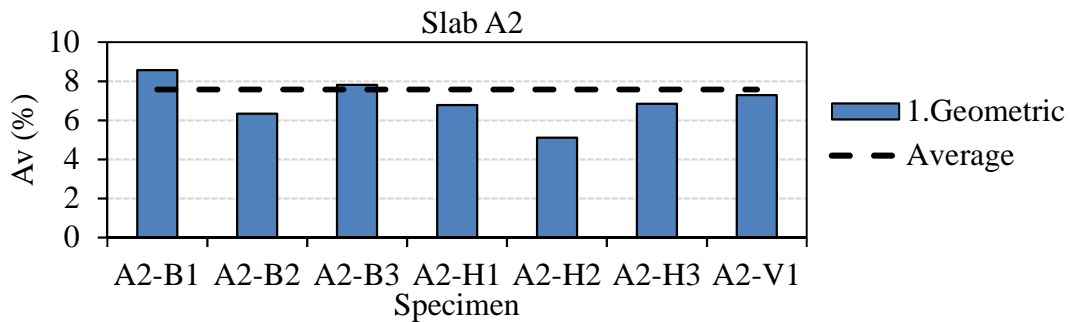


Figure 3-10. Air voids of the specimens cored from the slab A2

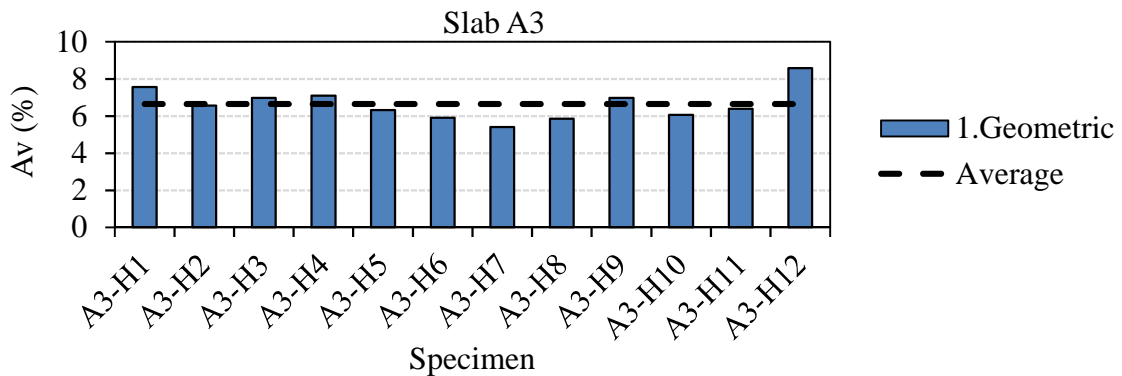


Figure 3-11. Air voids of the specimens cored from the slab A3

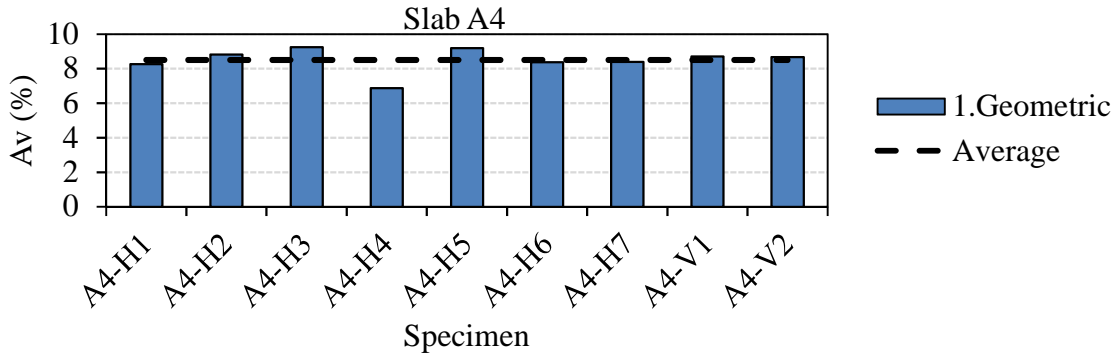


Figure 3-12. Air voids of the specimens cored from the slab A4

Table 3-3. Air voids contents, averages and standard deviations of specimens from configuration A slabs

Specimen (slab A1)	Air Voids (%)	Specimen (slab A2)	Air Voids (%)	Specimen (slab A3)	Air Voids (%)	Specimen (slab A4)	Air Voids (%)
A1-V1	8.9	A2-B1	8.6	A3-H1	7.6	A4-H1	8.3
A1-V2	8.5	A2-B2	6.3	A3-H2	6.6	A4-H2	8.8
A1-V3	7.9	A2-B3	7.8	A3-H3	7.0	A4-H3	9.2
A1-V4	7.4	A2-H1	6.8	A3-H4	7.1	A 4-H4	6.9
A1-V5	8.6	A2-H2	5.1	A3-H5	6.3	A4-H5	9.2
A1-V6	7.7	A2-H3	6.8	A3-H6	5.9	A4-H6	8.4
A1-V7	6.6	A2-V1	7.3	A3-H7	5.4	A4-H7	8.4
A1-V8	6.8			A3-H8	5.9	A4-V1	8.7
A1-V9	7.5			A3-H9	7.0	A4-V2	8.7
A1-V10	5.7			A3-H10	6.1		
A1-V11	6.3			A3-H11	6.4		
A1-H1	6.6			A3-H12	8.6		
A1-H2	5.6						
A1-H3	6.2						
A1-H4	6.0						
<b>Average</b>	7.1	<b>Average</b>	7.0	<b>Average</b>	6.6	<b>Average</b>	8.5
<b>Standard Deviation</b>	1.1	<b>Standard Deviation</b>	1.1	<b>Standard Deviation</b>	0.9	<b>Standard Deviation</b>	0.7

Figure 3-13 to Figure 3-15 graphically presents the air voids content obtained in the specimens from configuration B slabs. In this case, two different calculations are presented since the emulsion contained in interface should be removed from the *MVA* calculation. Thus, the actual air voids content is the one obtained from the *MVA*<sub>2</sub> (Eq. 3-2). Table 3-4 presents all air voids values obtained in specimens from configuration B slabs, as well as the averages and standard deviations.

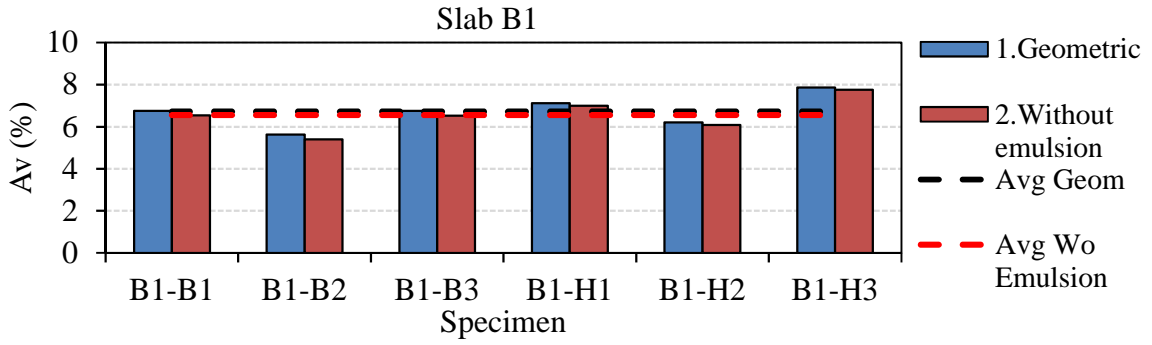


Figure 3-13. Air voids of the specimens cored from the slab B1

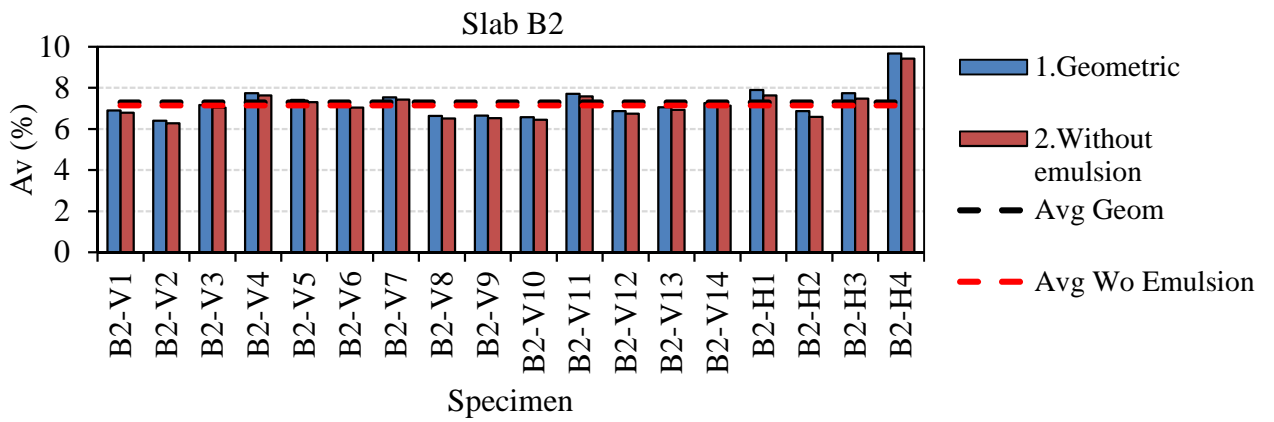


Figure 3-14. Air voids of the specimens cored from the slab B2

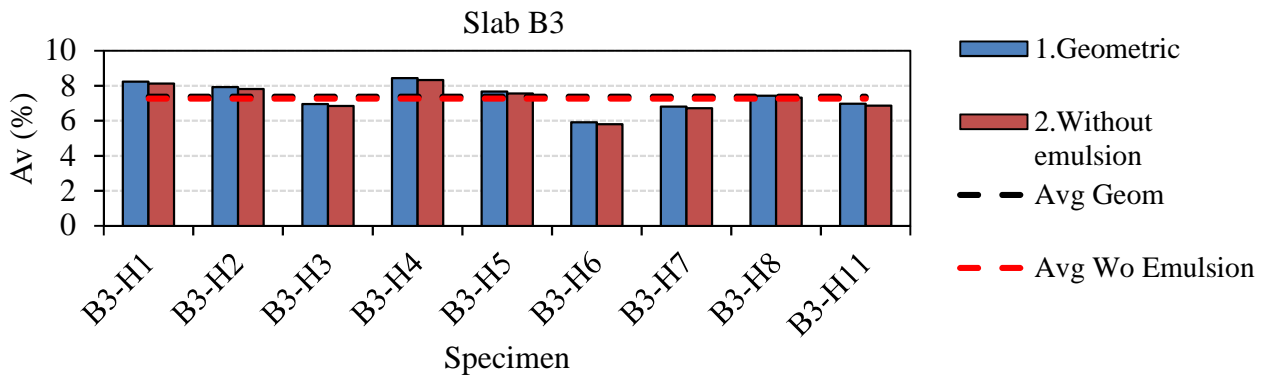


Figure 3-15. Air voids of the specimens cored from the slab B3

Table 3-4. Air voids contents, averages and standard deviations of specimens from configuration B slabs

Specimen (Slab B1)	Air Voids (%)		Specimen (Slab B2)	Air Voids (%)		Specimen (Slab B3)	Air Voids (%)	
	1. Geometric	2. Wo Emulsion		1. Geometric	2. Wo Emulsion		1. Geometric	2. Wo Emulsion
B1-B1	6.8	6.5	B2-V1	6.9	6.8	B3-H1	8.2	8.1
B1-B2	5.6	5.4	B2-V2	6.4	6.3	B3-H2	7.9	7.8
B1-B3	6.7	6.5	B2-V3	7.2	7.0	B3-H3	7.0	6.8
B1-H1	7.1	7.0	B2-V4	7.7	7.6	B3-H4	8.4	8.3
B1-H2	6.2	6.1	B2-V5	7.4	7.3	B3-H5	7.7	7.6
B1-H3	7.9	7.8	B2-V6	7.2	7.0	B3-H6	5.9	5.8
			B2-V7	7.5	7.4	B3-H7	6.8	6.7
			B2-V8	6.6	6.5	B3-H8	7.4	7.3
			B2-V9	6.7	6.5	B3-H11	7.0	6.9
			B2-V10	6.6	6.5			
			B2-V11	7.7	7.6			
			B2-V12	6.9	6.7			
			B2-V13	7.1	6.9			
			B2-V14	7.3	7.1			
			B2-H1	7.9	7.6			
			B2-H2	6.9	6.6			
			B2-H3	7.7	7.5			
			B2-H4	9.7	9.4			
<b>Average</b>	6.7	6.6	<b>Average</b>	7.3	7.1	<b>Average</b>	7.4	7.3
<b>Standard Deviation</b>	0.8	0.8	<b>Standard Deviation</b>	0.7	0.7	<b>Standard Deviation</b>	0.8	0.8

Concerning the reinforced slab configurations, the three aforementioned corrections were performed on air voids calculation. For those specimens, the third calculation represents actual the air voids content, considered in the development of this work. Figure 3-16 to Figure 3-20 presents the air voids content obtained for configuration C, more detailed in Table 3-5. Figure 3-21 to Figure 3-23 presents the air voids content obtained for configuration D, more detailed in Table 3-6 . Figure 3-24 to Figure 3-26 presents the air voids content obtained for configuration E, more detailed in Table 3-7.

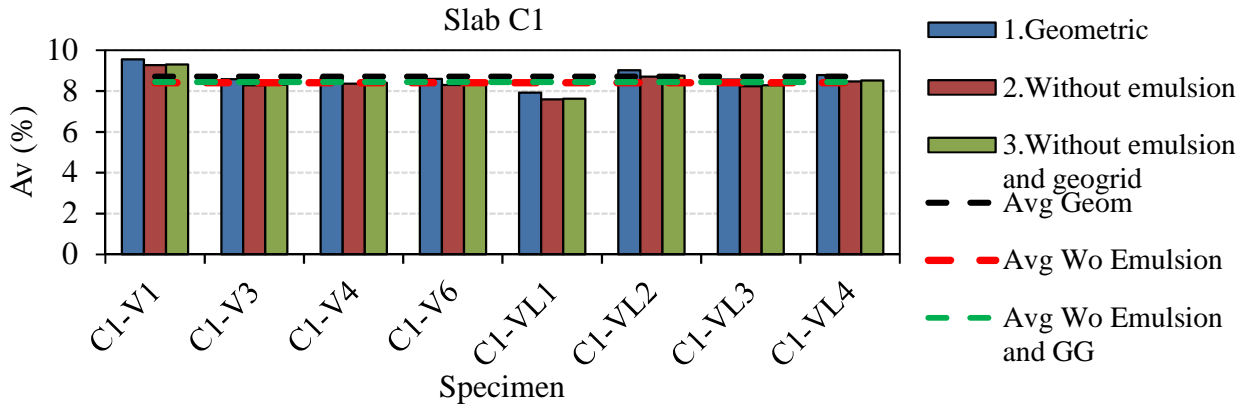


Figure 3-16. Air voids of the specimens cored from the slab C1

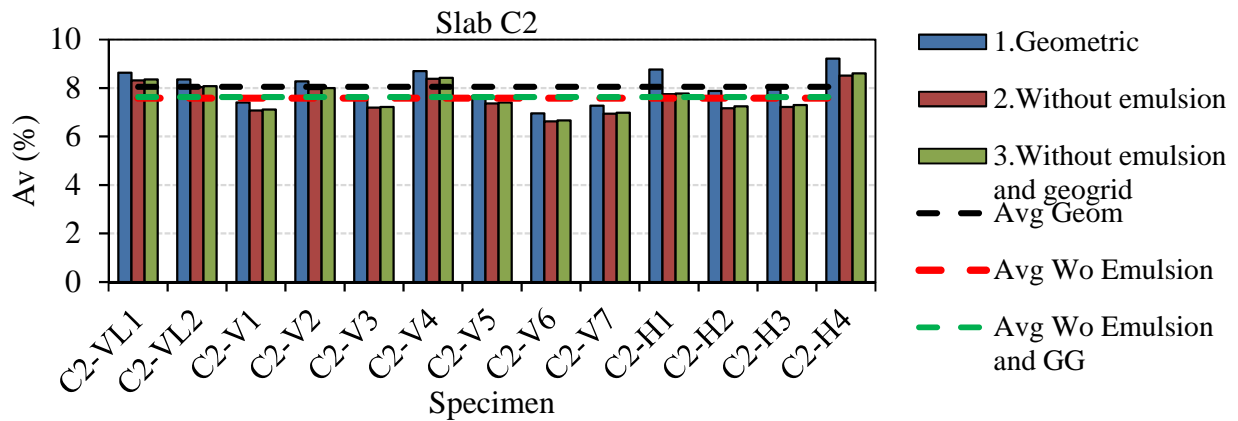


Figure 3-17. Air voids of the specimens cored from the slab C2

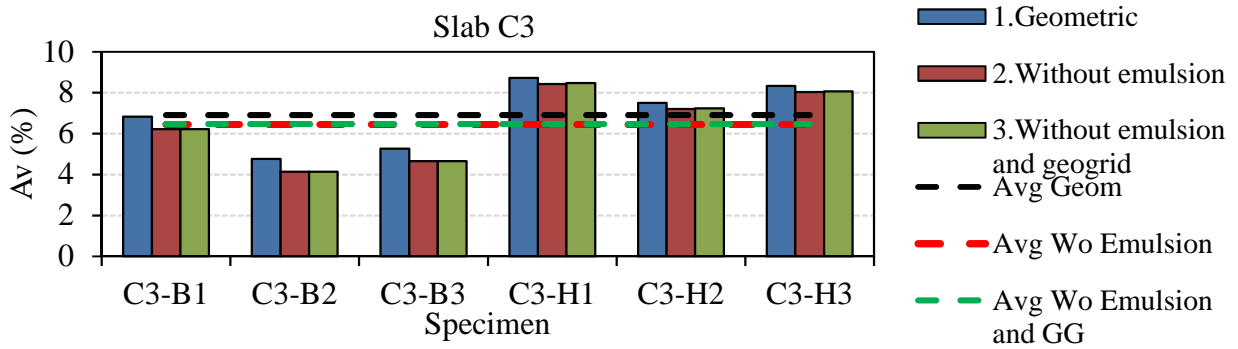


Figure 3-18. Air voids of the specimens cored from the slab C3

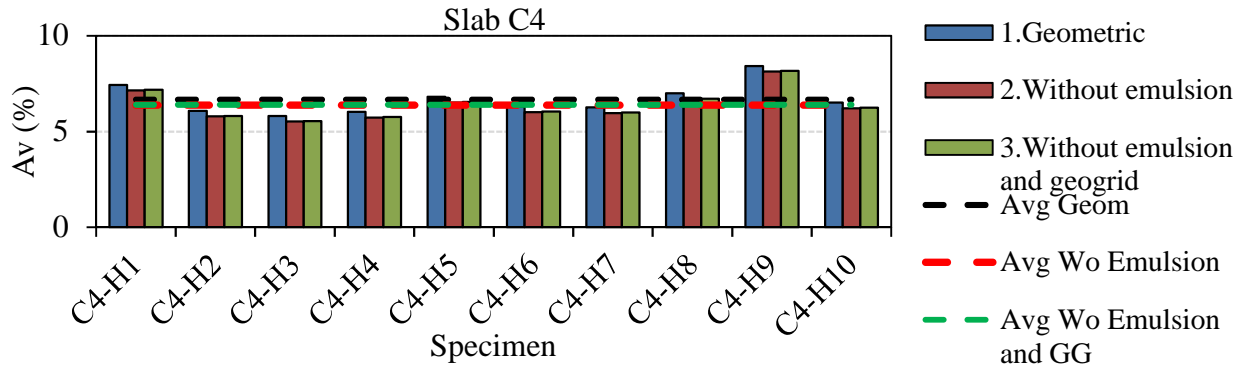


Figure 3-19. Air Voids of the specimens cored from the slab C4

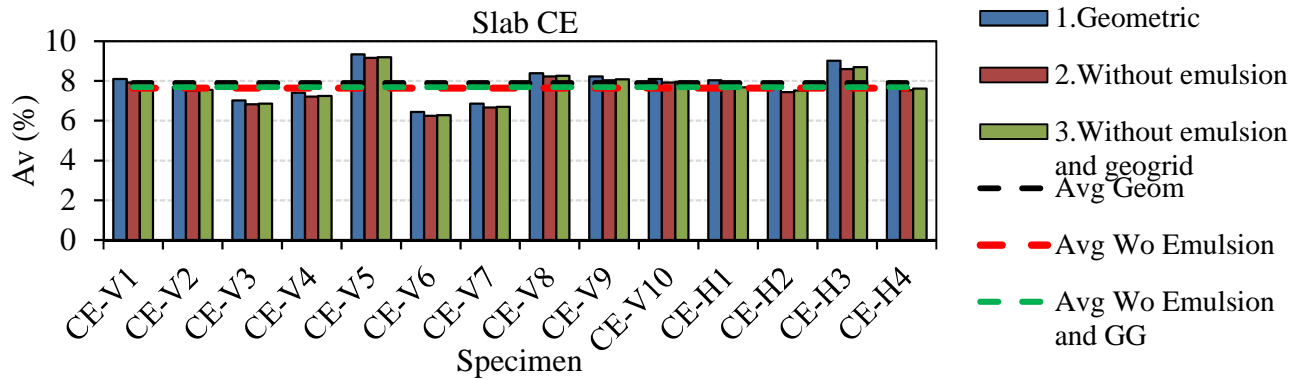


Figure 3-20. Air voids of the specimens cored from the slab CE (fabricated with  $2 \times 240 \text{g/m}^2$  of residual binder emulsion within the interface)

Table 3-5. Air voids contents, averages and standard deviations of specimens from configuration C slabs

Specimen (Slab C1)	Air Voids (%)			Specimen (Slab C2)	Air Voids (%)			Specimen (Slab C3)	Air Voids (%)			Specimen (Slab C4)	Air Voids (%)			Specimen (Slab CE)	Air Voids (%)		
	1.Geo- metric	2.Wo Emul- sion	3.Wo Emulsion and GG		1.Geo- metric	2.Wo Emul- sion	3.Wo Emulsion and GG		1.Geo- metric	2.Wo Emul- sion	3.Wo Emul- sion and GG		1.Geo- metric	2.Wo Emul- sion	3.Wo Emulsion and GG		1.Geo- metric	2.Wo Emul- sion	3.Wo Emulsion and GG
C1-V1	9.6	9.3	9.3	C2-VL1	8.6	8.3	8.4	C3-B1	6.8	6.2	6.2	C4-H1	7.4	7.2	7.2	CE-V1	8.1	7.9	8.0
C1-V3	8.6	8.3	8.3	C2-VL2	8.4	8.0	8.1	C3-B2	4.8	4.1	4.1	C4-H2	6.1	5.8	5.8	CE-V2	7.7	7.5	7.6
C1-V4	8.7	8.4	8.4	C2-V1	7.4	7.1	7.1	C3-B3	5.3	4.6	4.7	C4-H3	5.8	5.5	5.6	CE-V3	7.0	6.8	6.9
C1-V6	8.6	8.3	8.3	C2-V2	8.3	8.0	8.0	C3-H1	8.7	8.4	8.5	C4-H4	6.0	5.7	5.8	CE-V4	7.4	7.2	7.3
C1-VL1	7.9	7.6	7.6	C2-V3	7.5	7.2	7.2	C3-H2	7.5	7.2	7.2	C4-H5	6.8	6.5	6.5	CE-V5	9.3	9.2	9.2
C1-VL2	9.0	8.7	8.8	C2-V4	8.7	8.4	8.4	C3-H3	8.3	8.0	8.1	C4-H6	6.3	6.0	6.0	CE-V6	6.4	6.3	6.3
C1-VL3	8.6	8.2	8.3	C2-V5	7.7	7.4	7.4					C4-H7	6.3	6.0	6.0	CE-V7	6.9	6.7	6.7
C1-VL4	8.8	8.5	8.5	C2-V6	7.0	6.6	6.7					C4-H8	7.0	6.7	6.7	CE-V8	8.4	8.2	8.3
				C2-V7	7.3	6.9	7.0					C4-H9	8.4	8.1	8.2	CE-V9	8.2	8.0	8.1
				C2-H1	8.8	7.7	7.8					C4-H10	6.5	6.2	6.2	CE-V10	8.1	7.9	8.0
				C2-H2	7.9	7.2	7.2									CE-H1	8.0	7.6	7.7
				C2-H3	7.9	7.2	7.3									CE-H2	7.9	7.4	7.5
				C2-H4	9.2	8.5	8.6									CE-H3	9.0	8.6	8.7
																CE-H4	8.0	7.5	7.6
<b>Average</b>	8.7	8.4	8.4	<b>Average</b>	8.0	7.6	7.6	<b>Average</b>	6.9	6.4	6.5	<b>Average</b>	6.7	6.4	6.4	<b>Average</b>	7.9	7.6	7.7
<b>Standard Deviation</b>	0.5	0.5	0.5	<b>Standard Deviation</b>	0.7	0.6	0.6	<b>Standard Deviation</b>	1.6	1.8	1.8	<b>Standard Deviation</b>	0.8	0.8	0.8	<b>Standard Deviation</b>	0.8	0.8	0.8



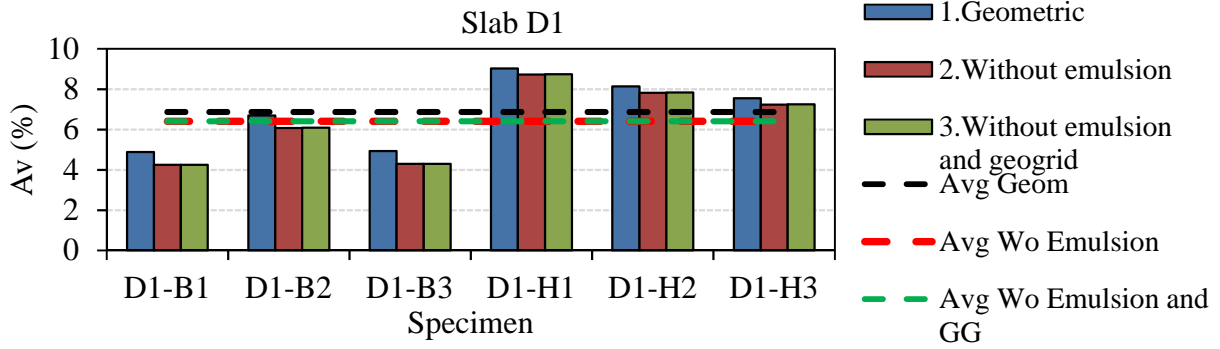


Figure 3-21. Air voids of the specimens cored from the slab D1

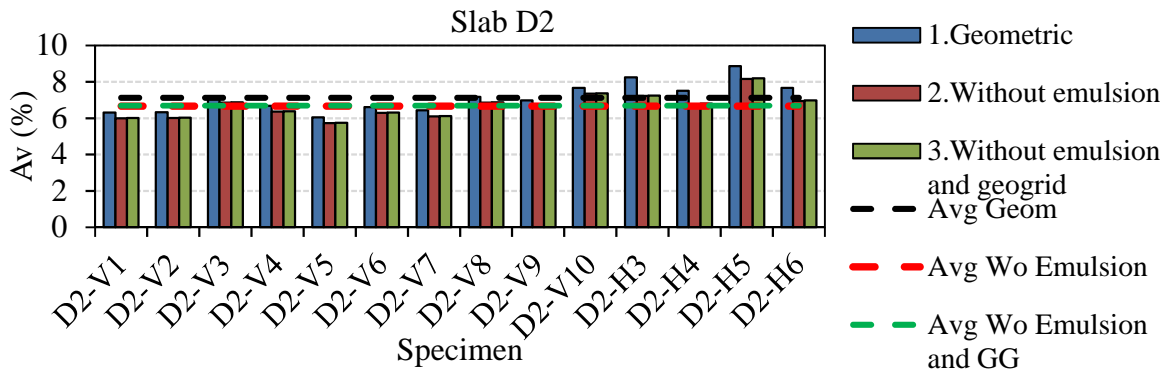


Figure 3-22. Air voids of the specimens cored from the slab D2

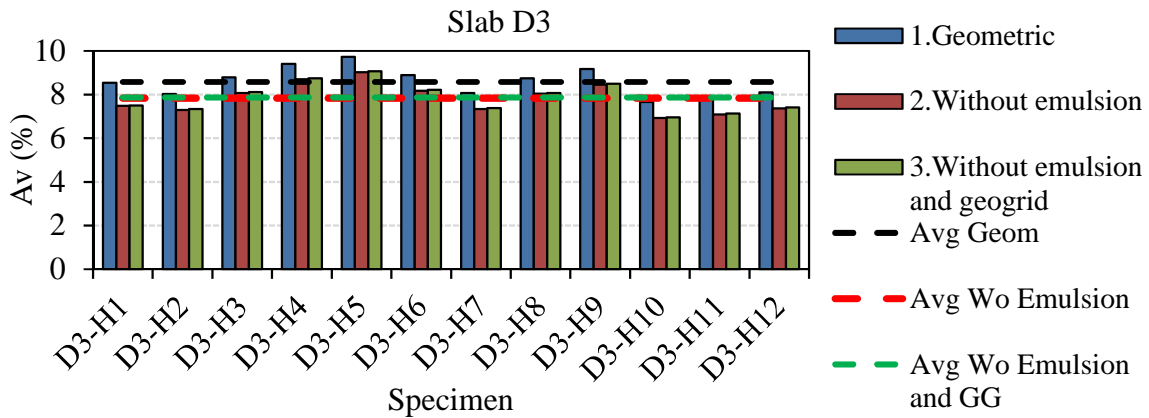


Figure 3-23. Air voids of the specimens cored from the slab D3

Table 3-6. Air voids contents, averages and standard deviations of specimens from configuration D slabs

Specimen (Slab D1)	Air Voids (%)			Specimen (Slab D2)	Air Voids (%)			Specimen (Slab D3)	Air Voids (%)		
	1. Geometric	2. Wo Emulsion	3. Wo Emulsion and GG		1. Geometric	2. Wo Emulsion	3. Wo Emulsion and GG		1. Geometric	2. Wo Emulsion	3. Wo Emulsion and GG
D1-B1	4.9	4.3	4.3	D2-V1	6.3	6.0	6.0	D3-H1	8.5	7.5	7.5
D1-B2	6.7	6.1	6.1	D2-V2	6.3	6.0	6.0	D3-H2	8.0	7.3	7.3
D1-B3	4.9	4.3	4.3	D2-V3	7.2	6.9	6.9	D3-H3	8.8	8.1	8.1
D1-H1	9.0	8.7	8.7	D2-V4	6.7	6.4	6.4	D3-H4	9.4	8.7	8.7
D1-H2	8.1	7.8	7.8	D2-V5	6.1	5.7	5.7	D3-H5	9.7	9.0	9.1
D1-H3	7.5	7.2	7.3	D2-V6	6.6	6.3	6.3	D3-H6	8.9	8.2	8.2
				D2-V7	6.4	6.1	6.1	D3-H7	8.1	7.3	7.4
				D2-V8	7.2	6.9	6.9	D3-H8	8.8	8.0	8.1
				D2-V9	7.0	6.7	6.7	D3-H9	9.2	8.5	8.5
				D2-V10	7.7	7.4	7.4	D3-H10	7.7	6.9	7.0
				D2-H3	8.3	7.2	7.2	D3-H11	7.8	7.1	7.1
				D2-H4	7.5	6.8	6.8	D3-H12	8.1	7.4	7.4
				D2-H5	8.9	8.2	8.2				
				D2-H6	7.7	6.9	7.0				
<b>Average</b>	6.9	6.4	6.4	<b>Average</b>	7.1	6.7	6.7	<b>Average</b>	8.6	7.8	7.9
<b>Standard Deviation</b>	1.7	1.9	1.9	<b>Standard Deviation</b>	0.8	0.6	0.7	<b>Standard Deviation</b>	0.7	0.7	0.7

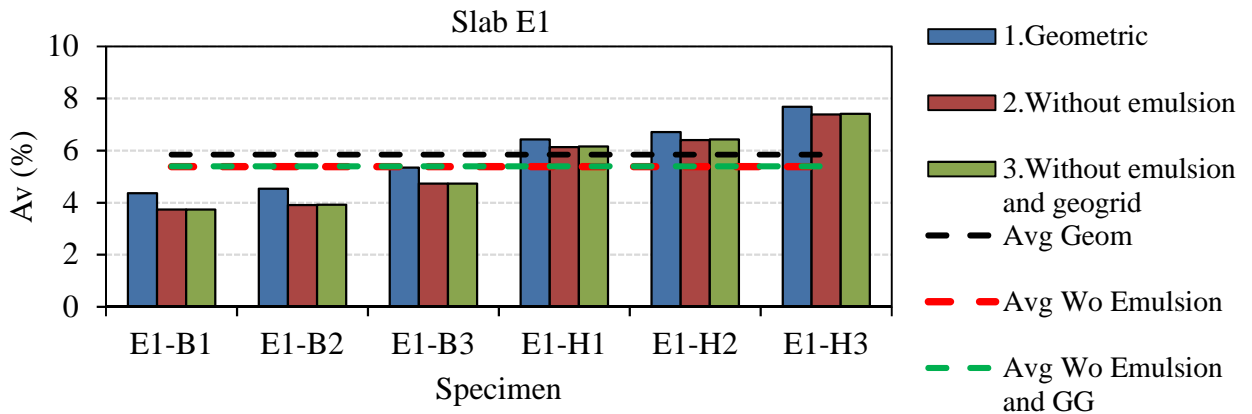


Figure 3-24. Air voids of the specimens cored from the slab E1

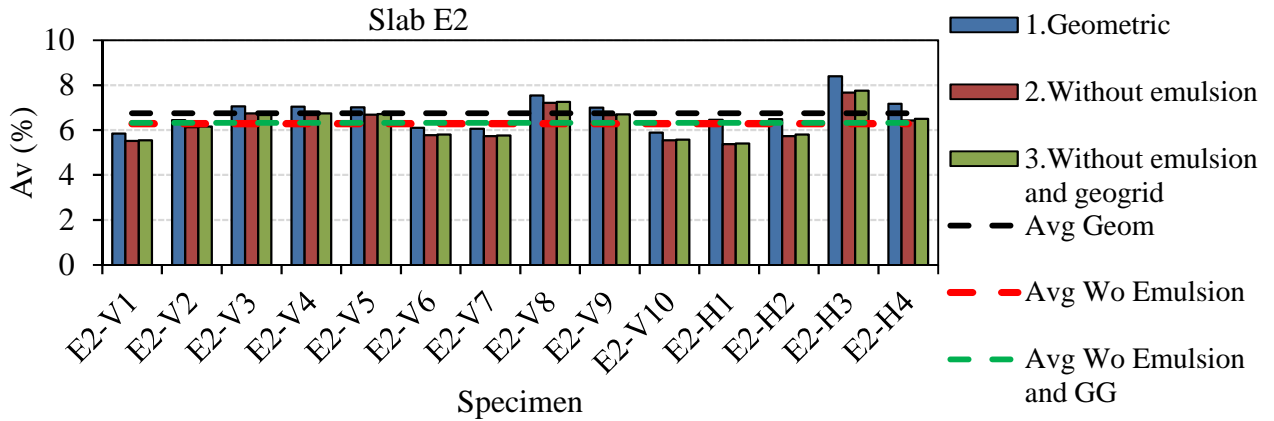


Figure 3-25. Air voids of the specimens cored from the slab E2

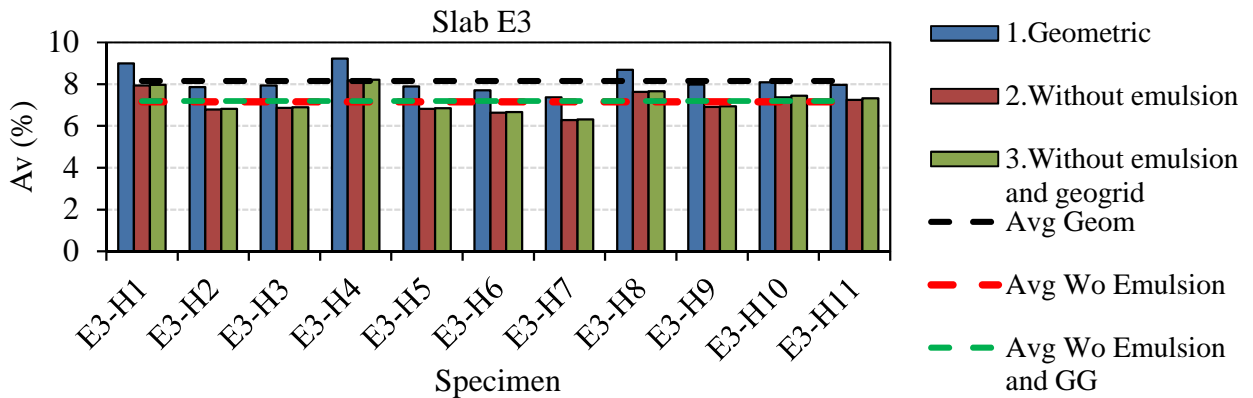


Figure 3-26. Air voids of the specimens cored from the slab E3

Table 3-7. Air voids contents, averages and standard deviations of specimens from configuration E slabs

Specimen (Slab E1)	Air Voids (%)			Specimen (Slab E2)	Air Voids (%)			Specimen (Slab E3)	Air Voids (%)		
	1. Geometric	2. Wo Emulsion	3. Wo Emulsion and GG		1. Geometric	2. Wo Emulsion	3. Wo Emulsion and GG		1. Geometric	2. Wo Emulsion	3. Wo Emulsion and GG
E1-B1	4.4	3.7	3.7	E2-V1	5.8	5.5	5.5	E3-H1	9.0	7.9	8.0
E1-B2	4.5	3.9	3.9	E2-V2	6.4	6.1	6.2	E3-H2	7.9	6.8	6.8
E1-B3	5.3	4.7	4.7	E2-V3	7.1	6.7	6.8	E3-H3	7.9	6.9	6.9
E1-H1	6.4	6.1	6.2	E2-V4	7.0	6.7	6.7	E3-H4	9.2	8.2	8.2
E1-H2	6.7	6.4	6.4	E2-V5	7.0	6.7	6.8	E3-H5	7.9	6.8	6.9
E1-H3	7.7	7.4	7.4	E2-V6	6.1	5.8	5.8	E3-H6	7.7	6.6	6.7
				E2-V7	6.1	5.7	5.8	E3-H7	7.4	6.3	6.3
				E2-V8	7.5	7.2	7.3	E3-H8	8.7	7.6	7.7
				E2-V9	7.0	6.7	6.7	E3-H9	8.0	6.9	6.9
				E2-V10	5.9	5.5	5.6	E3-H10	8.1	7.4	7.4

				E2-H1	6.5	5.4	5.4	E3-H11	8.0	7.2	7.3
				E2-H2	6.5	5.7	5.8				
				E2-H3	8.4	7.7	7.8				
				E2-H4	7.2	6.4	6.5				
<b>Average</b>	5.8	5.4	5.4	<b>Average</b>	6.7	6.3	6.3	<b>Average</b>	8.2	7.2	7.2
<b>Standard Deviation</b>	1.3	1.5	1.5	<b>Standard Deviation</b>	0.7	0.7	0.7	<b>Standard Deviation</b>	0.6	0.6	0.6

### 3.3. Experimental campaign overview

Four different tests were carried out during this doctoral thesis. The first one was the so-called complex modulus test. It measures the material behavior when subjected to small loading amplitudes, performed in cylindrical specimens. For this type of test, two specimens for each coring directions are necessary. All the details concerning the complex modulus tests will be discussed in the Chapter 4. The second tests it the tension test. It measures the material resistance to tension loading, also performed in cylindrical specimens. The tests are conducted at three temperatures (0, 19 and 40°C) and two strain rates of loading (slow (around 0.002%/min) and fast (2%/min)) resulting in 4 combination of testing parameters, as represented in Figure 3-27. For this type of test, two specimens for each parameter combination and for each coring direction are necessary, resulting in 16 specimens for each slab configuration (A, B, C, D, and E). Moreover, to evaluate the influence of specimen size effect, four more specimens of configuration C having 136mm of diameter (specimens type VL) are necessary. Tension test at 0 and 19°C and at 2%/min of strain loading rate were performed on those specimens. All the details concerning the tension tests will be discussed in Chapter 5. The third one is the fatigue test. It measures the material resistance to the cracking induced by cyclic repetitive loading. The tests were performed at 10Hz, 10°C and controlled strain in four amplitudes: 80, 90, 100 and 110µm/m. The test were performed only in specimens type H and repeated twice for each amplitude. Thus a total of 8 specimens for this test were necessary. Chapter 6 presents the fatigue campaign in full details. Finally, the four points bending test measures the specimen resistance to crack propagation. To perform this test, 3 prismatic bars in beam shape were necessary for each slab configuration. Chapter 7 discusses the crack propagation tests in full details. For each slab configuration, Table 3-8 summarizes the number of each type of specimens necessary for conducting the experimental campaign.

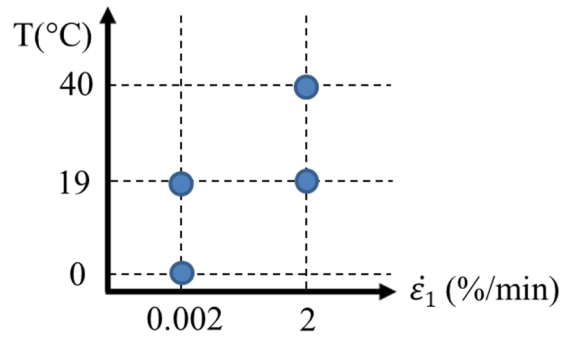


Figure 3-27. Testing parameters combination scheme for tension test (temperature and strain loading rate)

Table 3-8. Number of specimens necessity in function of each test on experimental campaign for each slab configuration

Test	Vertically cored	Horizontally cored	Beam
Complex Modulus	2	2	0
Tension	8 (or 12*)	8	0
Fatigue	0	8	0
Four Points Bending	0	0	3
Total	10	18	3

\*For configuration C, 4 more vertically cored specimens are necessary (VL type)

# Chapter 4: CYCLIC TENSION-COMPRESSION TEST CAMPAIGN

4.1. Introduction .....	120
4.2. Objectives .....	120
4.3. Experimental devices and procedures .....	121
4.3.1. Hydraulic press and instrumentation.....	121
4.3.2. Complex modulus test protocol.....	123
4.4. New method to characterize interface behavior .....	127
4.4.1. Bulk approach using continuum mechanics hypothesis.....	127
4.4.2. Infinitely thin interface.....	129
4.5. Tested Specimens .....	129
4.6. Bituminous mixtures and interfaces results and modeling.....	131
4.6.1. Example of result and modeling for specimens without interface: A1-H3...	131
4.6.2. Example of result and modeling for specimens containing interface .....	137
4.6.2.1. Specimen type V: C2-V1 (bituminous mixture) .....	137
4.6.2.1. Specimen type V: C2-V1 (interface).....	140
4.6.2.2. Specimen type H: C2-H3 .....	143
4.6.3. Complex modulus test results .....	145
4.6.3.1. Bituminous mixtures analysis and modelling .....	145
4.6.3.2. Interfaces analysis and modeling .....	152
4.6.4. Influence of fiberglass geogrid on H specimen's behavior.....	156
4.7. Chapter conclusions.....	159

## 4.1. Introduction

The purpose of this chapter is to present the experimental campaign conducted to characterize the specimens, from different configurations, at a small strain domain using cyclic tension-compression tests. Those tests are called complex modulus test and its procedure is fully described. Moreover, the hydraulic machine used to perform test, the transducers used to measure the physical variations, temperature, and force during the test are detailed.

Nowadays, many types of software are used for the multi-layer calculation in new pavement design, e.g. MEPD-G (United States of America) and Alizé (France). The geogrid reinforcement can be included as an equivalent layer if its properties (e.g. stiffness, Poisson's Ratio), as well as thickness, are known. Thus, it is necessary to characterize the interface mechanical properties in laboratory. In this chapter, a new methodology for the determination of the linear viscoelastic (LVE) behavior of interface reinforced with geogrids is presented. This methodology was published in Freire et al. (2018).

The analysis of a complex modulus test result for specimens containing or not interface is first presented as an example. The Time-Temperature Superposition Principle validation and the 2S2P1D model used to modelling the LVE behavior of specimens and interfaces are presented for these examples. Finally, the fiberglass geogrid influence on the behavior of specimens and interfaces at small strain domain is analyzed.

## 4.2. Objectives

For the investigation conducted in this chapter, some objectives can be drawn:

- To propose a new analysis methodology for the determination of the linear viscoelastic (LVE) behavior of interface reinforced with geogrids using laboratory thermomechanical tests.
- To validate the results obtained using the new analysis methodology with the results obtained from the specimen without interface and/or geogrid
- To verify if the interface presents a LVE behavior
- To evaluate the effect of the presence and type of geogrid in the interface behavior as well as the type of emulsion
- To evaluate the level of geogrid mobilization in specimens type H when subjected small strain amplitude loading

## 4.3. Experimental devices and procedures

### 4.3.1. Hydraulic press and instrumentation

Complex modulus tests were performed by a hydraulic press (INSTRON<sup>®</sup>) at LGCB/LTDS laboratory of the ENTPE at Vaulx-en-Velin, France. This press is equipped with a Dynacell<sup>®</sup> load cell having a maximum force capacity of  $\pm 25\text{kN}$  on the actuator, with a precision of 25N. The axial stress ( $\sigma$ ) during the tests was calculated from the measured force ( $F$ ) and the specimens' diameter ( $D$ ) according to Eq. 4-1.

$$\sigma = \frac{F}{\pi \cdot (D/2)^2} \quad \text{Eq. 4-1}$$

The actuator presents a displacement range of  $\pm 52\text{mm}$ . A thermal chamber type B.I.A. Climatic<sup>®</sup> MTH6-74 was used for temperature control during the tests. The tests performed within this thermal chamber can be set up from  $-40^\circ\text{C}$  to  $150^\circ\text{C}$  with  $\pm 0.3^\circ\text{C}$  stability. Figure 4-1 presents the mentioned hydraulic press and thermal chamber coupled to it.

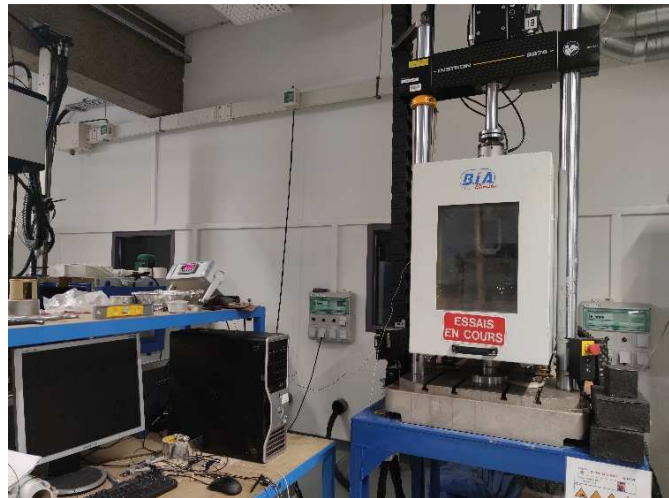


Figure 4-1. Hydraulic press INSTRON<sup>®</sup> with thermal chamber B.I.A. Climatic<sup>®</sup> used to carry out the experimental campaign

The axial deformation ( $\varepsilon$ ) measurements are done by four extensometers, a couple with 25mm length ( $l_1$ ) disposed  $180^\circ$  from one another, and another couple with 90mm length ( $l_2$ ) disposed  $180^\circ$  from one another (c.f. Figure 4-2), both fixed in the middle height of specimens.



The axial strain measured by each type of extensometer ( $i = 1, 2$  and  $j = 1, 2$ ) is obtained according to Eq. 4-2.

$$\varepsilon_{i,j} = \frac{\Delta l_{i,j}}{\Delta l_i} \quad \text{Eq. 4-2}$$

The strain amplitude commanded during the test is calculated by the average of the two smaller extensometers. The goal of using two different couples of extensometers is to obtain the interface behavior of the specimens type V, which will be subject to discussion in section 4.4. Moreover, this same instrumentation configuration was used for all other specimen's type, except for the specimens in the A configuration, for both V and H type. For those specimens, the test followed the classical instrumentation with three extensometers of 72.5mm length and two non-contact transducers, as performed in recent works from LTDS/ENTPE team (Mangiafico 2014, Cardona Ramirez 2016, Phan et al. 2017, and Pedraza 2018). The temperature is measured by a thermal gauge (PT100 temperature probe) fixed on the specimen surface. The probe precision is 0.1°C.

Two radial strains were obtained with the aid of four non-contact transducers. Two transducers disposed 180° from one another for each radial direction were used as shown in Figure 4-2. The non-contact transducers' head coil generates a magnetic field inducing currents in an aluminum target previously bonded on the surface of the specimen. The interaction between the magnetic field generated by the transducer and the magnetic field generated by the aluminum as a resistance to the current depends on the distance between them. From this principle, the electrical current can be transformed in distance between the transducers' head and the aluminum target, and this distance could be measured during the test. The non-contact transducers used during this work were from Microepsilon® and Lion Precision®. These devices presented a measure range of  $\pm 500\mu\text{m}$  with a resolution of  $0.05\mu\text{m}$ . Thus, radial strain in direction III ( $\varepsilon_{rIII}$ ) was obtained according to Eq. 4-3 and the radial strain in the direction I (obtained for type V specimens) or II (obtained for type H specimens) was obtained according to Eq. 4-4. More details about the radial strain will be discussed in the section 4.3.2.

$$\varepsilon_{rIII} = \frac{\Delta l_{r1} + \Delta l_{r2}}{D} \quad \text{Eq. 4-3}$$

$$\varepsilon_{r(I \text{ or } II)} = \frac{\Delta l_{r3} + \Delta l_{r4}}{D} \quad \text{Eq. 4-4}$$

To prepare the specimen for testing, two metallic caps were bonded with epoxy glue Huntsman® Araldite® 2000 Plus at the top and the bottom of the specimen. A bench, same as described in Cardona Ramirez (2016), was used to help the centralization of the specimen in the first cap gluing. A weight of 2kg was used to apply pressure during gluing. At least four hours wait was necessary because, after this period, the glue acquired enough hardening before gluing the second cap. The second cap was glued directly in the hydraulic press followed by the placement of the transducers as shown in Figure 4-2. This procedure was performed at least 12 hours prior to the test for the epoxy glue to harden, before subjecting the specimen to any load.

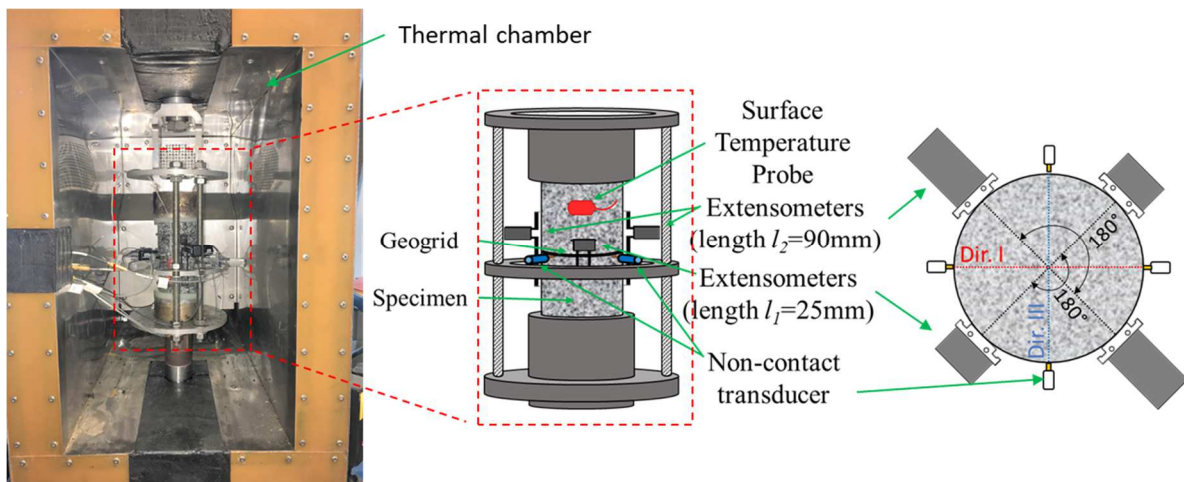


Figure 4-2. Picture and scheme presenting the specimen (reinforced type V) set up and instrumentation in the hydraulic press for testing

#### 4.3.2. Complex modulus test protocol

The complex modulus tests were carried out in sinusoidal tension-compression loading at strain-controlled with amplitude ( $\epsilon_0$ ) of  $50\mu\text{m/m}$ . According to previous works from LTDS/ENTPE, at this strain level, it is assumed that the material presents LVE behavior. The test was conducted at nine different temperatures from  $52$  to  $-25^\circ\text{C}$  and eight frequencies from  $0.003$  to  $10\text{Hz}$ . However, not all frequencies were performed for each temperature. At high temperatures ( $52$  and  $45^\circ\text{C}$ ), frequencies from  $0.003$  to  $1\text{Hz}$  were used. At low temperatures ( $25$  to  $-25^\circ\text{C}$ ), frequencies from  $0.03$  to  $10\text{Hz}$  were used. At  $35^\circ\text{C}$ , all eight frequencies. These combinations between temperatures and frequencies were chosen by experience from previous works from LTDS/ENTPE to avoid unnecessary points to build a master curve, optimizing the test. Figure 4-3 presents temperatures and frequencies during the complex modulus test, as well as the number of cycles performed for each frequency.

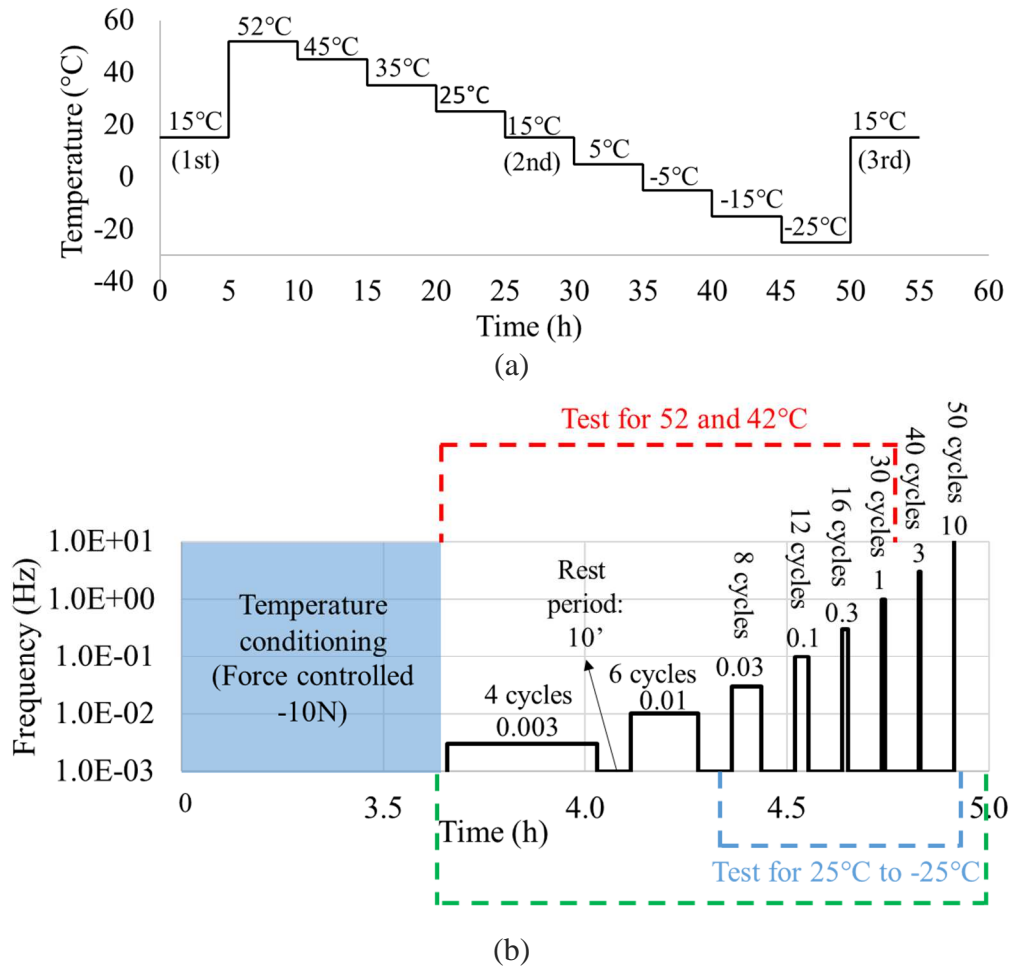


Figure 4-3. Complex modulus testing protocol: (a) temperatures, and (b) frequencies for the different temperatures and time for temperature conditioning

For each temperature, a period of temperature conditioning was respected to have a homogeneous temperature in the specimen. During this conditioning, the press was controlled by the force measured in the actuator, and a small compression of 10N was applied. This value was used to avoid a premature failure in the interface, for specimens type V, during temperature variation. It is caused by a lack of precision in the press force controlling during temperatures variation. At high temperatures, a low-tension value was enough to cause failure in the interface of those specimens. The temperature of 15°C was repeated at the beginning and at the end of the test, to verify the specimen condition concerning damage. In the three stages of 15°C, the complex modulus should not present considerable variation, which would happen if the specimens suffered damage during the test. The values presented in this thesis correspond to the average obtained for all the complete cycles of each loading at the correct strain amplitude. Moreover, the two first loading cycles were not taken into account in the average calculation

since they were affected by the period of loading stabilization (steady-state), and transitory effects also alter the results in these cycles (Gayte et al. 2016).

Due to the fact that there are two specimens coring directions (type V or H) the radial measurements direction should be correctly defined. Concerning the testing in type V specimens (c.f. Figure 4-4(a)), the loading is in the vertical direction (II) and the radial measurement are in the direction III ( $\varepsilon_{rIII}$ ) and I ( $\varepsilon_{rI}$ ). During the test, the pair of non-contact transducer 1 and 2 measures  $\varepsilon_{rIII}$ , following Eq. 4-3, and the pair of non-contact transducer 3 and 4 measures  $\varepsilon_{rI}$ , following Eq. 4-4. Concerning the testing in type H specimens (c.f. Figure 4-4(b)), the loading is in roller compaction direction (I) and the radial measurements are in the direction III ( $\varepsilon_{rIII}$ ) and II ( $\varepsilon_{rII}$ ). Similarly, the pair of non-contact transducer 1 and 2 measures  $\varepsilon_{rIII}$ , following Eq. 4-3, and the pair of non-contact transducer 3 and 4 measures  $\varepsilon_{rII}$ , following Eq. 4-4.

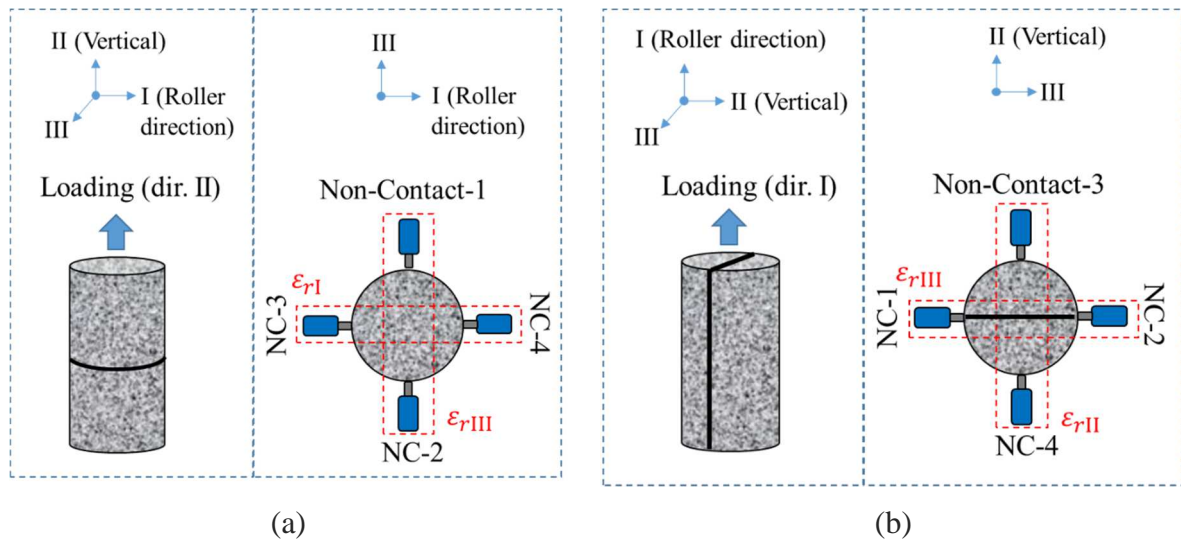


Figure 4-4. Scheme showing the radial measurement regarding the two specimen coring directions (a) type V and (b) type H

From Figure 4-4(a), the strain tensor can be defined according to Eq. 4-5, respecting the directions in specimen type V. The loading in this type of test is in direction II, thus, the stress tensor is written according to Eq. 4-6, where the components with respect to directions I and III are equal to zero. Thus, only three elements from strain tensor are non-null, as shown in Eq. 4-7, which are  $\varepsilon_{rI}$ ,  $\varepsilon_{rIII}$ ,  $\varepsilon_{ax}$ , directly obtained from the transducers measurements previously discussed.

$$\underline{\varepsilon}^* = \begin{pmatrix} \frac{1}{E_I^*} & -\frac{\nu_{I II}^*}{E_{II}^*} & -\frac{\nu_{I III}^*}{E_{III}^*} \\ -\frac{\nu_{II I}^*}{E_I^*} & \frac{1}{E_{II}^*} & -\frac{\nu_{II III}^*}{E_{III}^*} \\ -\frac{\nu_{III I}^*}{E_I^*} & -\frac{\nu_{III II}^*}{E_{II}^*} & \frac{1}{E_{III}^*} \end{pmatrix} \cdot \sigma^* \quad \text{Eq. 4-5}$$

$$\underline{\sigma}^* = \begin{vmatrix} 0 \\ \sigma^* \\ 0 \end{vmatrix} \quad \text{Eq. 4-6}$$

$$\underline{\varepsilon}^* = \begin{cases} -\frac{\nu_{I II}^*}{E_{II}^*} \cdot \sigma^* = \varepsilon_{rI} \\ \frac{1}{E_{II}^*} \cdot \sigma^* = \varepsilon_{ax} \\ -\frac{\nu_{III II}^*}{E_{II}^*} \cdot \sigma^* = \varepsilon_{rIII} \end{cases} \quad \text{Eq. 4-7}$$

Therefore, the Poisson's ratios in the two directions were calculated using test measurements. Eq. 4-8 presents the calculation of  $\nu_{I II}^*$ , or simply called  $\nu_I^*$ , which is the Poisson's ratio in the direction I. In addition, Eq. 4-9 presents the calculation of  $\nu_{III II}^*$ , or simply called  $\nu_{III}^*$  which is the Poisson's ratio in the direction III.

$$\nu_I^* = -\frac{\varepsilon_{rI}}{\varepsilon_{ax}} \quad \text{Eq. 4-8}$$

$$\nu_{III}^* = -\frac{\varepsilon_{rIII}}{\varepsilon_{ax}} \quad \text{Eq. 4-9}$$

Similarly, from Figure 4-4(b), the strain tensor for specimens type H is written according to Eq. 4-10. In this case, the loading is in direction I, and the stress tensor is written according to Eq. 4-11. Thus, only three elements from strain tensor are non-null, as shown in Eq. 4-12, which are  $\varepsilon_{rII}$ ,  $\varepsilon_{rIII}$ ,  $\varepsilon_{ax}$ . Finally, Eq. 4-13 presents the calculation of  $\nu_{II I}^*$ , or simply called  $\nu_{II}^*$ , which is the Poisson's ratio in the direction II. In addition, Eq. 4-14 presents the calculation of  $\nu_{III I}^*$ , or simply called  $\nu_{III}^*$  which is the Poisson's ratio in the direction III.

$$\underline{\varepsilon}^* = \begin{pmatrix} \frac{1}{E_I^*} & -\frac{\nu_{II}^*}{E_{II}^*} & -\frac{\nu_{III}^*}{E_{III}^*} \\ -\frac{\nu_{III}^*}{E_I^*} & \frac{1}{E_{II}^*} & -\frac{\nu_{II}^*}{E_{III}^*} \\ -\frac{\nu_{III}^*}{E_I^*} & -\frac{\nu_{III}^*}{E_{II}^*} & \frac{1}{E_{III}^*} \end{pmatrix} \cdot \sigma^* \quad \text{Eq. 4-10}$$

$$\underline{\sigma}^* = \begin{pmatrix} \sigma^* \\ 0 \\ 0 \end{pmatrix} \quad \text{Eq. 4-11}$$

$$\underline{\varepsilon}^* = \begin{cases} \frac{1}{E_I^*} \cdot \sigma^* = \varepsilon_{ax} \\ -\frac{\nu_{III}^*}{E_I^*} \cdot \sigma^* = \varepsilon_{rII} \\ -\frac{\nu_{III}^*}{E_I^*} \cdot \sigma^* = \varepsilon_{rIII} \end{cases} \quad \text{Eq. 4-12}$$

$$\nu_{III}^* = -\frac{\varepsilon_{rII}}{\varepsilon_{ax}} \quad \text{Eq. 4-13}$$

$$\nu_{III}^* = -\frac{\varepsilon_{rIII}}{\varepsilon_{ax}} \quad \text{Eq. 4-14}$$

Concerning specimens type H, the axial strain ( $\varepsilon_{ax}$ ) is simply obtained from the average of four extensometers. However, concerning the specimens type V, the measurements obtained from the extensometers are resulted from the strain measured in the bituminous mixtures combined with the strain measured in the interface. The next section will discuss this issue in detail.

## 4.4. New method to characterize interface behavior

Two approaches were used to characterize the bituminous mixture and the interface of a specimen type V during complex modulus test. The first one is a bulk approach that uses the continuum mechanics hypothesis. The second one assumes that the interface is infinitely thin.

### 4.4.1. Bulk approach using continuum mechanics hypothesis

The first interface analysis proposed in this work was done by considering the geogrid and the emulsion used to glue the geogrid in the specimen as an equivalent layer with a thickness

( $t$ ) as shown in Figure 4-5. In this case, each pair of extensometer allows obtaining the sum of interface displacement with the bituminous mixture displacement caught by the extensometer range. Thus, Eq. 4-15 could be written.

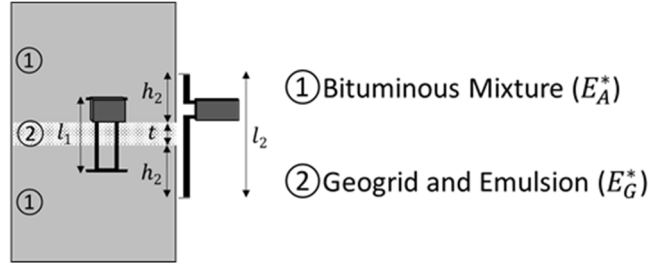


Figure 4-5. Continuous Mechanics interface calculation hypothesis scheme

$$\Delta l_i^* = \Delta t^* + 2\Delta h_i^* \quad i = 1, 2 \quad \text{Eq. 4-15}$$

Where  $\Delta l_i^*$  is the displacement (“\*” indicates complex notation) measured by the extensometer  $l_i$  during the test,  $\Delta t^*$  is the interface displacement and  $\Delta h_i^*$  is the mixture displacement caught by the extensometer  $l_i$  range. Eq. 4-15 can be rewritten as function of the complex modulus from each component:  $E_i^*$  = modulus measured by extensometer  $l_i$ ;  $E_G^*$  = interface complex modulus;  $E_A^*$  = mixture complex modulus (Eq. 4-16).

$$\frac{\sigma_i^* \cdot l_i}{E_i^*} = \frac{\sigma_G^* \cdot t}{E_G^*} + \frac{\sigma_A^* \cdot 2h_i}{E_A^*} \quad \text{Eq. 4-16}$$

Also, the stress is the same in all parts ( $\sigma_i^* = \sigma_G^* = \sigma_A^*$ ) and, thus, can be removed from the Eq. 4-16. From Fig. 3 it is possible to notice that  $2h_i = l_i - t$ , resulting in Eq. 4-17. Using both equation for  $i = 1$  and  $i = 2$ , it is possible to obtain the bituminous mixture complex modulus ( $E_A^*$ ) as function of the complex modulus measured by the extensometers  $l_1$  and  $l_2$  (Eq. 4-18). It should be noticed that  $E_1^*$  and  $E_2^*$  are obtained respectively from an averaged measurement of two couples of extensometers.

$$\frac{t}{E_G^*} = \frac{l_2}{E_2^*} - \frac{l_2 - t}{E_A^*} \quad \text{Eq. 4-17}$$

$$E_A^* = \frac{(l_2 - l_1) \cdot E_1^* \cdot E_2^*}{l_2 \cdot E_1^* - l_1 \cdot E_2^*} \quad \text{Eq. 4-18}$$

Once the bituminous mixture complex modulus ( $E_A^*$ ) is obtained, it can be used to calculate the interface complex modulus ( $E_G^*$ ). From Eq. (3),  $E_G^*$  can be isolated in the equation, resulting in Eq. 4-19, which returns the  $E_G^*$  for any chosen thicknesses values “ $t$ ”.

$$E_G^*(t) = \frac{t \cdot E_i^* \cdot E_A^*}{l_i \cdot E_A^* - (l_i - t) \cdot E_i^*} \quad \text{Eq. 4-19}$$

#### 4.4.2. Infinitely thin interface

The second interface analysis approach is performed by assuming interface as a thin film. In this case, behavior could be represented by an interface stiffness ( $K_G^*$ ) linking  $\sigma^*$  and vertical displacement observed between the interfaces of the two bituminous mixtures layers. The interface stiffness ( $K_G^*$ ) can be obtained by assuming the thickness equal to zero in Eq. 4-17, resulting in Eq. 4-20.

$$K_G^* = \frac{E_G^*}{t} = \frac{E_A^*}{l_i \cdot \left( \frac{E_A^*}{E_i^*} - 1 \right)} \quad \text{Eq. 4-20}$$

The great advantage of using this approach is to have an interface stiffness parameter that is non-dependent to its thickness.

## 4.5. Tested Specimens

To conduct the investigation in this chapter, the specimens were divided into two groups regarding the geogrid position resulted from slab coring. The first group is the H specimens, cored in the same compaction direction. In this case, the interface in the specimens containing it, are in specimens longitudinal direction, which is the same loading direction (c.f. section 3.2.3). The second group is composed of V specimens, cored perpendicularly in relation to the compaction direction. The interface in those specimens are perpendicular in relation to the loading direction (c.f. section 3.2.3). Table 4-1 presents all the tested specimens with interface composition and tack coat rate, air voids calculated for the bituminous mixture, and the instrumentation used for axial and radial measurements during the test.



Table 4-1. Tested specimens' composition, air voids and instrumentation information

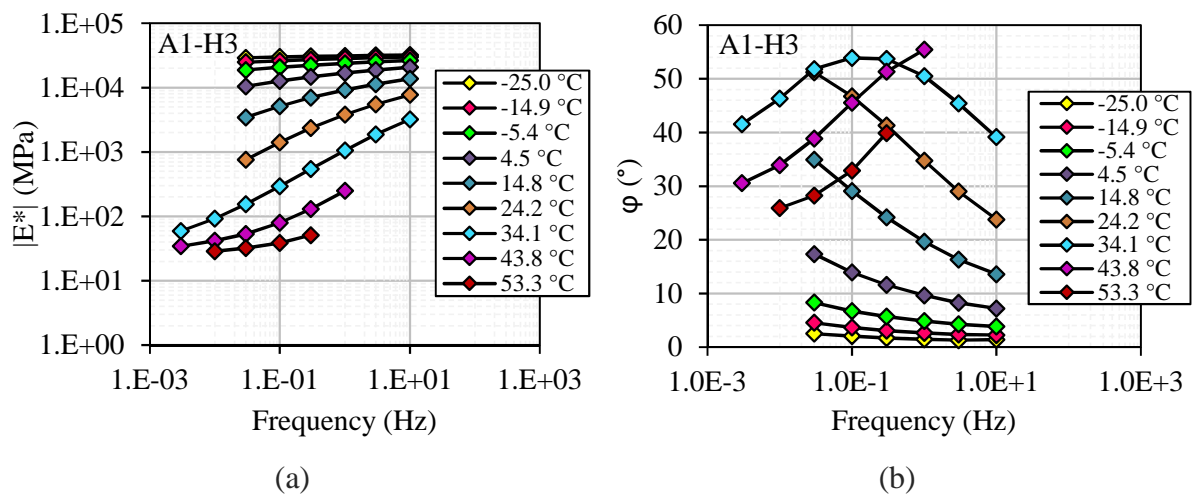
Specimen	Interface		Air voids in mix (%)	Axial measurements	Radial measurements			
	Composition	Tack coat rate						
A1-H3	Not applicable	Not applicable	6.2	3 (72.5mm) extensometers	1 direction			
A1-H4			6.0					
A1-V2			8.5					
A1-V5			8.6					
B1-H1	Emulsion Bitumen 160/220	292g/m <sup>2</sup>	7.0	2 (25mm) and 2 (90mm) extensometers	2 directions			
B1-H2			6.1					
B2-V1			6.8					
B2-V2			6.3					
CE-H4	Emulsion bitumen 160/220 and GG 100kN	2×240g/m <sup>2</sup>	7.6	3 (72.5mm) extensometers	1 direction			
CE-V9			8.1					
CE-V10			8.0					
C2-H1			2×400g/m <sup>2</sup>			7.8	2 (25mm) and 2 (90mm) extensometers	2 directions
C2-H3		7.3						
C1-V6		8.3						
C2-V1		7.1						
D1-H1		8.7						
D1-H3		7.3						
D2-V1		Emulsion bitumen 160/220 and GG 50kN	2×400g/m <sup>2</sup>	6.0	2 (25mm) and 2 (90mm) extensometers	1 direction		
D2-V3	6.9							
E1-H1	Emulsion bitumen 160/220 with SBS and GG 100kN			2×400g/m <sup>2</sup>		6.2	2 (25mm) and 2 (90mm) extensometers	2 directions
E1-H2						6.4		
E2-V4		6.8						
E2-V5		6.7						

GG 100kN: Geogrid Notex Glass<sup>®</sup> C 100/100-25; and GG 50kN: Geogrid Notex Glass<sup>®</sup> C 50/50-25

## 4.6. Bituminous mixtures and interfaces results and modeling

### 4.6.1. Example of result and modeling for specimens without interface: A1-H3

The measured temperatures during the tests are slightly different from the targeted ones. For the ensemble of tests, the maximum temperature variation measured on the specimens was  $\pm 1.5^\circ\text{C}$ . The isotherm curves present the complex modulus data for each temperature obtained during each frequency sweep, for specimen A1-H3. Figure 4-6 shows the norm of complex modulus ( $|E^*|$ ), phase angle ( $\phi$ ), Poisson's ratio ( $\nu^*$ ), and phase angle of Poisson's ratio ( $\phi_\nu$ ), respectively. These results are the most intuitive curves obtained from the complex modulus test.



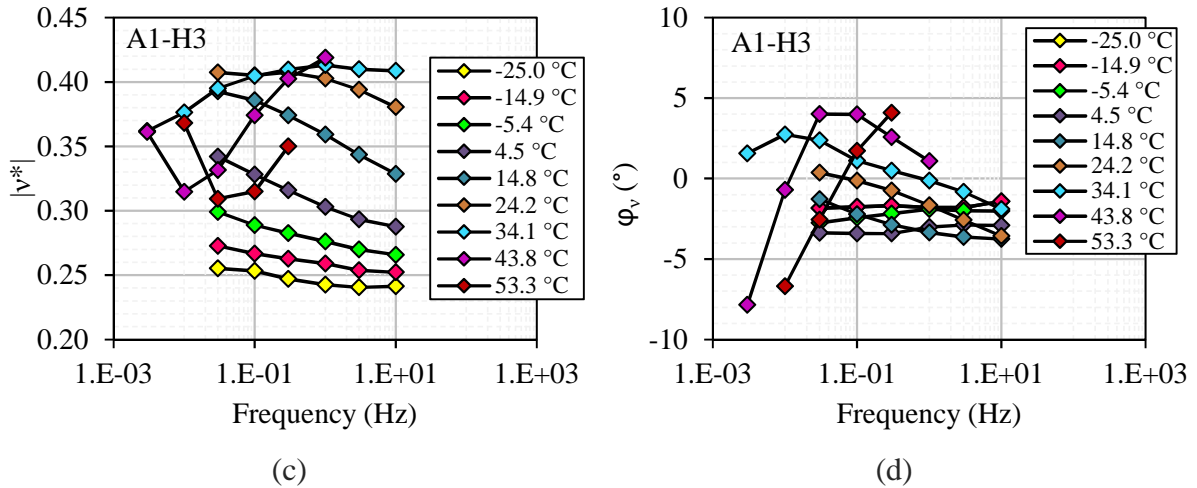


Figure 4-6. Results obtained for each tested temperature for A1-H3: (a) Norm of complex modulus, (b) Phase angle, (c) Norm of Poisson's ratio and (d) Phase angle of Poisson's ratio

From those figures, it is noticed that the norm of complex modulus and Poisson's ratio increase with the loading frequency increase and temperature decrease. Thus, at low temperatures and high frequency, the material presents an asymptotic value. In addition, in the opposite way, at high temperatures and low frequency, the material also presents an asymptotic value. To define these values, two plots are helpful: Cole-Cole (c.f. Figure 4-7(a)) and Black space (c.f. Figure 4-7(b)). Cole-Cole plot relates the real part of  $E^*$  ( $E_1 = E^* \cdot \cos \phi$ ) with the imaginary part of  $E^*$  ( $E_2 = E^* \cdot \sin \phi$ ). In these curves, it is possible to observe the material behavior at low temperatures, as shown in Figure 4-7(a) for specimen A1-H3. In the other hand, the black space curve relates the  $\phi$  with  $|E^*|$ , and from these curves, it is possible to observe the material behavior at high temperatures, as shown in Figure 4-7(b) for specimen A1-H3.

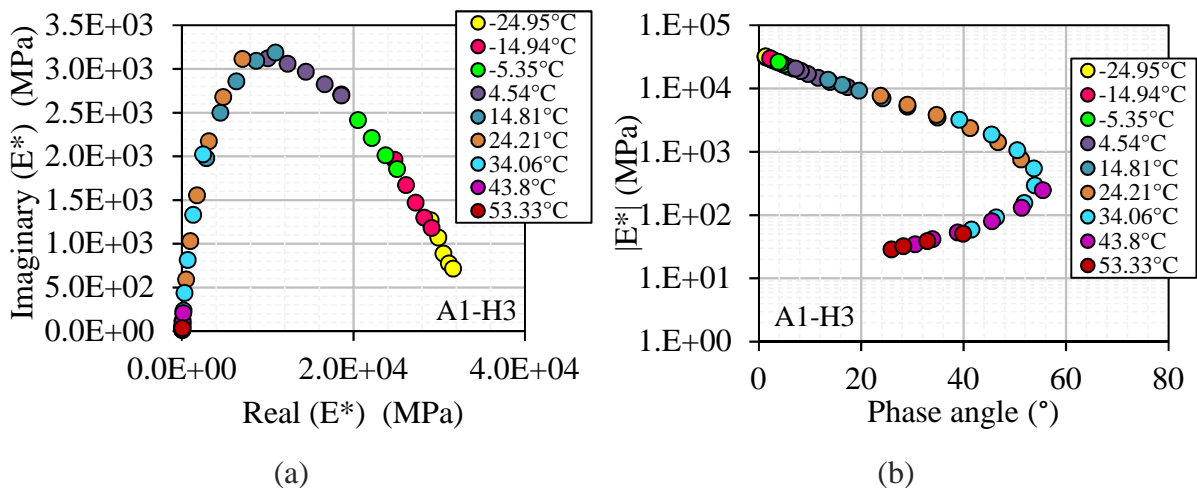


Figure 4-7. (a) Cole-Cole plot and (b) Black space obtained for specimen A1-H3

These curves can be seen like the material footprint of its LVE behavior (Cardona Ramirez 2016) and can be used to calibrate LVE behavior models. Another particularity of those plots concerns the validation of the Time-Temperature Superposition Principle (TTSP) for the mixtures. In order to validate the TTSP, those plots should present unique curves, which is the case obtained for A1-H3. The same curves can be plotted concerning Poisson's ratio. Figure 4-8(a) presents the Cole-Cole plot and Figure 4-8(b) presents the Black space. The results presented unique curves for the test conducted until 34.06°C, the higher temperatures presented scattered points, mainly at extreme conditions (high temperature and low frequency). This was related to the experimental difficulty to obtain these parameters at extreme conditions, and not with the material behavior.

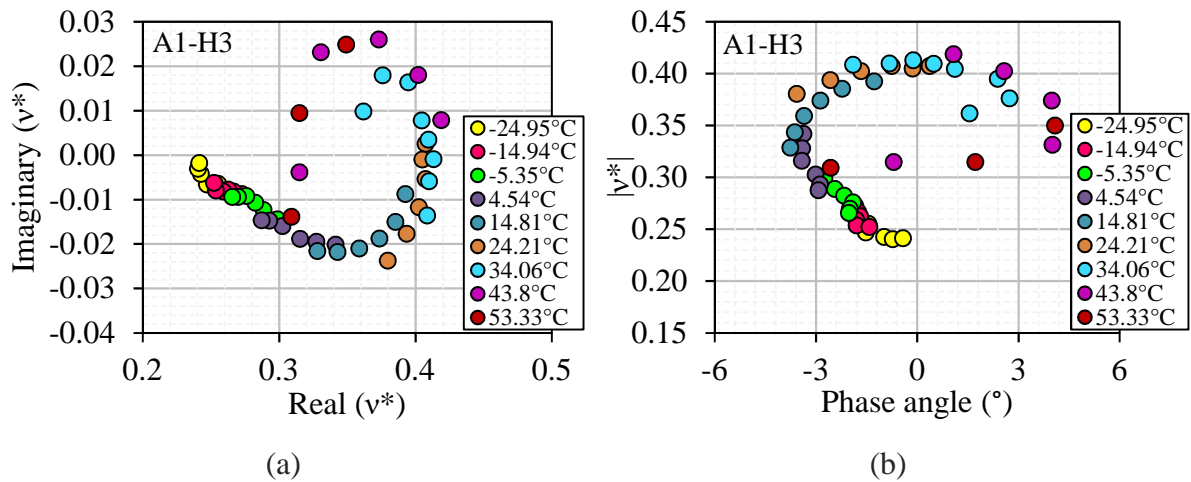


Figure 4-8. (a) Cole-Cole plot and (b) Black space of Poisson's ratio for A1-H3

The TTSP indicates that the effect of LVE behavior variation observed in temperature variation is equivalent to the LVE behavior variation observed in frequency variation. Thus, the experimental data points obtained at different temperatures can be shifted around a reference temperature creating a master curve for  $|E^*|$  (c.f. Figure 4-9(a)),  $\phi$  (c.f. Figure 4-9(b)),  $|v^*|$  (c.f. Figure 4-9(c)), and  $\phi_v$  (c.f. Figure 4-9(d)). These master curves present the LVE behavior of a material in a wider range of frequencies, for a specific reference temperature. Concerning specimen A1-H3, the reference temperature chose was 15°C, which was one of the temperatures from the testing procedure as discussed in section 4.3.2. Then, a shift factor  $a_T$  is chosen for each tested temperature, and is equal to 1 for 15°C, reference temperature.

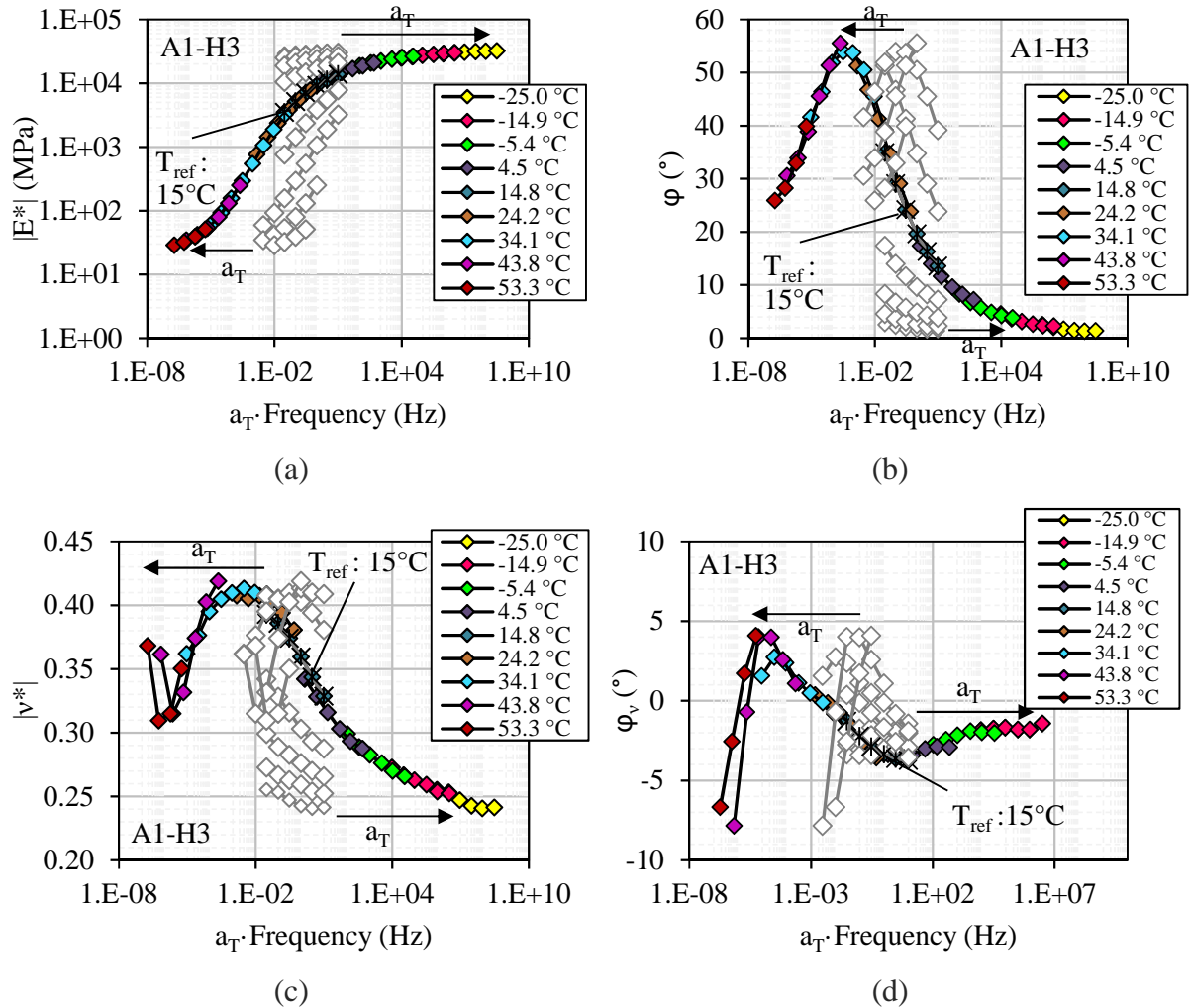


Figure 4-9. Construction of master curves of (a) norm of complex modulus, (b) phase angle of complex modulus, (c) Poisson's ratio, and (d) phase angle of Poisson's ratio

The  $a_T$  values were calibrated in the master curve of  $|E^*|$ , and the same values lead to the creation of all the master curves presented in Figure 4-9. This result was similar to previous studies from the LTDS/ENTPE team that validates the use of the same  $a_T$  values to characterize the 3-D LVE behavior of bituminous mixtures (Di Benedetto et al. 2007, Nguyen et al. 2013, Cardona Ramirez 2016). Afterward, the  $a_T$  values were plotted in function of temperature, and the WLF equation (Eq. 2-8) was used to fit the data, as presented in Figure 4-10(a) as well as the coefficients  $C_1$  and  $C_2$ . Quite similar results were obtained for all tested specimens, which allowed the maintenance of the same WLF coefficients, as can be observed in Figure 4-10(b). This result was similar to previous studies (Olard & Di Benedetto 2003, Olard, 2005, Di Benedetto et al. 2007, Cardona Ramirez 2016) arguing that  $a_T$  factor is inherent of the bitumen independent of the mineral aggregates that composes the bituminous mixture.

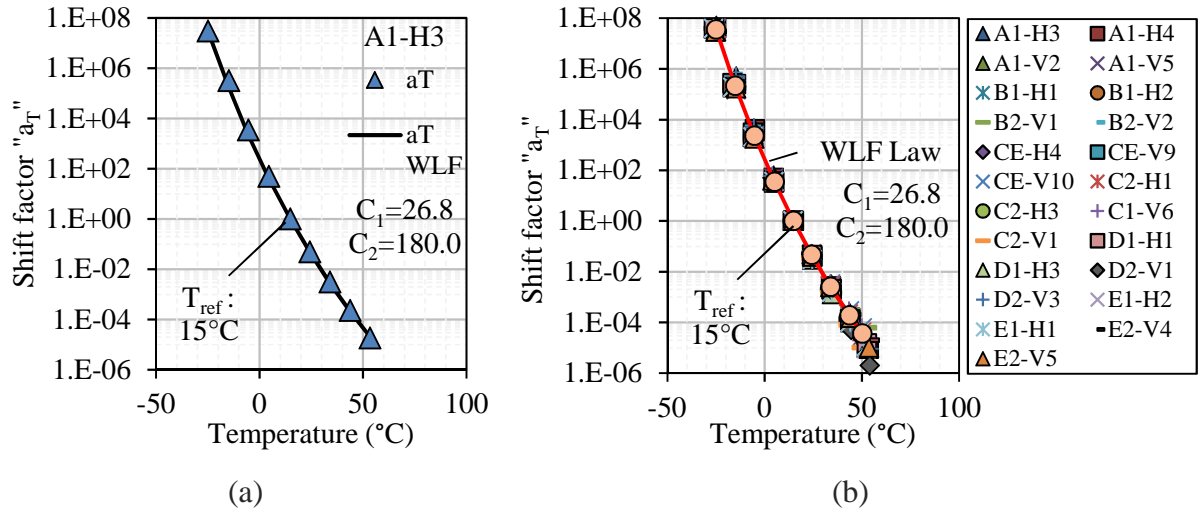
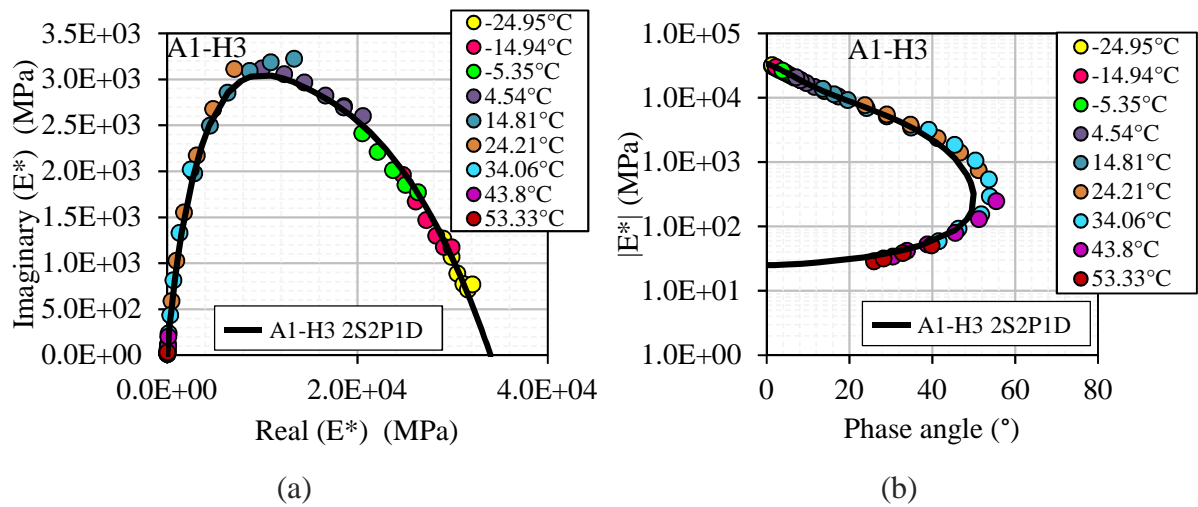


Figure 4-10. Shift factor ( $a_T$ ) values in function of testing temperature and WLF fitting for complex modulus test of (a) A1-H3 and (b) All specimens

In order to model the LVE behavior, the 2S2P1D was used by calibrating the model coefficients to fit the Cole-Cole and Black plots for both,  $E^*$  and  $\nu^*$ . Figure 4-11 presents the 2S2P1D modeling the experimental data for specimen A1-H3.



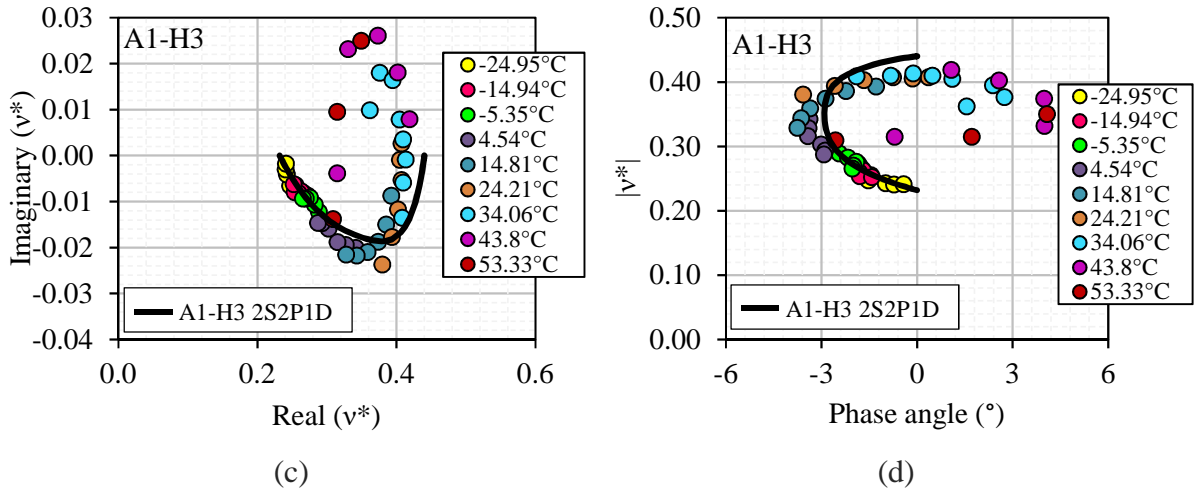
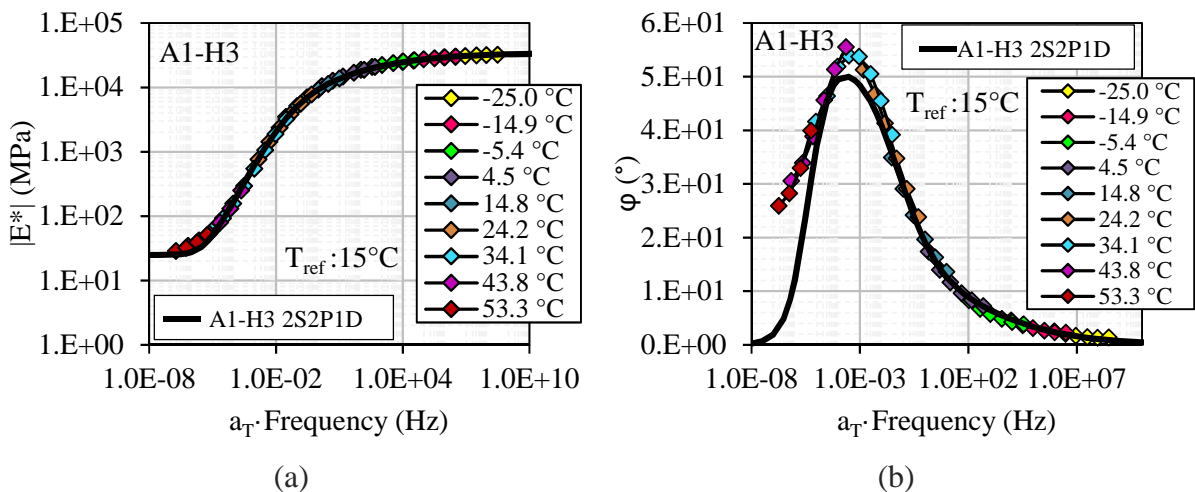


Figure 4-11. 2S2P1D model calibrated for A1-H3 testing results: (a) Cole-Cole of  $E^*$ , (b) Black space of  $E^*$ , (c) Cole-Cole of  $v^*$ , and (d) Black space of  $v^*$

From the Cole-Cole plot, the asymptotic glassy modulus ( $E_0$ ) could be obtained and from the Black plots, the asymptotic static modulus ( $E_{00}$ ) could be obtained. All the shape parameters ( $k$ ,  $h$ ,  $\delta$ , and  $\beta$ ) of the 2S2P1D model were, then, calibrated. However, the temperature-dependent parameter  $\tau$  and the asymptotic values for Poisson’s ratio ( $\nu_0$  and  $\nu_{00}$ ) were calibrated using the master curves. Figure 4-12 presents the master curves modeled using 2S2P1D. The calibrated coefficients are presented in Table 4-2.



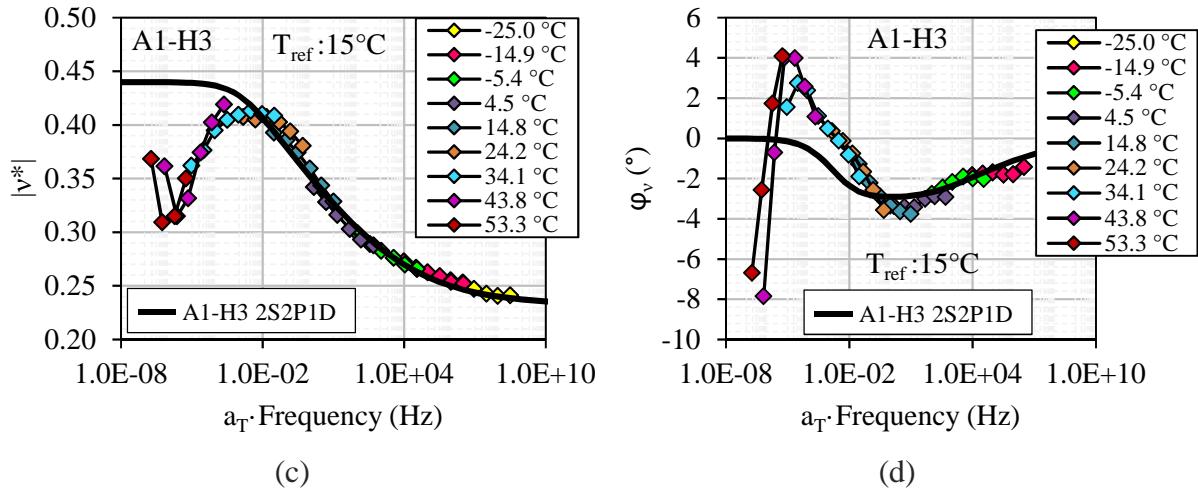


Figure 4-12. 2S2P1D model calibrated for A1-H3 testing master curves: (a) norm of complex modulus, (b) phase angle of complex modulus, (c) Poisson’s ratio, and (d) phase angle of Poisson’s ratio

Table 4-2. Coefficients of 2S2P1D model calibrated in A1-H3 test results ( $T_{ref} = 15^{\circ}\text{C}$ )

$E_{00}$ (MPa)	$E_0$ (MPa)	$k$	$h$	$\delta$	$\tau_E$ (s)	$\beta$	$\nu_{00}$	$\nu_0$
25	3.40E+04	0.185	0.60	2.35	0.27	200	0.44	0.23

#### 4.6.2. Example of result and modeling for specimens containing interface

Concerning the specimens containing interfaces, two examples were presented in this section. The first one concerns a specimen type V (C2-V1), which is also divided in the analysis of the result obtained for the bituminous mixture and the result obtained for the interface, both obtained from the calculation discussed in section 4.4. The second one concerns a specimen type H (C2-H3).

##### 4.6.2.1. Specimen type V: C2-V1 (bituminous mixture)

Figure 4-13(a) presents the results obtained for the specimen with geogrid reinforcement in a Cole-Cole graphic, and Figure 4-13(b) presents the same results in Black space. The complex modulus obtained with the two different couples of extensometers were remarkably distinct. The difference between them is caused by the interface behavior. For this reason, they were called “apparent E”, since their measures do not represent a physical material property. From these results, the complex modulus of bituminous mixture was calculated following Eq.



4-18 and result is also presented in Figure 4-13 with the 2S2P1D model curve calibrated over the calculated points. Obtained results showed a unique curve in this plot, which is a classical result for bituminous mixtures, which respect the TTSP. Another classical evolution with temperature and frequency is also obtained for the calculated complex modulus  $E_A^*$ . At higher frequencies and lower temperatures, higher values were found in relation to those obtained at lower frequencies and higher temperatures. Figure 4-14 presents master curves obtained with the two different couples of extensometers plotted with the calculated  $E_A^*$ , and the 2S2P1D model curve calibrated over the calculated points.

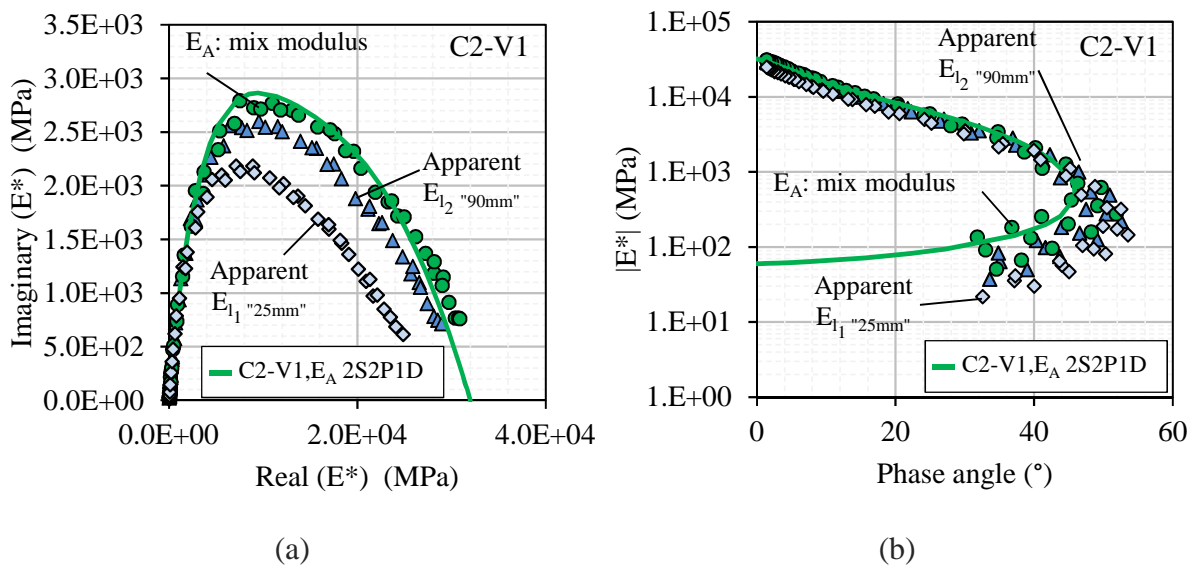


Figure 4-13. Experimental results ( $E_{I1}$  (25mm) and  $E_{I2}$  (90mm)) plotted with calculated bituminous mixture modulus ( $E_A^*$ ) for the specimen C2-V1 in (a) Cole-Cole plan and (b) Black space

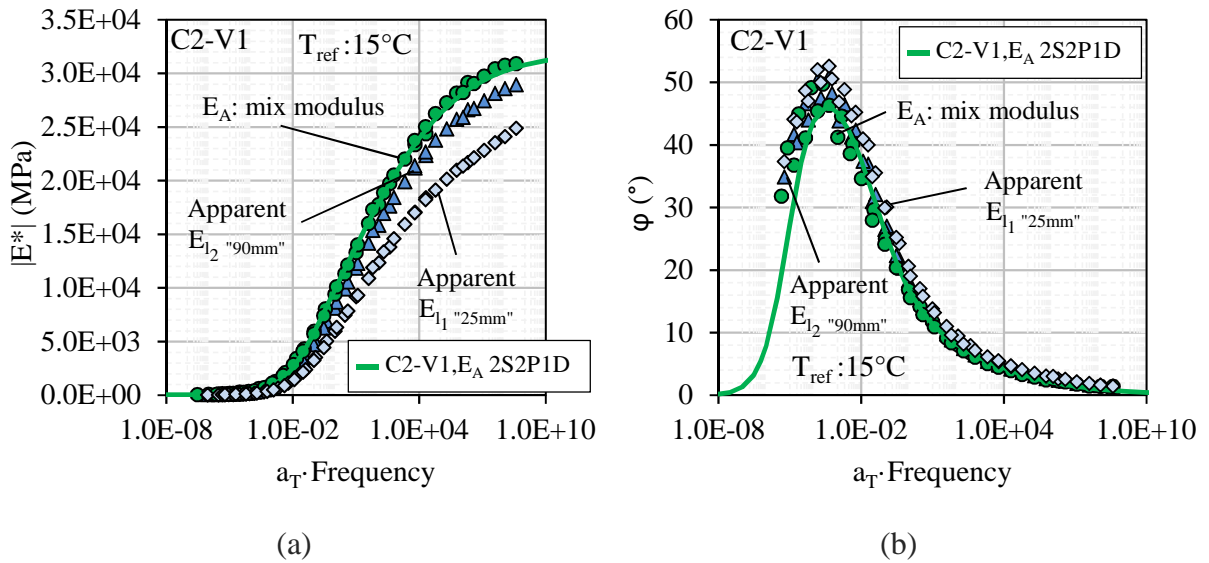


Figure 4-14. Master curves results ( $E_{I1}$  (25mm) and  $E_{I2}$  (90mm)) plotted with calculated bituminous mixture modulus ( $E_A^*$ ) for the specimen C2-V1 for (a) norm of complex modulus and (b) phase angle

Moreover, Figure 4-15 presents the master curves of the norm of Poisson’s ratio in directions III and I, respectively, for the reference temperature of 15°C. The difference observed between the two radial directions was mainly relates to the asymptotic values for Poisson’s ratio ( $\nu_0$  and  $\nu_{00}$ ), presenting a  $\Delta\nu_{00} = 0.30$ , the same observed for  $\Delta\nu_0$ . Finally, Table 4-3 presents the calibration coefficient values from 2S2P1D model.

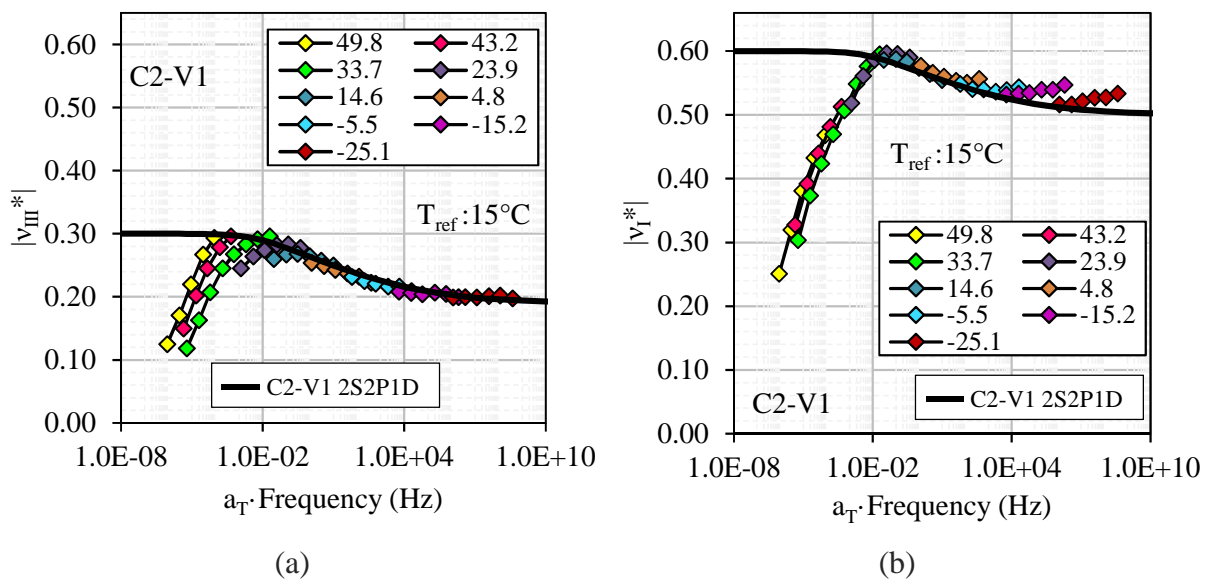


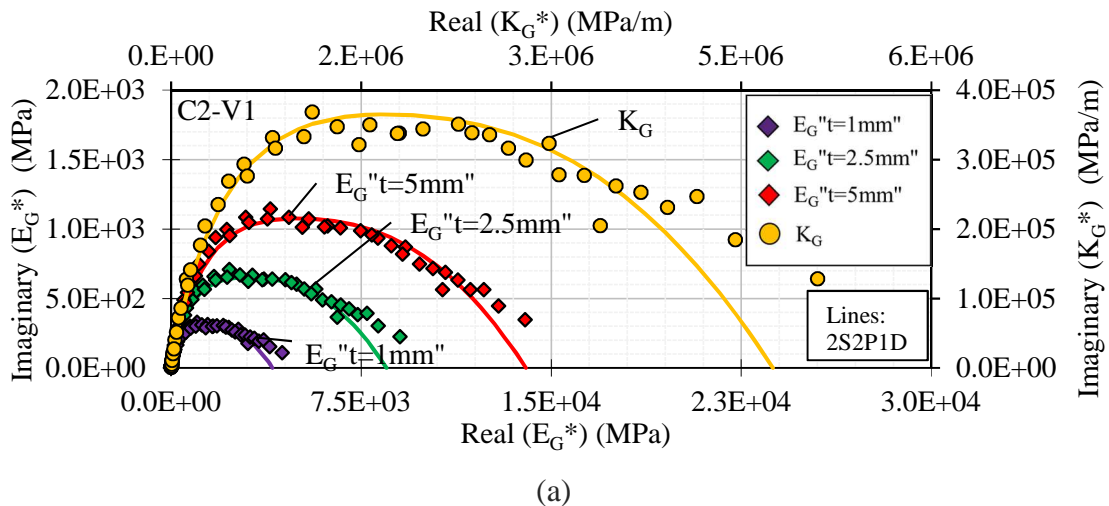
Figure 4-15. Specimen C2-V1 master curves of norm of Poisson’s ratio ( $T_{ref} = 15^\circ\text{C}$ ) obtained for the radial directions (a) III and (b) I

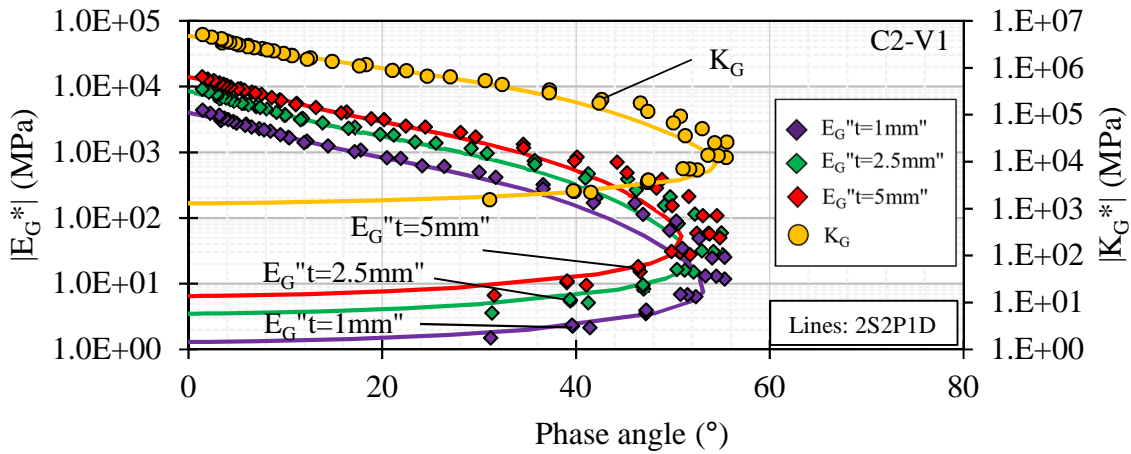
Table 4-3. Coefficients of 2S2P1D model calibrated for C2-V1 test results concerning the mixture  $E_A^*$

$E_{00}$ (MPa)	$E_0$ (MPa)	$k$	$h$	$\delta$	$\tau_E$ (s) (15°C)	$\beta$	$\nu_{I00}$	$\nu_{I0}$	$\nu_{III00}$	$\nu_{III0}$
60.0	3.20E+04	0.185	0.60	2.35	0.50	200	0.6	0.5	0.3	0.2

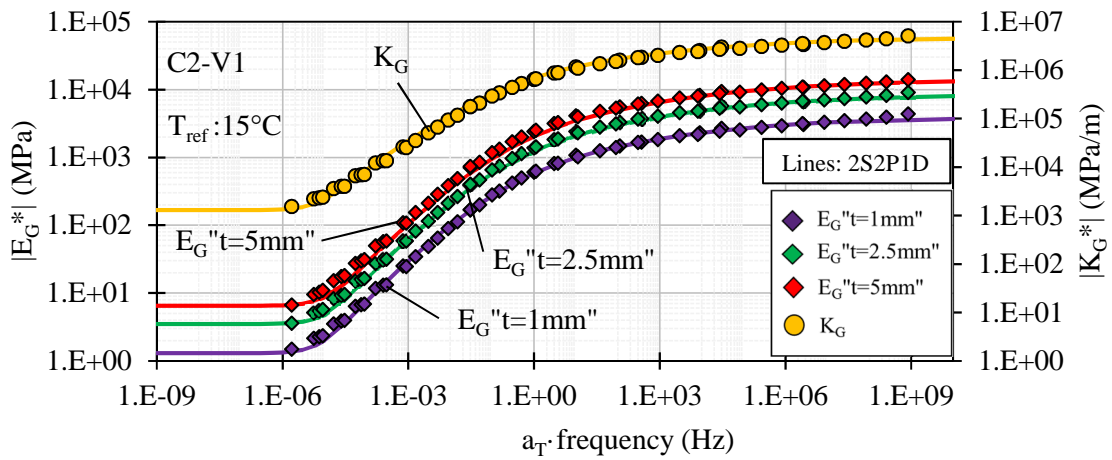
4.6.2.1. Specimen type V: C2-V1 (interface)

Regarding the interface behavior, three thicknesses (1.0, 2.5 and 5.0mm) were chosen for the continuum mechanics calculation represented in Eq. 4-19 ( $E_G^*$ ). In addition, the interface complex stiffness modulus ( $K_G^*$ ) was obtained by considering the interface between the bituminous mixtures layers infinitely fine. In this case, the interface complex stiffness characterization was obtained by the Eq. 4-20. Figure 4-16(a) presents the three complex modulus curves of the interface layer for the three chosen thicknesses plotted with the complex stiffness from interface infinitely fine in Cole-Cole plan. Figure 4-16(b) and (c) present the same four mentioned results in Black space and the master curve of the norm of complex modulus, respectively. 2S2P1D model was also calibrated to the interface results, and the constants are presented in Table 4-4.





(b)



(c)

Figure 4-16. Specimen C2-V1 interface complex modulus considering interface as an equivalent layer for three different thicknesses (1.0, 2.5 and 5.0mm) and considering interface infinitely fine in (a) Cole-Cole, (b) Black space, and (c) master curve of  $|E_G^*|$  or  $|K_G^*|$

Table 4-4. Coefficients of 2S2P1D model calibrated for C2-V1 test results concerning the interface

Specimens	$E_{G00}$ (MPa) or $K_{G00}$ (MPa/m)	$E_{G0}$ (MPa) or $K_{G0}$ (MPa/m)	$k$	$h$	$\delta$	$\tau_E$ (s) ( $T_{ref} = 15^\circ\text{C}$ )	$\beta$
$K_G$	1300.0	4.75E+06	0.175	0.550	2.800	0.03	250
$E_G$ ; t=1.0mm	1.3	4.00E+03					
$E_G$ ; t=2.5mm	3.5	8.50E+03					
$E_G$ ; t=5.0mm	6.5	1.40E+04					

The variation observed in the results are only caused by glassy modulus  $E_{G0}$  (or  $K_{G0}$ ) and static modulus  $E_{G\infty}$  (or  $K_{G\infty}$ ) values. The increase in the chosen thickness resulted in a direct increase in the increase in the stiffness of the interface. In order to remove the effects of glassy and static modulus, the normalization procedure described in section 2.4.5.1 was performed according to the Eq. 2-12. The normalized experimental data points and 2S2P1D model are presented in Figure 4-17 (a) to (d), in Cole-Cole, Black, master curve of norm of complex modulus, and master curve of phase angle, respectively.

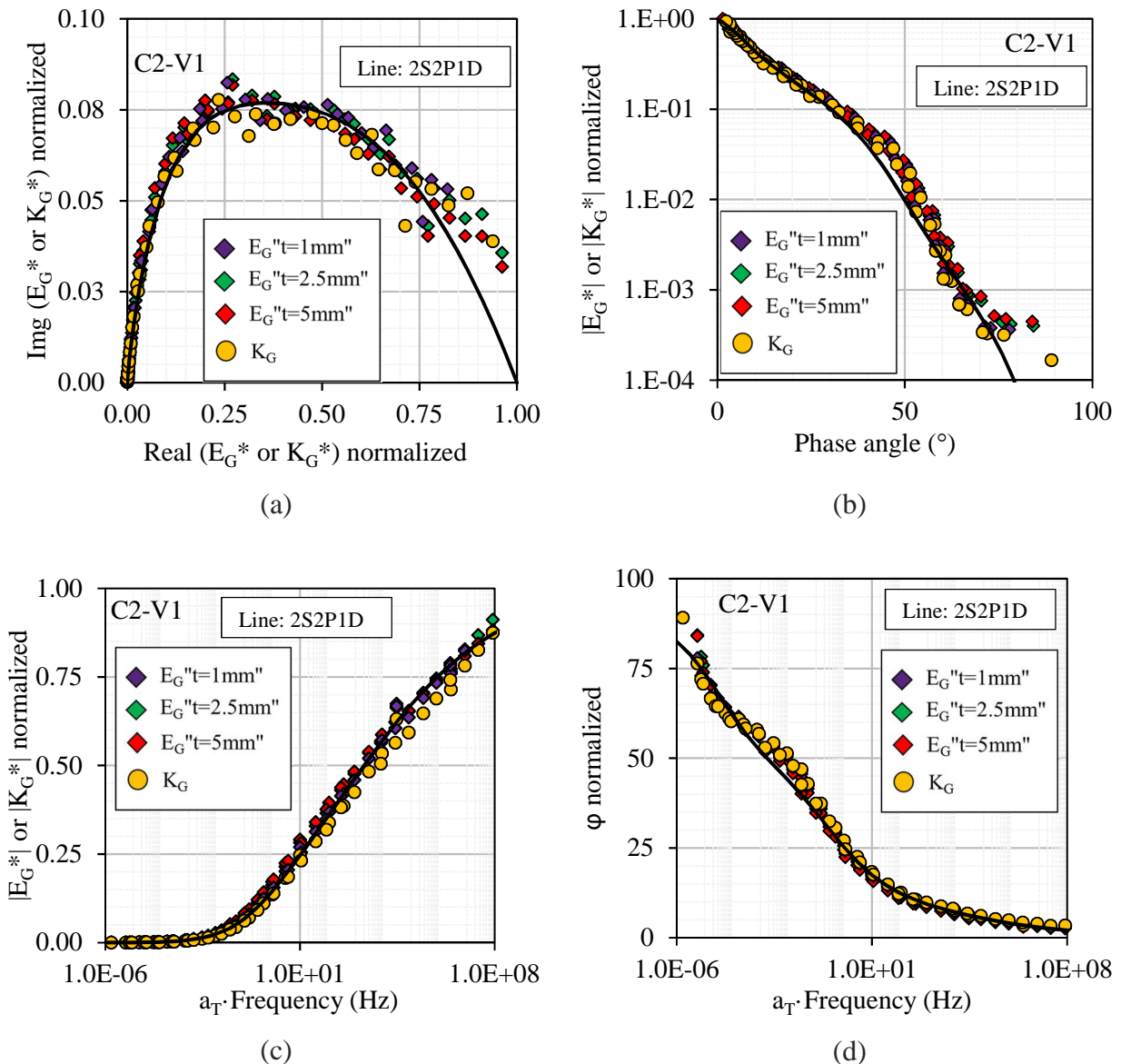


Figure 4-17. Interface of C2-V1 normalized complex modulus ( $E_{\text{norm}}^*$ ) and complex modulus stiffness ( $K_{\text{norm}}^*$ ) (points) and 2S2P1D model (line): (a) Cole-Cole plan, (b) Black space, (c) master curve of norm of complex modulus, and (d) master curve of phase angle

Both analysis approaches ( $K_G^*$  and  $E_G^*$ ) could be modelled by 2S2P1D, which indicates that the interface composed by geogrid and tack coat of bituminous emulsion have a LVE behavior. The normalized curves show that both analysis returns the same LVE information from the analyzed interface, since it is observed a superposition of points in the normalized plots. Finally, the normalized 2S2P1D model is the same for all data points, since they presented the same shape coefficients of the model ( $k$ ,  $h$ ,  $\delta$ , and  $\beta$ ), as can be seen in Table 4-4.

#### 4.6.2.2. Specimen type H: C2-H3

The last example of results analysis of specimens containing interfaces, concerns type H samples. C2-H3 was the result chosen to be presented. In those cases, the analysis of result is very similar to the one conducted on specimens without interfaces discussed in section 4.6.1. The main difference between the two cases is about the instrumentation used during test, two couples of extensometer with different lengths and two couples of non-contact transducers for radial measurements. Figure 4-18 presents the comparison between the results obtained for each couple of extensometer different (25 and 90mm) in (a) Cole-Cole plan and (b) Black space.

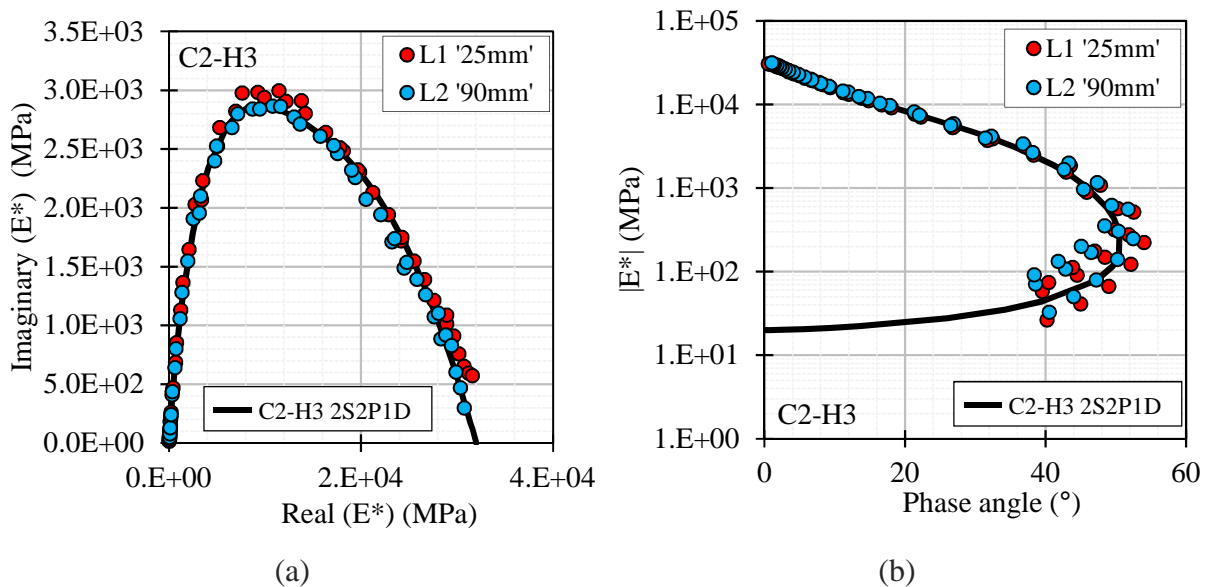


Figure 4-18. Experimental results ( $E_{l1}$  (25mm) and  $E_{l2}$  (90mm)) for the specimen C2-H3 in (a) Cole-Cole plan and (b) Black space

From the experimental points, it is possible to observe that the difference between the two measures is negligible. These differences are mostly related to the extensometer's calibration

and precision rather than a material property variation. Moreover, the geogrid interface presence seems to not changing the classical shape of a unique curve presented by bituminous mixtures. Regarding the radial measurements, the results obtained for the two analyzed directions (II and III) were remarkably different. The Poisson's ratio in direction II, which is perpendicular to the interface section, presented a wider range of variation comparing to the one obtained in direction III. The  $\nu_{00}$  in both directions were the same, however, the  $\nu_0$  value varied from 0.08 (direction II) to 0.27 (direction III). This variation can be explained by the greater level of strain in the interface occurring during loading in the direction perpendicular to the interface section (direction II). Figure 4-19 presents the master curves of the norm of Poisson's ratio in (a) direction II and (b) direction III, obtained for C2-H3 at  $T_{ref}$  of 15°C. The 2S2P1D model calibration coefficients are shown in Table 4-5.

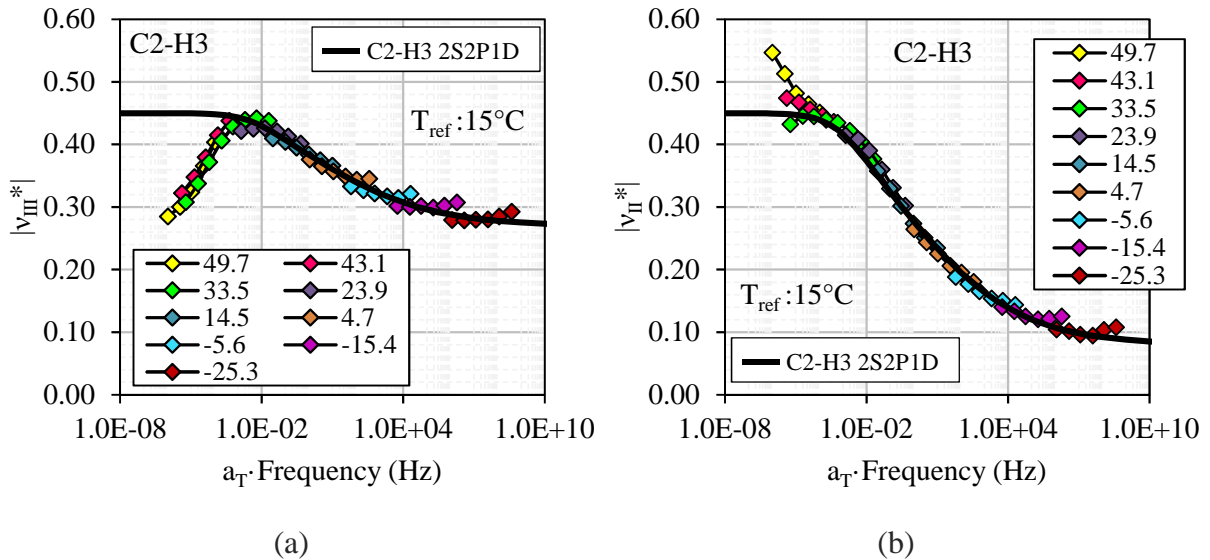


Figure 4-19. Specimen C2-H3 master curves of the norm of Poisson's ratio ( $T_{ref} = 15^\circ\text{C}$ ) obtained for the radial directions (a) III and (b) II

Table 4-5. Coefficients of 2S2P1D model calibrated for C2-H3 test results ( $T_{ref} = 15^\circ\text{C}$ )

$E_{00}$ (MPa)	$E_0$ (MPa)	$k$	$h$	$\delta$	$\tau_E$ (s)	$\beta$	$\nu_{II00}$	$\nu_{II0}$	$\nu_{III00}$	$\nu_{III0}$
20.0	3.20E+04	0.185	0.60	2.35	0.30	200	0.45	0.08	0.45	0.27



### 4.6.3. Complex modulus test results

#### 4.6.3.1. Bituminous mixtures analysis and modelling

Figure 4-20 presents the complex modulus test results obtained for specimens type V in Cole-Cole plan and Black space, respectively. Concerning specimens containing interface, the complex modulus obtained for bituminous mixture only ( $E_A^*$ ) was plotted to compare with the configuration A (no interface and no geogrid). Moreover, the 2S2P1D model for each specimen was also plotted. Figure 4-21 presents the complex modulus test results obtained for specimens type H in Cole-Cole plan and Black space, respectively. In addition, the 2S2P1D model for each specimen was also plotted for those results. The coefficients used in the calibration are presented in Table 4-6. From Cole-Cole plan and Black space plots, the results presented a unique curve for both, specimens type V and H. Thus, the TTSP was validated for all specimens tested during this work.

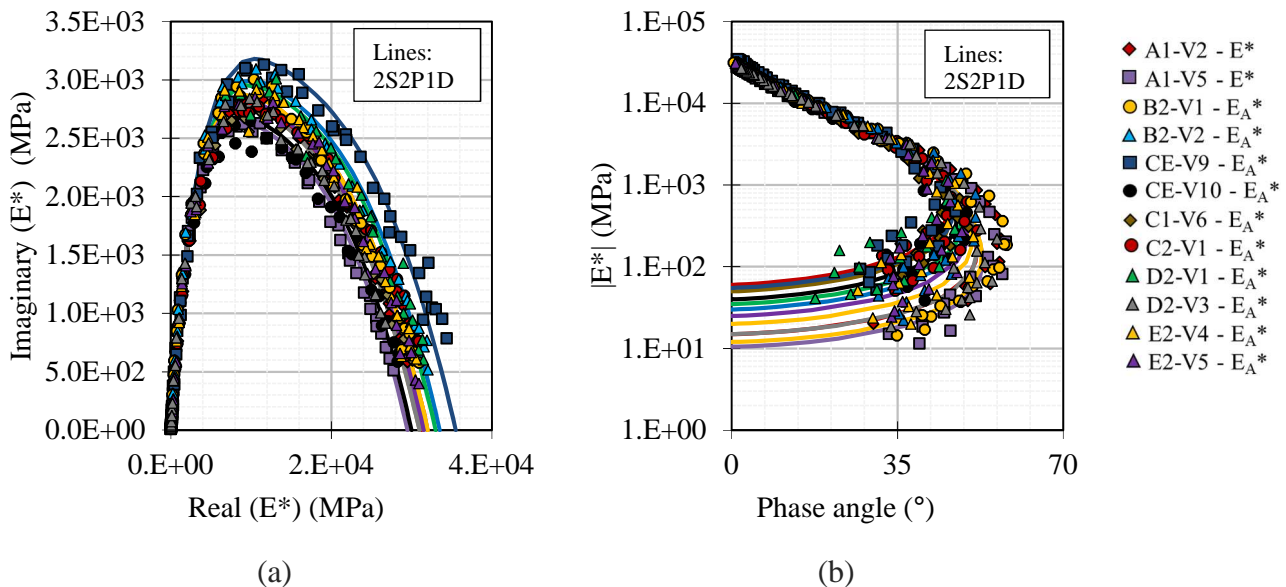


Figure 4-20. Complex modulus test results for type V samples and 2S2P1D model for each test in (a) Cole-Cole plan and (b) Black space



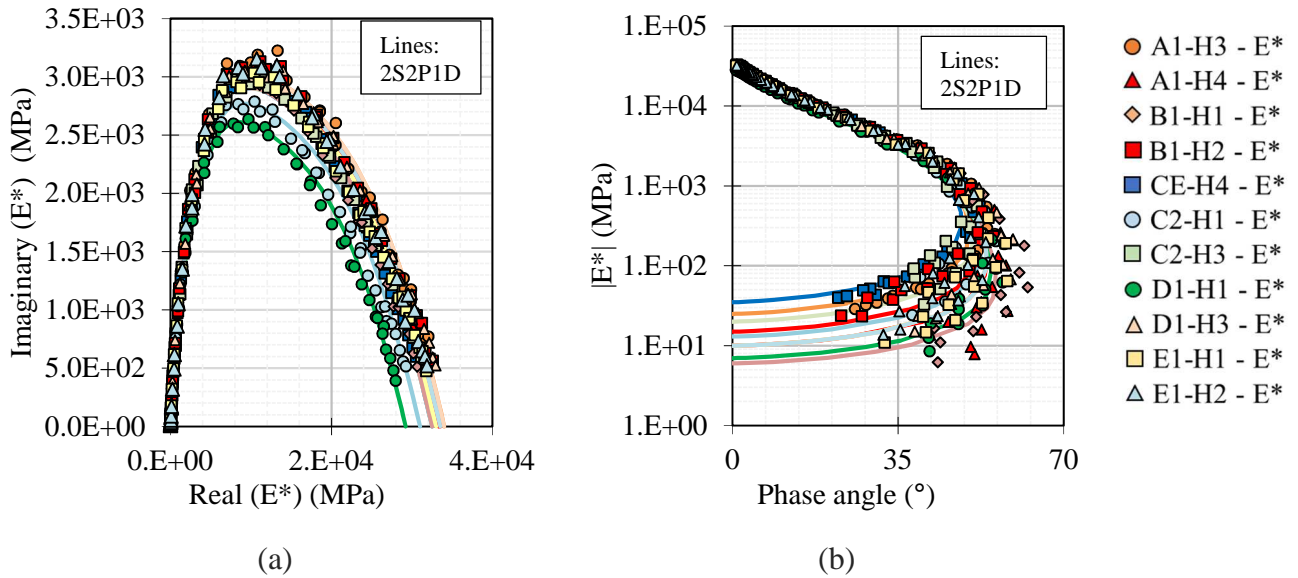


Figure 4-21. Complex modulus test results for type H samples and 2S2P1D simulations for each test in (a) Cole-Cole plan and (b) Black space

Table 4-6. Coefficients of 2S2P1D model calibrated for mixtures test results

Specimen	$E_{00}$ (MPa)	$E_0$ (MPa)	$\tau_E$ (s) ( $T_{ref} = 15^\circ\text{C}$ )	$k$	$h$	$\delta$	$\beta$
A1-V2	15.0	3.12E+04	0.27	0.185	0.60	2.35	200
A1-V5	10.5	2.95E+04					
A1-H3	25.0	3.40E+04					
A1-H4	10.0	3.33E+04					
B2-V1 $E_A^*$	12.0	3.20E+04	0.40				
B2-V2 $E_A^*$	30.0	3.35E+04	0.27				
B1-H1	6.0	3.25E+04	0.32				
B1-H2	15.0	3.35E+04	0.40				
CE-V9 $E_A^*$	55.0	3.55E+04	0.80				
CE-V10 $E_A^*$	40.0	3.00E+04	0.27				
C1-V6 $E_A^*$	50.0	3.10E+04	0.50				
C2-V1 $E_A^*$	60.0	3.20E+04					
CE-H4	35.0	3.25E+04	0.27				
C2-H1	13.0	3.10E+04	0.30				
C2-H3	20.0	3.25E+04	0.50				
D2-V1 $E_A^*$	35.0	3.30E+04	0.40				
D2-V3 $E_A^*$	15.0	3.10E+04					

D1-H1	7.0	2.92E+04					
D1-H3	10.0	3.40E+04					
E2-V4 $E_A^*$	20.0	3.20E+04	0.50				
E2-V5 $E_A^*$	25.0	3.15E+04					
E1-H1	10.0	3.30E+04	0.40				
E1-H2	10.0	3.35E+04					

The calculation  $E_A^*$  resulted in unique curves, presenting the same shape coefficients of the 2S2P1D model ( $k$ ,  $h$ ,  $\delta$ , and  $\beta$ ) than the specimen in configuration A, as observed in Table 4-6. The difference in the results is related to the glassy modulus ( $E_0$ ) and static modulus ( $E_{00}$ ) of the specimens. In order to explain these differences, the  $E_0$  values were plotted against the air voids content of the specimen in Figure 4-22. The red circles stand for the specimens type H, and red dash line is the linear fit done for those specimens. The blue circles stand for the specimens type V, and the blue dash line is the linear fit for V. Finally, the black dash line is the linear fit for all the tested specimens.

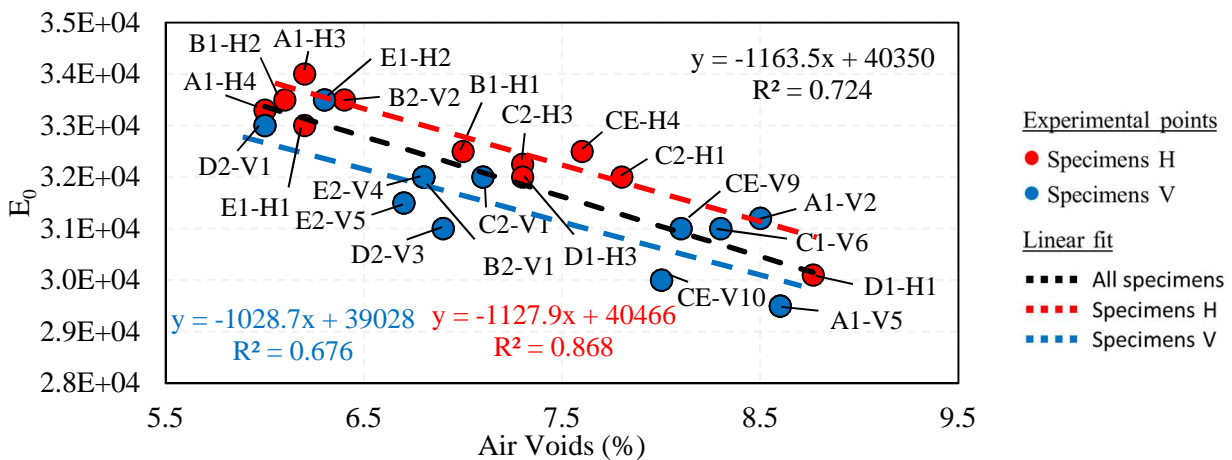


Figure 4-22. Glassy modulus ( $E_0$ ) against voids content for all tested samples

The linear fit obtained for specimens V was worse than the fit obtained for specimens H, since the  $R^2$  was 67.6% for specimens V, while the  $R^2$  for specimens H was 86.8%. However, the  $R^2$  obtained in the fitting for all specimens was 72.4%. Thus, the variation of  $E_0$  obtained in the test results is highly related to the air voids variation on the specimens. This statement agrees with the previous works conducted in the LTDS/ENTPE team (Pham et al. 2015, Cardona Ramirez 2016, Pedraza 2018). In addition, the good fit obtained for all specimens (black dash line) is an indicator that the anisotropy for the tested specimens could be negligible.

Nonetheless, the glassy modulus ( $E_0$ ) and static modulus ( $E_{00}$ ) are parameters that vary from sample to sample in the function of its particularities, such as air voids. Thus, they do not represent the LVE behavior of the material. In order to compare the LVE behavior of the tested specimens, the normalization described in section 2.4.6 was again performed. Figure 4-23 presents the complex modulus test results of all specimens with the 2S2P1D model in Cole-Cole plan, while Figure 4-24 in Black space. Figure 4-25 presents the normalized master curves for norm of complex modulus of all specimens with the 2S2P1D model, while Figure 4-26 presents the master curve for phase angle.

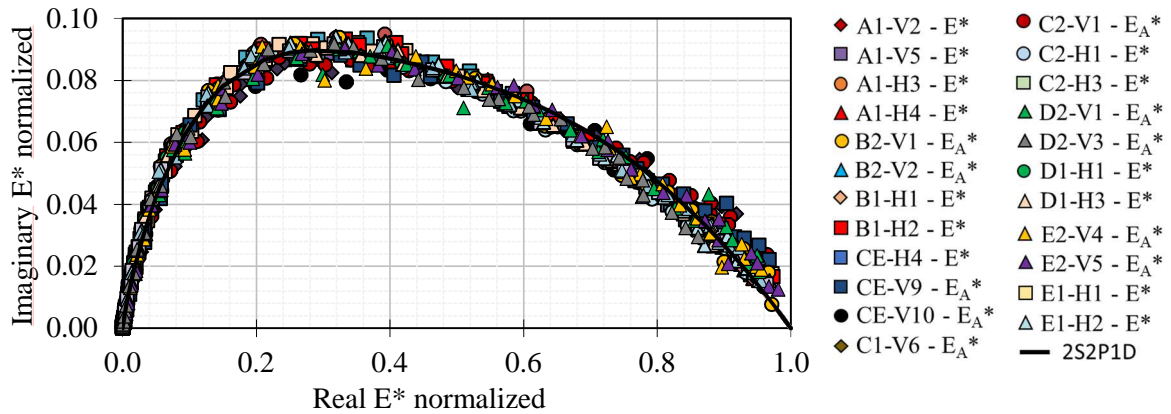


Figure 4-23. Complex modulus test results of all specimens in normalized Cole-Cole plan

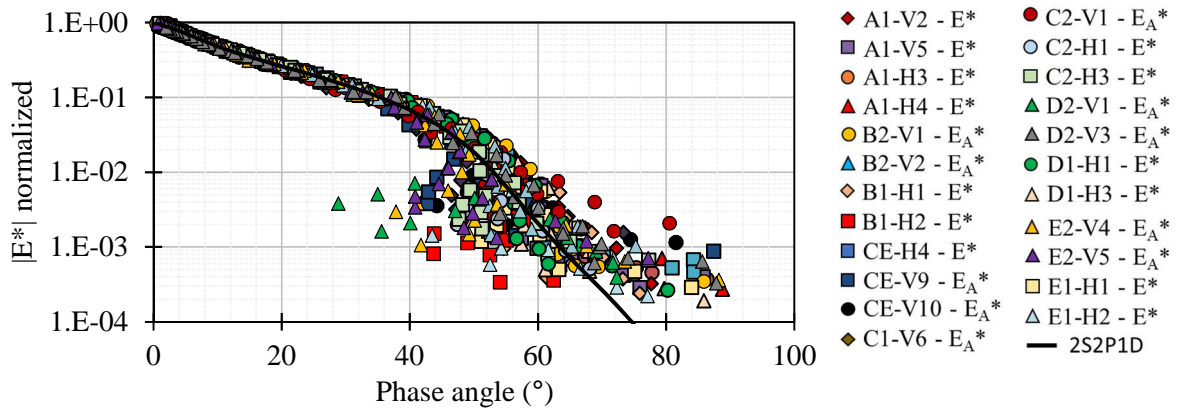


Figure 4-24. Complex modulus test results of all specimens in normalized Black space

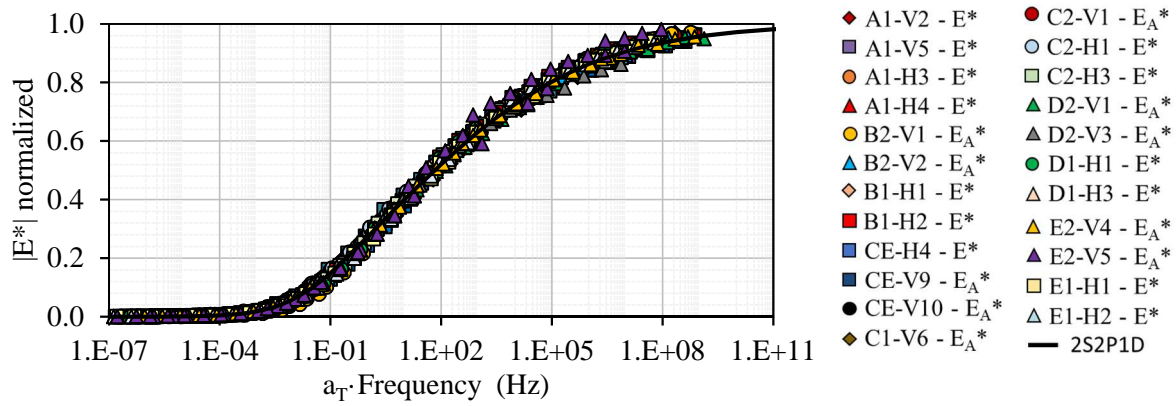


Figure 4-25. Normalized master curve of the norm of the complex modulus of all specimens

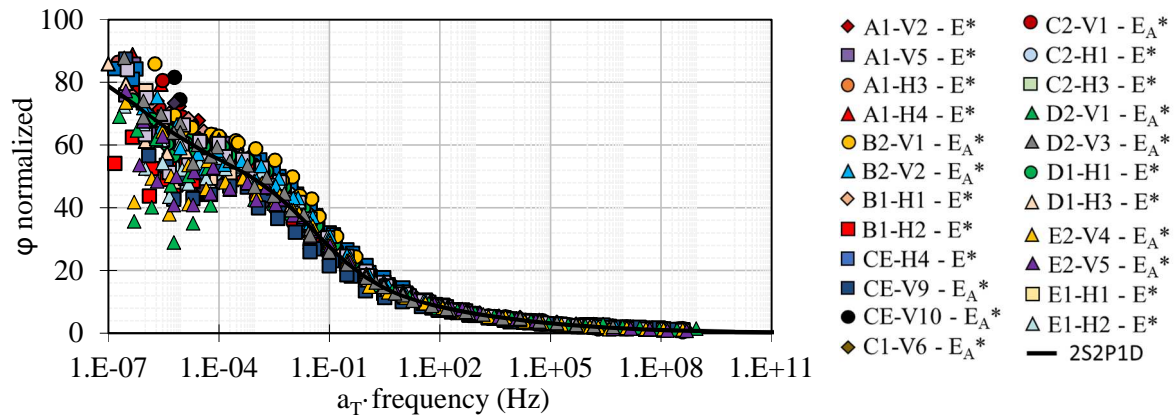


Figure 4-26. Normalized master curve of the norm of the phase angle of all specimens

From the normalized curves, it can be observed that there is a superposition in all experimental points. This superposition observed indicates that the LVE behavior of all results is the same. A same LVE behavior was expected from the results since the same bituminous mixture constituted all specimens. Moreover, this result corroborates with the effectiveness of the  $E_A^*$  obtained through the calculation described in section 4.4.1. This demonstrates that the new proposed analysis in this investigation is a reliable tool for interface LVE characterization including interface with geogrid reinforcement. Finally, a good repeatability was verified for the tested specimens.

Regarding the results concerning Poisson's ratio, Table 4-7 presents the coefficients  $\nu_{00}$  and  $\nu_0$  for 2S2P1D model in 3-Dimensions calibrated over test results depending on the radial direction analyzed. Figure 4-27 presents a normalized master curve of the norm of Poisson's ratio for all the tested specimens.

Table 4-7. Coefficients  $\nu_{00}$  and  $\nu_0$  of 2S2P1D model calibrated for mixtures test results

Specimen	$\nu_{00I}$	$\nu_{0I}$	$\nu_{00II}$	$\nu_{0II}$	$\nu_{00III}$	$\nu_{0III}$
A1-V2					0.34	0.19
A1-V5					0.45	0.17
A1-H3	0.44	0.23				
A1-H4	0.45	0.19				
B2-V1	0.66	0.21			0.50	0.16
B2-V2	0.36	0.22			0.40	0.13
B1-H1			0.56	0.22	0.36	0.18
B1-H2			0.50	0.23	0.50	0.28
CE-V9	0.23	0.15			0.15	0.14
CE-V10	0.34	0.17			0.40	0.24
C1-V6	0.25	0.18			0.14	0.12
C2-V1	0.60	0.50			0.30	0.19
CE-H4			0.70	0.12		
C2-H1			0.40	0.08	0.37	0.26
C2-H3			0.45	0.08	0.45	0.27
D2-V1					0.28	0.20
D2-V3					0.18	0.11
D1-H1			0.44	0.23	0.30	0.18
D1-H3			0.46	0.21	0.32	0.26
E2-V4					0.13	0.20
E2-V5					0.27	0.15
E1-H1			0.51	0.19	0.37	0.15
E1-H2			0.37	0.14	0.42	0.24

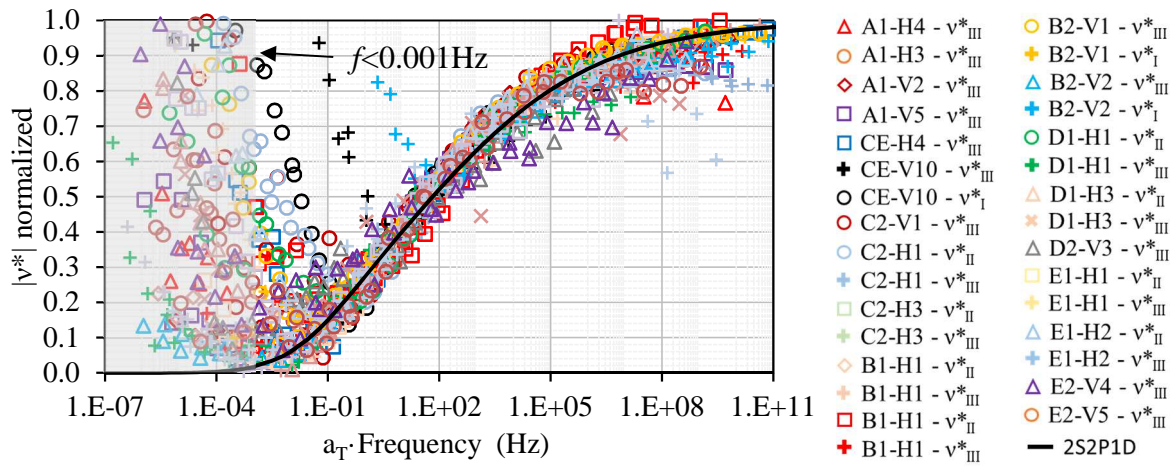


Figure 4-27. Normalized master curve of the norm of Poisson's ratio of all specimens

As aforementioned, the radial measurements at low frequencies and high temperatures were scattered points. At these conditions, different mechanisms interfere in the radial measurements. For this reason, the results obtained for frequencies smaller than 0.001Hz should be removed. Moreover, the dispersions observed for  $\nu^*$  are related to the specimens' heterogeneity due to the interface presence. Finally, Figure 4-28 presents the normalized master curve of the norm of complex modulus and Poisson's ratio plotted together with all tested specimens. This result indicates that all the tested specimens presented the same LVE behavior regardless of the analyzed direction. Moreover, the most scattered points were due to the geogrid presence in the analyzed specimen.

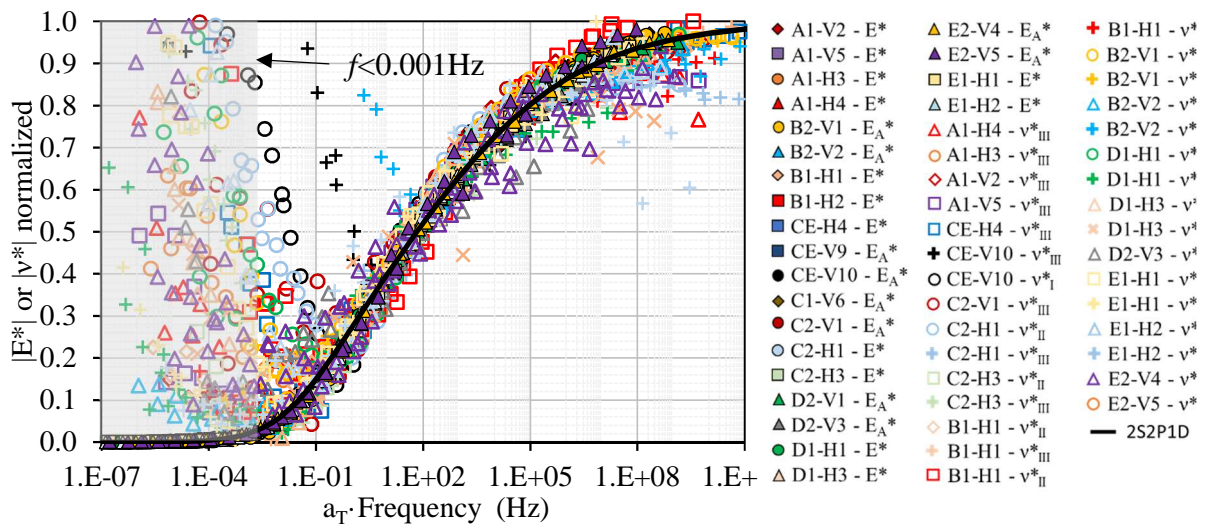


Figure 4-28. Normalized master curve of the norm of complex modulus and Poisson's ratio of all specimens



4.6.3.2. Interfaces analysis and modeling

Regarding the interface analysis, the interface stiffness ( $K_G^*$ ) was used to compare the results obtained, since it is not dependent on an arbitrarily chosen thickness, as discussed in section 4.4.2. Figure 4-29 presents all interface complex modulus test results in Cole-Cole plan with the 2S2P1D model.

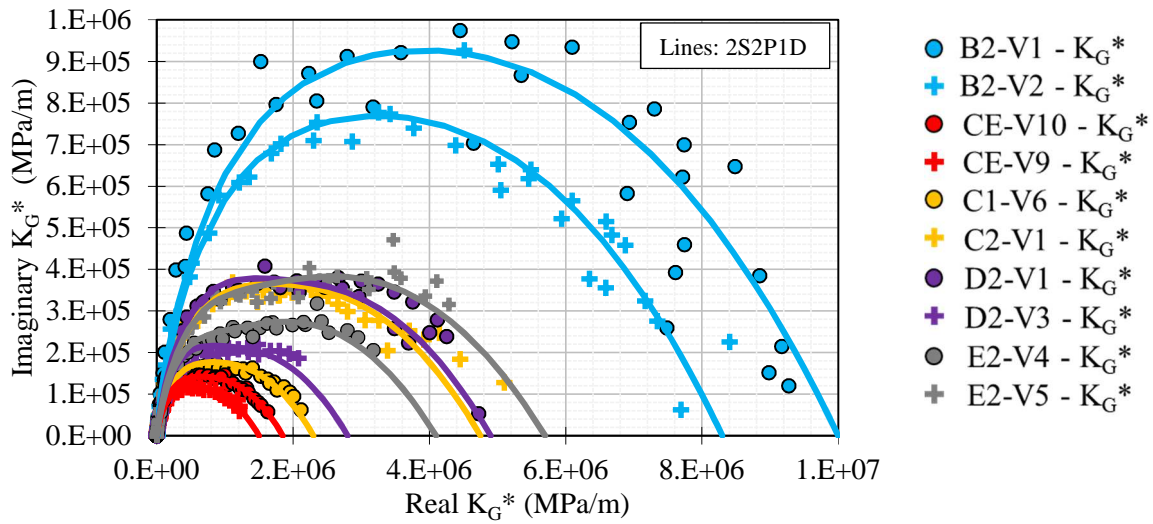


Figure 4-29. Interface complex modulus ( $K_G^*$ ) test results in Cole-Cole plan

From the results, it can be observed that the specimens in configuration B (interface composed only by emulsion bitumen) presented higher stiffness, when compared to the other configurations. Figure 4-30 presents the  $K_{G0}$  obtained for the tested specimens.

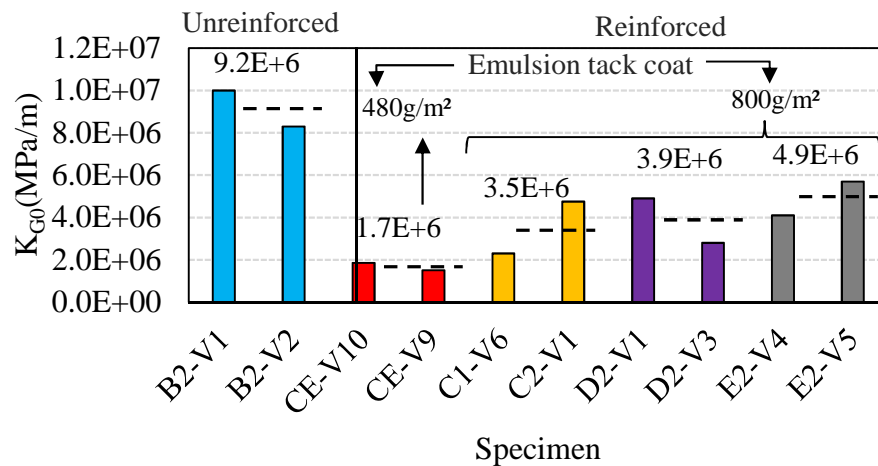


Figure 4-30.  $K_{G0}$  obtained for each tested specimen

From the previous figure, it can be observed that the unreinforced specimens (configuration B) presented almost twice more stiffness than the second stiffer configuration. Thus, the results indicate that the fiberglass geogrid presence in the interface decreases its stiffness, which was already expected. As there is no geogrid in the interface, more contact exists between the two layers of bituminous mixtures, creating friction that could increase its stiffness during loading cycles. Concerning the reinforcement specimens, the configuration C containing less emulsion (480g/m<sup>2</sup>) called CE, presented the lower interface stiffness than the C specimens with 800g/m<sup>2</sup> of emulsion. It indicates that the emulsion rate used to bond the geogrid between the mixtures has a direct influence on the interface stiffness. Configurations C (geogrid of 100kN) and D (geogrid of 50kN) presented similar interface stiffness. However, configuration E (geogrid of 100kN with emulsion modified by SBS) presented the stiffest interface among the reinforced interfaces. The modification increases the adhesive properties of the bitumen present in the emulsion. Thus, the quality of the emulsion adhesion creates stiffer interfaces between bituminous mixtures reinforced by fiberglass geogrid. This result corroborates with the work done by Cho et al. (2016), showing that the tack coat quality can overlap the influence of geogrid type. Table 4-8 presents all the 2S2P1D model coefficients calibrated for  $K_G^*$ .

Table 4-8. Coefficients of 2S2P1D model calibrated for interface complex modulus ( $K_G^*$ )

Specimen	$K_{G00}$ (MPa/m)	$K_{G0}$ (MPa/m)	<b>k</b>	<b>h</b>	$\delta$	$\tau_E$ (s) (15°C)	$\beta$
B2-V1	4000	1.00E+07	0.210	0.600	2.800	0.200	30
B2-V2	7000	8.30E+06				0.100	
CE-V9	450	1.50E+06	0.175	0.550		0.030	250
CE-V10	230	1.85E+06				0.008	
C1-V6	800	2.30E+06				0.030	
C2-V1	1300	4.75E+06					
D2-V1	888	4.90E+06		0.590	150		
D2-V3	500	2.80E+06					
E2-V4	400	4.10E+06	0.165	3.700	0.007	500	
E2-V5	700	5.70E+06			0.011		

In order to evaluate the LVE behavior of the interfaces studies, the normalization described in section 2.4.6 was again performed. Figure 4-31 presents the normalized interface complex



stiffness results plotted in Cole-Cole plan. The interfaces LVE behavior obtained for configuration C was the same regardless the emulsion rate. Moreover, comparing configurations C and D, very similar behavior was found. However, the SBS modification in configuration E and the lack of geogrid in configuration B yield in considerable variation in LVE behavior of interfaces.

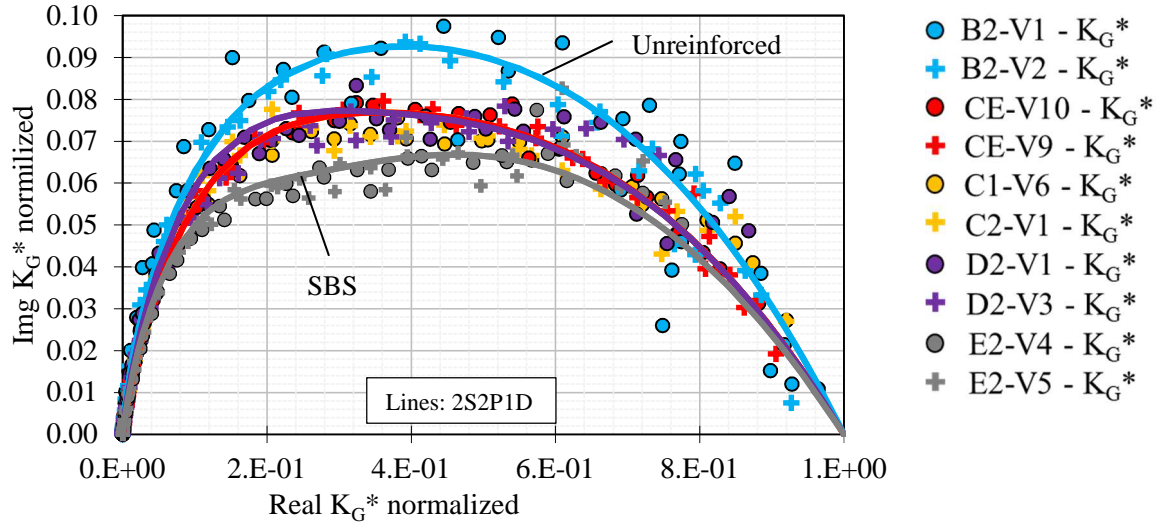


Figure 4-31. Normalized interface complex stiffness ( $K_G^*$ ) test results in Cole-Cole plan

The interface complex modulus  $E_G^*$  defined in section 4.4.1, yields an interface stiffness for a given thickness. However, the contrary can be done by imposing the interface stiffness and obtaining an equivalent thickness. Thus, the bitumen stiffness was imposed by fixing the  $E_0$  value of 3GPa, which can be considered as an average value for bitumen (Mangiafico 2014). The  $E_G^*$  values obtained for the tested specimens were fixed at the mentioned  $E_0$  value, and the thicknesses for each test were calculated. Figure 4-32 presents the  $E_G^*$  in Cole-Cole plan fixing  $E_0 = 3\text{GPa}$  and Figure 4-33 presents the thickness to consider in order to have the same  $E_G^*$  of the interface for all tested specimens.

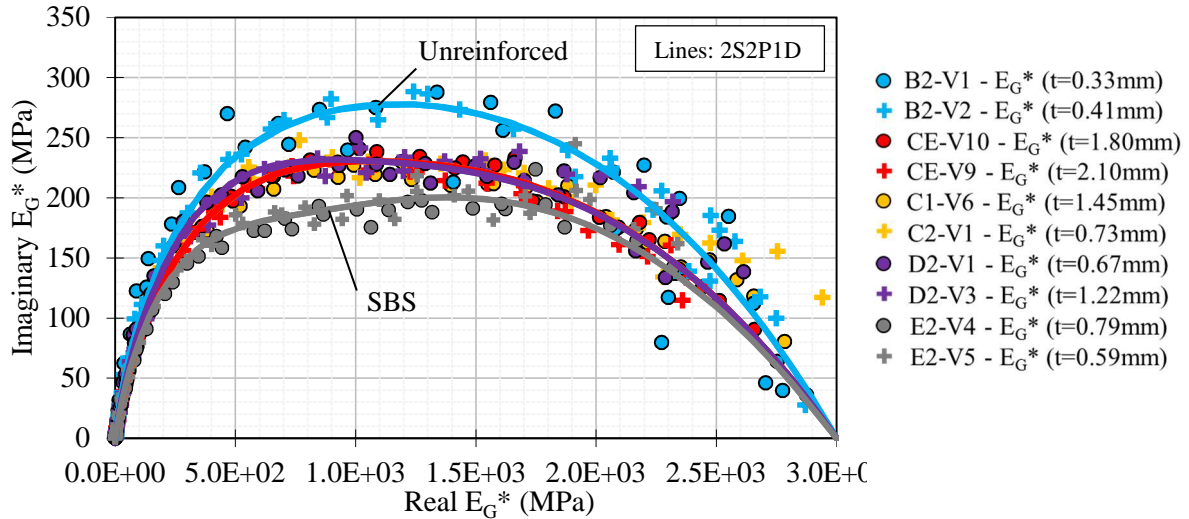


Figure 4-32. Interface complex modulus ( $E_G^*$ ) test results in Cole-Cole plan fixing  $E_0 = 3\text{GPa}$  as reference

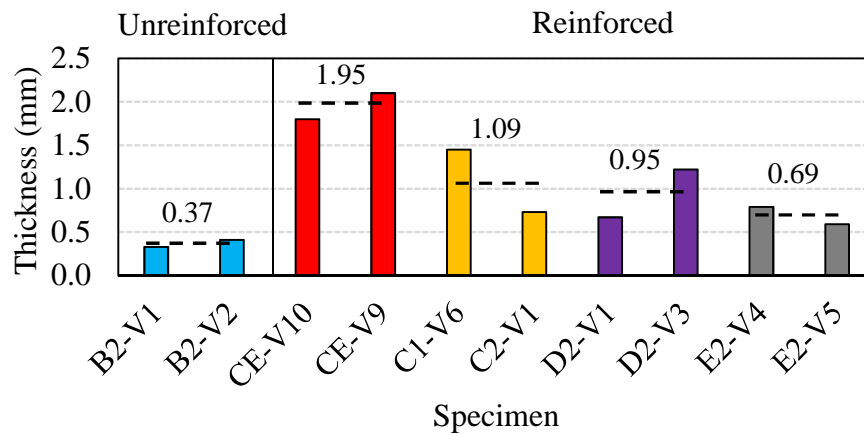


Figure 4-33. Thicknesses to consider to obtain the same  $E_G^*$  of the interface using  $E_0 = 3\text{GPa}$  as reference

Regarding the configuration B, the average thickness was 0.37mm. In the specimens of this slab configuration, the interface is composed only by the residual bitumen remaining after the break of the emulsion. According to (need reference), the bitumen film involving an aggregate particle measures about 300 $\mu\text{m}$ , which is closed to the thickness obtained for configuration B. Therefore, the proposed methodology was capable to measure the stiffness of a bitumen film present on the interface, which corroborates with the reliability of this new interface analysis method proposed in this work.

#### 4.6.4. Influence of fiberglass geogrid on H specimen's behavior

Specimens type H have the geogrid in the interface oriented in the axial direction, same of loading for the complex modulus tests. Assuming that the complex modulus measured ( $E_M^*$ ) during the test is a composition of the bituminous mixtures complex modulus ( $E_A^*$ ) plus the geogrid stiffness ( $K_{G\_SPC}$ ). However, the geogrid stiffness does not have viscous component, since it an elastic material. Thus, the complex modulus of bituminous mixtures can be obtained using the following equation.

$$E_A^* = E_{M1} - C * \frac{K_{G\_SPC}}{S} + iE_{M2} \quad \text{Eq. 4-21}$$

Where  $C$  stands for geogrid mobilization in percentage during the test and  $S$  is the area of specimen section. To calculate  $K_{G\_SPC}$ , the information presented on section 3.1.2 was used. Concerning Notex Glass<sup>®</sup> C 100/100-25, a maximum of 100kN/m is obtained at 3% of strain. The mesh opening is 25mm, thus, for 1m there are 40 yarns. In the specimen's section there is 3 yarns, and its diameter is 75mm. From this information, the  $K_{G\_SPC}$  for the mentioned grid is approximately 61MPa, and the one for Notex Glass<sup>®</sup> C 50/50-25 is half of the value, approximately 30.5MPa. In order to obtain the percentage of geogrid mobilization during the complex modulus tests, three hypotheses were assumed: (i) the geogrid was totally mobilized ( $C = 100\%$ ), (ii) the geogrid was half mobilized ( $C = 50\%$ ), and (iii) the geogrid was not mobilized ( $C = 0\%$ ). The results were plotted with the results obtained concerning the specimens without geogrid (A1-H3, A1-H4, B1-H1, and B1-H2) in Black space. Furthermore, it was observed that, those unreinforced specimens presented similar curve shapes, having a peak of phase angle value between 35 and 45°C, classically obtained for bituminous mixtures. Moreover, the geogrid influence is only noticeable at high temperatures, since at low temperatures the bituminous mixture have a high modulus that overlaps the geogrid contribution to support of the loading. Thus, based on that, the criterion of mobilization was defined as phase angle maximum of 62°. Figure 4-34 presents an example for specimen CE-H4 of the mentioned procedure.

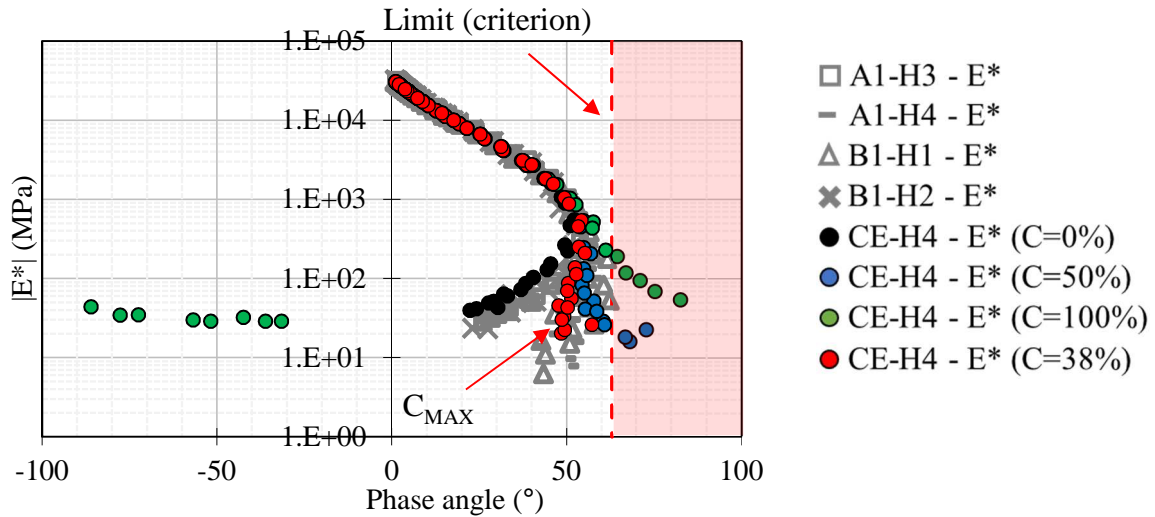


Figure 4-34. Complex modulus test results in Black space of unreinforced specimens plotted with CE-H4 with different percentages of geogrid mobilization for the definition of the real percentage of mobilization

From the figure, it is possible to observe that for values of  $C$  of 50 and 100%, the points at high temperature crossed the defined limit, meaning that the geogrid present a lower percentage of mobilization for CE-H4. Then, the maximum value of  $C$  ( $C_{MAX}$ ) represents the real percentage of geogrid mobilization of the analyzed specimen. Thus, simulations of  $C$  values were performed in order to defined the  $C_{MAX}$  value, which was 38% for CE-H4. The same simulation was performed for all reinforced specimens and they are presented in Black space in Figure 4-35. Finally, Figure 4-36 presents the percentage of geogrid mobilization in the complex modulus test concerning specimens H for each studied slab configuration.

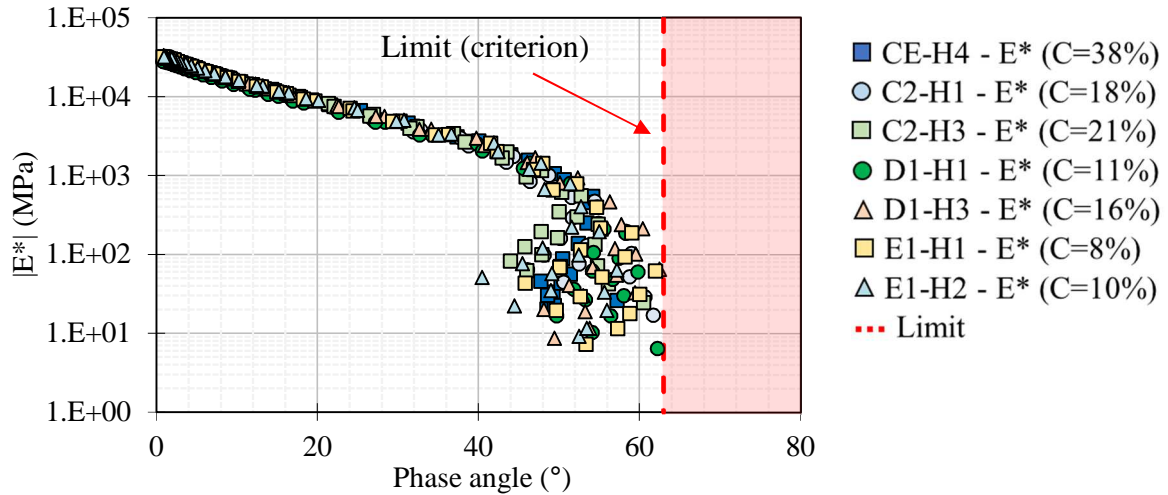


Figure 4-35. Complex modulus test in Black space for all type H reinforced specimens considering at the percentage of geogrid mobilization during the test ( $C_{MAX}$ )

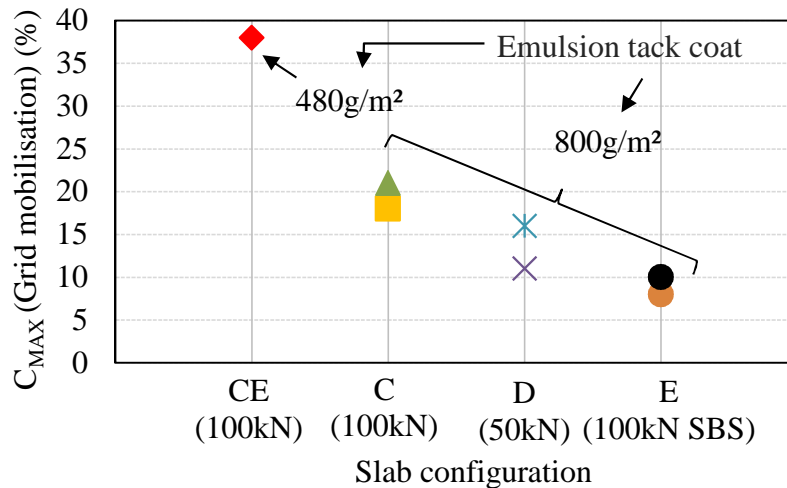


Figure 4-36. Percentage of geogrid mobilization in specimens H during complex modulus test for each slab configuration

The specimen containing less emulsion on the interface (CE) presented higher percentage of geogrid mobilization during the test. It was approximately twice more mobilized than average of all other specimens' mobilization. Regarding the other slabs configurations, a trend was observed from configuration C presenting the highest geogrid mobilization level and configuration E presenting the lowest geogrid mobilization level. However, the specimens presented considerably low level of geogrid mobilization at small strain amplitudes tension-compression

tests, especially configuration E (8 and 10%). A phenomenon of slippage occurring in the interface could be the responsible for this low level of geogrid mobilization obtained from test results. At high temperatures, the bitumen remaining from the emulsion break in the interface presents low stiffness and could facilitate the geogrid slippage during loading cycles. Which could explain the fact that the specimen containing less emulsion in his interface presented a higher percentage of geogrid mobilization.

## 4.7. Chapter conclusions

The presented work in this chapter was focused on the behavior of reinforced specimens cored in different directions when subjected to small strain amplitude loading. Moreover, it proposes a new interface analysis method for complex modulus tests of specimens reinforced by geogrid. Therefore, some conclusion can be drawn:

- The unreinforced materials presented a LVE behavior that was successfully modeled using 2S2PD model.
- The complex modulus concerning bituminous mixture layers ( $E_A^*$ ) in reinforced specimens was successfully obtained and validated with the results obtained for mixtures without reinforcement.
- The interface behavior obtained is LVE and it could be modeled by 2S2PD.
- The complex modulus concerning interface ( $E_G^*$ ) in reinforced specimens was successfully obtained and validated using specimen B (interface without geogrid) by obtaining the same order of magnitude of a bitumen film thickness and modulus.
- The method considering bulk continuum mechanics in the interface layer and the one based on infinitely small thickness interface give similar LVE information.
- The proposed methodology could be a very useful tool for improving the design calculation of geogrid-reinforced pavement structures.
- Interface bond quality, concerning the correct emulsion rate application and adhesion improvement by SBS modification, presented higher influence in the interface stiffness than the type of geogrid.
- Considerable low level of geogrid mobilization was obtained at small strain amplitudes tension-compression tests concerning specimens horizontally cored. Especially for specimens with interface with bitumen modified by SBS.

# Chapter 5: TENSION TEST CAMPAIGN

5.1. Introduction .....	161
5.2. Objectives .....	161
5.3. Experimental procedures and devices .....	162
5.3.1. Hydraulic press and instrumentation.....	162
5.3.2. Tension test protocol .....	162
5.3.3. Analysis of interface concerning specimens type V .....	164
5.4. Tested Specimens .....	165
5.5. Bituminous mixtures and interfaces results.....	168
5.5.1. Example of result of specimens without interface: A3-H4, 19°C, 2%/min .	168
5.5.2. Example of result obtained from specimens having interface .....	170
5.5.2.1. Specimen type V: C2-V5, 19°C, 2%/min (Bituminous Mixture) .....	170
5.5.2.2. Specimen type V: C2-V5, 19°C, 2%/min (Interface).....	171
5.6. Verification of specimen's diameter size effect for specimens type V .....	172
5.7. Verification of time-Temperature superposition principle.....	174
5.7.1. Frequency sweep test results .....	174
5.7.2. Specimens type H.....	179
5.7.3. Specimens type V.....	189
5.8. Fiberglass geogrid contribution to the maximum tensile strength of bituminous mixture.....	199
5.9. Effect of fiberglass geogrid on maximum interface tensile strength.....	203
5.10. Chapter conclusions .....	206

## 5.1. Introduction

Most studies in literature related to geogrid reinforcement agreed with its benefits to limit reflective cracking development. The further step in the investigation of geogrid reinforcement benefits is the identification of other reinforcement mechanisms that can improve pavement performances. Some authors have been working on the pavement structural capacity increasing due to the reinforcement, specially the control of permanent vertical strain in pavement layers (Laurinavicius and Oginskas 2006, Graziani et al. 2014, Guler and Atalay 2016, Correia and Zornberg, 2018).

The purpose of this chapter is to present the experimental campaign conducted to characterize the five different slab configurations, subjected to monotonic axial tension loading. The experimental procedure and devices are presented, as well as the tested specimens for this characterization. In this chapter, discussions about the diameter size effect and interface behavior in specimens type V, based on test results are held. Furthermore, a TTSP verification in bituminous mixtures plastic behavior and non-linear domains for reinforced and unreinforced configurations, types V and H, is conducted. Lastly, the geogrid contribution to the tension support for reinforced type H specimens is evaluated.

## 5.2. Objectives

For the investigation conducted in this chapter, some objectives can be listed:

- To verify the applicability of the methodology described in section 4.4 to the interface behavior characterization at axial monotonic tension loading.
- To verify the diameter size effect on the tension strength resistance results of reinforced specimen type V (perpendicularly cored in relation to the slab compaction direction).
- To validate the TTSP for interface and bituminous mixture for monotonic tension tests
- To evaluate the contribution of the geogrid to the maximum tensile strength of bituminous mixtures in specimens type H (cored in the same direction of the slab compaction direction). As well as, the effect of maximum geogrids strength resistances and the type of emulsion used as tack coat.



- To assess the interface behavior, containing geogrid or not, its maximum tensile strength (bond quality) and the effect of polymer modification (SBS) on the emulsion used as tack coat.

## **5.3. Experimental procedures and devices**

### ***5.3.1. Hydraulic press and instrumentation***

The equipment used for conducting the investigation performed in this chapter is the same used in Chapter 4 concerning the complex modulus experimental campaign. The description of the hydraulic press and the transducers used to control and collect the experimental data are detailed in Section 4.3.1. Regarding the instrumentation, the same extensometers used for complex modulus tests were used to allow the interface characterization during tension tests. The first couple of extensometers had a 25mm length ( $l_1$ ) and they were disposed at 180° from one another. The other couple had a 90mm length ( $l_2$ ) and extensometers were disposed at 180° from one another. The loading strain amplitude was controlled during the test from the average of the two smaller extensometers ( $l_1$ ). However, the non-contact transducers were not used, due to the unpredictable behavior of the specimen at failure that could cause damage to the mentioned transducers. Thus, no radial strain data was collected during the tension tests presented in this chapter.

### ***5.3.2. Tension test protocol***

The tension tests were carried out on cylindrical specimens using tension loading at strain-controlled mode. Two strain rates were combined with three temperatures composing the tension experimental campaign, as can be seen in Figure 5-1. The first strain rate used was the “fast” one: 2%/min, whereas the second one was approximately 0.002%/min, as a “slow” rate. Concerning the tested temperatures, 40, 19 and 0°C were chosen.

According to Nguyen et al. (2009), the TTSP can be also verified in bituminous mixtures plastic behavior and non-linear domains. In the mentioned work, the authors used the LVE WLF equation parameters to choose the pair frequency-temperature that gives the same mechanical response before plastic failure. Thus, the results at 40°C and fast strain rate (2%/min) are compared with the results at 19°C and slow strain rate, which is defined from LVE WLF equation parameters. Whereas the results at 19°C and fast strain rate (2%/min) are compared

with the results at 0°C and slow strain rate, which is also defined from LVE WLF equation parameters. For each specimen, the slow rate was obtained using the LVE behavior obtained prior to the tension test. Similar results in these two comparisons validate the TTSP for tension tests.

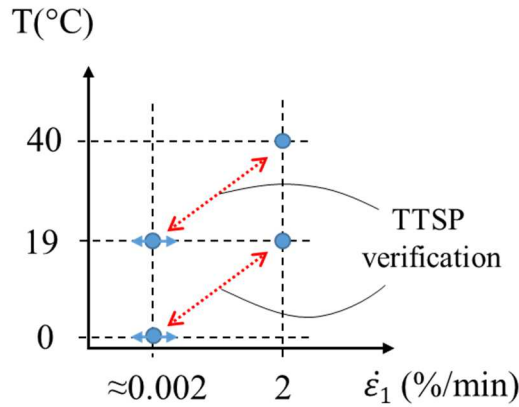
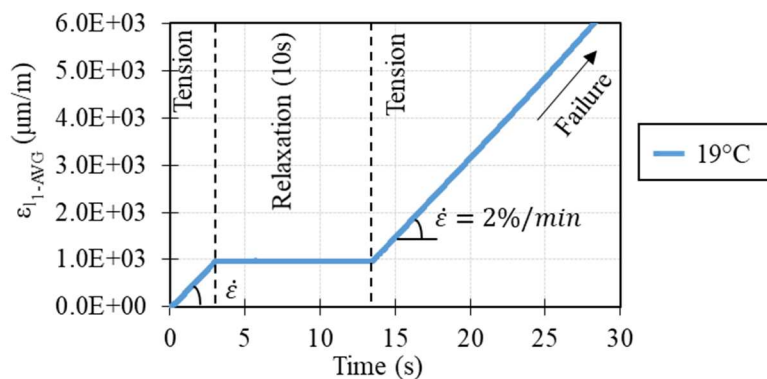


Figure 5-1. Experimental program: combinations between temperatures and strain rates

Aforetime the tension test itself, a frequency sweep test was carried out using sinusoidal tension-compression loading at strain-controlled with amplitude ( $\epsilon_0$ ) of  $50\mu\text{m/m}$  (in smaller extensometers), in order to obtain the LVE behavior of the specimens just before being subjected to failure. Seven frequencies were used in this step: 0.01, 0.03, 0.1, 0.3, 1, 3 and 10Hz, using the same number of loading cycles used for complex modulus test, as described in section 4.3.2, Figure 4-3(b). The tension tests in this work are composed of three steps, as shown



in

Figure 5-2:

- i. Initial tension at constant strain rate ( $\dot{\epsilon}$ ), controlled by the average of extensometer  $l_l$  (25mm), until the strain reaches  $1000\mu\text{m/m}$ .

- ii. Relaxation test at  $1000\mu\text{m/m}$  strain-controlled during: (a) 10s at fast rate ( $\dot{\epsilon} = 2\%/min$ ), and (b) 10 multiplied by the  $a_T$  obtained in the frequency sweep (c.f. Figure 5-3) at slow rate.
- iii. Final tension at constant strain rate ( $\dot{\epsilon}$ ) until the specimen reaches the complete failure (total loss of loading support).

However, for some tests, the maximum range measurement capacity of the smaller extensometers was reached and the test was stopped in order to avoid harm in the extensometer.

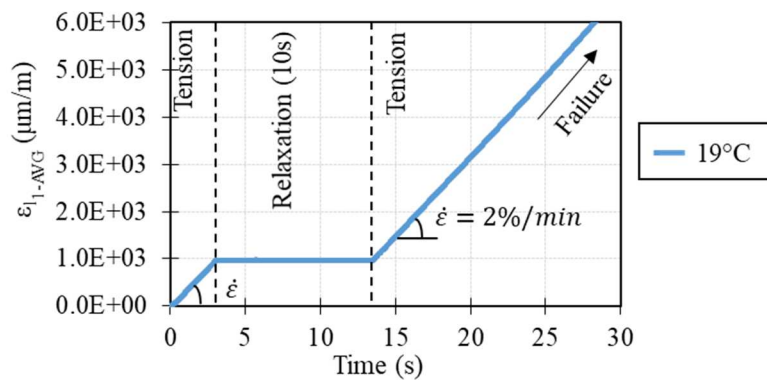


Figure 5-2. Example of the tension test for  $19^{\circ}\text{C}$  and  $2\%/min$

Finally, the slow strain rate is defined by dividing the fast strain rate by the  $a_T$  obtained in the frequency sweep test conducted before the tension test. Figure 5-3 presents an example of the tension test for  $19^{\circ}\text{C}$  at  $2\%/min$  and the  $0^{\circ}\text{C}$  at slow strain rate plotted in equivalent time. On this axis, the curves are the same, and the TTSP can be verified from test results.

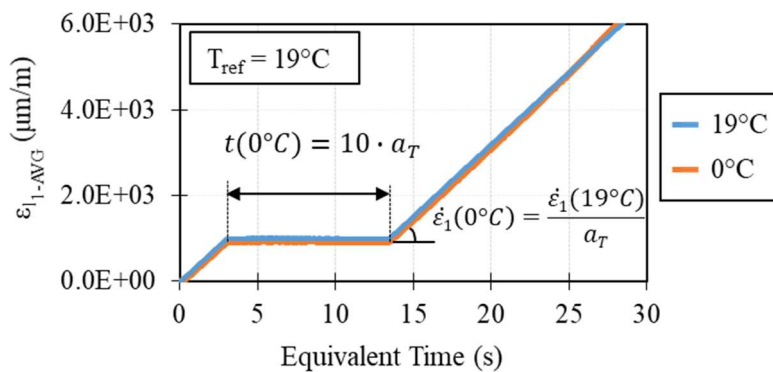


Figure 5-3. Example of slow rate determination in tension test concerning  $19^{\circ}\text{C}$ , fast rate ( $2\%/min$ ) and  $0^{\circ}\text{C}$ , slow rate.

### 5.3.3. Analysis of interface concerning specimens type V

Similar to the calculation performed in Section 4.4, the data obtained from the two couples of extensometers were used to calculate the axial strain of the bituminous mixture ( $\varepsilon_A$ ) and the axial strain of the interface layer ( $\varepsilon_G$ ). This method assumes that the axial strain measurement from each extensometer is the composition of  $\varepsilon_A$  and  $\varepsilon_G$ . The strain values measured by each couple of extensometer could be expressed according to the following equations:

$$\varepsilon_{m1} \cdot l_1 = \varepsilon_A \cdot (l_1 - t) + \varepsilon_G \cdot t \quad \text{Eq. 5-1}$$

$$\varepsilon_{m2} \cdot l_2 = \varepsilon_A \cdot (l_2 - t) + \varepsilon_G \cdot t \quad \text{Eq. 5-2}$$

Where  $\varepsilon_{m1}$  and  $\varepsilon_{m2}$  are the measured strains (respectively from couple 1 and 2 of extensometers),  $l_1$  and  $l_2$  are the length of smaller (25 mm) and longer (90 mm) extensometers, respectively. From these equations,  $\varepsilon_A$  can be obtained as shown in Eq. 5-3 and it can be used to calculate as shown in Eq. 5-4. This strain  $\varepsilon_G$  depends on the interface thickness ( $t$ ).

$$\varepsilon_A = \frac{\varepsilon_{m1} \cdot l_1 - \varepsilon_{m2} \cdot l_2}{l_1 - l_2} \quad \text{Eq. 5-3}$$

$$\varepsilon_G(t) = \frac{\varepsilon_{m1} \cdot l_1 - \varepsilon_A \cdot (l_1 - t)}{t} \quad \text{Eq. 5-4}$$

However, the interface strain is calculated by assuming an interface thickness value, which is another variable for the analysis. Moreover, this interface thickness could not be easily and accurately determined. In order to remove its influence, the interface has been assimilated to a surface. The parameter to be considered is not the strain in a layer but becomes the displacement gap ( $\Delta u$ ) observed at the interface. The interface displacement gap ( $\Delta u$ ) is calculated from Eq. 5-4 when considering  $t$  infinitively small (Eq. 5-5).

$$\Delta u = \varepsilon_{m1} \cdot l_1 - \varepsilon_A \cdot l_1 \quad \text{Eq. 5-5}$$

## 5.4. Tested Specimens

For each slab configuration, the specimens were divided into two groups regarding the geogrid position from slab coring. The first group is the H specimens, cored in the same compaction direction. In this case, the interface in the specimens containing it, are in specimens longitudinal direction, which is the same loading direction (c.f. section 3.2.3). The second group is composed of V specimens, cored perpendicularly in relation to the compaction direction. The interface in those specimens are perpendicular in relation to the loading direction (c.f. section 3.2.3). Four additional V specimens were fabricated with a larger diameter evaluate the diameter size effect in the specimen behavior. Table 5-1 presents all the tested specimens with interface composition and tack coat rate, air voids calculated in the bituminous mixture, and the testing temperature and strain rate of loading.

Table 5-1. Tested specimens' composition, air voids and testing temperatures and strain rates

Specimen	Coring direction	Interface		Air Voids (Mix) (%)	Temperature (°C)	Strain rate (%/min)
		Composition	Tack coat rate			
A1-H2	Horizontal	Not applicable	Not applicable	5.6	40	2
A3-H11				6.4		
A3-H5				6.3	19	0.005
A3-H10				6.1		0.002
A3-H4				7.1		2
A3-H7				5.4	0	0.001
A3-H6				5.9		0.002
A3-H9				7.0		
A1-V4				Vertical	Not applicable	Not applicable
A1-V11	6.3					
A1-V8	6.8	19	0.002			
A2-V1	7.3		0.006			
A1-V9	7.5		2			
A4-V1	8.7	0	0.001			
A1-V7	6.6		0.003			
A4-V2	8.7					
B1-H1	Horizontal	Emulsion Bitumen 160/220	292g/m <sup>2</sup>			
B2-H2				6.6		

TENSION TEST CAMPAIGN

---

B2-H1				7.6	19	0.005			
B2-H4				9.4		0.004			
B1-H2				6.1		2			
B2-H3				7.5					
B1-H3				7.8	0	0.002			
B3-H11				6.9		0.001			
B2-V5				Vertical			7.3	40	2
B2-V9							6.5		
B2-V8							6.5	19	0.001
B2-V12							6.7		0.003
B2-V6							7.0		2
B2-V10							6.5		
B2-V11							7.6	0	0.002
B2-V14							7.1		0.001
C2-H1	Horizontal			7.8	40	2			
C3-H3				8.1					
C2-H2				7.2	19	0.003			
C4-H1				7.2		0.005			
C2-H3				7.3		2			
C3-H1				8.5					
C2-H4				8.6	0	0.003			
C3-H2				7.2		0.001			
C1-V6				Vertical	Emulsion bitu- men 160/220 and GG 100kN/m	2×400g/m <sup>2</sup>	8.3	40	2
C2-V4							8.4		
C1-VL2	8.8								
C1-VL3	8.3								
C2-V3	7.2	19	0.001						
C2-V6	6.7		0.002						
C2-V1	7.1		2						
C2-V5	7.4								
C1-VL4	8.5								
C2-VL1	8.4								
C2-V2	8.0	0	0.003						

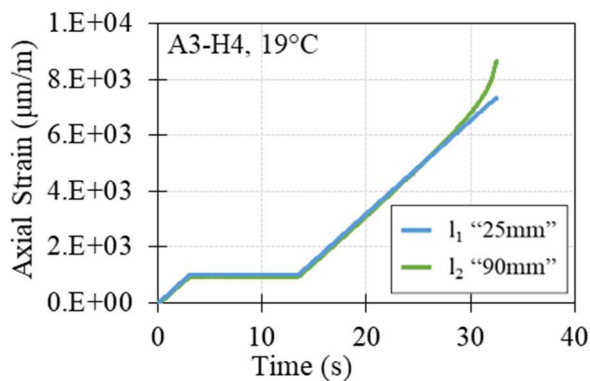
C2-V7				7.0		0.001			
D2-H3	Horizontal	Emulsion bitumen 160/220 and GG 50kN/m		7.2	40	2			
D3-H11				7.1					
D2-H4				6.8	19	0.005			
D3-H12				7.4		0.003			
D1-H1				8.8		2			
D2-H5				8.2					
D1-H3				7.3	0	0.001			
D2-H6				7.0		0.001			
D2-V1				Vertical			6.0	40	2
D2-V10							7.4		
D2-V4	6.4	19	0.002						
D2-V7	6.1		0.004						
D2-V3	6.9		2						
D2-V8	6.9								
D2-V5	5.8	0	0.001						
D2-V9	6.7		0.001						
E1-H3	Horizontal	Emulsion bitumen 160/220 with SBS and GG 100kN/m					7.4	40	2
E3-H3							6.9		
E2-H2				5.8	19	0.004			
E3-H2				6.8		0.003			
E1-H2				6.4		2			
E2-H3				7.8					
E2-H4				6.5	0	0.003			
E2-H5				6.9		0.001			
E2-V3				Vertical			6.8	40	2
E2-V8							7.3		
E2-V6	5.8	19	0.003						
E2-V9	6.7		0.005						
E2-V4	6.8		2						
E2-V5	6.7								
E2-V7	5.8	0	0.001						
E2-V10	5.6		0.001						

GG 100kN: Geogrid Notex Glass<sup>®</sup> C 100/100-25; and GG 50kN: Geogrid Notex Glass<sup>®</sup> C 50/50-25

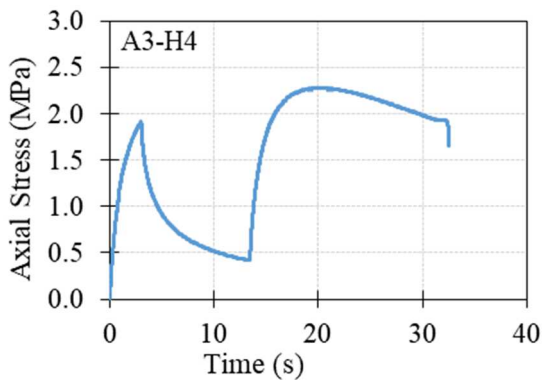
## 5.5. Bituminous mixtures and interfaces results

### 5.5.1. Example of result of specimens without interface: A3-H4, 19°C, 2%/min

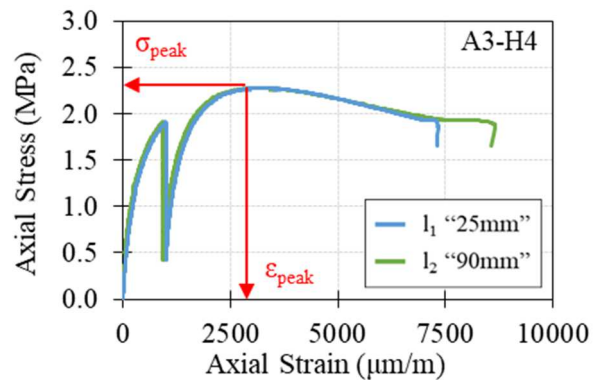
Figure 5-4(a) presents the axial strain loading concerning the two couples of extensometers used on specimen A3-H3 at 19°C and 2%/min, as an example of a tension test result. It is noticeable that the strain measured by the extensometer  $l_2$  is very similar to the couple used to control the test ( $l_1$ ). A variation between the values was observed at the end of the test, due to the failure. Figure 5-4(b) presents the axial stress measured during loading in function of testing time. Finally, Figure 5-4(c) presents the classical plot axial stress vs axial strain for the measurements of extensometers  $l_1$  and  $l_2$ .



(a)



(b)



(c)



Figure 5-4. Example of tension test result of specimen A3-H4: (a) axial strain vs testing time for  $l_1$  “25mm” (controlling) and  $l_2$  “90mm” (measuring), (b) axial stress vs testing time, and (c) classical stress-strain curve for  $l_1$  “25mm” (controlling) and  $l_2$  “90mm” (measuring).

From Figure 5-4(c), is noticeable that the two couples present again very similar curves, indicating that the strain is homogeneous throughout the specimen during the loading. Thus, the axial strain considered is the average of the four measurements obtained from each extensometer. Thus, the use of the individual measurements of each couple of extensometer is limited to the analysis of specimens type V containing interface. Moreover, is observed in the mentioned plot that it presents a peak point, which characterizes the maximum stress supported by the material ( $\sigma_{peak}$ ) and the strain level associated with this stress ( $\epsilon_{peak}$ ). These peak values will be later used in the maximum strength characterization of the tested configurations

### ***5.5.2. Example of result obtained from specimens having interface***

In this section, only an example of specimen type V is presented, since the result for specimen type H are similar to those explained for configuration A in the last section. Then, this section is divided into results of bituminous mixture and interface, concerning type V specimen.

#### *5.5.2.1. Specimen type V: C2-V5, 19°C, 2%/min (Bituminous Mixture)*

C2-V5 tested at 19°C and 2%/min was used as an example of specimen type V having interface. Figure 5-5(a) presents the strain measured by the two couple of extensometers ( $l_1$  and  $l_2$ ) plotted with the strain in the bituminous mixture only ( $\epsilon_A$ ) obtained using the procedure described in Section 5.3.3. Figure 5-5(b) presents the stress response to the strain loading and Figure 5-5(c) presents the stress vs strain graphic for  $l_1$ ,  $l_2$  and  $\epsilon_A$ .

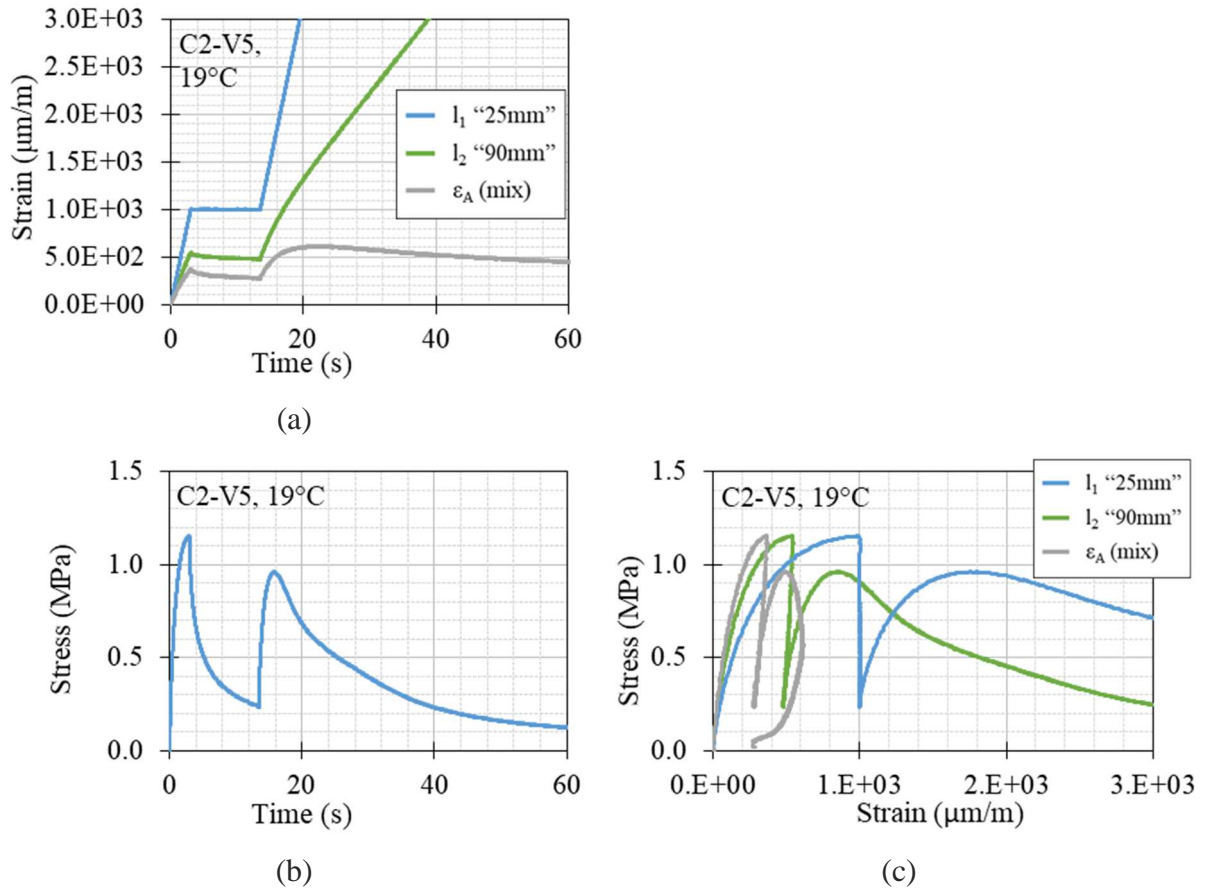


Figure 5-5. Example of tension test result of specimen C2-V5: (a) axial strain vs testing time for  $l_1$  "25mm",  $l_2$  "90mm", and bituminous mixture only ( $\epsilon_A$ ), (b) axial stress vs testing time, and (c) classical stress-strain curve for  $l_1$  "25mm",  $l_2$  "90mm", and bituminous mixture only ( $\epsilon_A$ ).

From Figure 5-5(a) and (c), it can be observed that the strain in the bituminous mixture is very small when compared to the strain measured in the two couples of extensometers. It indicates that most of the strain on the specimen during testing is concentrated at the interface level. Then, the strain in the interface can be calculated from a randomly given thickness ( $t$ ) and it is fully discussed in the next section.

#### 5.5.2.2. Specimen type V: C2-V5, 19°C, 2%/min (Interface)

Similarly to the interface analysis of complex modulus test results, the same three thicknesses (1.0, 2.5 and 5.0mm) were chosen for the calculation represented in Eq. 5-4. Figure 5-6(a) presents the interface behavior of the three chosen thicknesses due to the tension loading. It can be noticed that the increase in the interface thickness yields a decrease in the interface strain ( $\epsilon_G$ ). The strain obtained for 1mm is approximately 4.6 times higher than the one obtained

for 5mm. The same trend was already observed in the complex modulus analysis of interfaces discussed in Section 4.6.2.1. Figure 5-6(b) presents the displacement gap ( $\Delta u$ ) observed at the interface for the aforementioned specimen. The parameter  $\Delta u$  is preferable to be used for the comparison between different specimens since it is independent of an arbitrary interface thickness.

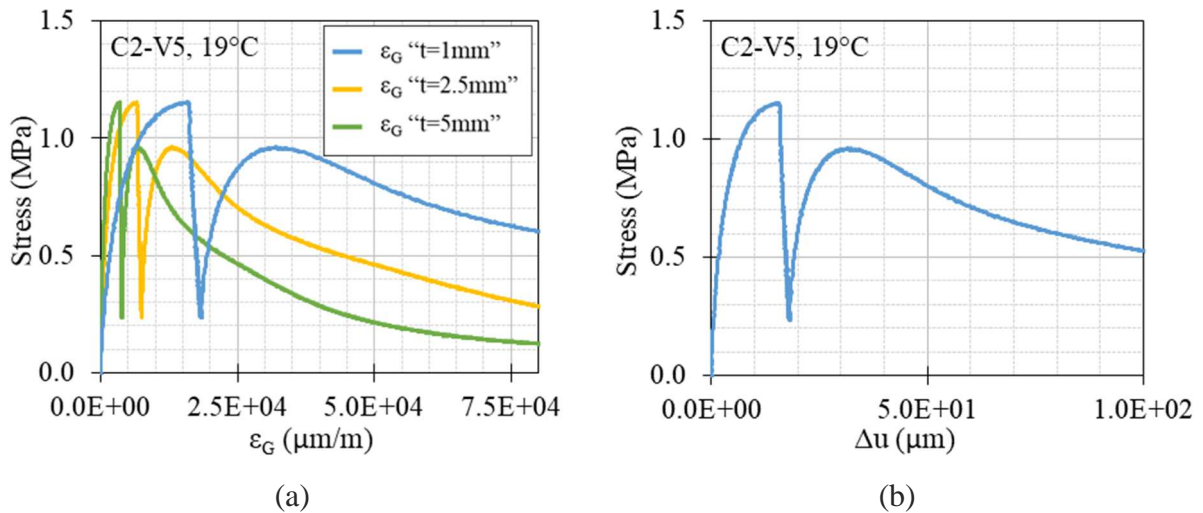


Figure 5-6. Interface strain behavior to tension loading for specimen C2-V5: (a) Stress vs interface strain graphic for the three chosen thicknesses: 1.0, 2.5 and 5.0mm, and (b) Stress vs interface gap ( $\Delta u$ )

Figure 5-7 presents the relationship between  $\epsilon_A$  and the three  $\epsilon_G$  evolution during the tension test, for each chosen thickness (1, 2.5 and 5mm) in logarithmic axis. From the graphic, it can be observed that  $\epsilon_G$  is approximately 20 times higher than  $\epsilon_A$  at the beginning of the test, considering 1mm thickness curve. For 5mm thickness curve, it is approximately 5 times higher. At the peak of  $\epsilon_A$ , the ratio ranges from 1393 (5mm curve) to 6731 (1mm curve).

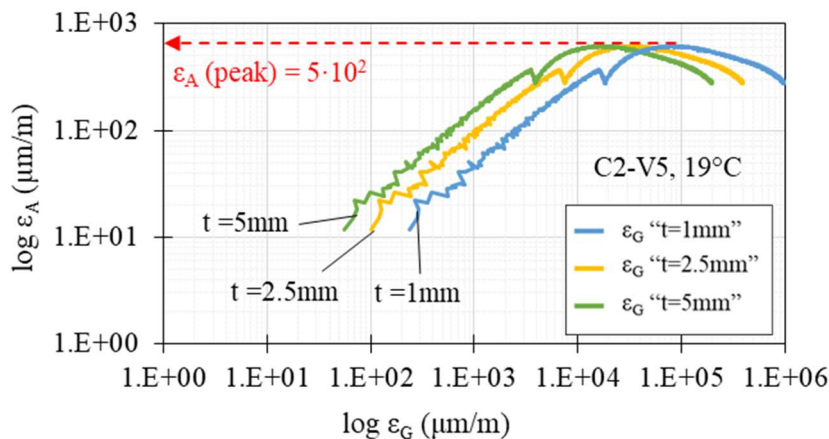


Figure 5-7. Relationship between  $\varepsilon_A$  (bituminous mixture) and the  $\varepsilon_G$  (interface) evolution during the tension test, concerning the three chosen thickness (1, 2.5 and 5mm)

During the first tension step on the test, a linear behavior was observed in the graphic plotted in log scale. At this moment, both strains increase linearly along with the loading. During the creep step,  $\varepsilon_A$  decreases and  $\varepsilon_G$  increases as compensation to maintain still the global strain of the specimen. Finally, in the last tension step on the test, a peak of  $\varepsilon_A$  was observed. This point represents the moment when the bituminous mixture ceased supporting the load, which was fully concentrated in the interface level, from this point. This loading concentration in the interface results in the total interface deterioration, debonding the two layers of bituminous mixtures apart. This failure was observed in all the type V specimens containing interfaces.

## 5.6. Verification of specimen's diameter size effect for specimens type V

In this section, results obtained from four specimens type V with a larger diameter (136mm) are compared with the result obtained from four specimens type V with classical diameter size (75mm) tested in the same conditions. The geogrid in the specimens of 136mm diameter contains 5 yarns on each direction, whereas the one in the specimens of 75mm diameter contains 3 yarns. Two tests were carried out at 40°C and 2%/min strain rate and two tests were carried out at 19°C and 2%/min strain rate. The results are divided into two: bituminous mixture and interface. Figure 5-8 presents the results obtained for the tests carried out at 40°C and 2%/min strain rate, concerning: (a) bituminous mixture,  $\varepsilon_A$ , and (b) interface,  $\Delta u$ .

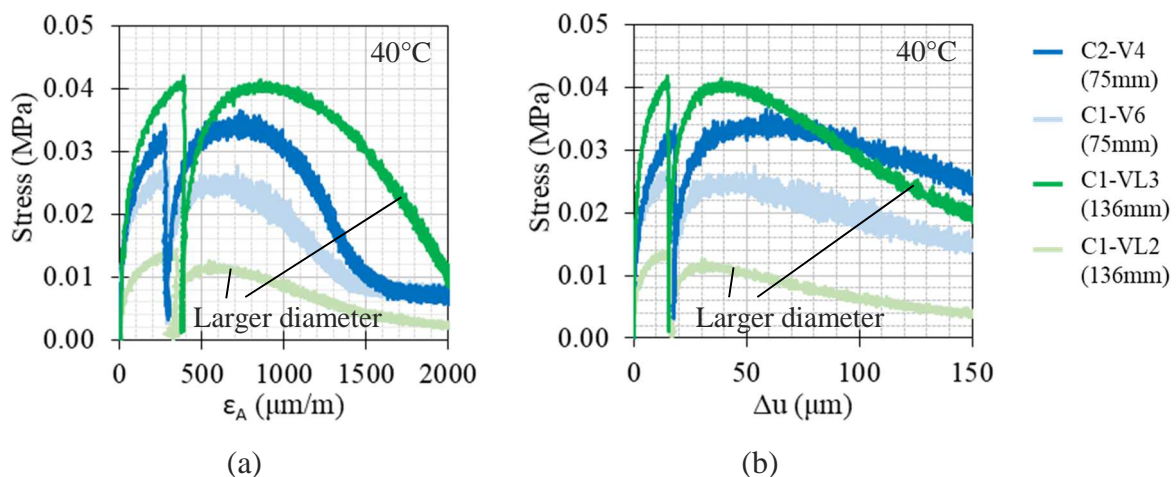


Figure 5-8. Tension test carried out at 40°C and 2%/min in specimens type V with two different diameters (75 and 136mm): (a) stress vs  $\epsilon_A$ , and (b) stress vs  $\Delta u$ .

From the graphics presented in Figure 5-8, for both  $\epsilon_A$  and  $\Delta u$ , the same sequence of results was observed. Specimens with larger diameter presented higher variation when compared with the specimens with classical diameter, for this testing temperature. The result indicates that the variation is mainly due to the quality of the interface bond and smaller differences encountered in the specimens interface. It is impossible to have two specimens with identical interfaces since they were cored from different slab positions, which could slightly differ the amount of emulsion and geogrid on it. Moreover, at 40°C, minimal variation in the interface composition could lead to high dispersion in the test results. Thus, for these testing conditions, the diameter size did not influence specimen performance. Figure 5-9 presents the results obtained for the tests carried out at 19°C and 2%/min strain rate, concerning: (a) bituminous mixture, denoted by  $\epsilon_A$ , and (b) interface, denoted by interface gap  $\Delta u$ .

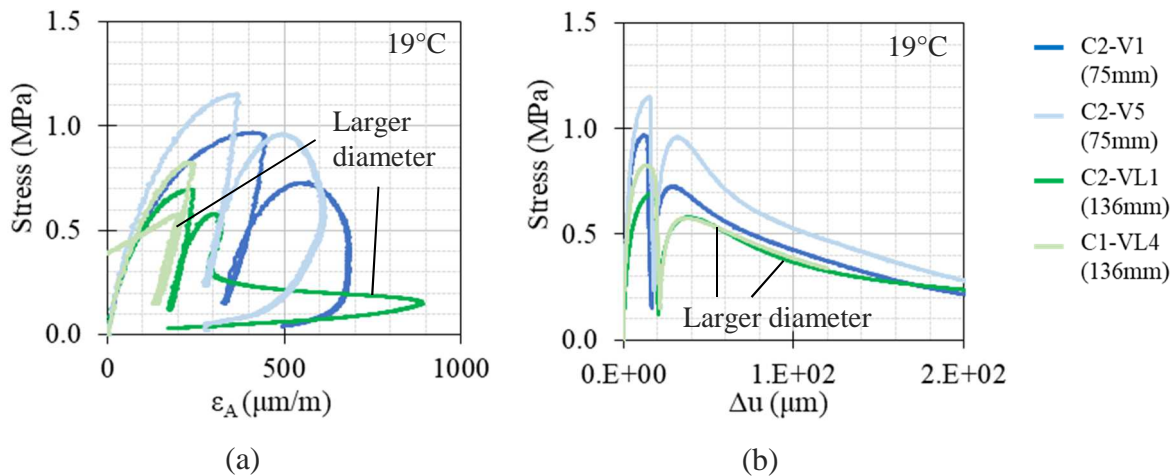


Figure 5-9. Tension test carried out at 19°C and 2%/min in specimens type V with two different diameters (75 and 136mm): (a) stress vs  $\epsilon_A$ , and (b) stress vs  $\Delta u$ .

From Figure 5-9, it can be observed that the results presented less variation when compared to the results obtained at 40°C, especially at the beginning of the test, where the curves overlap. Specimens with classical diameter needed more strain to reach failure in the interface and pre-

sented higher resistance to the loading. As well as the results obtained at 40°C, the ones obtained at 19°C were highly influenced by the quality of interface bond and smaller differences encountered in the specimens interface.

## 5.7. Verification of time-Temperature superposition principle

### 5.7.1. Frequency sweep test results

In order to verify the TTSP in the non-linear and plastic domain of behavior of bituminous mixture, the pairs of temperature and strain rate of loading are obtained using the  $a_T$  from LVE properties of the material. Classically, the WLF model (cf. Eq. 2-8) is used after the calibration of the coefficients  $C_1$  and  $C_2$  (already done in the last chapter). From the complex modulus tests, the same coefficients  $C_1$  and  $C_2$  were obtained for all different configurations disregarding to the coring direction as presented in Section 4.6. Thus,  $a_T$  calculated using WLF equation and the corresponding slow strain rate ( $\dot{\epsilon}_{slow}$ ) are presented in Table 5-2.

Table 5-2. Slow strain rate ( $\dot{\epsilon}_{slow}$ ) calculated using  $a_T$  calculated from WLF model from LVE properties

$T_{ref}$ (°C)	$T$ (°C)	$a_T$	$\dot{\epsilon}_{slow}$ (%/min)
40	19	509	0.004
19	0	1015	0.002

However, for the work presented in this section, a different method was conducted, which resulted in  $a_T$  slightly different from those presented in Table 5-2, and particular for each specimen tested at slow strain rate. Before every tension test, a frequency sweep test was performed to collect the LVE information at the exact temperature from the sample would be tested next. Thus, the frequency sweep test result was plotted along with the 2S2P1D model curve obtained from the coefficients calibration performed in the last chapter, and the data was shifted to fit one another. The  $a_T$  was obtained for each specimen and the slow strain rate was calculated in function of this value. Figure 5-10 presents the frequency sweep test results fitted over the 2S2P1D model curve for specimens from configuration A (no interface), for both coring directions, V and H. Figure 5-10(a) presents the shifted data obtained at 19°C to fit the 2S2P1D

curve at  $T_{ref}$  of 40°C. Figure 5-10(b) presents the shifted data obtained at 0°C to fit the 2S2P1D curve at  $T_{ref}$  of 19°C. Figure 5-11 presents the same couple of graphics but concerning specimens from configuration B (interface containing only emulsion bitumen). Figure 5-12 for specimens from configuration C (geogrid 100kN/m with emulsion bitumen). Figure 5-13 for specimens from configuration D (geogrid 50kN/m with emulsion bitumen). Figure 5-14 for specimens from configuration E (geogrid 100kN/m with emulsion bitumen modified by SMS). Concerning the specimens type V containing interface, the complex modulus of bituminous mixture ( $E_A^*$ , c.f. Section 5.3.3) was used for the shifting. Table 5-3 presents the  $a_T$  obtained from frequency sweep tests and the slow strain rate calculated from those  $a_T$  and used in the tension tests.

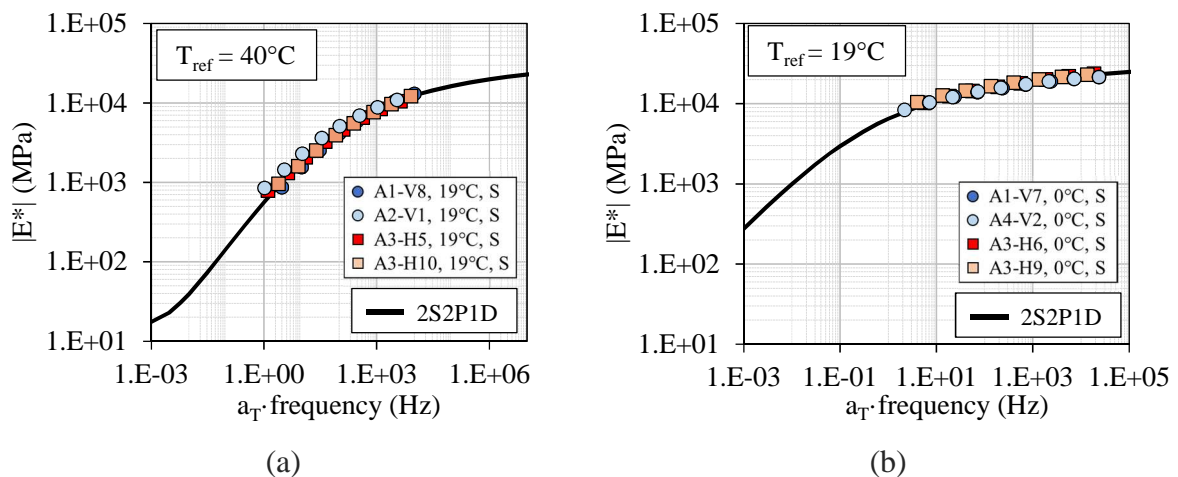


Figure 5-10. Frequency sweep test shifted curves for configuration A (no interface): (a) test results at 19°C shifted to fit the 2S2P1D curve at  $T_{ref}=40^{\circ}\text{C}$ , and (b) test results at 0°C shifted to fit the 2S2P1D curve at  $T_{ref}=19^{\circ}\text{C}$



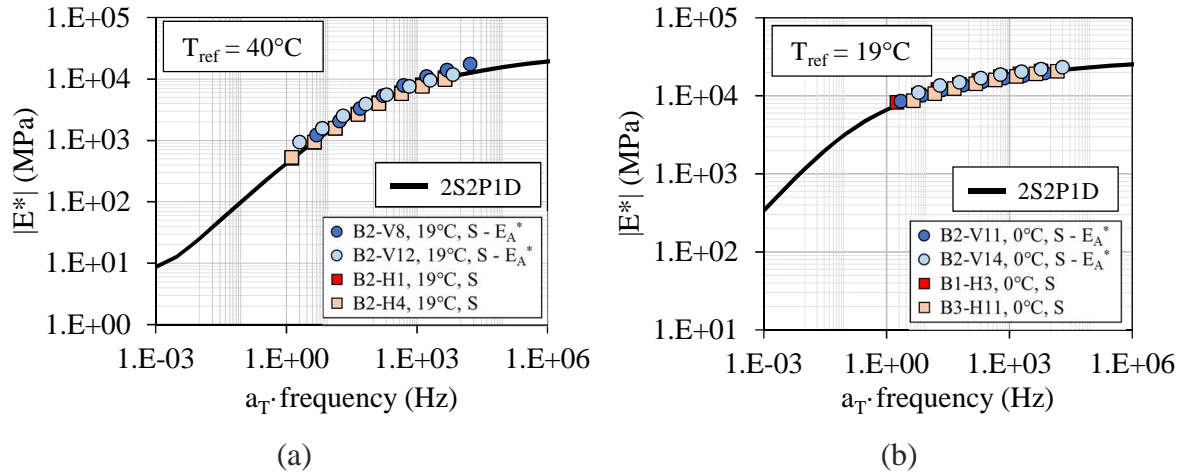


Figure 5-11. Frequency sweep test shifted curves for configuration B (interface containing only emulsion bitumen): (a) test results at 19°C shifted to fit the 2S2P1D curve at  $T_{ref} = 40^\circ\text{C}$ , and (b) test results at 0°C shifted to fit the 2S2P1D curve at  $T_{ref} = 19^\circ\text{C}$

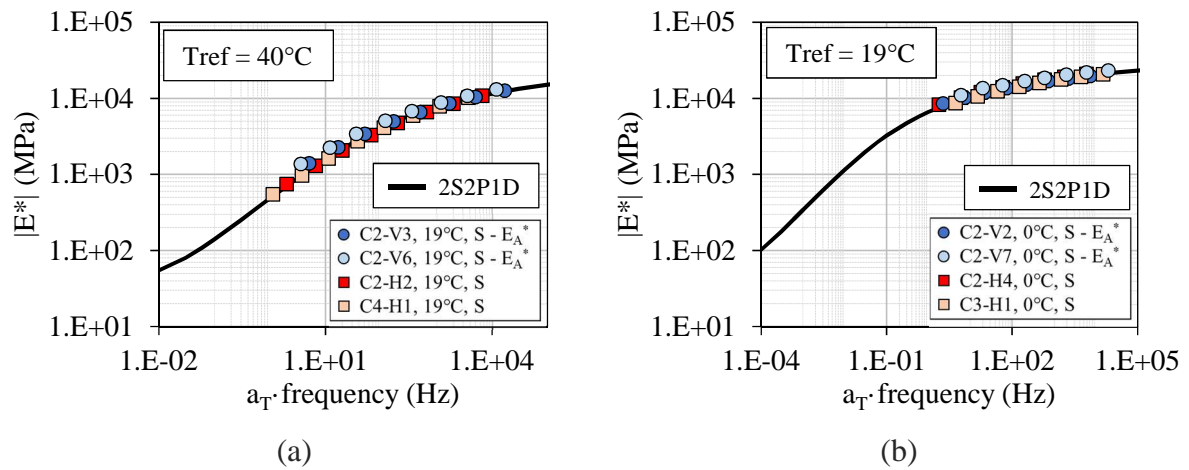


Figure 5-12. Frequency sweep test shifted curves for configuration C (geogrid 100kN/m with emulsion bitumen): (a) test results at 19°C shifted to fit the 2S2P1D curve at  $T_{ref} = 40^\circ\text{C}$ , and (b) test results at 0°C shifted to fit the 2S2P1D curve at  $T_{ref} = 19^\circ\text{C}$



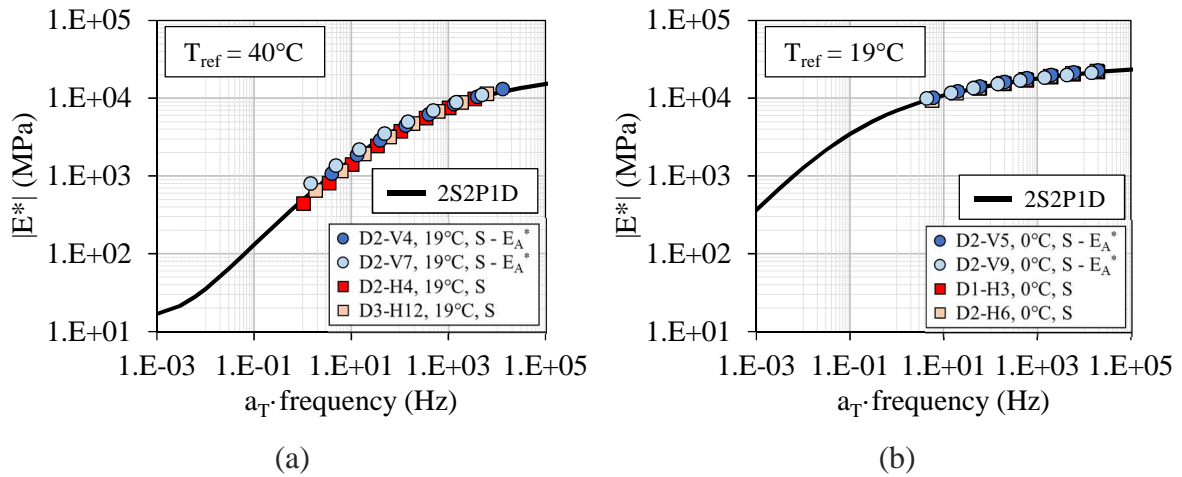


Figure 5-13. Frequency sweep test shifted curves for configuration D (geogrid 50kN/m with emulsion bitumen): (a) test results at 19°C shifted to fit the 2S2P1D curve at  $T_{ref}=40^{\circ}\text{C}$ , and (b) test results at 0°C shifted to fit the 2S2P1D curve at  $T_{ref}=19^{\circ}\text{C}$

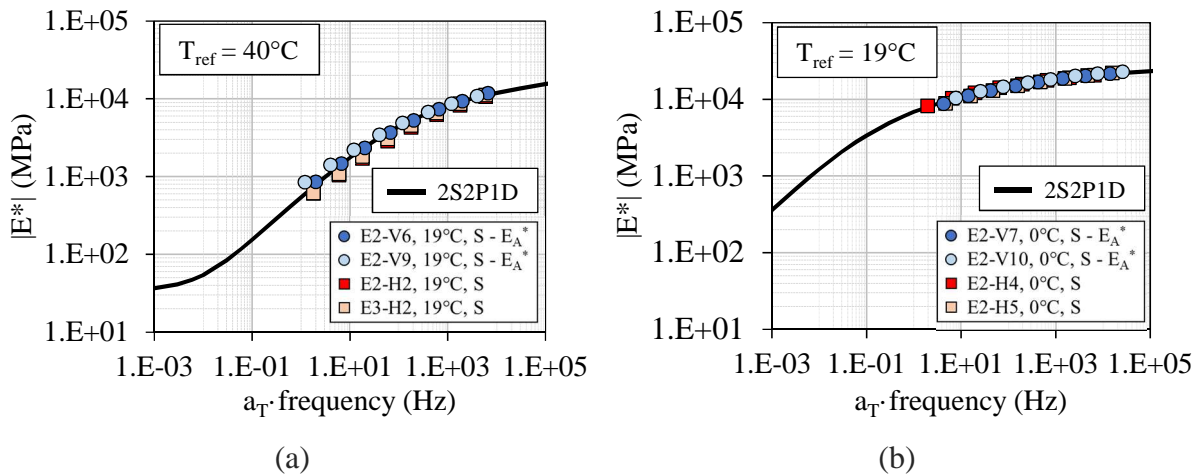


Figure 5-14. Frequency sweep test shifted curves for configuration E (geogrid 50kN/m with emulsion bitumen modified by SBS): (a) test results at 19°C shifted to fit the 2S2P1D curve at  $T_{ref}=40^{\circ}\text{C}$ , and (b) test results at 0°C shifted to fit the 2S2P1D curve at  $T_{ref}=19^{\circ}\text{C}$

Table 5-3. Slow strain rate ( $\dot{\epsilon}_{slow}$ ) calculated using  $a_T$  obtained from frequency sweep tests and used for the tension tests

Specimen	Coring direction	T(°C)	T <sub>ref</sub> (°C)	$a_T$	$\dot{\epsilon}_{slow}$ (%/min)
A3-H5	Horizontal	19	40	450	0.005
A3-H10				900	0.002
A3-H6		0	19	1900	0.001
A3-H9				1300	0.002

TENSION TEST CAMPAIGN

A1-V8	Vertical	19	40	1000	0.002
A2-V1				350	0.006
A1-V7		0	19	2300	0.001
A4-V2				725	0.003
B2-H1	Horizontal	19	40	400	0.005
B2-H4				450	0.004
B1-H3		0	19	1000	0.002
B3-H11				1500	0.001
B2-V8	Vertical	19	40	1700	0.001
B2-V12				700	0.003
B2-V11		0	19	1000	0.002
B2-V14				2000	0.001
C2-H2	Horizontal	19	40	700	0.003
C4-H1				400	0.005
C2-H4		0	19	600	0.003
C3-H2				1500	0.001
C2-V3	Vertical	19	40	1700	0.001
C2-V6				1200	0.002
C2-V2		0	19	740	0.003
C2-V7				2000	0.001
D2-H4	Horizontal	19	40	350	0.005
D3-H12				625	0.003
D1-H3		0	19	2000	0.001
D2-H6				1900	0.001
D2-V4	Vertical	19	40	1300	0.002
D2-V7				500	0.004
D2-V5		0	19	2000	0.001
D2-V9				2000	0.001
E2-H2	Horizontal	19	40	500	0.004
E3-H2				600	0.003
E2-H4		0	19	650	0.003
E2-H5				1600	0.001
E2-V6		19	40	650	0.003

E2-V9	Vertical	0	19	400	0.005
E2-V7				1600	0.001
E2-V10				2000	0.001

### 5.7.2. Specimens type H

Figure 5-15(a) presents the stress vs strain graphic concerning configuration A (no interface), type H, pair 40°C with fast strain rate and 19°C with slow strain rate. Figure 5-15(b) presents the strain vs equivalent time ( $t/a_T$ ) plot (test loading input), using  $a_T$  obtained from the WLF model for  $T_{ref}$  of 40°C, previously presented in Table 5-2. This last graphic when plotted in function of equivalent time using  $a_T$  obtained from frequency sweep test results, discussed in the last section, results in an overlap of the four curves. Thus, it is possible to observe the differences between the strain rate loading caused by the change in the  $a_T$  used in this work, allowing a better interpretation of test results. It is noticed in Figure 5-15(a), from the beginning of the test until the creep step, the results were almost overlapped, which can be used to validate the TTSP for this configuration and testing condition. After the creep, the curves separated and took different behaviors, especially after  $10^4 \mu\text{m/m}$ . However, after this strain level, the strain homogeneity throughout the specimen was not assured and local effects were no more negligible.

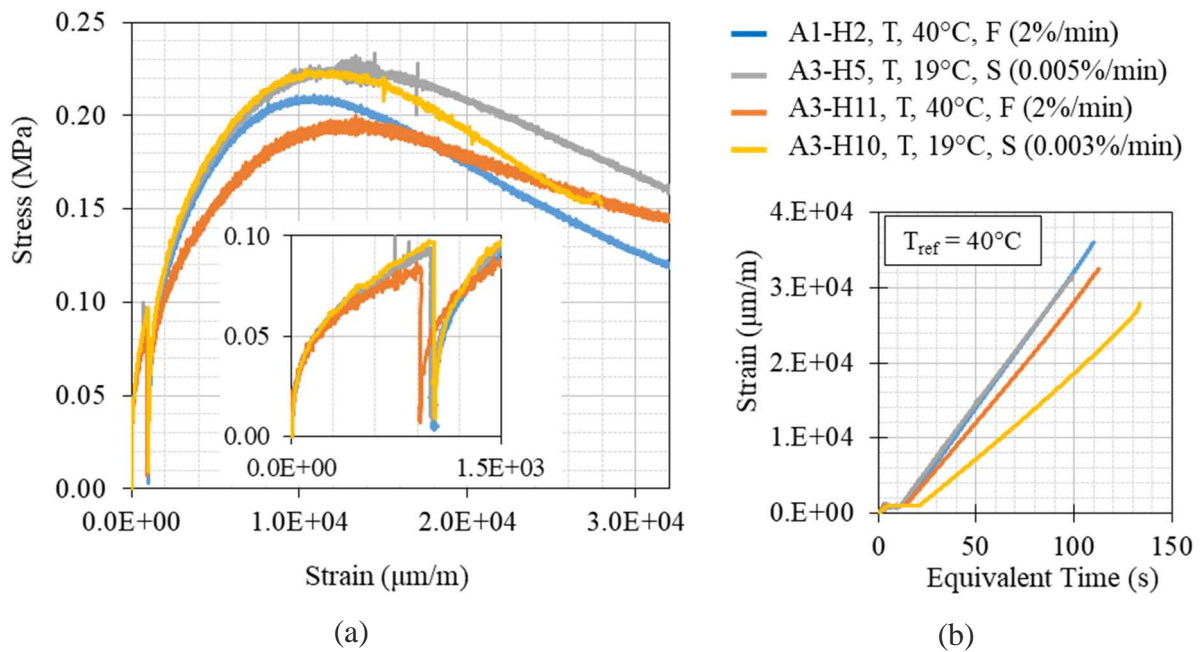


Figure 5-15. Tension test results concerning configuration A, type H, pair 40°C with fast strain rate and 19°C with slow strain rate: (a) stress vs strain, and (b) strain vs equivalent time (test loading input)

Figure 5-16 Figure 5-15 presents the same set of graphic as previously presented, configuration A (no interface), type H specimens, but concerning the pair 19°C with fast strain rate and 0°C with slow strain rate, at this time. The results tested at 19°C and 2%/min along with the specimen A3-H9 tested at 0°C and 0.002%/min presented similar curves. However, the A3-H6 tested at 0°C and 0.001%/min presented a curve slightly below the other curves, which do not invalidate the TTSP for this pair of testing conditions. Moreover, Figure 5-16(b) indicates that the strain input chosen is slower (lower strain rate) than it should be in order to obtain overlapped stress vs strain curves. An increase in the strain rate loading for the mentioned test result would increase the stiffness of the specimen yielding a climbing in the stress vs strain curves. This indicates that  $a_T$  definition aiming at validating the TTSP for non-linear and plastic domains should be done based on WLF modelling, same as performed by Di Benedetto et al. (2008), Nguyen et al. (2009), and Gayte (2016).

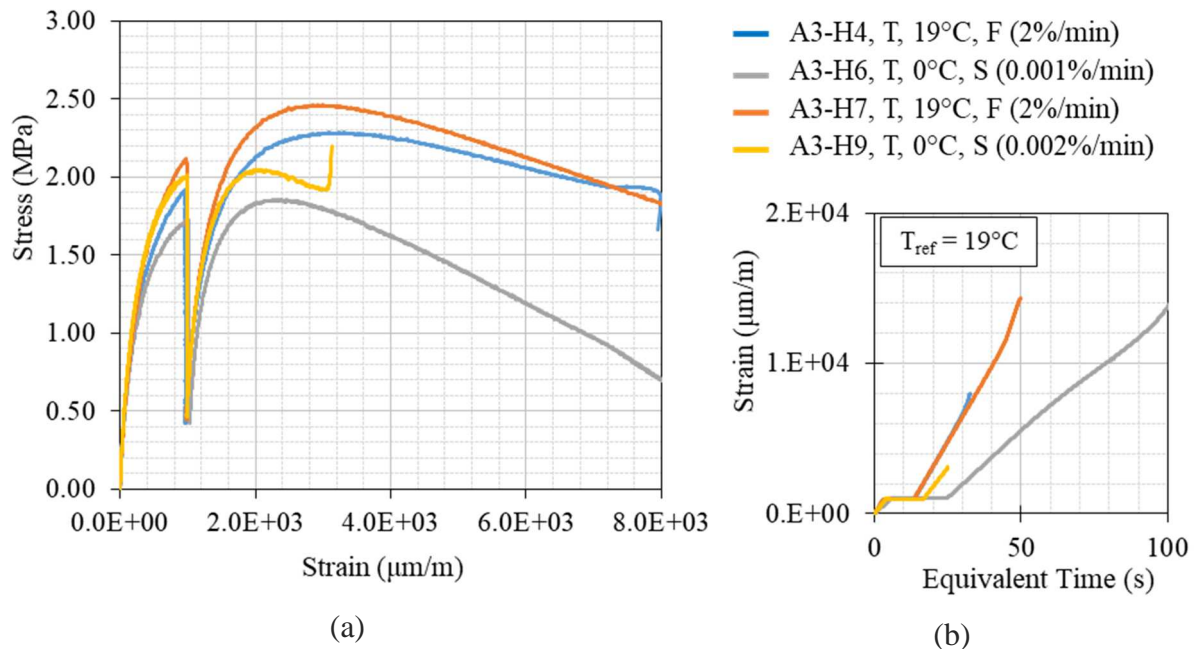


Figure 5-16. Tension test results concerning configuration A, type H, pair 19°C with fast strain rate and 0°C with slow strain rate: (a) stress vs strain, and (b) strain vs equivalent time (test loading input)

Figure 5-17(a) presents the stress vs strain results for configuration B (interface with only emulsion), type H specimens, pair 40°C with fast strain rate and 19°C with slow strain rate. Curves overlapped despite the presence of interface in the specimen, validating the TTSP for these testing conditions. Figure 5-17(b) evidences the difficulties in strain controlling during test. From the point that the specimen reaches an important value of strain (higher than  $10^4 \mu\text{m/m}$ ), the lack of loading homogeneity in the specimen is evidenced by the pair of extensometers  $l_2$  (90mm) on its measures. Furthermore, Figure 5-17(b) also explains the smaller resistance of B2-H2 observed in relation to the other curve results in Figure 5-17(a) since its strain rate was lower than it should be in order to present its stress vs strain curve closer to the others.

Figure 5-18(a) presents the stress vs strain results for configuration B, type H specimens, pair 19°C with fast strain rate and 0°C with slow strain rate. Regarding specimen B3-H11, its low stress level could be explained in Figure 5-18(b), caused by the low strain rate tested in the specimen. However, a premature failure occurred in specimen B1-H3, immediately after the creep step, and located in the top of the specimen near to the glued cap. The same problem was already reported in Gayte (2016) for tests at low temperatures. The condensation observed in the specimen tested at 0°C could have weakened the specimen, especially near to the top and bottom of it, which was also affected by the glue used to bond it onto the caps. However, the stress vs strain curves was tolerably close to validate the TTSP (c.f. Figure 5-18(a)).

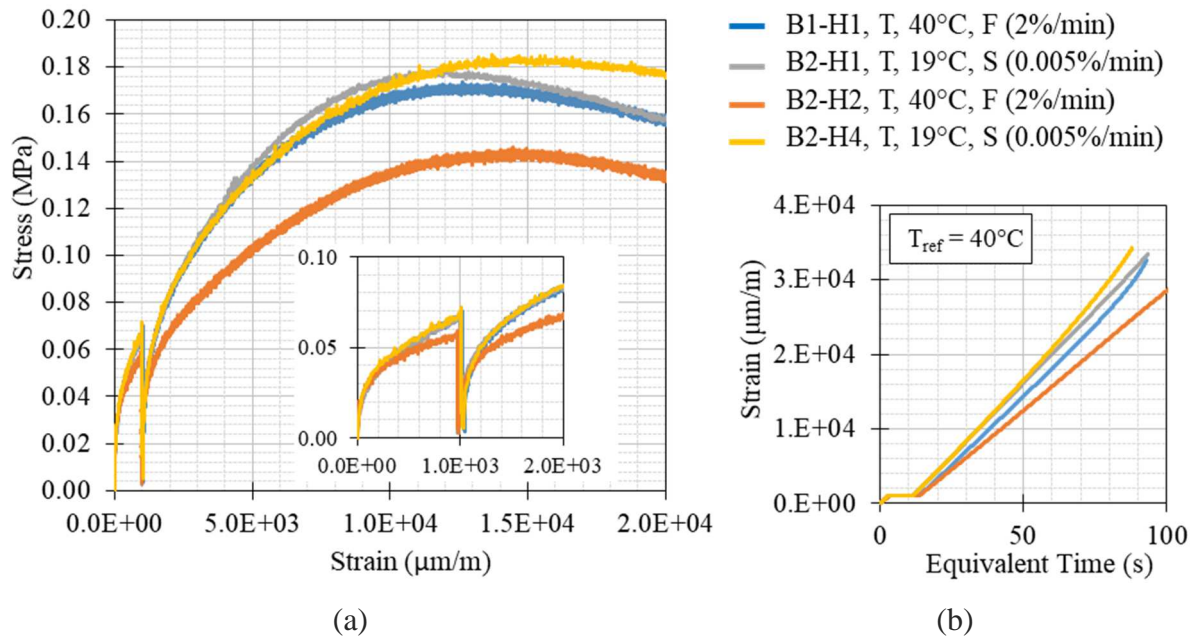


Figure 5-17. Tension test results concerning configuration B, type H, pair 40°C with fast strain rate and 19°C with slow strain rate: (a) stress vs strain, and (b) strain vs equivalent time (test loading input)

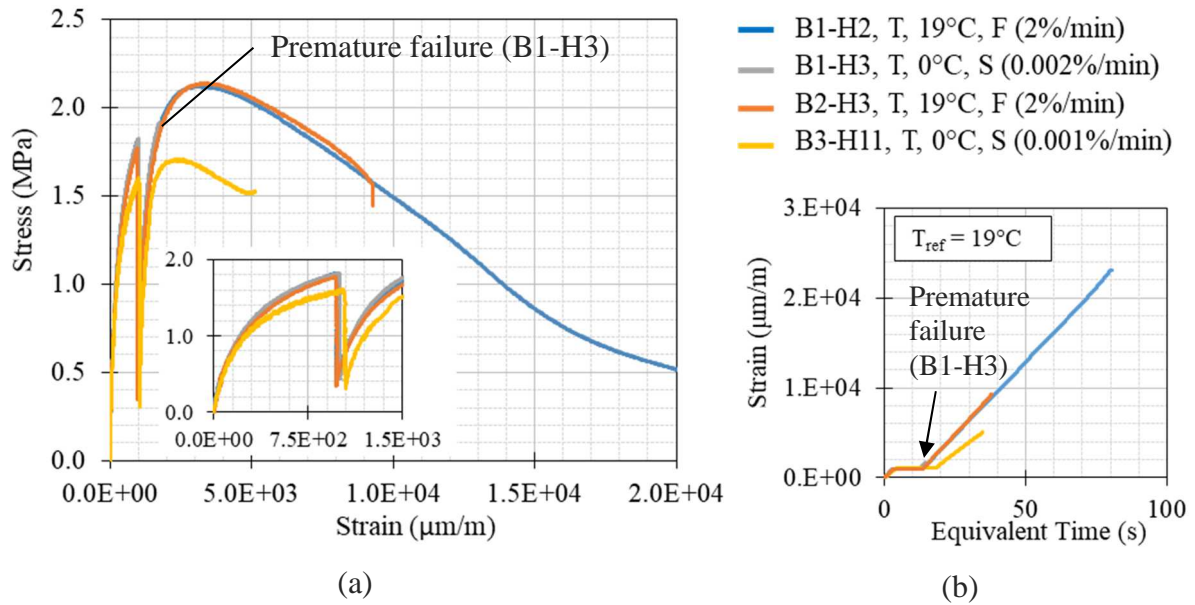


Figure 5-18. Tension test results concerning configuration B, type H, pair 19°C with fast strain rate and 0°C with slow strain rate: (a) stress vs strain, and (b) strain vs equivalent time (test loading input)

Figure 5-19(a) presents the stress vs strain results for the first reinforced configuration: C (geogrid 100kN/m and emulsion bitumen), type H specimens, pair 40°C with fast strain rate and 19°C with slow strain rate. Moreover, a line was plotted with the results representing the linear response in the characterization of the elastic behavior of the geogrid of 100kN/m, assuming it is the only element supporting the load during the test. The higher variation between the results was obtained due to the greater heterogeneity in the specimens, especially from strain level higher than  $0.5 \cdot 10^4 \mu\text{m/m}$ , which occurred in the final tension step from testing. This variation can be also noticed in Figure 5-19(b) due to the increase of local effects, from which distance the values measured in the pair of extensometers  $l_2$  (90mm) from those measured (controlled as test loading input) in the pair of extensometers  $l_1$  (25mm) during the test. However, despite the higher variation obtained in test results, the curves were tolerably close to validating the TTSP for this configuration and test conditions. Furthermore, the behavior of the curves in the first tension step, by presenting the same slope of geogrid linear relation could indicate a geogrid mobilization at the beginning of the test. However, after the creep step, the positioning of the curves below the geogrid line indicates that the geogrid is not mobilized after that point. Given the high temperature and low strain rate of loading, the bitumen present in the emulsion used to bond the geogrid in the interface could present high viscous properties, causing the



geogrid slippage phenomenon within the interface during the test. Thus, this test is not able to measure the geogrid contribution to the tension support in bituminous mixtures.

Figure 5-20 presents the set of graphics for the reinforced configuration C (geogrid 100kN/m and emulsion bitumen), type H specimens, pair 19°C with fast strain rate and 0°C with slow strain rate. Likewise the previous pair of testing conditions, a higher variation between curves was observed. However, the curves were tolerably close to validating the TTSP for this configuration and test conditions. In this case, comparing the geogrid line with the curves in Figure 5-20(a), there is a greater possibility of geogrid mobilization during the test. However, it does not have significant influence on the tensile strength due to the elevated stiffness of the bituminous mixture at these combinations of testing conditions.

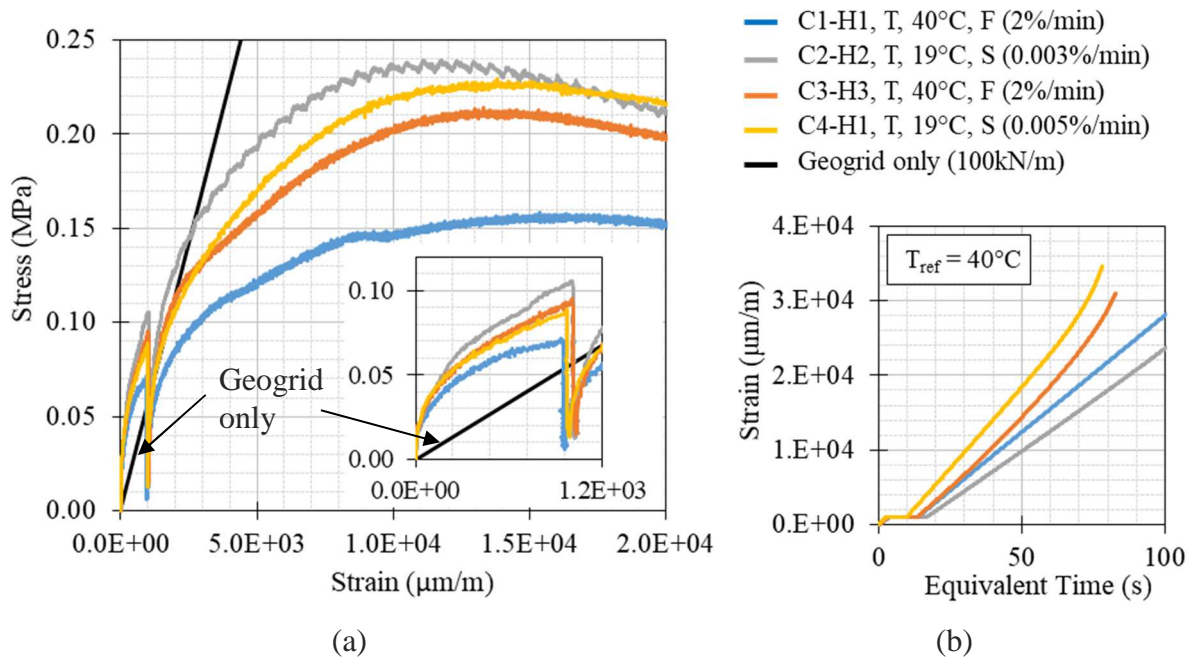


Figure 5-19. Tension test results concerning configuration C, type H, pair 40°C with fast strain rate and 19°C with slow strain rate: (a) stress vs strain, and (b) strain vs equivalent time (test loading input)

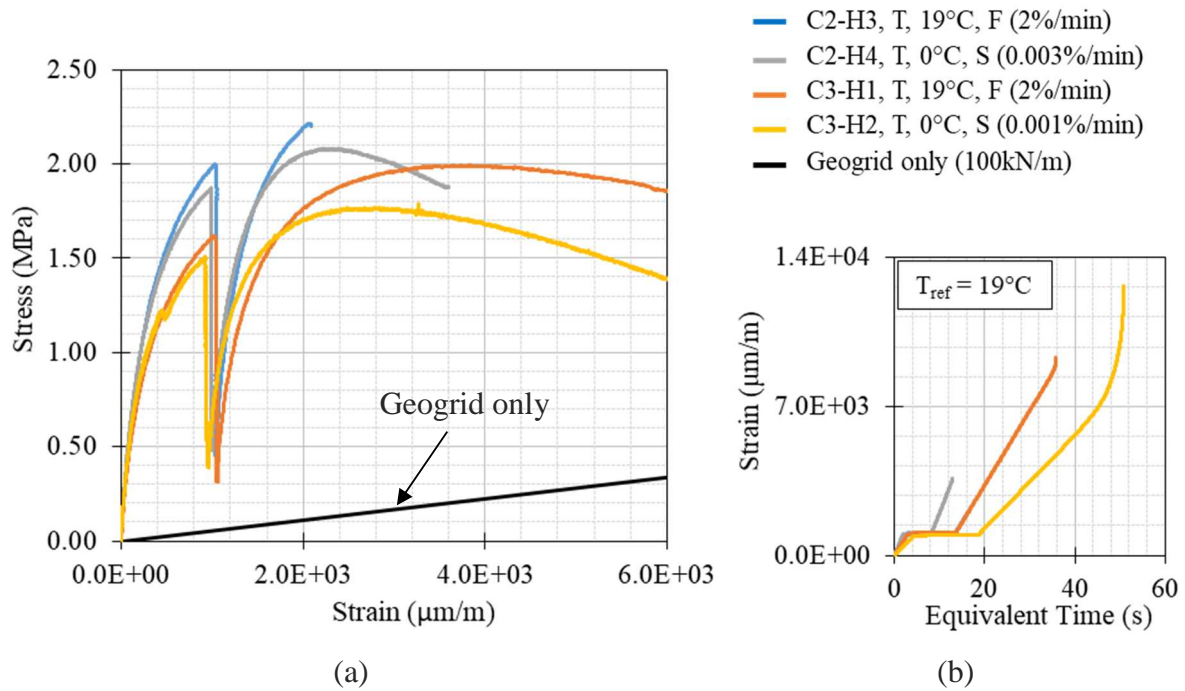


Figure 5-20. Tension test results concerning configuration C, type H, pair  $19^\circ\text{C}$  with fast strain rate and  $0^\circ\text{C}$  with slow strain rate: (a) stress vs strain, and (b) strain vs equivalent time (test loading input)

Figure 5-21 presents the set of graphics for the second reinforced configuration: D (geogrid 50kN/m and emulsion bitumen), type H specimens, pair  $40^\circ\text{C}$  with fast strain rate and  $19^\circ\text{C}$  with slow strain rate. The variation between curves observed is higher than the one obtained for configuration C at the same testing conditions. At  $10^3 \mu\text{m/m}$ , just before the creep step, the less stiff specimen (D2-H3) presented approximately 0.06MPa of stress, whereas the stiffest specimen (D3-H12) presented approximately 0.1MPa of stress (c.f. Figure 5-21(a)). However, the two specimens tested at the exact same conditions (D2-H3 and D3-H11, at  $40^\circ\text{C}$  and 2%/min) presented similar variation between curves. Thus, it is mostly related to the heterogeneity of the specimen rather than to the TTSP discordance. Furthermore, the same remark previously done about the difficulties to control the strain was again observed in Figure 5-21(b). Finally, the slope observed in the first tension step was again similar to the slope of the geogrid line, obtained for 50kN/m geogrid, which could be indicative of geogrid mobilization. However, as well as obtained for configuration C, in the third step of the test the curves were placed below the geogrid line, indicating a non-mobilization of the geogrid, possibly due to the slippage in the interface.

Figure 5-22 presents the set of graphics for the reinforced configuration D (geogrid 50kN/m and emulsion bitumen), type H specimens, pair  $19^\circ\text{C}$  with fast strain rate and  $0^\circ\text{C}$  with



slow strain rate. From Figure 5-22(a), a very low variation between the curves was observed, which validates the TTSP for this configuration and test conditions. However, the same problem of premature failure reported in specimen B1-H3 occurred in the two tests carried out at 0°C. Regarding the comparison between the geogrid line with the curves in Figure 5-22(a), even if the geogrid is fully mobilized during the test, the contribution of the geogrid in the loading support is negligible given the specimen stiffness at this test conditions.

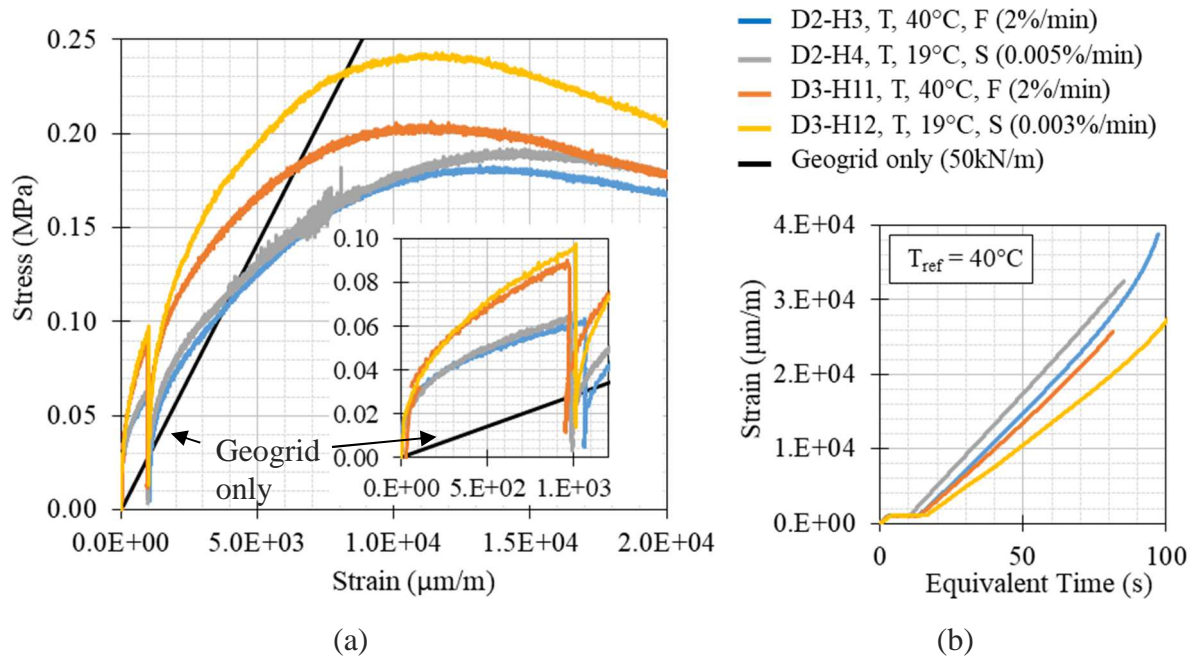


Figure 5-21. Tension test results concerning configuration D, type H, pair 40°C with fast strain rate and 19°C with slow strain rate: (a) stress vs strain, and (b) strain vs equivalent time (test loading input)

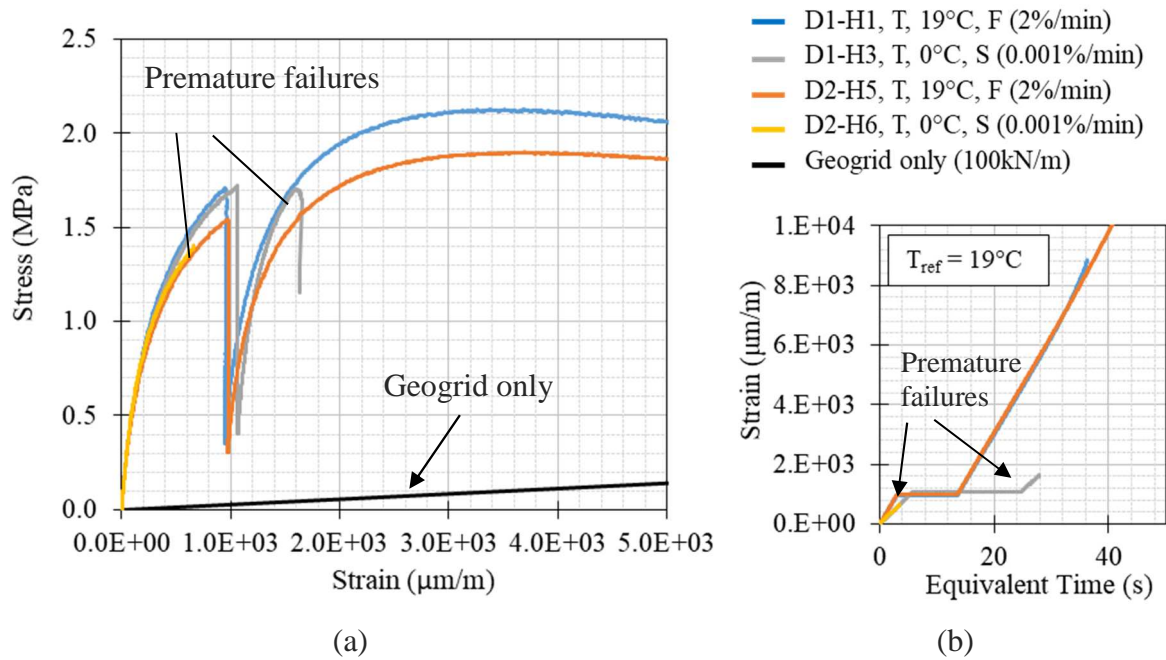


Figure 5-22. Tension test results concerning configuration D, type H, pair 19°C with fast strain rate and 0°C with slow strain rate: (a) stress vs strain, and (b) strain vs equivalent time (test loading input)

Lastly, Figure 5-23 presents the set of graphics for the reinforced configuration E (geogrid 100kN/m and emulsion modified by SMS), type H specimens, pair 40°C with fast strain rate and 19°C with slow strain rate. Afterward, Figure 5-24, which presents the set of graphics for the reinforced configuration E, type H specimens, pair 19°C with fast strain rate and 0°C with slow strain rate. In both test conditions, low variation between curves was observed, and the TTSP was validated. Moreover, the slope observed in the first tension step in Figure 5-23(a) was similar to the slope of the geogrid line and the curves were below the geogrid line after the creep step, same as configurations C and D. The same conclusions can be made as the mentioned configurations regarding the geogrid mobilization. Finally, one more time, the same conclusion can be made as the mentioned configurations regarding the negligible contribution of the geogrid in the loading support observed for tests 19°C with fast strain rate and 0°C with slow strain rate.

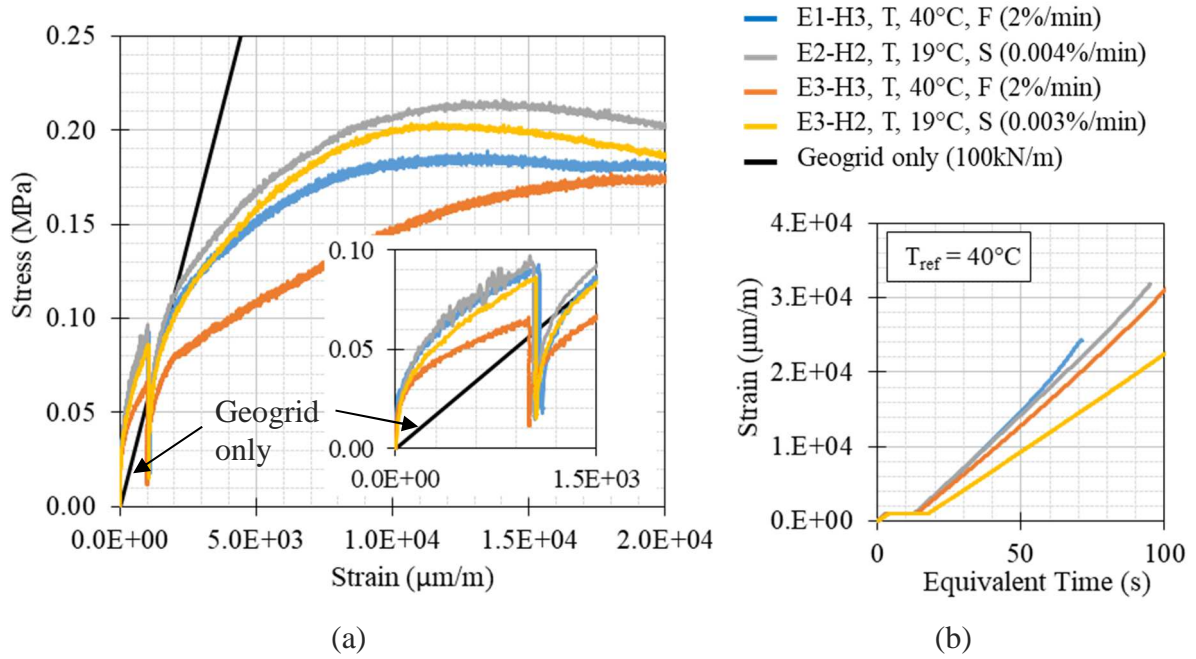


Figure 5-23. Tension test results concerning configuration E, type H, pair 40°C with fast strain rate and 19°C with slow strain rate: (a) stress vs strain, and (b) strain vs equivalent time at (test loading input)

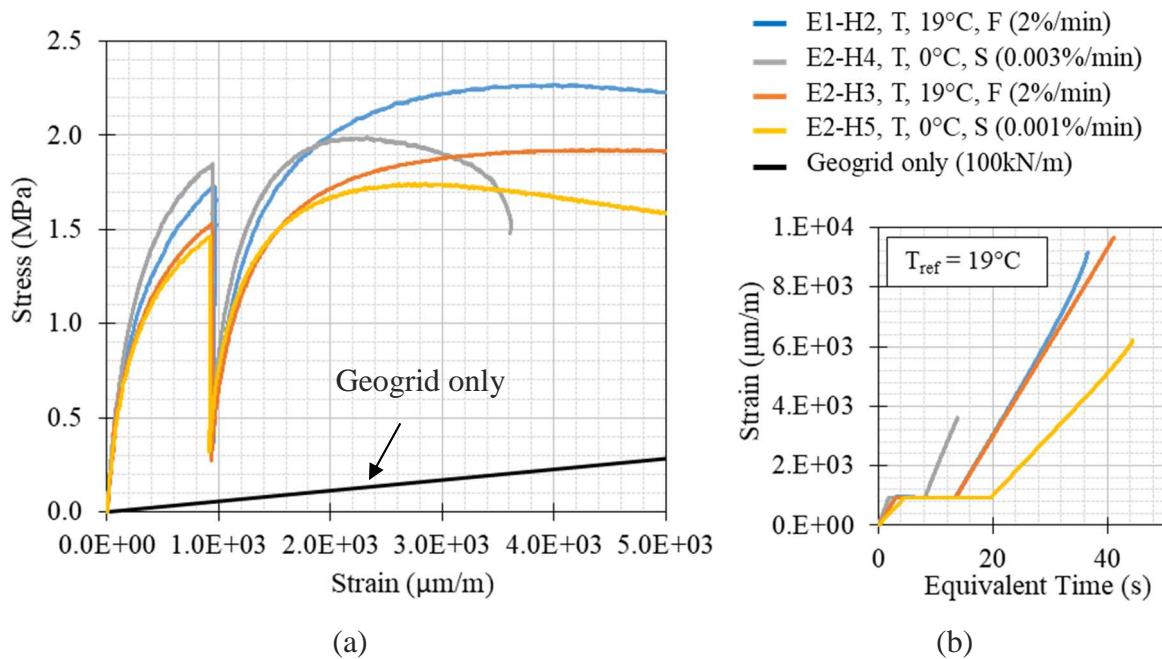


Figure 5-24. Tension test results concerning configuration E, type H, pair 19°C with fast strain rate and 0°C with slow strain rate: (a) stress vs strain, and (b) strain vs equivalent time (test loading input)

### 5.7.3. Specimens type V

In this section, the results obtained concerning specimens vertically cored V (perpendicularly cored in relation to the slab compaction direction) are presented. The results concerning specimens A are similar to those presented in last section since they are composed of only bituminous mixtures without interface. However, the results concerning the other four configurations are divided into two parts: bituminous mixtures ( $\epsilon_A$ ) and interface gap ( $\Delta u$ ).

Figure 5-25(a) presents the stress vs strain graphic concerning configuration A (no interface), type V, pair 40°C with fast strain rate and 19°C with slow strain rate. Figure 5-25(b) presents the strain in function of equivalent time ( $t/a_T$ ) using  $a_T$  from WLF model for  $T_{ref}$  of 40°C. For the type V specimen presented in this section, the equivalent time was obtained using  $a_T$  from WLF model, the same procedure as presented in last section. From Figure 5-25(a), a very important variation between curves was observed, especially after the creep step of the test. However, these specimens presented heterogeneous distributions of air voids in relation to the type H specimens. Those specimens present higher air voids in its top and bottom, in relation to the central part. This occurred because the slab has 150mm of height and the specimen has 140mm height, thus, only 5mm from top and bottom were sawn of each specimen. A minimum of 30mm distance away from the slab boundaries should be taken in order to avoid edges heterogeneity. However, it was physically impossible for type V specimens.

Figure 5-26 presents the same set of graphics of Figure 5-25, but for the pair 19°C with fast strain rate and 0°C with slow strain rate, and the equivalent time for  $T_{ref}$  of 19°C. A smaller variation was observed between curves, and the TTSP was validated for this configuration and testing conditions.

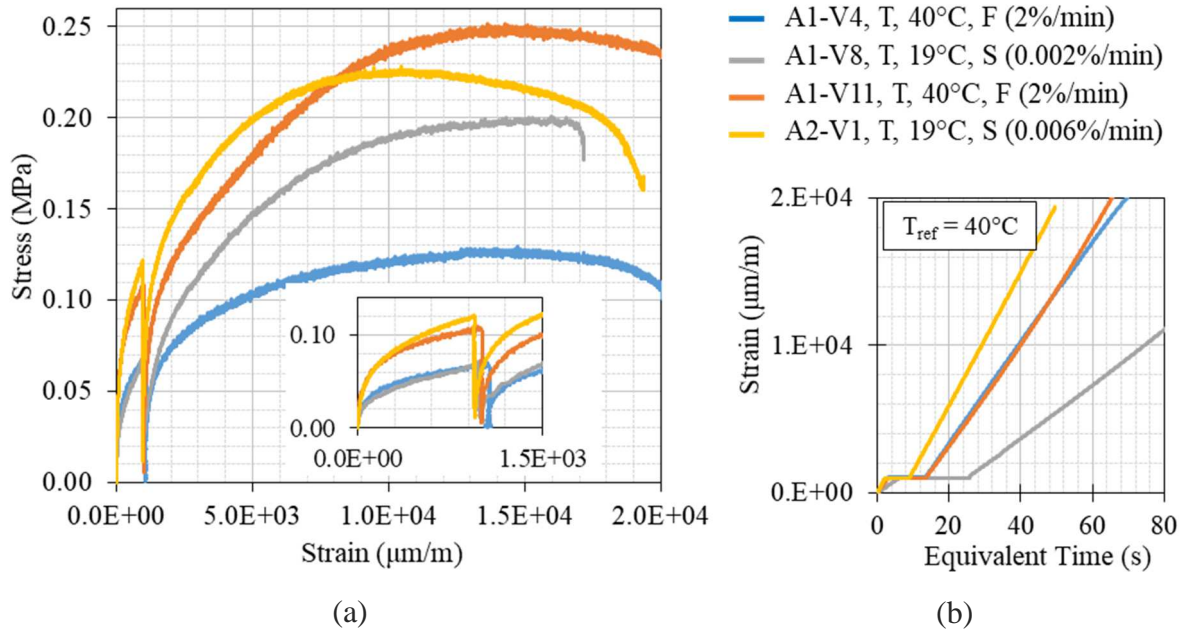


Figure 5-25. Tension test results concerning configuration A, type V, pair  $40^\circ\text{C}$  with fast strain rate and  $19^\circ\text{C}$  with slow strain rate: (a) stress vs strain, and (b) strain vs equivalent (test loading input)

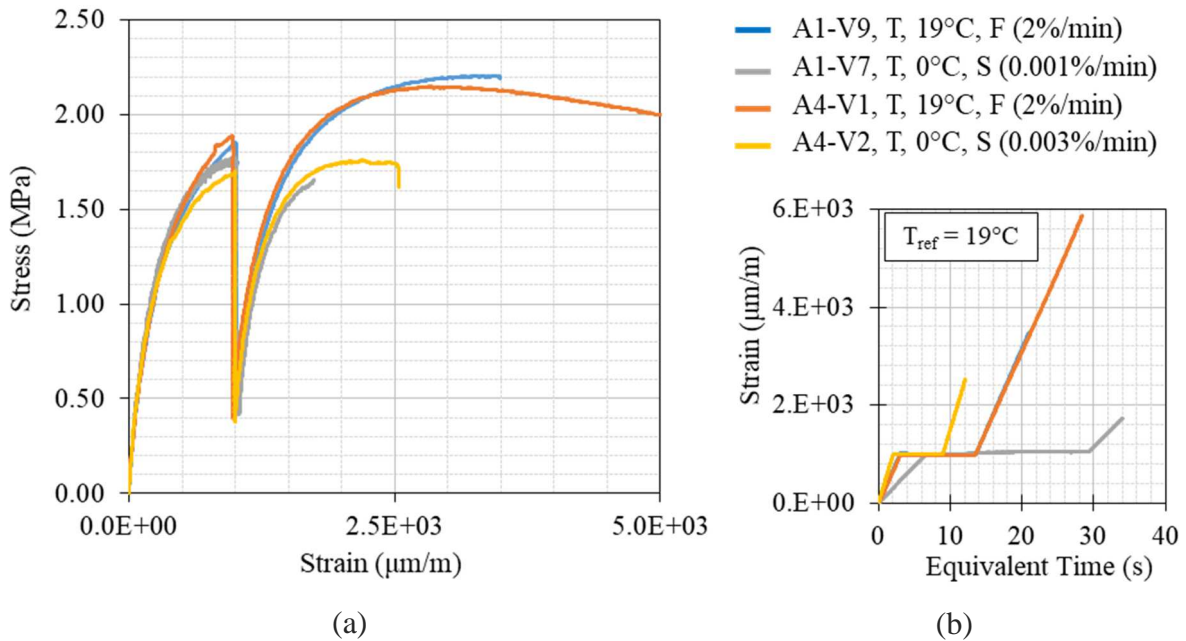


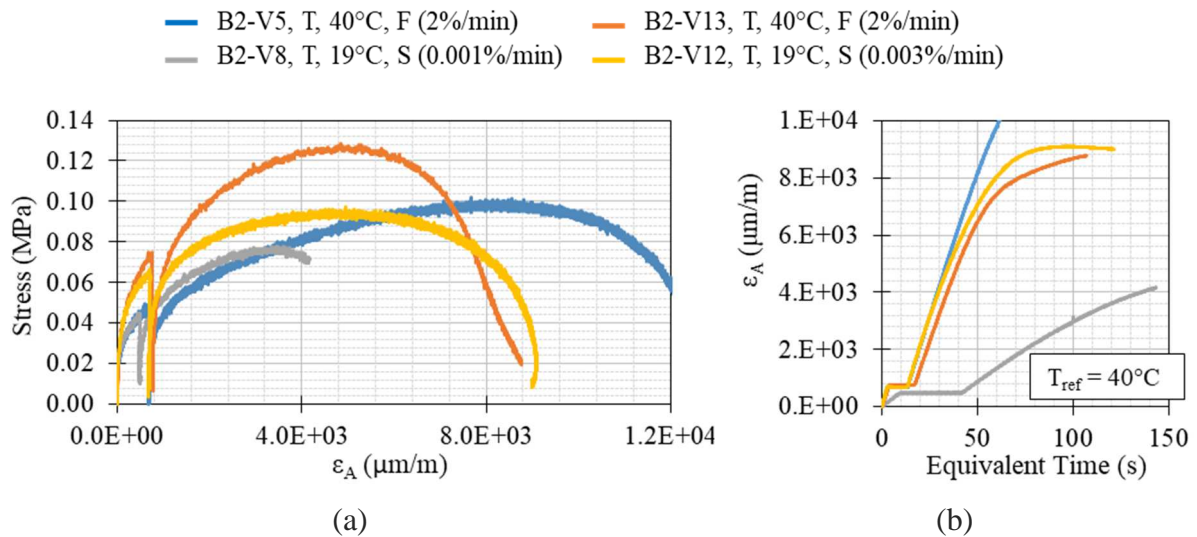
Figure 5-26. Tension test results concerning configuration A, type V, pair  $19^\circ\text{C}$  with fast strain rate and  $0^\circ\text{C}$  with slow strain rate: (a) stress vs strain, and (b) strain vs equivalent time (test loading input)

Figure 5-27 presents the tension results for configuration B (interface with emulsion bitumen), type V, pair  $40^\circ\text{C}$  with fast strain rate and  $19^\circ\text{C}$  with slow strain rate. Figure 5-27(a)



presents the stress vs strain ( $\epsilon_A$ ) curves for bituminous mixture, (b)  $\epsilon_A$  vs equivalent time for  $T_{ref}$  of 40°C, (c) stress vs interface gap ( $\Delta u$ ) curves, and (d)  $\Delta u$  vs equivalent time for  $T_{ref}$  of 40°C.

High variation between curves was observed in the results for both, bituminous mixtures and interfaces. However, for the specimen type V containing interface, the interface bond quality is the most responsible in the load supporting during tension test. As discussed in Section 5.5.2.2, the most part of the strain is concentrated in the interface level. When it deteriorates, the amount of strain in the bituminous mixture decreases, being concentrated only in the interface. Thus, the tension tests carried out in type V specimens are inconclusive regarding the validation of TTSP for bituminous mixtures. Furthermore, the interface behavior is unpredictable, which makes impossible to control the strain rate on it, in order to verify the TTSP for the interface (c.f. Figure 5-27(d)). On the other hand, the tension test are useful to rank the interface bond quality of different specimens.



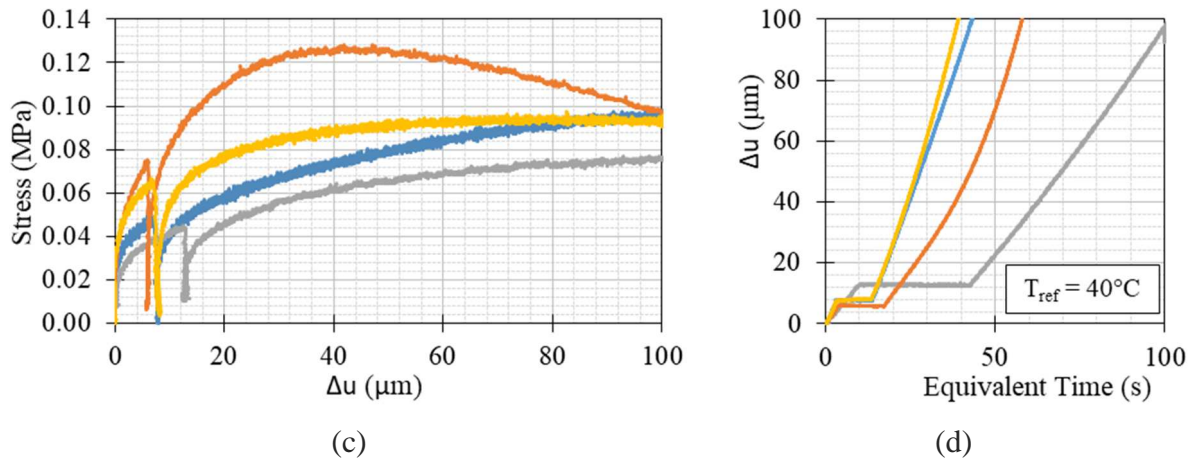


Figure 5-27. Tension test results concerning configuration B, type V, pair  $40^\circ\text{C}$  with fast strain rate and  $19^\circ\text{C}$  with slow strain rate: (a) stress vs  $\varepsilon_A$ , (b)  $\varepsilon_A$  vs equivalent time (test loading input), (c) stress vs  $\Delta u$ , and (d)  $\Delta u$  vs equivalent time (interface rate of loading)

Figure 5-28 presents the tension results for configuration B (interface with emulsion bitumen), type V, pair  $19^\circ\text{C}$  with fast strain rate and  $0^\circ\text{C}$  with slow strain rate. Figure 5-28(a) presents the stress vs strain ( $\varepsilon_A$ ) curves for bituminous mixture, (b)  $\varepsilon_A$  vs equivalent time for  $T_{\text{ref}}$  of  $19^\circ\text{C}$ , (c) stress vs interface gap ( $\Delta u$ ) curves, and (d)  $\Delta u$  vs equivalent time for  $T_{\text{ref}}$  of  $19^\circ\text{C}$ .

From the beginning of the test until  $\varepsilon_A$  of  $400\mu\text{m}/\text{m}$ , the curves were overlapped in Figure 5-28(a), and B2-V14 should have been tested at a higher strain loading in order to yield the same result. It occurs because the bitumen stiffness increased at lower temperatures and the ratio  $\varepsilon_G/\varepsilon_A$  was not as big as the one obtained at higher temperatures. This result indicates that the TTSP could be validated only for small strain levels, characteristic of the beginning of the test, for this configuration and testing conditions. Concerning interface gap results, comparing the two test conducted at the same test conditions (B2-V6 and B2-V10), similar results were obtained since they had similar interface loading conditions (c.f. Figure 5-28(d)). This result indicates that no significant difference concerning the bond quality in these two specimens was verified. Finally, the results obtained at  $0^\circ\text{C}$  for interface presented less tensile strength in relation to those at  $19^\circ\text{C}$ . The specimen condensation could be responsible for this decrease in the interface resistance.

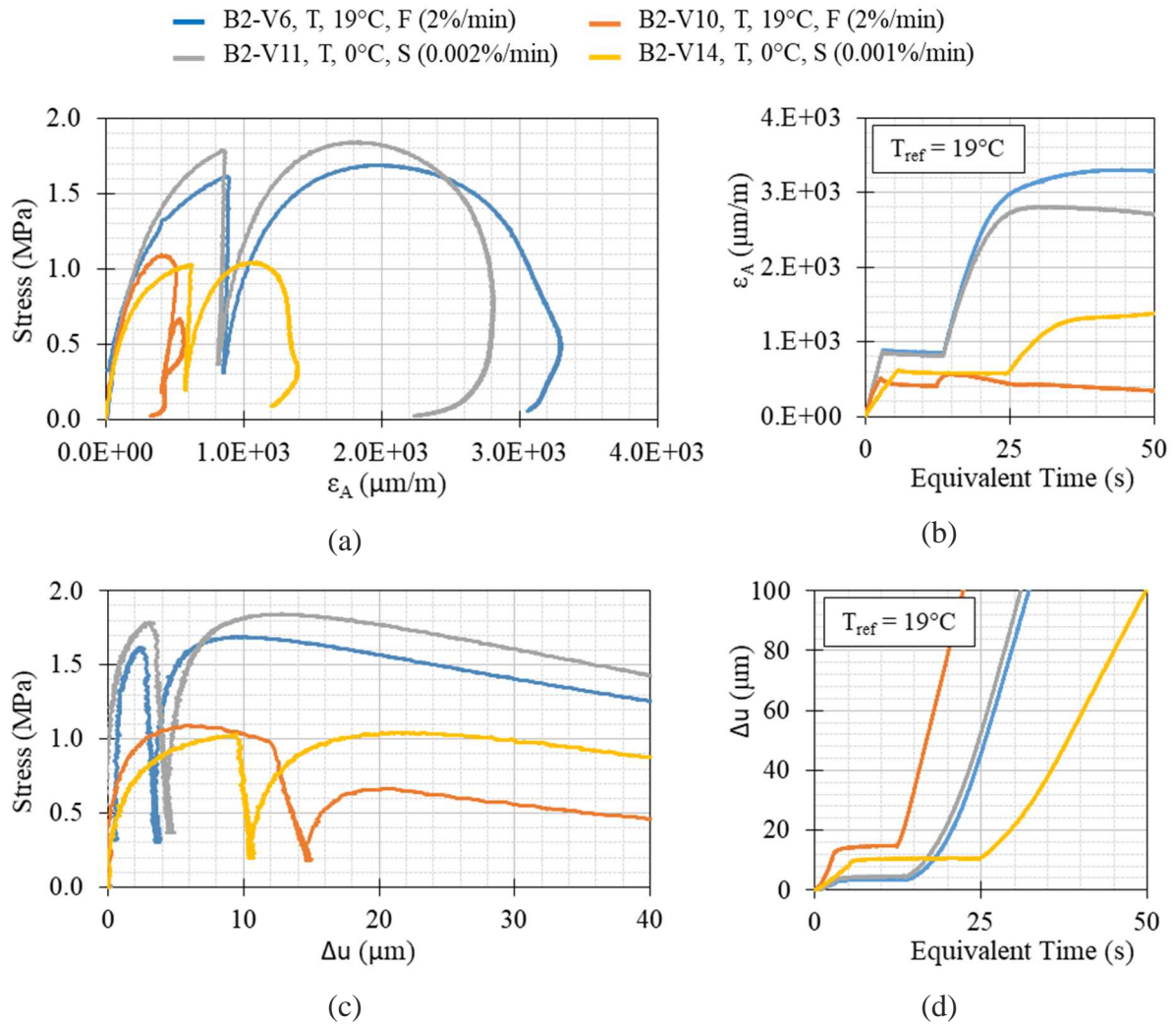


Figure 5-28. Tension test results concerning configuration B, type V, pair 19°C with fast strain rate and 0°C with slow strain rate: (a) stress vs  $\epsilon_A$ , (b)  $\epsilon_A$  vs equivalent time (test loading input), (c) stress vs  $\Delta u$ , and (d)  $\Delta u$  vs equivalent time (interface rate of loading)

Figure 5-29 presents the results for first reinforced configuration C (geogrid 100kN/m and emulsion bitumen), type V, pair 40°C with fast strain rate and 19°C with slow strain rate. Figure 5-29(a) presents the stress vs strain ( $\epsilon_A$ ) curves for bituminous mixture, (b)  $\epsilon_A$  vs equivalent time for  $T_{\text{ref}}$  of 40°C, (c) stress vs interface gap ( $\Delta u$ ) curves, and (d)  $\Delta u$  vs equivalent time for  $T_{\text{ref}}$  of 40°C.

Unlike the configuration B, low variation between curves was obtained for both, bituminous mixtures and interfaces. This result could have occurred due to the higher amount of emulsion present in the interface, 800g/m<sup>2</sup> instead of 290g/m<sup>2</sup> of residual bitumen. Thus, the viscous



properties present in the interface due to this combination of temperature and strain rate, a ductile failure occurred for all analyzed interfaces. Finally, for this configuration and testing conditions, the TTSP was validated.

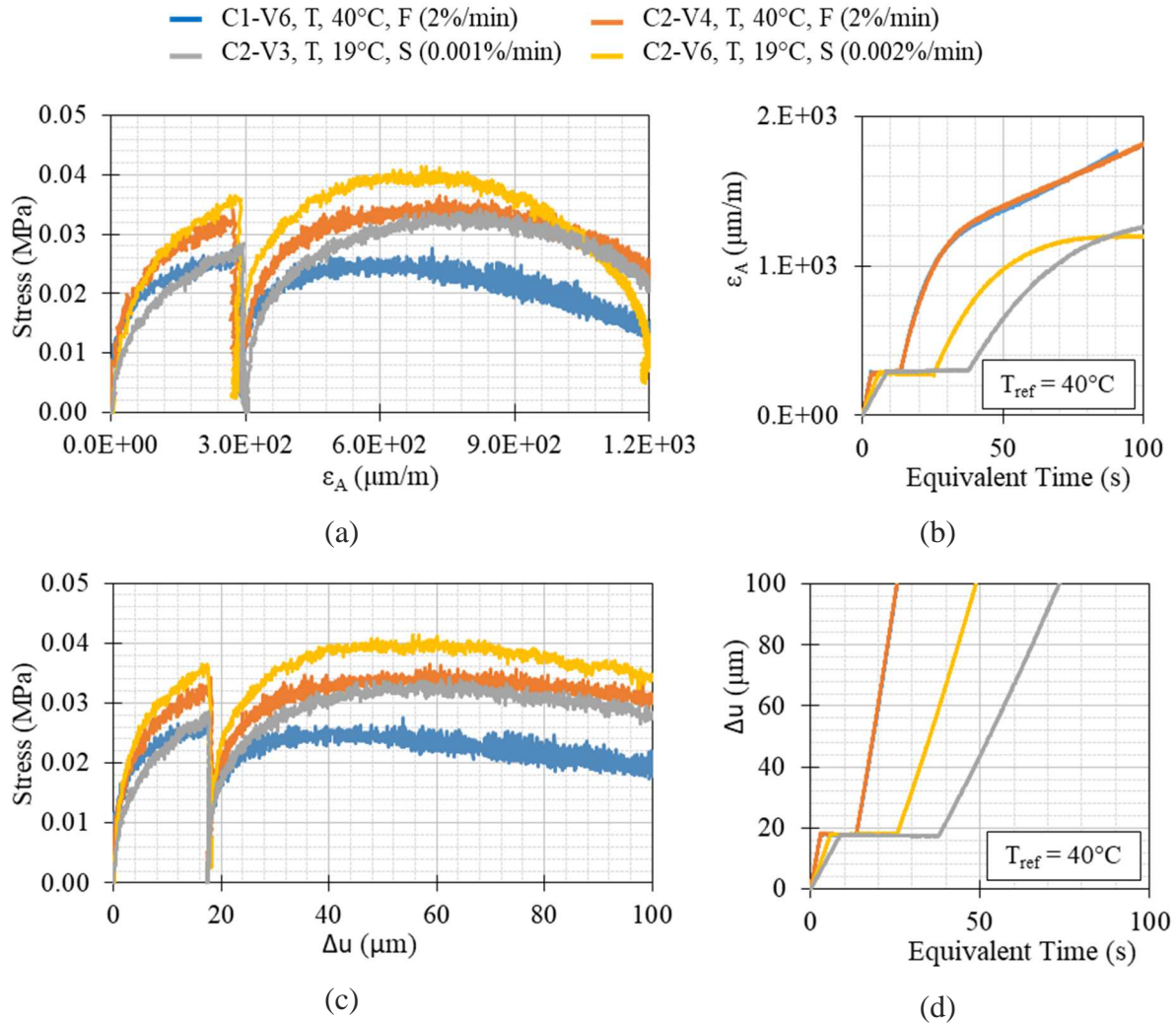


Figure 5-29. Tension test results concerning configuration C, type V, pair 40°C with fast strain rate and 19°C with slow strain rate: (a) stress vs  $\epsilon_A$ , (b)  $\epsilon_A$  vs equivalent time (test loading input), (c) stress vs  $\Delta u$ , and (d)  $\Delta u$  vs equivalent time (interface rate of loading)

Figure 5-30 presents the results for reinforced configuration C (geogrid 100kN/m and emulsion bitumen), type V, pair 19°C with fast strain rate and 0°C with slow strain rate. Figure 5-30(a) presents the stress vs strain ( $\epsilon_A$ ) curves for bituminous mixture, (b)  $\epsilon_A$  vs equivalent time for  $T_{ref}$  of 19°C, (c) stress vs interface gap ( $\Delta u$ ) curves, and (d)  $\Delta u$  vs equivalent time for  $T_{ref}$  of 19°C.

The results were very similar than those obtained for configuration B at same testing conditions. Once again the interfaces tested at 0°C presented less tensile strength than those tested at 19°C. Finally, the curves overlapped only at  $\epsilon_A < 120\mu\text{m/m}$ .

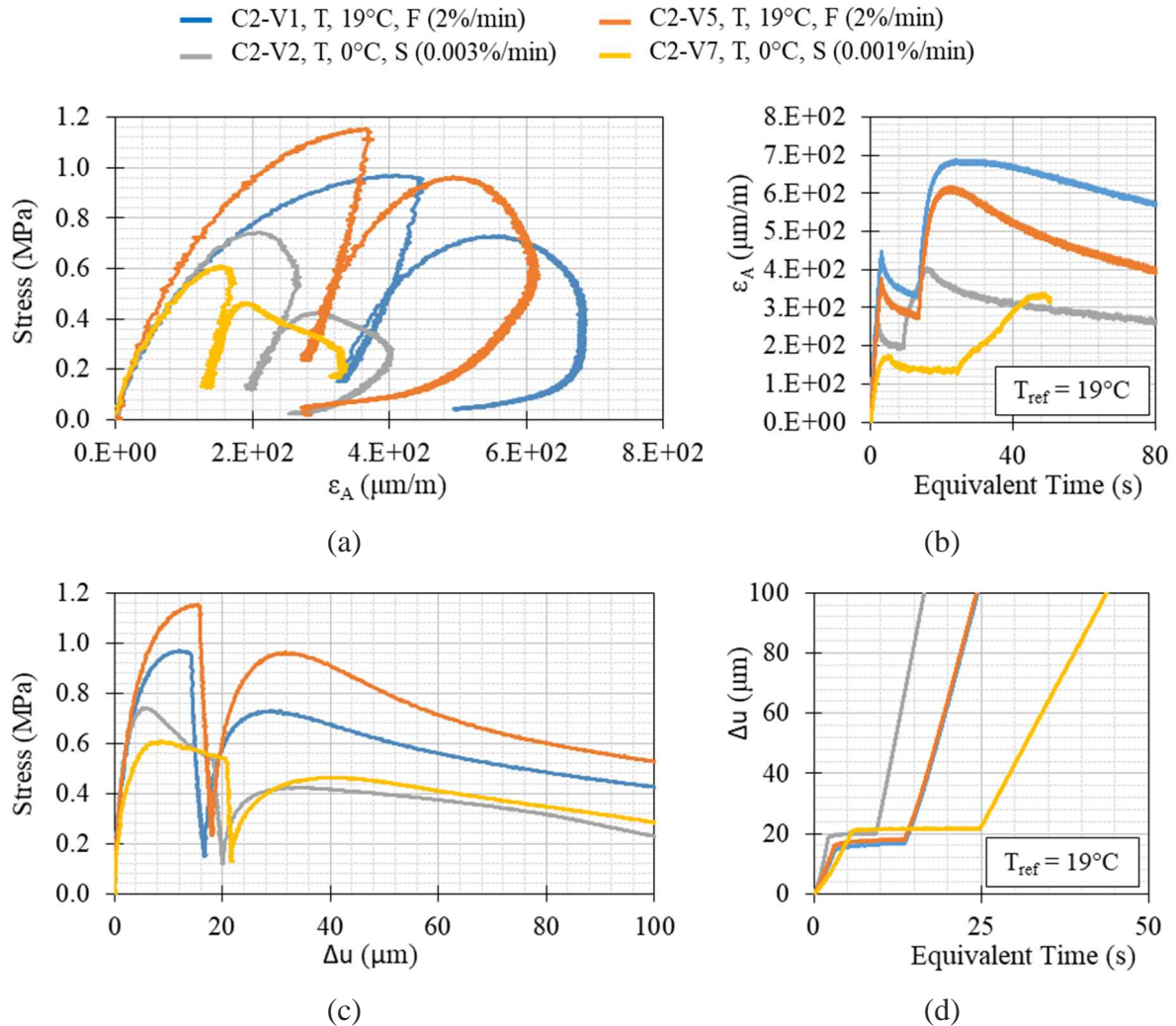


Figure 5-30. Tension test results concerning configuration C, type V, pair 19°C with fast strain rate and 0°C with slow strain rate: (a) stress vs  $\epsilon_A$ , (b)  $\epsilon_A$  vs equivalent time (test loading input), (c) stress vs  $\Delta u$ , and (d)  $\Delta u$  vs equivalent time (interface rate of loading)

Figure 5-31 presents the results for reinforced configuration D (geogrid 50kN/m and emulsion bitumen), type V, pair 40°C with fast strain rate and 19°C with slow strain rate. Figure 5-31(a) presents the stress vs strain ( $\epsilon_A$ ) curves for bituminous mixture, (b)  $\epsilon_A$  vs equivalent time for  $T_{ref}$  of 40°C, (c) stress vs interface gap ( $\Delta u$ ) curves, and (d)  $\Delta u$  vs equivalent time for  $T_{ref}$  of 40°C. Similar behavior as configuration C at same loading conditions was obtained in terms of variation between curves for bituminous mixtures and interfaces. In addition, the same order of

magnitude of stress was obtained. Moreover, the TTSP validation was tolerably acceptable for this configuration and test results.

Likewise, Figure 5-32 presents the results for reinforced configuration D (geogrid 50kN/m and emulsion bitumen), type V, pair 19°C with fast strain rate and 0°C with slow strain rate. Figure 5-32(a) presents the stress vs strain ( $\epsilon_A$ ) curves for bituminous mixture, (b)  $\epsilon_A$  vs equivalent time for  $T_{ref}$  of 19°C, (c) stress vs interface gap ( $\Delta u$ ) curves, and (d)  $\Delta u$  vs equivalent time for  $T_{ref}$  of 19°C. Once again, similar behavior as configuration C was obtained. On the other hand, an overlaps in Figure 5-32(a) was only obtained at  $\epsilon_A < 120\mu\text{m/m}$ . Finally, D2-V8 presented the highest tensile strength between the tested interfaces, evidencing the high variation between the bond qualities of different specimens with same interface constitution.

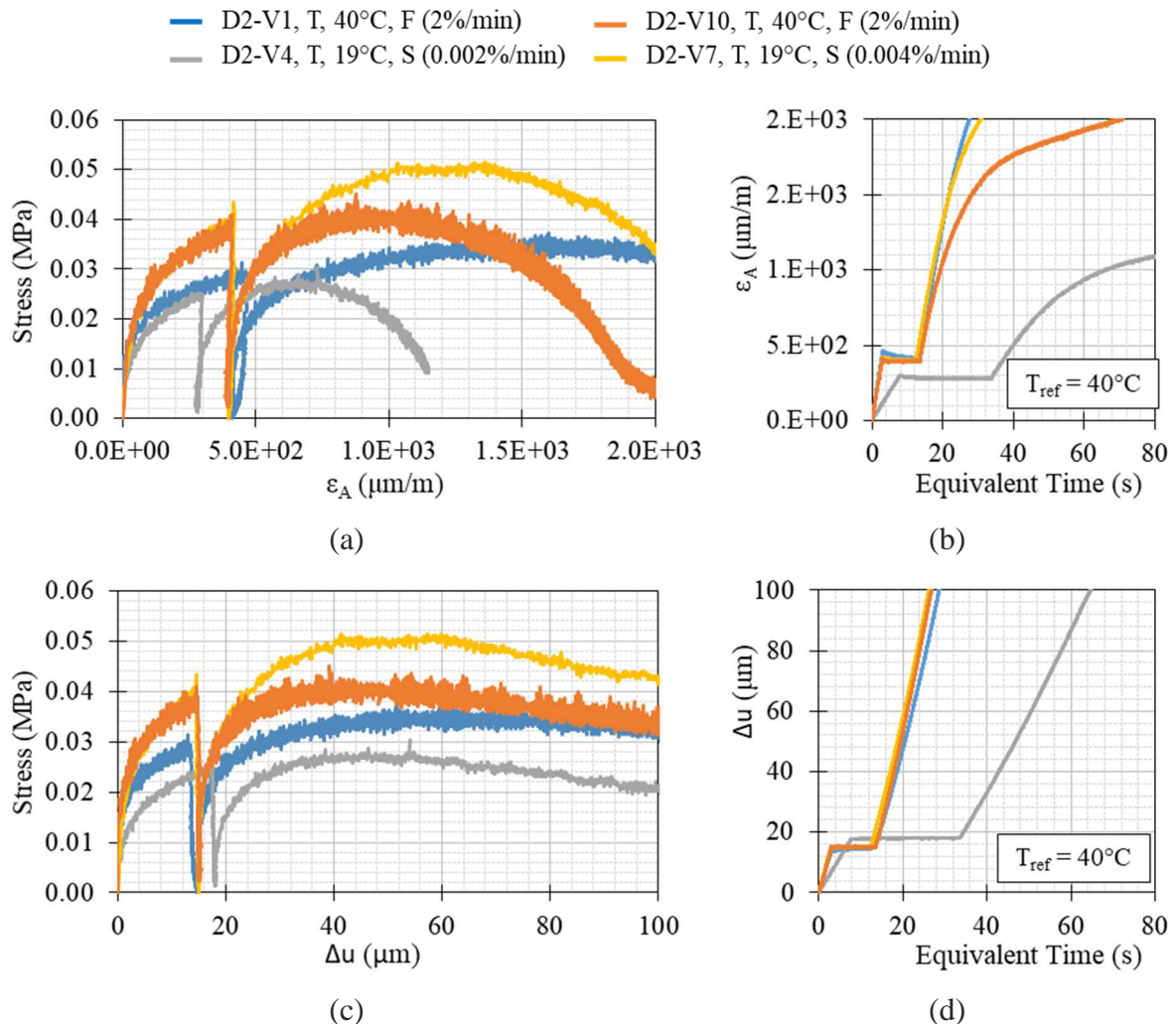


Figure 5-31. Tension test results concerning configuration D, type V, pair 40°C with fast strain rate and 19°C with slow strain rate: (a) stress vs  $\epsilon_A$ , (b)  $\epsilon_A$  vs equivalent time (test loading input), (c) stress vs  $\Delta u$ , and (d)  $\Delta u$  vs equivalent time (interface rate of loading)

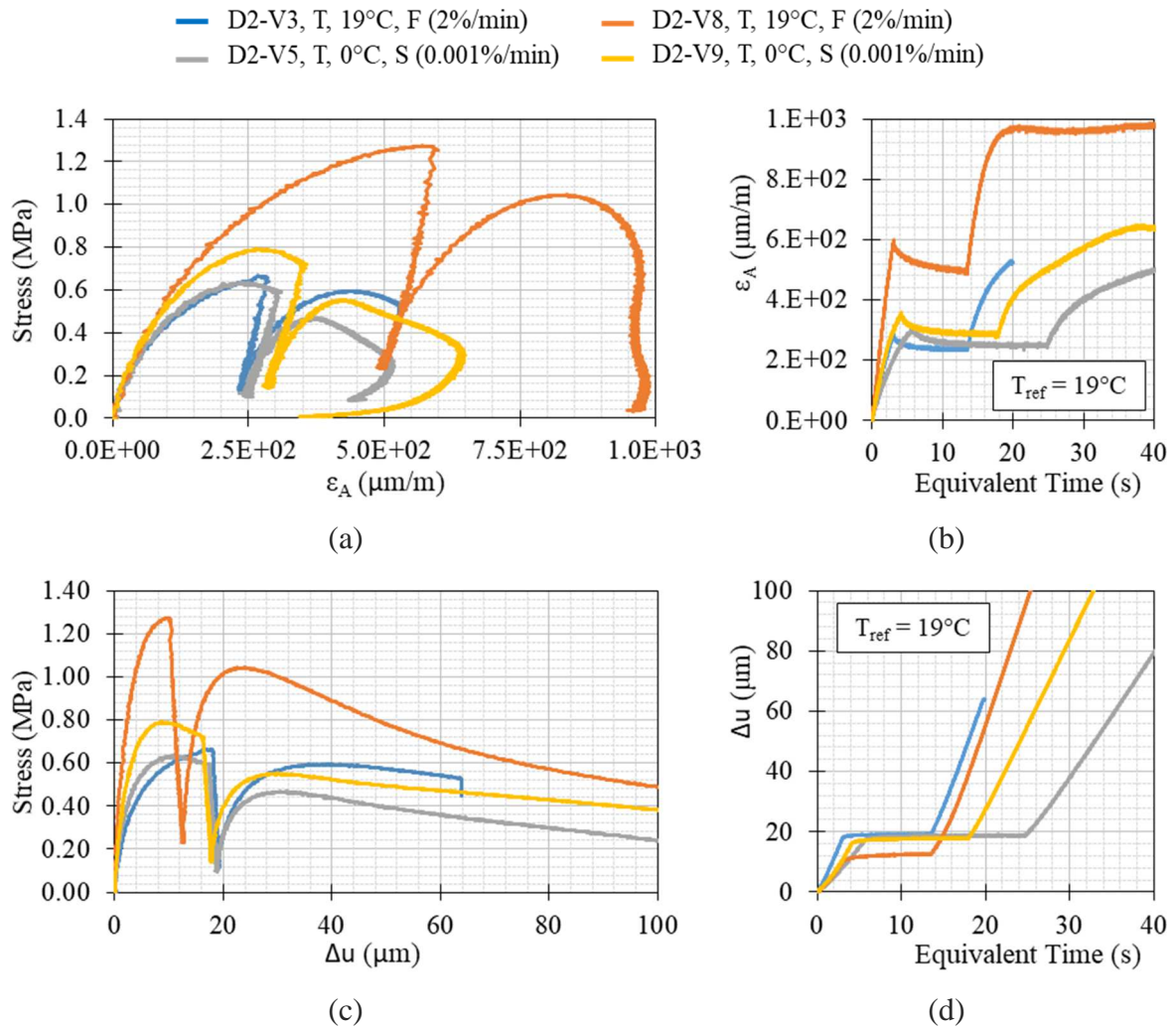


Figure 5-32. Tension test results concerning configuration D, type V, pair  $19^\circ\text{C}$  with fast strain rate and  $0^\circ\text{C}$  with slow strain rate: (a) stress vs  $\varepsilon_A$ , (b)  $\varepsilon_A$  vs equivalent time (test loading input), (c) stress vs  $\Delta u$ , and (d)  $\Delta u$  vs equivalent time (interface rate of loading)

Figure 5-33 presents the results for the last reinforced configuration: E (geogrid 100kN/m and emulsion modified by SMS), type V, pair  $40^\circ\text{C}$  with fast strain rate and  $19^\circ\text{C}$  with slow strain rate. Figure 5-31(a) presents the stress vs strain ( $\varepsilon_A$ ) curves for bituminous mixture, (b)  $\varepsilon_A$  vs equivalent time for  $T_{ref}$  of  $40^\circ\text{C}$ , (c) stress vs interface gap ( $\Delta u$ ) curves, and (d)  $\Delta u$  vs equivalent time for  $T_{ref}$  of  $40^\circ\text{C}$ . For this test conditions, the validation of TTSP was inconclusive and a high variation between curves of bituminous mixtures and interfaces was observed, one more time.

Finally, Figure 5-34 presents the results for reinforced configuration E, type V, pair  $40^\circ\text{C}$  with fast strain rate and  $19^\circ\text{C}$  with slow strain rate. Figure 5-31(a) presents the stress vs strain



( $\varepsilon_A$ ) curves for bituminous mixture, (b)  $\varepsilon_A$  vs equivalent time for  $T_{ref}$  of 19°C, (c) stress vs interface gap ( $\Delta u$ ) curves, and (d)  $\Delta u$  vs equivalent time for  $T_{ref}$  of 19°C. Similarly to the reinforced specimens, the validation of TTSP was inconclusive.

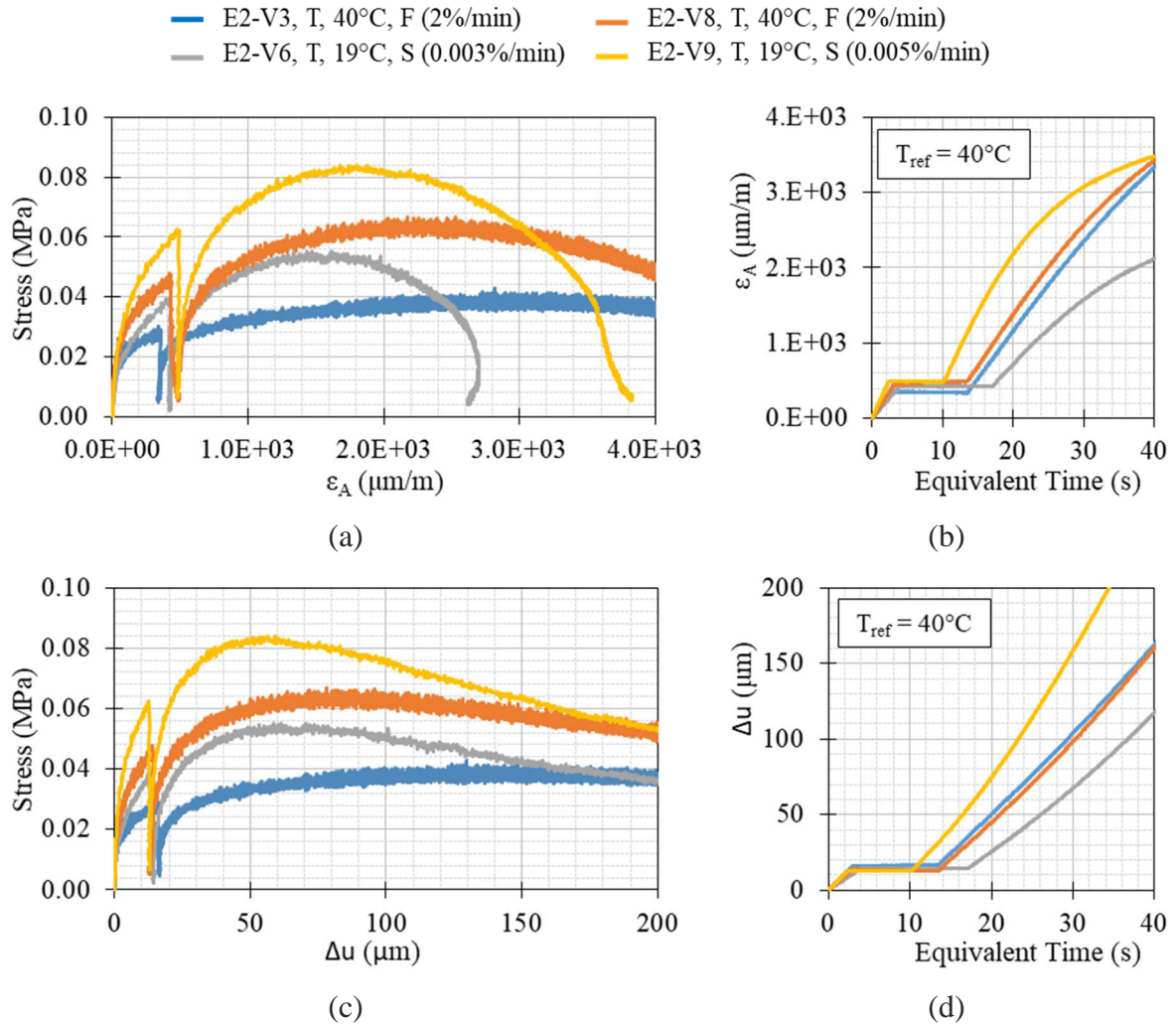


Figure 5-33. Tension test results concerning configuration E, type V, pair 40°C with fast strain rate and 19°C with slow strain rate: (a) stress vs  $\varepsilon_A$ , (b)  $\varepsilon_A$  vs equivalent time (test loading input), (c) stress vs  $\Delta u$ , and (d)  $\Delta u$  vs equivalent time (interface rate of loading)

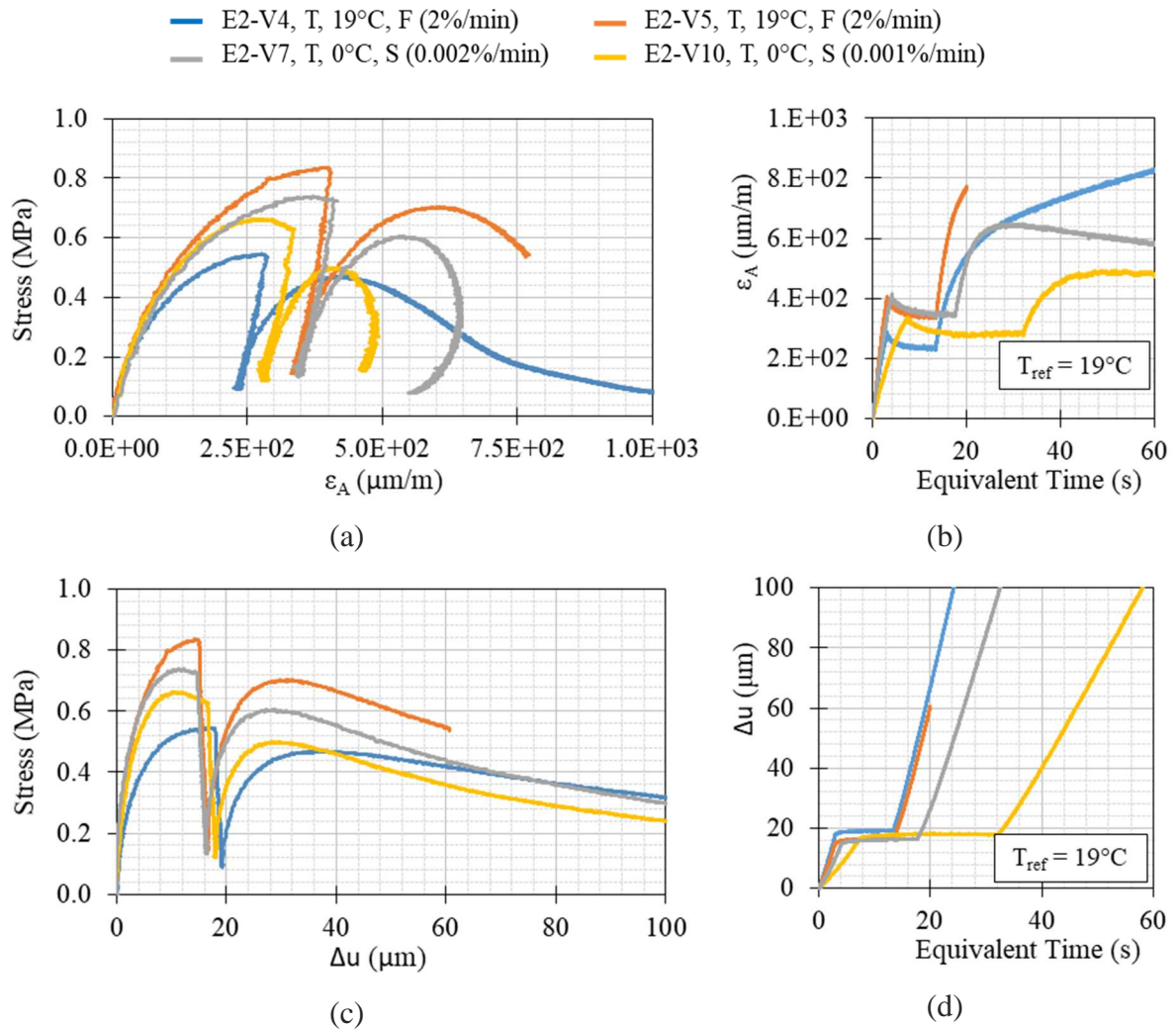
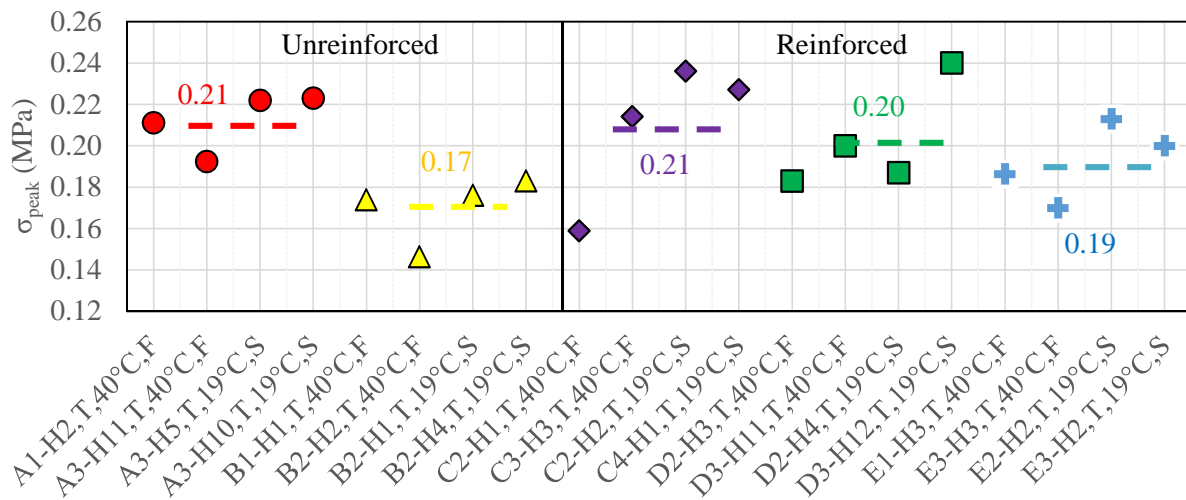


Figure 5-34. Tension test results concerning configuration E, type V, pair 19°C with fast strain rate and 0°C with slow strain rate: (a) stress vs  $\varepsilon_A$ , (b)  $\varepsilon_A$  vs equivalent time (test loading input), (c) stress vs  $\Delta u$ , and (d)  $\Delta u$  vs equivalent time (interface rate of loading)

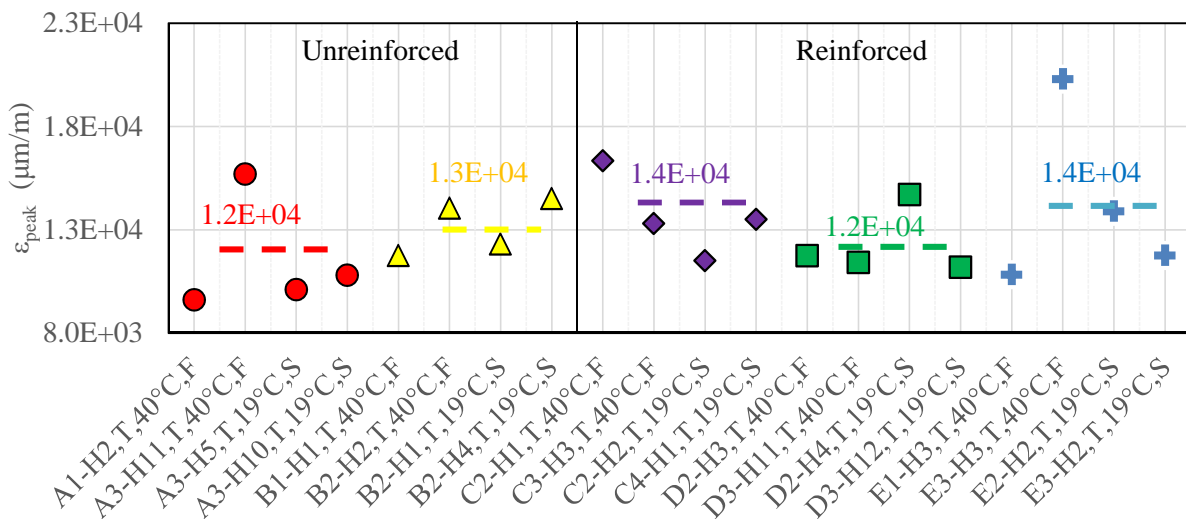
## 5.8. Fiberglass geogrid contribution to the maximum tensile strength of bituminous mixture

In order to assess the fiberglass geogrid contribution in the maximum tensile strength in a reinforced specimen (type H), an analysis of peak points, as the one illustrated in Figure 5-4(c), was performed for all specimens, unreinforced and reinforced. Figure 5-35 presents the results for the pair 40°C with fast strain rate and 19°C with slow strain rate, (a)  $\sigma_{\text{peak}}$  and (b)  $\varepsilon_{\text{peak}}$ . According to Figure 5-35(a), configuration A (no interface) and C (100kN/m with emulsion bitumen) presented the higher maximum tensile strength and configuration B (interface emulsion) presented the lowest. Concerning the reinforced configurations D (50kN/m with emulsion

bitumen) and E (100kN/m with emulsion bitumen modified by SBS), very close values were obtained. The configuration containing modified bitumen presented slightly lower than the other did, measured by their averages. The results indicate that the presence of interface weakened the specimen at this test condition. In addition, the results presented in Section 5.7.2 suggest that the geogrid was not mobilized during the moment of the test when the peak point occurs. Regarding  $\epsilon_{peak}$  presented in Figure 5-35(b), the inverse was observed. Configuration A presented the lowest strain value at the peak point, whereas configuration E presented the highest.



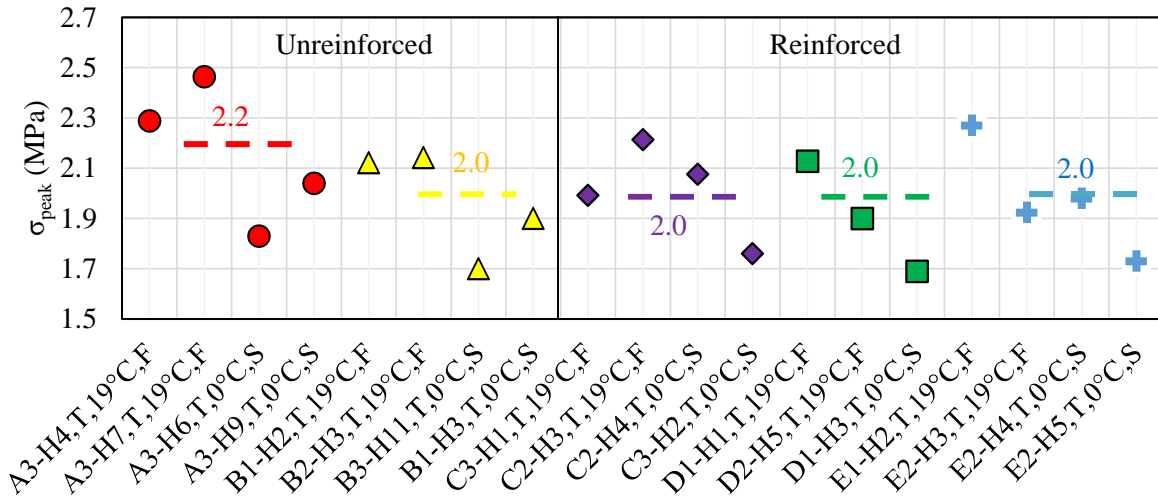
(a)



(b)

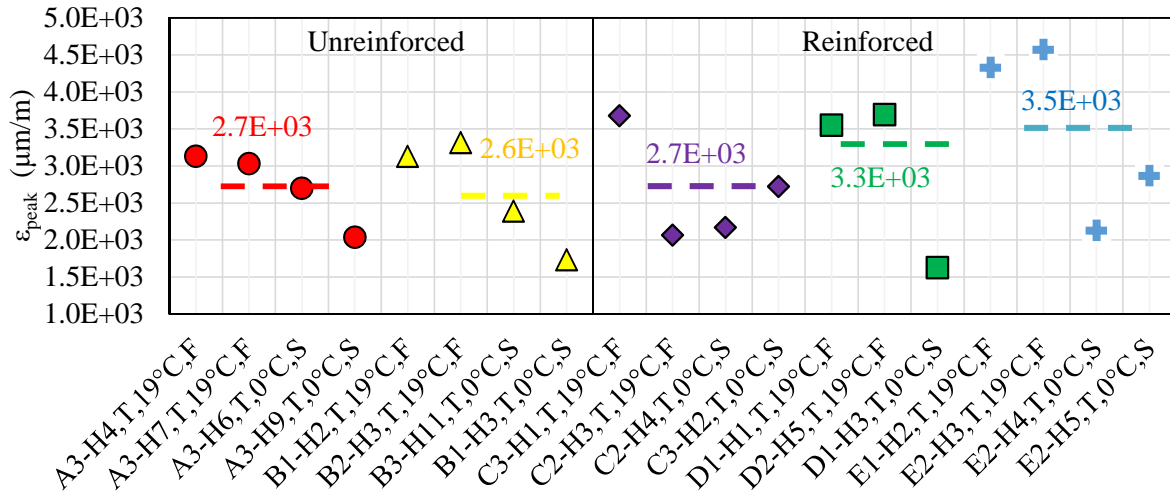
Figure 5-35. Peak points obtained from the tension tests results plotted in stress vs strain, concerning the pair 40°C with fast strain rate and 19°C with slow strain rate, type H specimen: (a) maximum tensile strength ( $\sigma_{peak}$ ) and (b)  $\epsilon_{peak}$

Figure 5-36 presents the results for the pair 19°C with fast strain rate and 0°C with slow strain rate, (a)  $\sigma_{peak}$  and (b)  $\epsilon_{peak}$ . According to Figure 5-36(a), the configuration A (no interface) presented the higher maximum tensile strength at this testing condition. All the other configurations (B, C, D and E) presented the same averages of maximum tensile strength (2.0MPa), slightly lower the one obtained for configuration A (2.2MPa). Configuration D only contains three results because occurred premature failure in the fourth specimen. For this test condition, the interface weakened the specimen, decreasing its maximum tensile strength, one more time. However, in this case, the presence and type of the geogrid, as well as the amount and type of emulsion do not influence this performance parameter. Regarding Figure 5-36(b), the reinforced configurations presented higher strain values at peak points, especially the configuration E.



(a)





(b)

Figure 5-36. Peak points obtained from the tension tests results plotted in stress vs strain, concerning the pair 19°C with fast strain rate and 0°C with slow strain rate, type H specimen:

(a) tensile strength ( $\sigma_{peak}$ ) and (b)  $\epsilon_{peak}$

However, the slow strain rates were very different, which could lead to errors on analysis. Thus, another analysis of peak points was performed excluding the points obtained from slow strain rate tests, presented in Figure 5-37.

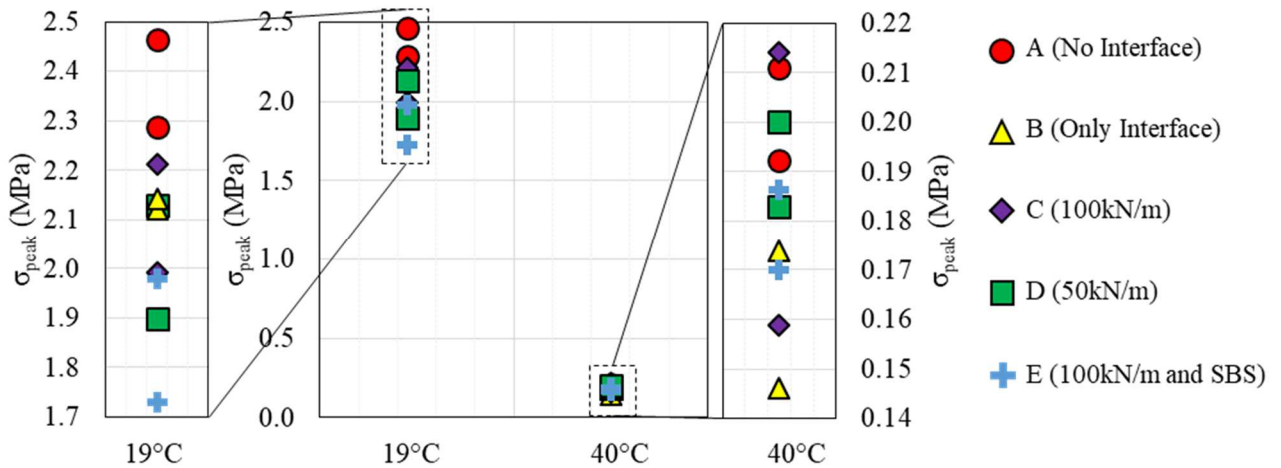


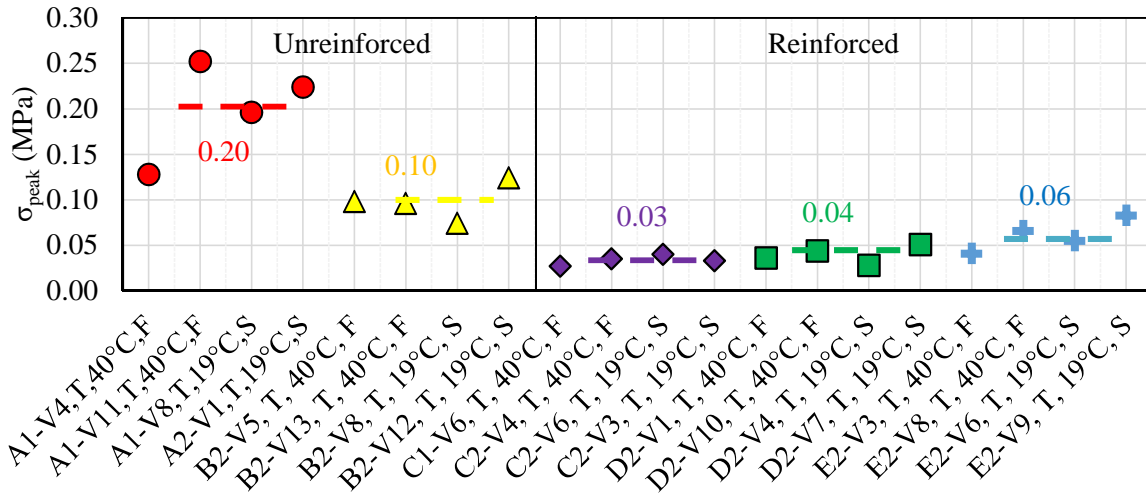
Figure 5-37. Maximum tensile strength ( $\sigma_{peak}$ ) of type H specimens tested at 40°C and 19°C and at 2%/min

From Figure 5-37, concerning the tests at 40°C and 2%/min, once again configuration A presented the highest maximum tensile strength and configuration B the lowest. Regarding the

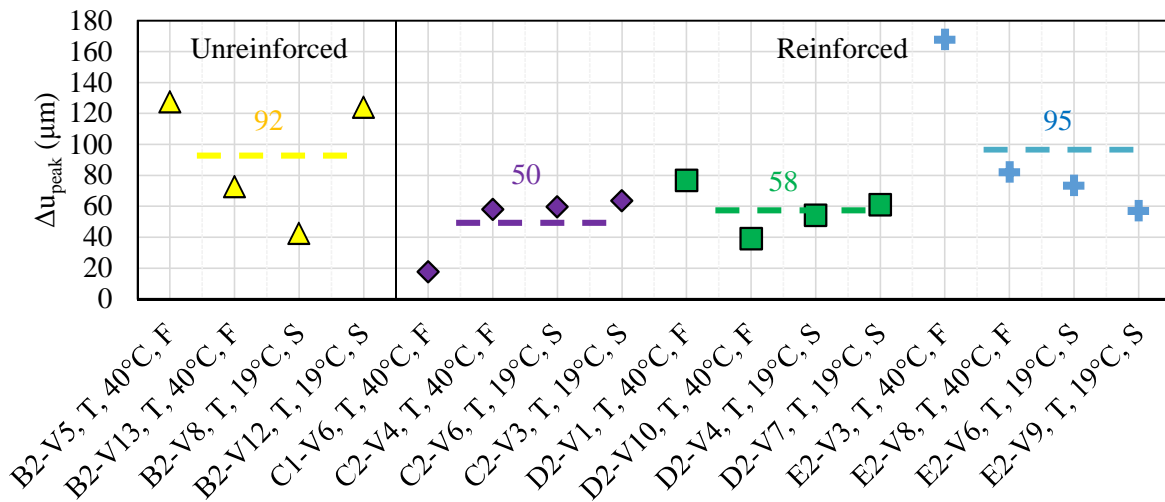
reinforced configurations, C and D presented similar results, slightly superior than the configuration E. These results indicate that the type of emulsion has more influence than the type of geogrid. Regarding the tests at 19°C and 2%/min, once again configuration A presented the highest maximum tensile strength. However, concerning the other configurations, a difference between the results was observed. Configurations B and C presented again similar results, but higher than D and E. Configuration E presented again the lowest maximum tensile strength.

## 5.9. Effect of fiberglass geogrid on maximum interface tensile strength

Another peak point analysis can be performed in the specimens type V in order to assess the interface maximum tensile strength to tension loading. Figure 5-38 presents the results for the couple 40°C fast and 19°C slow strain rate, (a)  $\sigma_{peak}$  and (b)  $\Delta u_{peak}$ . The results for configuration A are presented in Figure 5-38(a) for comparison purposes only since the mentioned configuration does not have interface on its specimens constitution. Regarding the configurations containing interfaces, B presented the highest interface resistance (average of 0.1MPa), which was the half of resistance obtained for configuration A (average of 0.2MPa). Comparing the A type V with the A type H previously done, their averages were similar. Regarding the reinforced configuration, E (100kN/m with emulsion bitumen modified by SBS) presented the highest, followed by D (50kN/m with emulsion bitumen) and C (100kN/m with emulsion bitumen). The SBS present in the emulsion in the interface of configuration E increases the bond quality, which explains the increase in the interface strength. Configuration B presented approximately 1.67 times higher strength than E, the second highest. Comparing with configuration D, which contains the same type of emulsion than B, this ratio increases to 2.5 times. However, the interface strength should be influenced by its real thickness. The reinforced specimens' interface presents 2.76 times more emulsion, besides the geogrid presence, compared to the unreinforced one. Thus, the reinforced specimens' interface is at least three times thicker, which could explain its lower maximum tensile strengths. Moreover, a decrease in the effective bonding surface and the decrease in the indentation of the two granular layers one another is caused due to the geogrid presence, could result in lower maximum tensile strength. From Figure 5-38(b) using averages comparison, configuration E presented the highest interface gap at the peak, even greater than configuration B. Finally, configuration C presented the lowest interface gap.



(a)

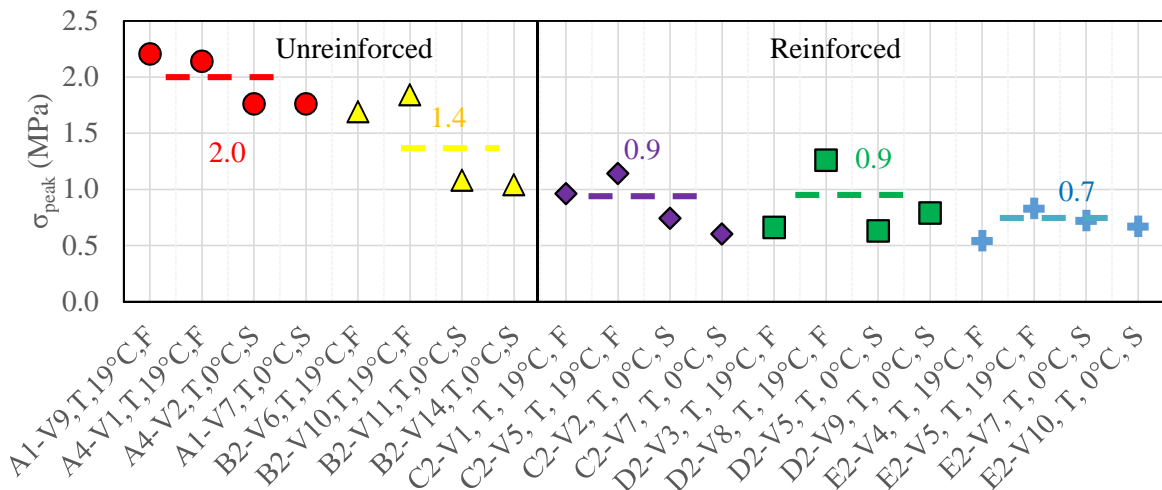


(b)

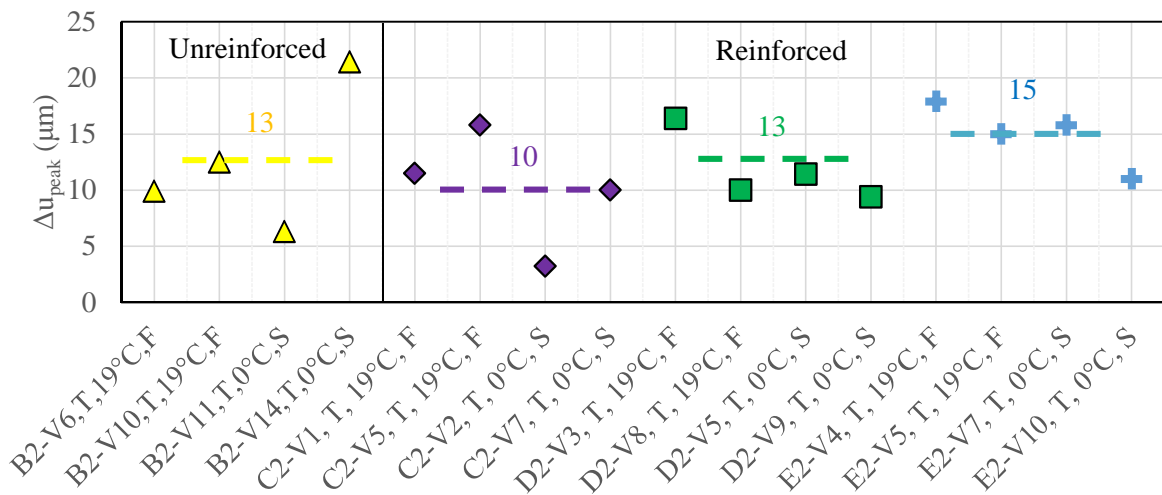
Figure 5-38. Peak points obtained from the tension tests results plotted in stress vs strain, concerning the pair 40°C with fast strain rate and 19°C with slow strain rate, type V specimen: (a) maximum tensile strength ( $\sigma_{peak}$ ) and (b)  $\Delta u_{peak}$

Figure 5-39 presents the results for the pair 19°C with fast strain rate and 0°C with slow strain rate, (a)  $\sigma_{peak}$  and (b)  $\Delta u_{peak}$ . One more time, the configuration A (no interface) results were plotted for comparison purposes. Once again, configuration B presented the highest maximum tensile strength in the interface than the reinforced configurations. The same explanation for 40°C fast and 19°C slow is valid for 19°C fast and 0°C slow. Regarding the reinforced specimens, the averages of configuration C and D were the same (0.9MPa) and slightly higher than the average of results of configuration E (0.7MPa) for this testing conditions. This result

indicate that the bitumen modified by SBS presents less sensitivity to temperature and/or loading rate variation when compared to the bitumen without modification presented in configurations B, C and D. Regarding the  $\Delta u_{peak}$  presented in Figure 5-39(b), configuration E presented again the highest average value for this testing conditions. Moreover, configuration C presented again the lowest  $\Delta u_{peak}$  average value.



(a)



(b)

Figure 5-39. Peak points obtained from the tension tests results plotted in stress vs strain, concerning the pair 19°C with fast strain rate and 0°C with slow strain rate, type V specimen: (a) maximum tensile strength ( $\sigma_{peak}$ ) and (b)  $\Delta u_{peak}$

One more time, another analysis of peak points was performed excluding the points obtained from slow strain rate tests and is presented in Figure 5-40. For both, 40°C and 19°C at 2%/min, the ranking obtained in Figure 5-38(a) and Figure 5-39(a), respectively, was the same.

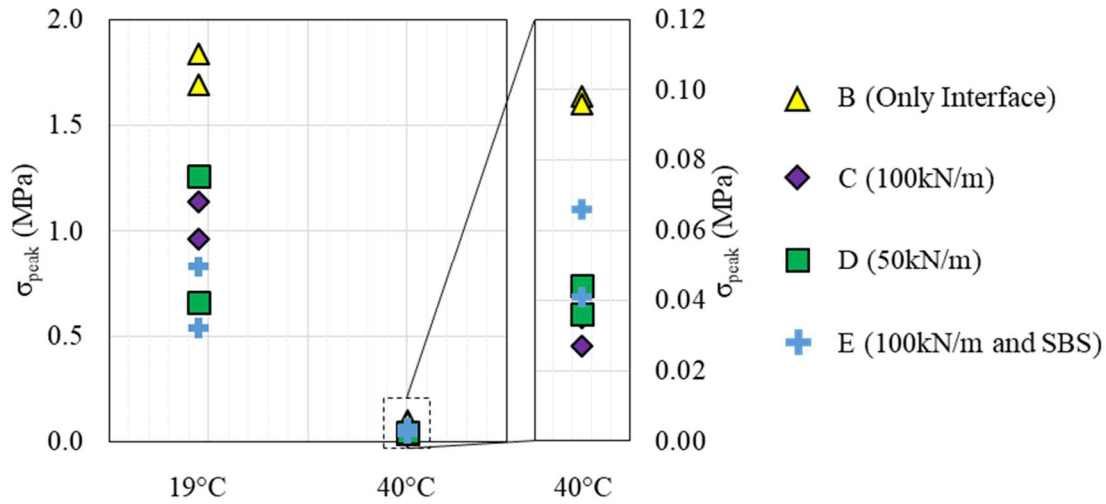


Figure 5-40. Interface tensile strength ( $\sigma_{peak}$ ) of type V specimens tested at 40°C and 19°C and at 2%/min

## 5.10. Chapter conclusions

This chapter presented the tension experimental campaign of the five studied slab configurations. Monotonic tension with creep loading test were carried out in specimens cored in two different directions, called type V and H. In addition, an interface analysis method was proposed to measure amount of strain concentrated in the interface and evaluate the interface bond quality of the specimens type V. Therefore, some conclusion can be drawn:

- The interface analysis methodology based on the one presented for the complex modulus test was successfully used to measure of strain in the interface level. This method was capable of characterize the interface behavior to the tension tests.
- During the tension tests carried out in type V specimens containing interface (reinforced or not), the interface was the most responsible to the load supporting during tension test. The strain in bituminous mixture much smaller than the strain in the interface. Thus, the interface bond quality had a direct influence on the maximum tensile strength of type V specimens.

- The variation on the diameter size of reinforced specimen type V presented no significant difference concerning the tension behavior. Moreover, the variation obtained was mainly due to the quality of the interface bond and smaller differences encountered in the specimens interface, mostly related to its position in the slab before coring.
- The slow strain rate used to TTSP validation should be calculated based on the  $a_T$  calculated using the LVE WLF model equation, obtained in the Chapter 4, as is classically done in the works from LTSD/ENPTE. The  $a_T$  obtained from the frequency sweep tests could lead to errors.
- Although the slow strain rates were slightly different, the TTSP was validated for all slab configurations (reinforced or not), type H specimens.
- The type V specimens configuration A, the TTSP was also tolerably validated. However, for specimens containing interfaces, the TTSP was mostly inconclusive since the tests were controlled by the extensometer measure, which is a composition of the strain in bituminous mixture and interface. Thus, it was not possible solicit the bituminous mixture and the interface of the specimen correctly.
- The reinforced specimens type H at high temperatures, the geogrid was not mobilized, possibly due to the slippage in the interface caused by the high viscosity of the bitumen. However, before the creep step, the stress vs strain curve presented the same slope as the line corresponding to the geogrid elastic response, which could indicate a geogrid mobilization at this point.
- The reinforced specimens type H at low temperatures, there is a greater possibility of geogrid mobilization during the test. However, it does not have significant influence on the tensile strength due to the elevated stiffness of the bituminous mixture at these combinations of testing conditions.
- The interface containing only emulsion bitumen presented the higher tensile strength than the reinforced specimens. However, the interface strength should be influenced by its real thickness, and the reinforced specimens' interface is at least three times thicker. Moreover, a decrease in the effective bonding surface and the decrease in the indentation of the two granular layers one another is caused due to the geogrid presence, could result in lower maximum tensile strength.

# Chapter 6: FATIGUE TEST CAM- PAIGN

6.1. Introduction .....	209
6.2. Objectives .....	209
6.3. Experimental procedures and devices .....	210
6.3.1. Hydraulic press and instrumentation.....	210
6.3.2. Fatigue test protocol.....	211
6.4. Tested specimens.....	213
6.5. Example of fatigue tests results: B3-H4, 90 $\mu$ m/m.....	215
6.6. Classical analysis of fatigue tests in cylindrical samples results.....	219
6.6.1. Influence of strain level on fatigue.....	219
6.6.2. Analysis of fatigue life (number of cycles to failure) .....	222
6.6.3. The Wöhler curve and determination of the $\epsilon_6$ value .....	227
6.6.4. Influence of geogrid on fatigue resistance .....	231
6.7. Chapter conclusions.....	233

## 6.1. Introduction

Some studies are found in literature investigating the geogrid reinforcement to the fatigue life of bituminous mixture. According to De Bondt (2012), Arsenie et al. (2012), Millien et al. (2012), and Godard et al. (2019), the geogrid increases the fatigue life of reinforced bituminous mixtures. French design method presents a fatigue resistance verification on its procedure using the parameter  $\varepsilon_6$  (strain amplitude corresponding to one million cycles loading fatigue life) in the calculation of admissible strain ( $\varepsilon_{adm}$ ). Thus, an increase in fatigue resistance due to geogrid reinforcement could lead to a great improvement in the design of new pavement structures. Furthermore, it could lead to a decrease in the bituminous mixture layer thickness in the final pavement structure (Godard et al. 2019) that has a great impact on the roadways construction costs.

The purpose of this chapter is to present the fatigue test experimental campaign studied in this work. Sinusoidal tension-compression tests at 10°C, 10Hz, and controlled strain at different amplitudes are carried out to the characterization of the fatigue life. Only specimens cored in the same compaction direction (type H) from the five different slab configurations are used to conduct the experimental campaign. The testing procedure, as well as the hydraulic press and the transducers used to measure the physical variations, temperature, and force during the test are fully detailed in this chapter. Moreover, the procedure of analysis is presented, as well as the failure criteria definition. Discussions concerning the influence of geogrid presence and type as well as the type of emulsion tack coat on the fatigue resistance of bituminous mixtures are held. Lastly, the geogrid effect in the fatigue parameters used in the French design method of flexible pavements is obtained.

## 6.2. Objectives

For the investigation conducted in this chapter, some objectives can be listed:

- To evaluate the effect of the strain amplitude used to control the test in the fatigue life of reinforced and unreinforced specimens.
- To verify the effect of the five different failure criteria chosen from the literature to define fatigue life of reinforced and unreinforced specimens.
- To assess the influence of the presence of fiberglass geogrid and its maximum tensile strength on fatigue life of bituminous mixtures.



- To assess the influence of the type of emulsion tack used as tack coat to bond the bituminous mixture layers together, on fatigue life of bituminous mixtures.
- To analyze the fiberglass geogrid influence on the fatigue parameters used in the French design method for flexible pavements.

### 6.3. Experimental procedures and devices

#### 6.3.1. Hydraulic press and instrumentation

Once again, the equipment used for conducting the investigation performed in this chapter is the same used in Chapter 4, concerning the complex modulus tests. The information is detailed in Section 4.3.1. However, the instrumentation set up slightly differed from the previous tests presented in Chapters 4 and 5. The first couple of extensometers had a 72.5mm length ( $l_1$ ) and they were disposed at  $180^\circ$  from one another, always placed next to the interface. The other couple had a 75mm length ( $l_2$ ) and extensometers were disposed at  $180^\circ$  from one another. Figure 6-1 presents a setup scheme detailing the extensometer position in function of the interface of the specimen. The loading strain amplitude was controlled during the test from the average of the two smaller extensometers ( $l_1$ ). However, the non-contact transducers were not used, due to the unpredictable behavior of the specimen at failure that could cause damage to the transducers, the same reason for the last chapter. Thus, no radial strain data was collected during the tests.

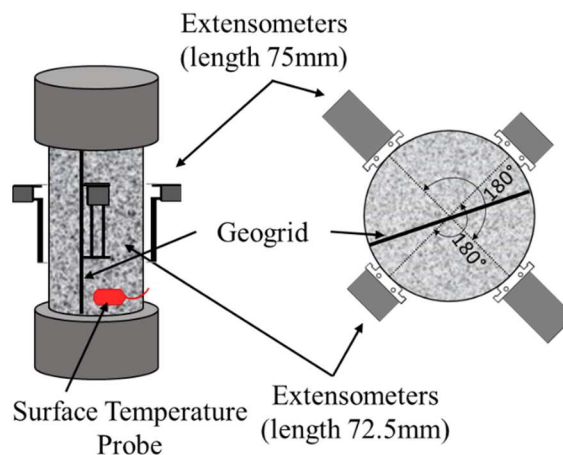


Figure 6-1. Instrumental setup scheme: extensometers and temperature probe location

### ***6.3.2. Fatigue test protocol***

The tests were carried out by applying axial tension-compression sinusoidal loading centered on zero stress with a controlled strain amplitude until the specimen reaches failure. Four strain amplitudes were targeted: 80, 90, 100 and 110 $\mu\text{m}/\text{m}$ , with two test repetitions of each. The specimens of all configurations were tested at frequency of 10hz and temperature of 10°C with a minimum of stabilization waiting time of 4h. During the test, the chosen strain amplitude was repeated until the end of the test, as characteristic of a classic time sweep test, which is largely used to fatigue characterization in laboratory. Three criteria were programmed to define the end of the test: physical failure dividing the specimen into two pieces, the achievement of the maximum capacity of extensometer opening (1mm) and decrease of 70% of force amplitude in relation to the force measured at the first loading cycle. From each strain amplitude, a number of cycle to failure was obtained and it represents the fatigue life of the specimen. From the number of cycles to failure associated with their corresponding strain amplitudes, Wöhler curves can be plotted (c.f. Figure 2-14).

The data collecting is very extensive for each tested specimen. A total of 250 points is collected of each loading cycle during the test, and it frequently finishes with around 2 million of loading cycles. Thus, a reduction in the loading cycles recorded was performed in accordance with the previous works done at LTDS/ENTPE (Mangiafico 2014 and Cardona Ramirez 2016). According to the theory of fatigue testing in laboratory, it is observed a fastest modulus loss during the first loadings cycles before the phase II (Cardona Ramirez 2016), as discussed in Section 2.5.2. For this reason, all the points from the first loading cycles are recorded and the data acquisition performed for the consequent cycles was according to as follows:

- From cycles 1 to 1000: all cycles recorded.
- From cycles 1 000 to 10 000: two consecutive cycles recorded every 20 cycles.
- From cycles 10 000 to 100 000: two consecutive cycles recorded every 200 cycles.
- From cycles 100 000 to 1 000 000: two consecutive cycles recorded every 2 000 cycles.
- From cycles 1 000 000 until the end: two consecutive cycles recorded every 5 000 cycles.

A minimum of two consecutive cycles are necessary to perform the data analysis, which is the same used for complex modulus test, described in Section 2.4.3. Figure 6-2 presents a

scheme exemplifying the data acquisition during a fatigue test used in this work and same as found in Mangiafico (2014) and Cardona Ramirez (2016).

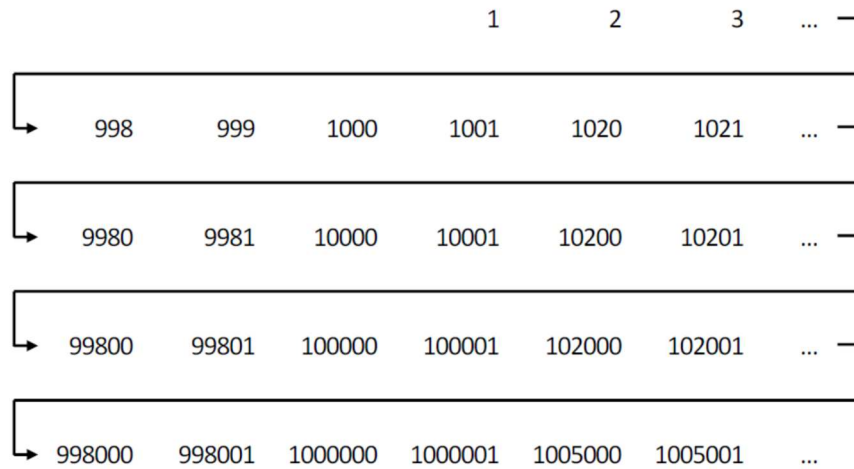


Figure 6-2. Scheme of recorded cycles during the fatigue test (adapted from Mangiafico, 2014)

In order to analyse the fatigue test, especially defining the failure criteria based on global measurements of the sample, the evolution of  $|E^*|$  and  $\varphi$  are important. Thus, the parameters calculated in the complex modulus test were also calculated for the fatigue test. Moreover, five failure criterion to the fatigue tests results were chosen to define the failure in the results presented in this work. Three criterion are based on the monitoring of global properties of the sample, whereas two criterion are based on the monitoring of local measurements of the sample. Table 6-1 presents the list of failure criterion used in this work and the application of those criteria is presented in a further section.

Table 6-1. Considered fatigue criteria and graphics to be used

Failure criteria	Symbol	Condition	Graphic
Classical approach	$N_{f\_50\%}$	$ E^* _n = 0.5 \cdot  E^* _0$	$ E^*  vs N$
Concavity change	$N_{f\_concavity}$	$\Delta b_i = \left  \frac{b_i}{\Delta b_{i-1}} \right  = 0.2$ With $b$ the slope of the cycles interval $i$	$ E^*  vs N$
Phase angle slope approach	$N_{f\_slope\_phi}$	Variation of the slope after a linear phase angle behavior	$\varphi vs N$

Loss of homogeneity with respect to average strain amplitude	$N_{f_{\Delta\epsilon_{ax}}}$	$(\Delta\epsilon_i)_n = \left  \left( \frac{\epsilon_i}{\epsilon_0} \right)_n \right  = 0.25$	$\Delta\epsilon_i \text{ vs } N$
Loss of homogeneity with respect to the phase angle of the average strain signal	$N_{f_{\Delta\phi}}$	$(\Delta\phi_i)_n =  (\phi_i - \phi)_n  = 5^\circ$	$\Delta\phi_i \text{ vs } N$

## 6.4. Tested specimens

For the fatigue resistance characterization held in this chapter, only the H specimens of each slab configuration were used. These are the specimens cored in the same compaction direction (c.f. section 3.2.3). Table 6-2 presents all the tested specimens with interface composition and tack coat rate, air voids calculated in the bituminous mixture, and strain amplitude of loading cycles.

Table 6-2. Tested specimens' composition, air voids and strain amplitudes

Specimen	Interface		Air Voids (Mix) (%)	Strain amplitude ( $\mu\text{m/m}$ )
	Composition	Tack coat rate		
A4-H1	Not applicable	Not applicable	8.3	112
A4-H5			9.2	108
A4-H7			8.4	105
A4-H2			8.8	104
A3-H12			8.6	92
A4-H6			8.4	91
A2-H2			5.1	83
A4-H4			6.9	79
B3-H6	Emulsion Bitumen 160/220	292g/m <sup>2</sup>	5.8	115
B3-H5			7.6	108
B3-H2			7.8	97

B3-H8			7.3	97
B3-H4			8.3	95
B3-H7			6.7	85
B3-H3			6.8	85
C4-H8	Emulsion bitumen 160/220 and GG 100kN/m	2×400g/m <sup>2</sup>	6.7	116
C4-H10			6.3	109
C4-H9			8.2	102
C4-H4			5.8	98
C4-H2			5.8	94
C4-H5			6.5	89
C4-H7			6.0	79
D3-H9	Emulsion bitumen 160/220 and GG 50kN/m		8.5	120
D3-H10			7.0	112
D3-H2			7.3	104
D3-H8			8.1	104
D3-H1			7.5	100
D3-H5			9.1	89
D3-H6			8.2	83
D3-H7	7.4		82	
E3-H11	Emulsion bitumen 160/220 with SBS and GG 100kN/m		7.3	116
E3-H8			7.7	111
E3-H6			6.7	104
E3-H9			7.0	93
E3-H5			6.9	86
E3-H4			8.2	86
E3-H7	6.3		84	

## 6.5. Example of fatigue tests results: B3-H4, 90 $\mu\text{m}/\text{m}$

In this section an example of fatigue test results is presented concerning specimen B3-H4, containing only interface with emulsion bitumen, and with a strain level targeted at 90 $\mu\text{m}/\text{m}$ . The results are divided into local measurements (Figure 6-3) and global measurements (Figure 6-4). In addition, the five failure criteria are presented in their respective plot. The couple of extensometers of 72.5mm control the targeted strain amplitude. Whereas the couple of extensometers of 75mm measures the strain. The considered strain used for complex modulus calculation was the average of the four extensometers. In addition, the strain amplitude controlled slightly increases during the tests. Thus, an average of the strain amplitude of the number of loading cycles to failure, considering the earliest criteria, was used to define the actual strain amplitude of the test. For these reasons, some strain amplitudes were different from the one targeted before the test, with a maximum of  $\pm 10\mu\text{m}/\text{m}$  variation. The individual extensometers data, as well as the average of the four extensometers are plotted in Figure 6-3(a). In this example, the targeted strain amplitude was 90 $\mu\text{m}/\text{m}$ , but the tested strain calculated from the average was 95 $\mu\text{m}/\text{m}$ . Figure 6-3(b) presents the strain variation in relation to the mean strain value. A higher variation (25%) in one extensometer indicates that the strain is heterogeneous due to the appearance of local macro-cracks, which represents failure. For the example of this section, the strain variation criterion of failure ( $N_{f\_{\Delta\epsilon_{ax}}}$ ) was  $7.2 \cdot 10^5$  cycles. Figure 6-3(c), on the other hand, presents the phase angle variation observed on each extensometer measurement. One more time, the failure criterion is based on the appearance of local macro-cracks, translated into a variation of  $\pm 5^\circ$  of measure in one extensometer. For the example of this section, the strain variation criterion of failure ( $N_{f\_{\Delta\phi}}$ ) was  $9.0 \cdot 10^5$  cycles.

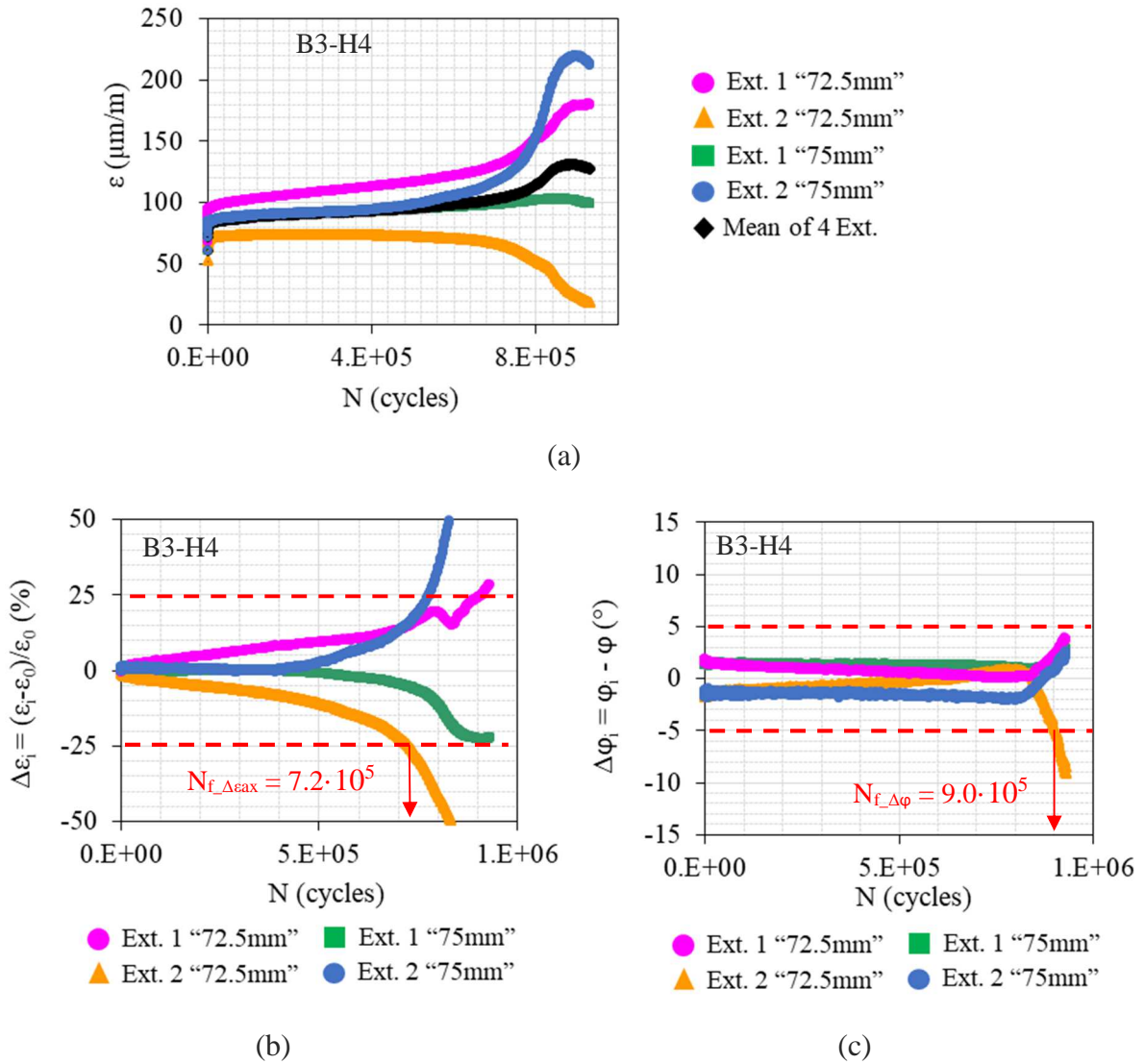
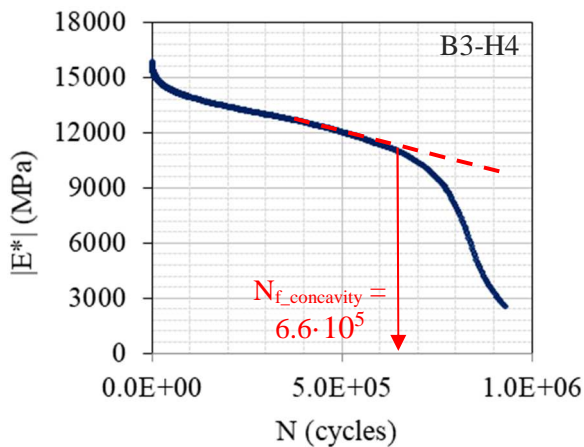


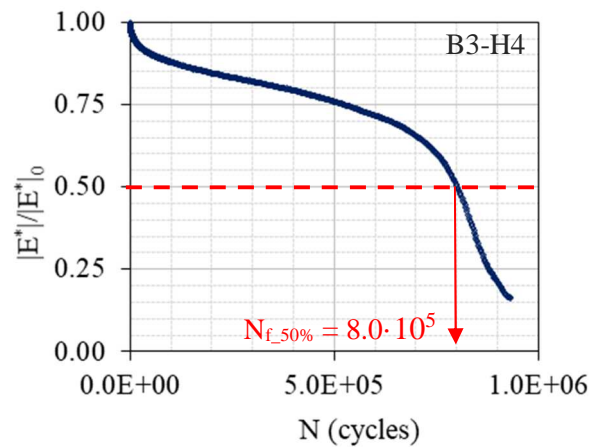
Figure 6-3. Local measurements during fatigue tests, concerning B3-H4: (a) extensometers  $l_1$  (72.5mm) and  $l_2$  (75mm) and their average vs testing number of cycles, (b) divergence of individual extensometer measurement in relation to the strain average, and (c) divergence of individual extensometer phase angle measurement in relation to the average phase angle

Concerning the global measurements, Figure 6-4(a) presents the complex modulus evolution during the test when subjected to the cyclic loading. The failure based on the concavity change ( $N_{f\_concavity}$ ) obtained from this plot, which was  $6.6 \cdot 10^5$  cycles. Figure 6-4(b) presents the complex modulus evolution during the test expressed in terms of its normalized value, which is the value of complex modulus of the cycle  $n$  ( $|E^*|_n$ ) divided by the initial modulus value ( $|E^*|_0$ ). When the normalized value reaches 0.5, it means the complex modulus measured in the specimen has decreased 50% of its initial value. Thus, the failure based on this decrease

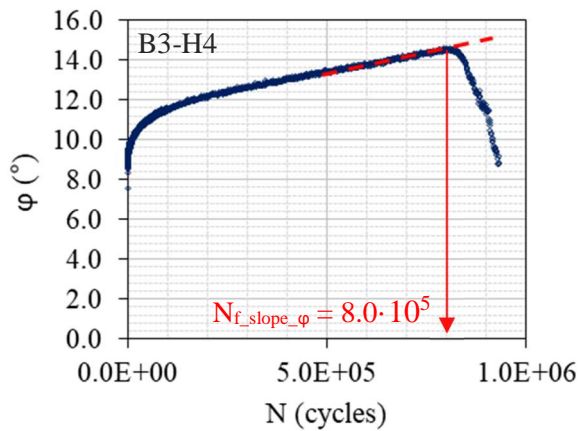
( $N_{f_{50\%}}$ ) is easily obtained from this plot, which was  $8.0 \cdot 10^5$  cycles for B3-H4. Another important global measurement is the phase angle, presented in Figure 6-4(c). From this plot, the last failure criterion used in this work is obtained, which is the variation in the slope of linear fit from the curve phase angle un function of the number of loading cycles ( $N_{f_{slope_\phi}}$ ), as illustrated in the mentioned figure. For this example, the number of cycles to failure was  $8.0 \cdot 10^5$  cycles. Figure 6-4(d) presents the stress measured during the test when subjected to the cyclic loading. Figure 6-4(e) presents the Cole-Cole plot and Figure 6-4(f) presents the fatigue test in black space. Finally, Figure 6-4(f) presents the temperature measured by the PT100 transducer on the specimen's surface. From this last plot, a self-heating was observed due to the loading cycles that could explain the complex modulus variation at the beginning of the test, in accordance with Di Benedetto et al. (2011), Nguyen et al. (2012), Tapsoba et al. (2013), Mangiafico et al. (2015) and Babadopoulos (2017).



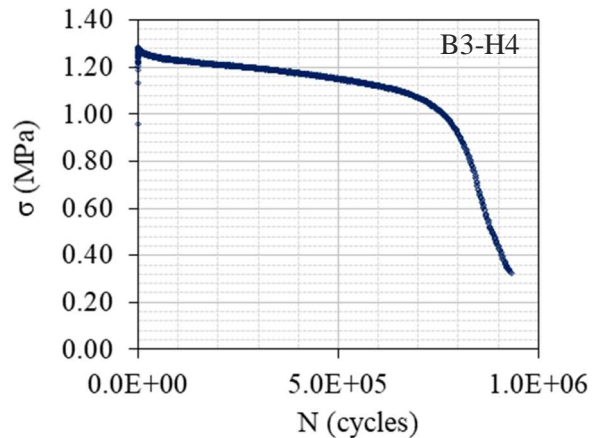
(a)



(b)



(c)



(d)



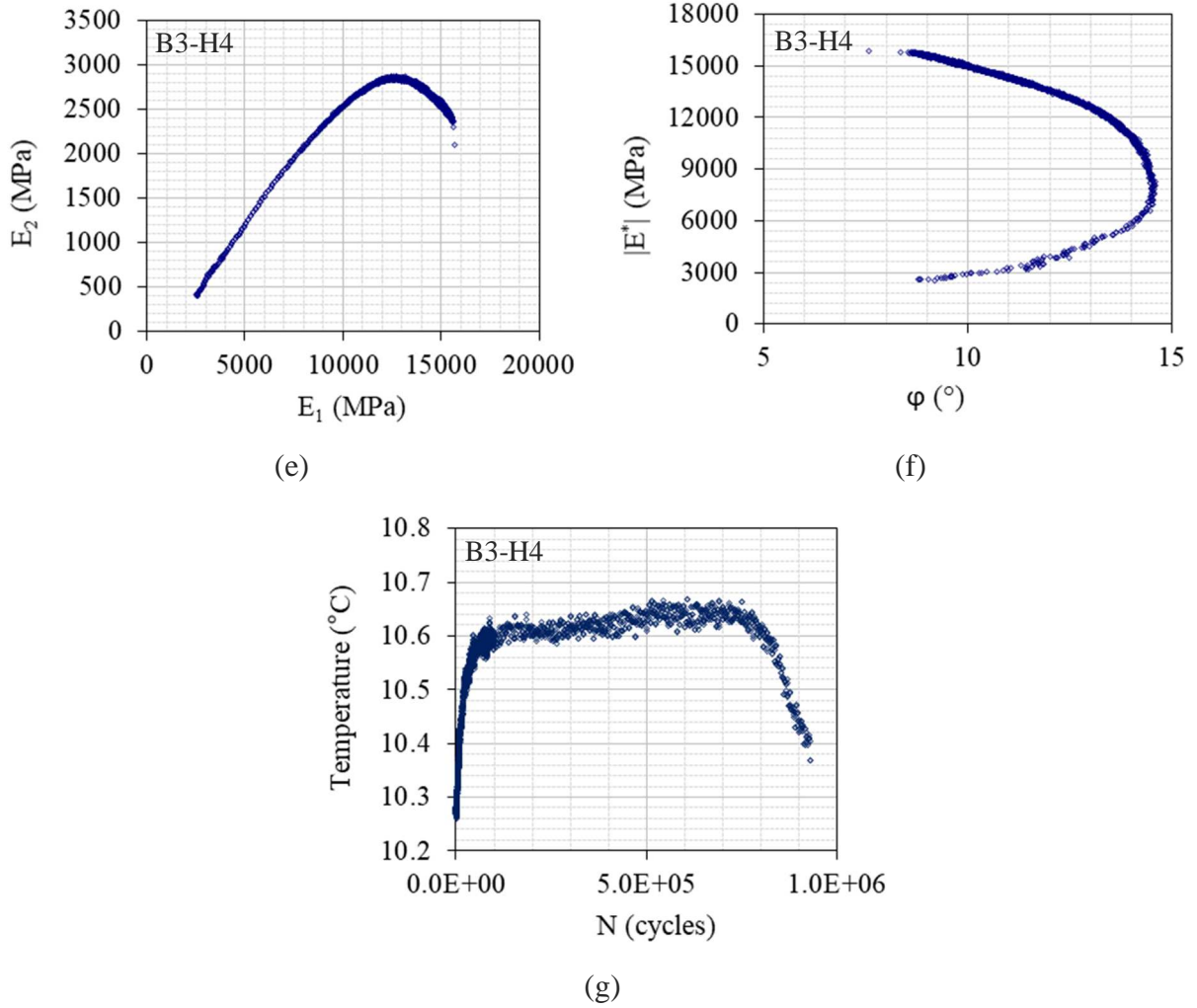


Figure 6-4. Global measurements during fatigue tests, concerning B3-H4: (a)  $|E^*|$  vs  $N$  curve, (b)  $|E^*|/|E^*|_0$  vs  $N$  curve, (c) Phase angle vs  $N$  curve, (d) stress vs  $N$  curve, (e) Cole-cole plot, (f) Black diagram, and (g) Temperature vs  $N$  curve.

Non-negligible differences were found between the  $N_f$  values obtained concerning the five different criteria. Figure 6-5 presents the  $|E^*|$  vs  $N$  curve with the five different  $N_f$  values for comparison purposes. The criterion with the highest sensibility to the variation in the slope of the mentioned curve is the  $N_{f\_concavity}$ . Thus, it is the most accurate criterion to identify the transition between phase II to phase III. Moreover, it was the earliest failure criterion between the five used criteria. The classical  $N_{f\_slope\_phi}$  and  $N_{f\_50\%}$  criteria yielded the same value, which was a higher number of cycles to failure than the concavity criterion. Finally, the latest failure was indicated by local criterion  $N_{f\_Delta phi}$ , resulting in an overestimation of the failure. However, the  $N_f$  considered in the work presented in this chapter is the mean value from the five different failure criteria chosen.

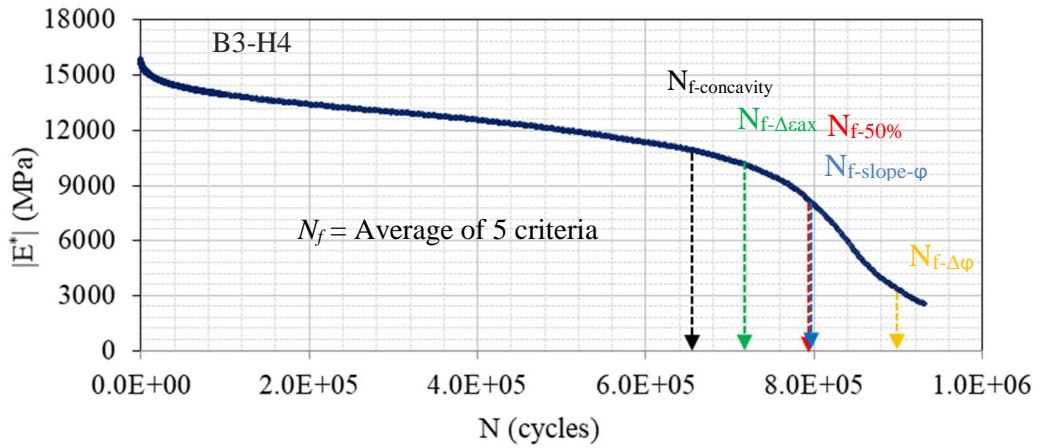


Figure 6-5. Representation of the different  $N_f$  values of the B3-H4 fatigue test according to each failure criterion

## 6.6. Classical analysis of fatigue tests in cylindrical samples results

This section presents the fatigue test results obtained for the ensemble of configurations analyzed in this thesis. Initially, eight tests were programmed, but for configurations B, C, and E, only seven results are presented. This was consequence of the limited amount of samples available due to the reduction caused by some experimental difficulties (e.g. problems during the test concerning temperature controlling, or strain controlling, press calibration, etc) resulting in the waste of samples.

### 6.6.1. Influence of strain level on fatigue

Figure 6-6 presents the normalized complex modulus in function of the number of cycles during the fatigue tests for specimens from configuration A (no interface). From test results, it is noticeable that higher strain amplitudes supported less number of cycles before the deterioration. Some tests did not present the rapid decrease of complex modulus measurements characteristic of phase III: A4-H1, A4-H2, A4-H6, and A4-H7. It was due to the appearance of localized physical macro-cracks usually outside of the span of the extensometers, causing a total deterioration of the specimen in few cycles.

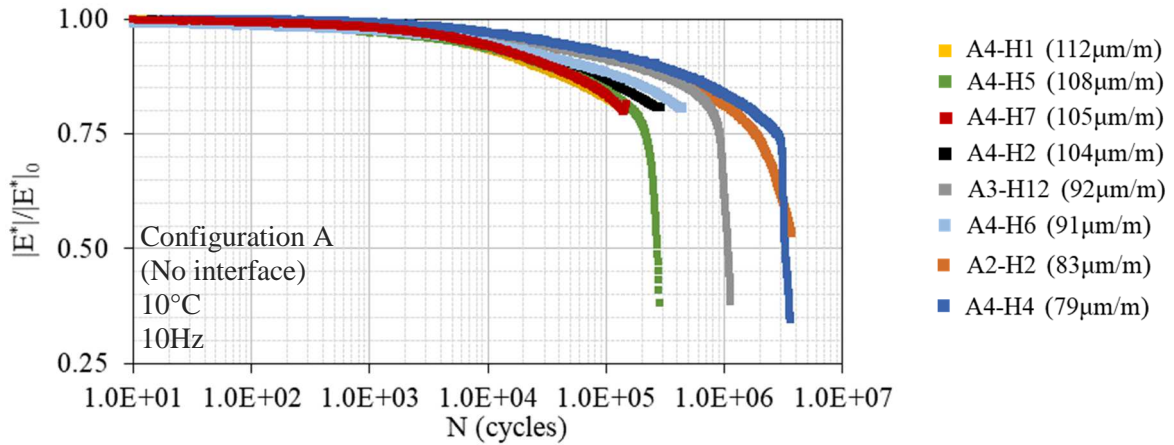


Figure 6-6. Fatigue test results in normalized complex modulus vs number of cycles at different strain levels concerning configuration A

Figure 6-7 presents the normalized complex modulus in function of the number of cycles during the fatigue tests for specimens from configuration B (interface containing only emulsion bitumen). Once again, the increase in the strain amplitude caused a faster decrease in the modulus during the fatigue tests. In this case, only specimen B3-H2 did not present phase III on its curve shape, for the same reasons as mentioned concerning configuration A.

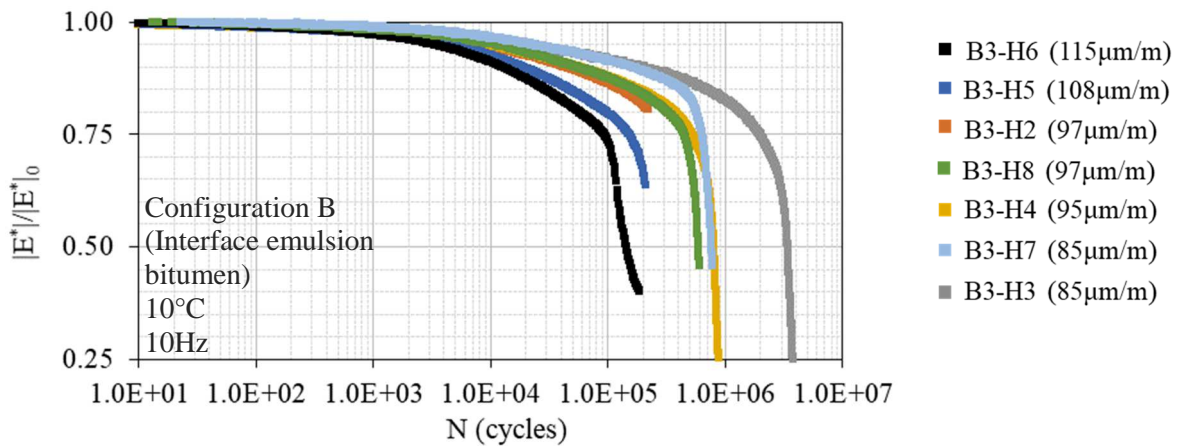


Figure 6-7. Fatigue test results in normalized complex modulus vs number of cycles at different strain levels concerning configuration B

Figure 6-8 presents the normalized complex modulus in function of the number of cycles during the fatigue tests for specimens from configuration C (geogrid of 100kN/m and emulsion bitumen). Similar to the results obtained for configuration A and B, the tests conducted at higher strain levels presented a faster decrease in the complex modulus during the test. The geogrid presence in these results had no influence on this subject, concerning configuration C. However,

specimen C4-H4 presented two abrupt variations on its curve: approximately on cycles 30 and 200.

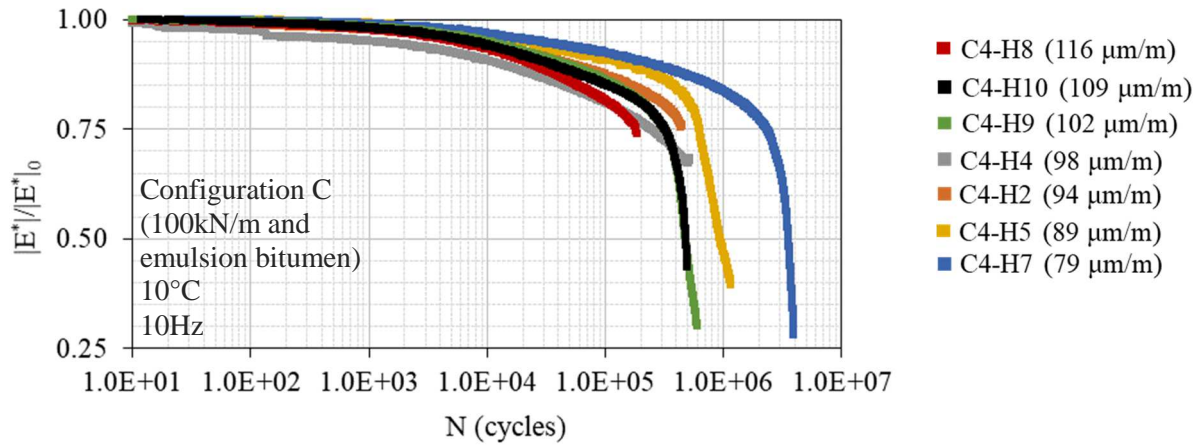


Figure 6-8. Fatigue test results in normalized complex modulus vs number of cycles at different strain levels concerning configuration C

Figure 6-9 presents the normalized complex modulus in function of the number of cycles during the fatigue tests for specimens from configuration D (geogrid of 50kN/m and emulsion bitumen). One more time, for the mentioned configuration, the same trend of results was obtained concerning the strain level influence on fatigue results. Moreover, the type of geogrid (variation of its resistance) did not influence the subject discussed in this section.

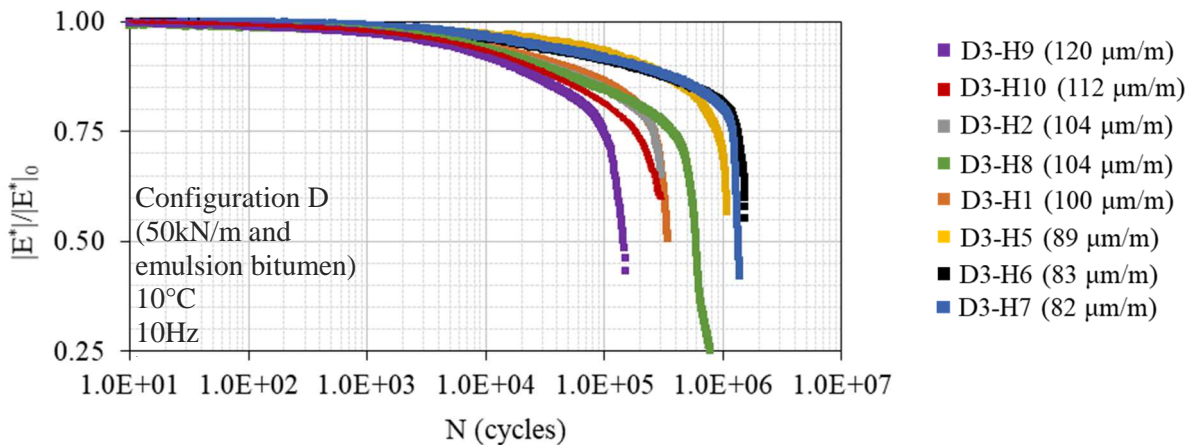


Figure 6-9. Fatigue test results in normalized complex modulus vs number of cycles at different strain levels concerning configuration D

Finally, Figure 6-10 presents the normalized complex modulus in function of the number of cycles during the fatigue tests for specimens from configuration E (geogrid of 100kN/m and

emulsion bitumen modified by SBS). The variation in the emulsion used to bond the geogrid in the interface did not influence the strain level influence, in accordance with the results obtained for the other four configurations.

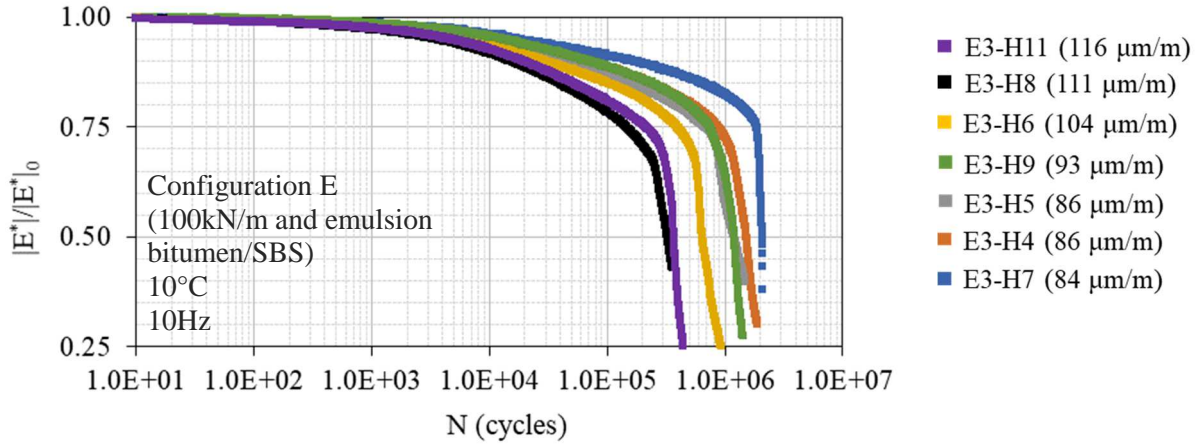


Figure 6-10. Fatigue test results in normalized complex modulus vs number of cycles at different strain levels concerning configuration E

### 6.6.2. Analysis of fatigue life (number of cycles to failure)

The bituminous mixture fatigue performance is evaluated by the number of cycles to failure, which represents its fatigue life. Five different criteria were used in this investigation and were previously presented in Table 6-1. Figure 6-11 presents the  $N_f$  obtained from the different criteria and the average, concerning the specimens of configuration A (no interface). Table 6-3 presented the five different  $N_f$  obtained with average, standard deviation and coefficient of variation, concerning the specimens of configuration A.

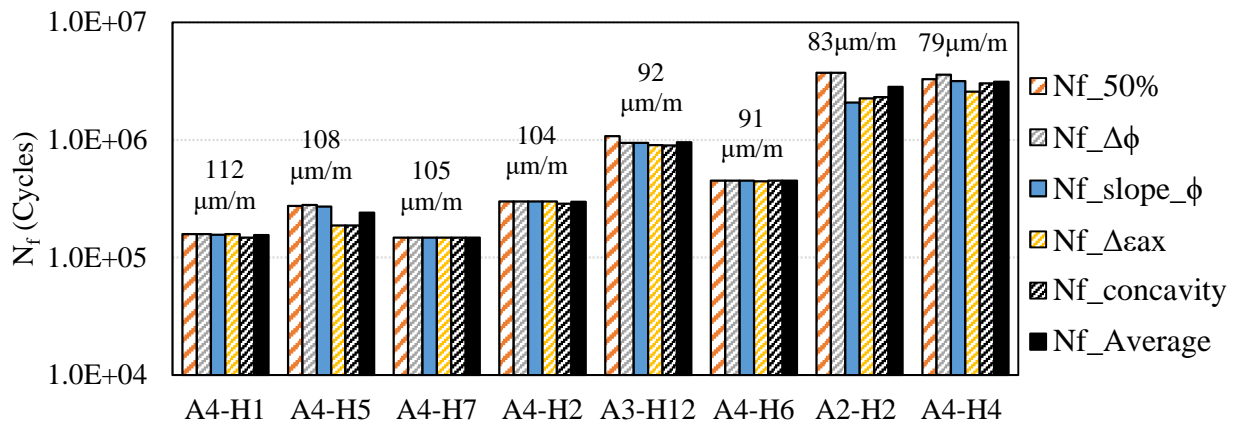


Figure 6-11.  $N_f$  values obtained from to the five different criteria and their average at different strain levels concerning configuration A

Table 6-3. Variation between the five different  $N_f$  concerning the specimens from configuration A

Specimen	$\Delta\varepsilon$	$N_{f_{50\%}}$ (cycles)	$N_{f_{slope_\phi}}$ (cycles)	$N_{f_{\Delta\phi}}$ (cycles)	$N_{f_{\Delta\varepsilon_{ax}}}$ (cycles)	$N_{f_{concavity}}$ (cycles)	$N_{f_{Average}}$ (cycles)	Standard deviation	Coef. of variation
A4-H1	112	1.6E+05	1.6E+05	1.6E+05	1.6E+05	1.5E+05	1.6E+05	4.3E+03	2.8%
A4-H5	108	2.7E+05	2.7E+05	2.8E+05	1.9E+05	1.9E+05	2.4E+05	4.8E+04	19.9%
A4-H7	105	1.5E+05	1.5E+05	1.5E+05	1.5E+05	1.5E+05	1.5E+05	N/A	N/A
A4-H2	104	3.0E+05	3.0E+05	3.0E+05	3.0E+05	2.9E+05	3.0E+05	5.4E+03	1.8%
A3-H12	92	1.1E+06	9.5E+05	9.4E+05	9.0E+05	9.0E+05	9.5E+05	7.3E+04	7.7%
A4-H6	91	4.5E+05	4.5E+05	4.5E+05	4.5E+05	4.5E+05	4.5E+05	N/A	N/A
A2-H2	83	3.7E+06	2.1E+06	3.7E+06	2.3E+06	2.3E+06	2.8E+06	8.3E+05	29.5%
A4-H4	79	3.3E+06	3.2E+06	3.6E+06	2.6E+06	3.0E+06	3.1E+06	3.7E+05	11.8%

N/A: Not applicable

From the figure, it is observed that  $N_{f_{50\%}}$ ,  $N_{f_{slope_\phi}}$ , and  $N_{f_{\Delta\phi}}$ , presented similar values and higher than  $N_{f_{concavity}}$  and  $N_{f_{\Delta\varepsilon_{ax}}}$  for the results of configuration A. Concerning the specimens A4-H7 and A4-H6, they did not reach the failure criteria, due to the appearance of macro-cracks outside the extensometers span, as previously discussed. In this case, the last cycle recorded was considered as the  $N_f$  for both specimens. In addition, A4-H5 and A2-H2 presented the higher variation of failure criteria values, 19.9% and 29.5% respectively. It indicates that, for these specimens, a higher heterogeneity of loading distribution during the test occurred. Different reasons could have caused it, e.g. sawing imperfections, extensometer misplacement (positioned slightly inclined in relation to specimen's height), etc.

Figure 6-12 presents the  $N_f$  obtained from the different criteria with the average, concerning the specimens of configuration B (interface containing only emulsion bitumen). Table 6-4 presented the five different  $N_f$  obtained with average, standard deviation and coefficient of variation, concerning the specimens of configuration B.



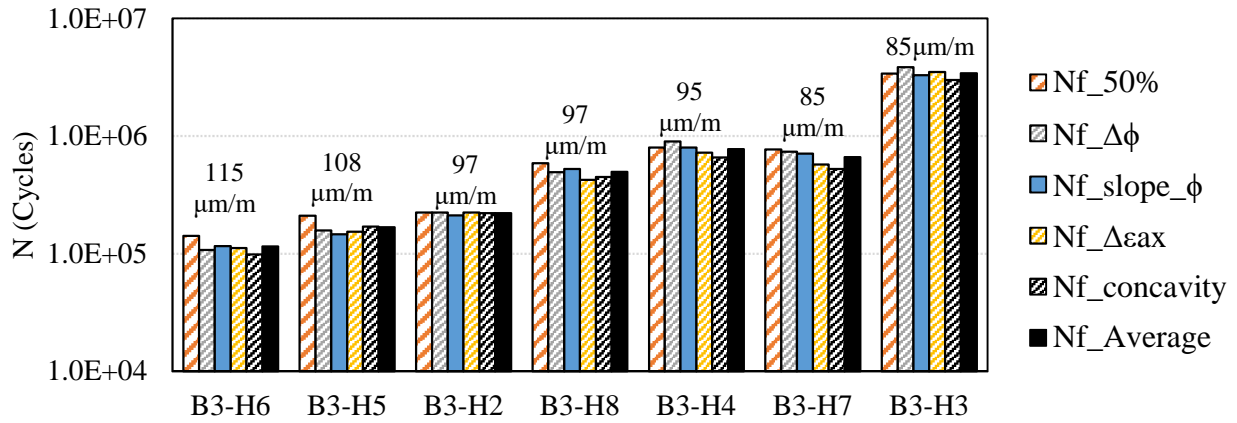


Figure 6-12.  $N_f$  values obtained from the five different criteria and their average at different strain levels concerning configuration B

Table 6-4. Variation between the five different  $N_f$  concerning the specimens from configuration B

Specimen	$\Delta\epsilon$	$N_{f_{50\%}}$ (cycles)	$N_{f_{slope_\phi}}$ (cycles)	$N_{f_{\Delta\phi}}$ (cycles)	$N_{f_{\Delta\epsilon_{ax}}}$ (cycles)	$N_{f_{concavity}}$ (cycles)	$N_{f_{Average}}$ (cycles)	Standard deviation	Coef. of variation
B3-H6	115	1.4E+05	1.2E+05	1.1E+05	1.1E+05	9.9E+04	1.2E+05	1.6E+04	14.1%
B3-H5	108	2.1E+05	1.5E+05	1.6E+05	1.5E+05	1.9E+05	1.7E+05	2.5E+04	15.1%
B3-H2	97	2.2E+05	2.1E+05	2.2E+05	2.2E+05	2.2E+05	2.2E+05	5.2E+03	2.4%
B3-H8	97	5.9E+05	5.3E+05	4.9E+05	4.3E+05	4.5E+05	5.0E+05	6.4E+04	12.9%
B3-H4	95	8.0E+05	8.0E+05	9.0E+05	7.2E+05	6.6E+05	7.8E+05	9.1E+04	11.7%
B3-H7	85	7.7E+05	7.1E+05	7.4E+05	5.7E+05	5.2E+05	6.6E+05	1.1E+05	16.2%
B3-H3	85	3.4E+06	3.3E+06	3.9E+06	3.5E+06	3.0E+06	3.4E+06	3.1E+05	9.1%

The  $N_{f_{50\%}}$  was the highest failure criterion and  $N_{f_{concavity}}$  the lowest for almost all the results obtained from specimens of configuration B. Concerning the variation between the five criteria, the values were closed for all the specimens (ranging from 9.1% to 16.2%), except B3-H2 (2.4%). This last specimen was also one that the test ended in the transition between phases II and III due to macro-cracks outside the extensometer’s span.

Figure 6-13 presents the  $N_f$  obtained from the different criteria with the average, concerning the specimens of configuration C (geogrid of 100kN/m and emulsion bitumen). Table 6-5 presented the five different  $N_f$  obtained with average, standard deviation and coefficient of variation, concerning the specimens of configuration C.

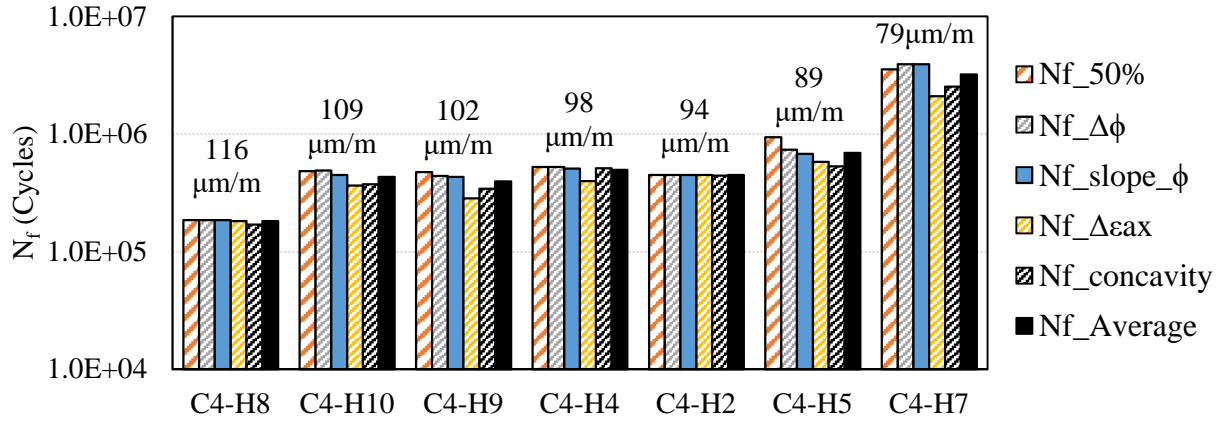


Figure 6-13.  $N_f$  values obtained from the five different criteria and their average at different strain levels concerning configuration C

Table 6-5. Variation between the five different  $N_f$  concerning the specimens from configuration C

Specimen	$\Delta\epsilon$	$N_{f_{50\%}}$ (cycles)	$N_{f_{slope_\phi}}$ (cycles)	$N_{f_{\Delta\phi}}$ (cycles)	$N_{f_{\Delta\epsilon_{ax}}}$ (cycles)	$N_{f_{concavity}}$ (cycles)	$N_{f_{Average}}$ (cycles)	Standard deviation	Coef. of variation
C4-H8	116	1.9E+05	1.9E+05	1.9E+05	1.8E+05	1.7E+05	1.8E+05	6.9E+03	3.8%
C4-H10	110	4.8E+05	4.5E+05	4.9E+05	3.7E+05	3.7E+05	4.3E+05	5.9E+04	13.7%
C4-H9	102	4.8E+05	4.3E+05	4.4E+05	2.8E+05	3.4E+05	4.0E+05	7.9E+04	19.9%
C4-H4	98	5.3E+05	5.1E+05	5.3E+05	4.0E+05	5.1E+05	5.0E+05	5.4E+04	10.8%
C4-H2	94	4.5E+05	4.5E+05	4.5E+05	4.5E+05	4.4E+05	4.5E+05	N/A	N/A
C4-H5	89	9.4E+05	6.8E+05	7.4E+05	5.8E+05	5.3E+05	6.9E+05	1.6E+05	23.1%
C4-H7	79	3.6E+06	3.9E+06	3.9E+06	2.1E+06	2.5E+06	3.2E+06	8.4E+05	26.2%

N/A: Not applicable

Concerning configuration C, the same trend observed in configurations A and B was again observed.  $N_{f_{50\%}}$  was the highest failure criterion, whereas  $N_{f_{concavity}}$  and  $N_{f_{\Delta\epsilon_{ax}}}$ , the lowest. However, a higher coefficient of variation was observed, ranging from 10.8% (C4-H4) to 26.2% (C4-H7). Specimens C4-H2 and C4-H8 were the ones presenting the test end in the transition between phases II and III, as previously discussed for configurations A and B.

Figure 6-14 presents the  $N_f$  obtained from the different criteria with the average, concerning the specimens of configuration D (geogrid of 50kN/m and emulsion bitumen). Table 6-6 presented the five different  $N_f$  obtained with average, standard deviation and coefficient of variation, concerning the specimens of configuration D.



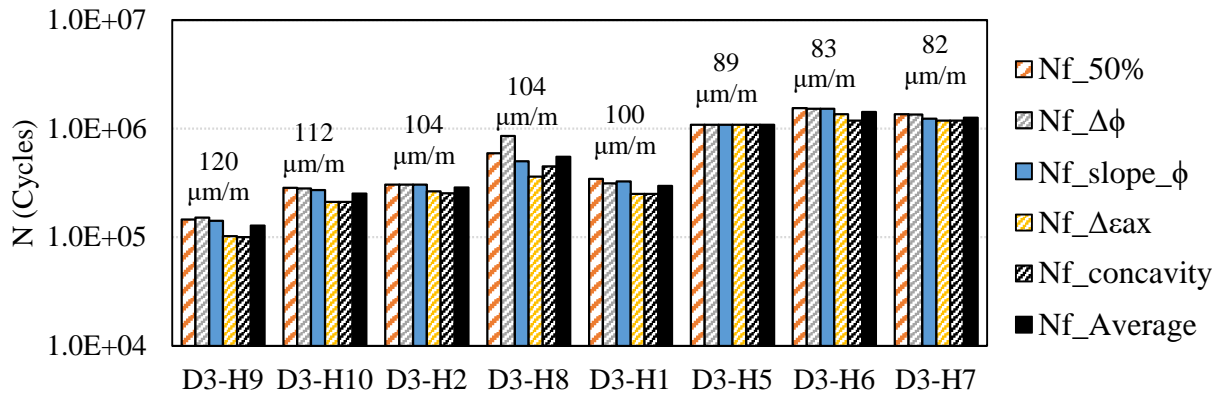


Figure 6-14.  $N_f$  values obtained from the five different criteria and their average at different strain levels concerning configuration D

Table 6-6. Variation between the five different  $N_f$  concerning the specimens from configuration D

Specimen	$\Delta\epsilon$	$N_{f_{50\%}}$ (cycles)	$N_{f_{slope_\phi}}$ (cycles)	$N_{f_{\Delta\phi}}$ (cycles)	$N_{f_{\Delta\epsilon_{ax}}}$ (cycles)	$N_{f_{concavity}}$ (cycles)	$N_{f_{Average}}$ (cycles)	Standard deviation	Coef. of variation
D3-H9	120	1.5E+05	1.4E+05	1.5E+05	1.0E+05	1.0E+05	1.3E+05	2.5E+04	19.7%
D3-H10	111	2.9E+05	2.7E+05	2.8E+05	2.1E+05	2.1E+05	2.5E+05	3.8E+04	14.9%
D3-H2	104	3.1E+05	3.1E+05	3.1E+05	2.6E+05	2.5E+05	2.9E+05	2.6E+04	9.0%
D3-H8	104	5.9E+05	5.0E+05	8.6E+05	3.6E+05	4.5E+05	5.5E+05	1.9E+05	34.3%
D3-H1	100	3.5E+05	3.3E+05	3.1E+05	2.5E+05	2.5E+05	3.0E+05	4.5E+04	15.0%
D3-H5	89	1.1E+06	1.1E+06	1.1E+06	1.1E+06	1.1E+06	1.1E+06	N/A	N/A
D3-H6	83	1.5E+06	1.5E+06	1.5E+06	1.4E+06	1.2E+06	1.4E+06	1.5E+05	10.7%
D3-H7	82	1.4E+06	1.2E+06	1.4E+06	1.2E+06	1.2E+06	1.3E+06	8.5E+04	6.7%

N/A: Not applicable

Concerning configuration D, once again  $N_{f_{50\%}}$  was the highest failure criterion and  $N_{f_{concavity}}$  the lowest for almost all the results obtained. However, specimen D3-H8 presented the highest coefficient of variation of all specimens from all configurations, 34.3%. In addition, the coefficients of variation observed for the others specimens were approximately the same obtained for configuration B.

Figure 6-15 presents the  $N_f$  obtained from the different criteria with the average, concerning the specimens of configuration E (geogrid of 100kN/m and emulsion bitumen modified by SBS). Table 6-7 presented the five different  $N_f$  obtained with average, standard deviation and coefficient of variation, concerning the specimens of configuration E.

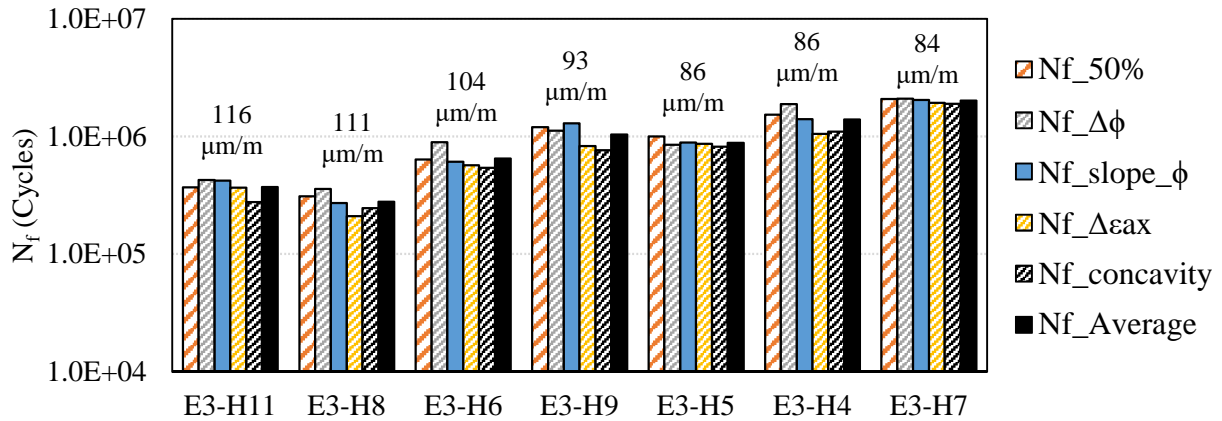


Figure 6-15.  $N_f$  values obtained from the five different criteria and their average at different strain levels concerning configuration E

Table 6-7. Variation between the five different  $N_f$  concerning the specimens from configuration E

Specimen	$\Delta\epsilon$	$N_{f\_50\%}$ (cycles)	$N_{f\_slope\_φ}$ (cycles)	$N_{f\_Δ\phi}$ (cycles)	$N_{f\_Δ\epsilon_{ax}}$ (cycles)	$N_{f\_concavity}$ (cycles)	$N_{f\_Average}$ (cycles)	Standard deviation	Coef. of variation
E3-H11	116	3.7E+05	4.2E+05	4.3E+05	3.7E+05	2.8E+05	3.7E+05	6.1E+04	16.3%
E3-H8	111	3.1E+05	2.7E+05	3.6E+05	2.1E+05	2.5E+05	2.8E+05	5.7E+04	20.5%
E3-H6	104	6.4E+05	6.1E+05	9.0E+05	5.7E+05	5.4E+05	6.5E+05	1.4E+05	21.8%
E3-H9	93	1.2E+06	1.3E+06	1.1E+06	8.3E+05	7.7E+05	1.0E+06	2.3E+05	22.3%
E3-H5	90	1.0E+06	8.9E+05	8.5E+05	8.6E+05	8.2E+05	8.8E+05	6.9E+04	7.8%
E3-H4	86	1.5E+06	1.4E+06	1.9E+06	1.1E+06	1.1E+06	1.4E+06	3.4E+05	24.3%
E3-H7	84	2.1E+06	2.0E+06	2.1E+06	1.9E+06	1.9E+06	2.0E+06	9.0E+04	4.5%

Finally, unlike the previous test results, concerning configuration E,  $N_{f\_Δ\phi}$  was the highest value between the other criteria, followed by  $N_{f\_50\%}$ . However, once again  $N_{f\_concavity}$  was the lowest for almost all the results obtained. Concerning the coefficient of variation, a similar range of configuration C was obtained.

### 6.6.3. The Wöhler curve and determination of the $\epsilon_6$ value

Each strain amplitude provides a number of cycles to failure associated with it. Plotting the values obtained from the fatigue tests previously presented, a Wöhler curve was obtained for each slab configuration. This curve represents a linear relationship between loading and failure, which is useful to characterize the fatigue resistance of a bituminous mixture. This linear relation is obtained from a linear regression in logarithmic axis, according to the following equation.

$$\log(N) = a + \frac{1}{b} \cdot \log(\varepsilon) \tag{Eq. 6-1}$$

Where  $a$  and  $b$  are fitting constants. Moreover, coefficient of determination of the linear fit ( $R^2$ ) is calculated from the regression. From this fitted equation, strain amplitude corresponding to one million cycles loading fatigue life, called  $\varepsilon_6$ , is estimated according to the following equation.

$$\varepsilon_6 = 10^{b(6-a)} \tag{Eq. 6-2}$$

Therefore, Figure 6-16 presents the plot  $\log(N)$  vs  $\log(\varepsilon)$  concerning the test results obtained for configuration A (no interface) with the Wöhler curve obtained from regression. In addition, the equation of regression,  $R^2$ , and  $\varepsilon_6$  are indication in the figure. Figure 6-17 presents the same plot and information, but concerning configuration B (interface containing only emulsion bitumen). Figure 6-18 presents the same plot and information, but concerning configuration C (geogrid of 100kN/m and emulsion bitumen). Figure 6-19 presents the same plot and information, but concerning configuration D (geogrid of 50kN/m and emulsion bitumen). Figure 6-20 presents the same plot and information, but concerning configuration E (geogrid of 100kN/m and emulsion bitumen modified by SBS).

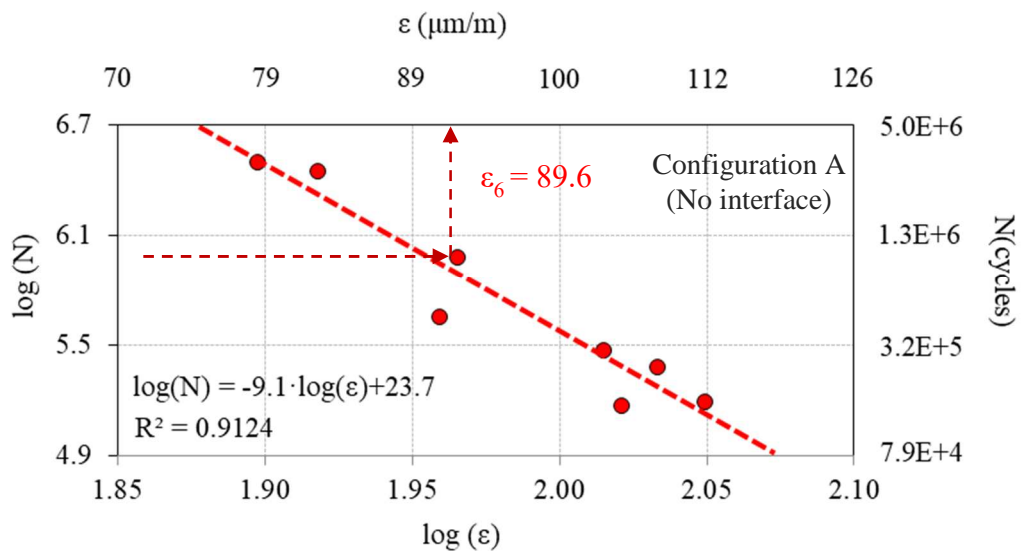


Figure 6-16. Wöhler curve of configuration A and  $\varepsilon_6$  estimation

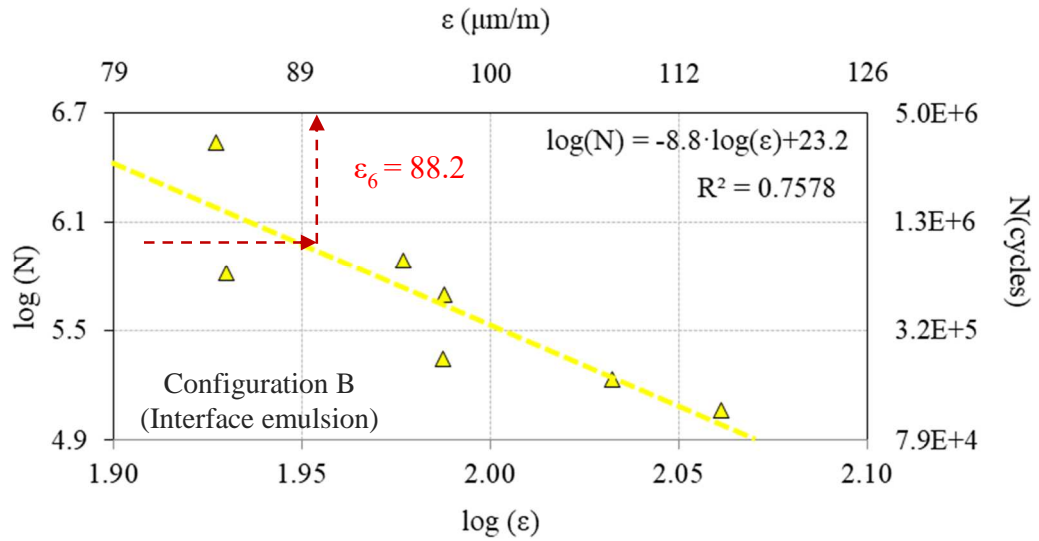


Figure 6-17. Wöhler curve of configuration B and  $\epsilon_6$  estimation

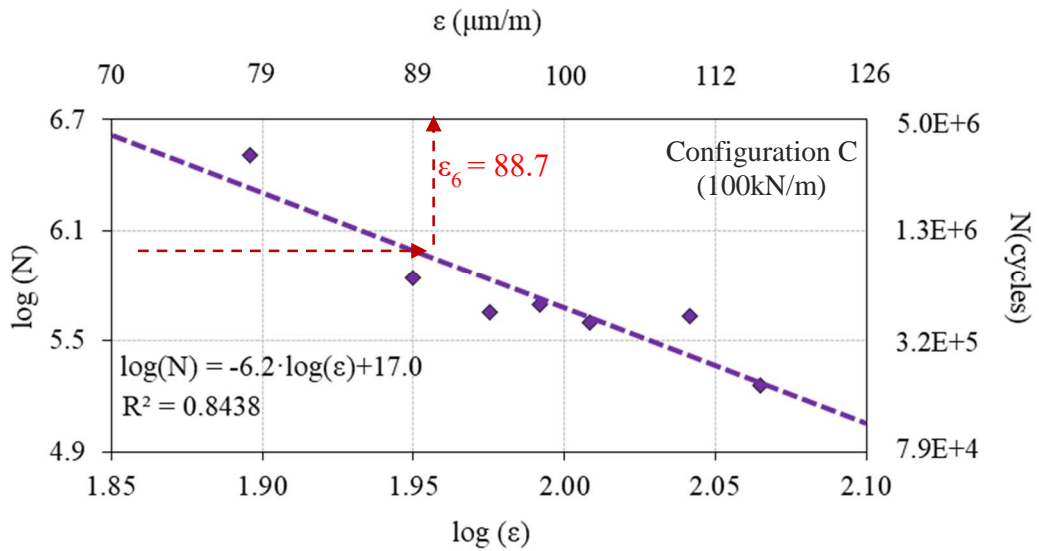


Figure 6-18. Wöhler curve of configuration C and  $\epsilon_6$  estimation

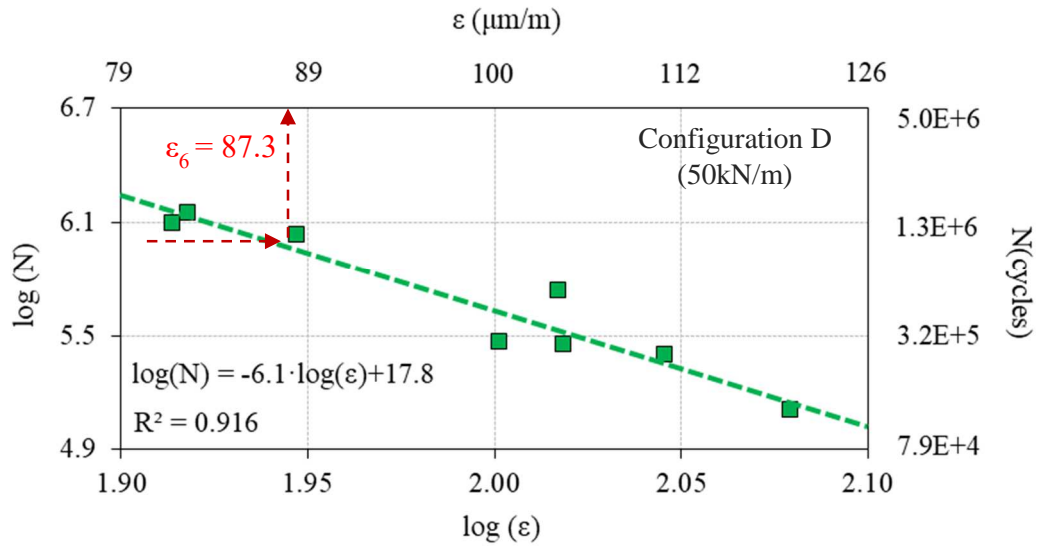


Figure 6-19. Wöhler curve of configuration D and  $\epsilon_6$  estimation

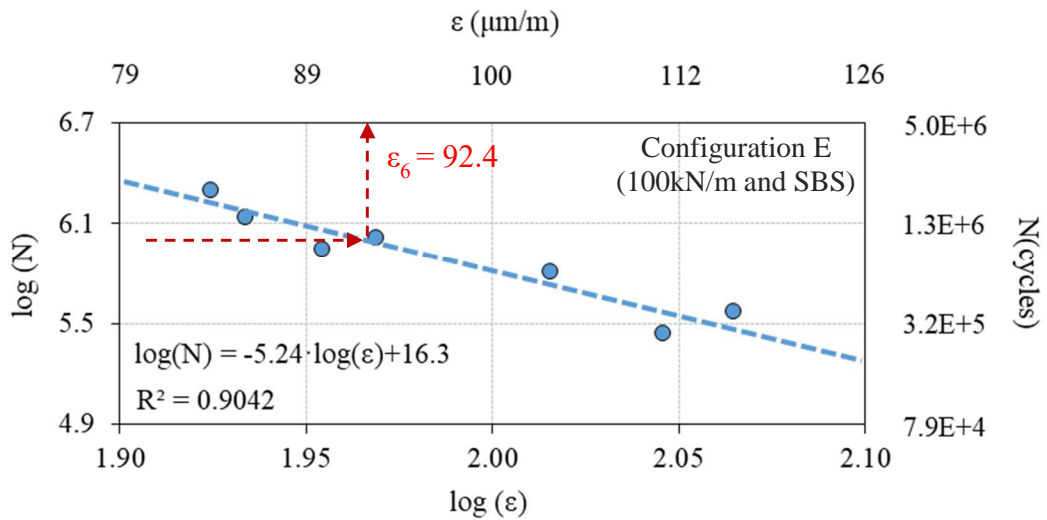


Figure 6-20. Wöhler curve of configuration E and  $\epsilon_6$  estimation

From the results, configurations A, D and E presented elevated  $R^2$  values, 91.24%, 91.60%, and 90.42%, respectively. These results indicate low dispersions in the fatigue test results concerning the mentioned configurations. Configuration C also presented an elevated  $R^2$  (84.38%), and configuration B presented the lowest  $R^2$  (75.78%) between the analyzed configurations. The comparisons between the different configurations' Wöhler curves and  $\epsilon_6$  are held in the next section.

### 6.6.4. Influence of geogrid on fatigue resistance

Figure 6-21 presents the Wöhler curves obtained for all five analyzed slab configurations. The different configurations presented distinct susceptibility to strain amplitude variation. At high strain amplitudes, more cycles were necessary to lead the reinforced specimens (configurations C, D and E) to failure. Moreover, configuration E, which contains emulsion modified by SBS, presented the highest fatigue resistance at high strain amplitudes, possibly related to the presence of polymer in the interface. At low strain amplitudes, the reinforced specimens presented less and similar fatigue resistance than the unreinforced specimens (configurations A and B). Configurations C (100kN/m and emulsion bitumen) and D (50kN/m and emulsion bitumen) presented very similar Wöhler curves, the same observation was made for configurations A (no interface) and B (interface with only emulsion bitumen). This result indicates that the increase of interface bond quality due to the presence of SBS was more significant on fatigue resistance than the maximum tensile strength of geogrid. However, similarly to what occurred in the complex modulus and tension test carried out in the type H specimen from the last chapters, the geogrid might not be entirely mobilized during the test. This could lead to an underestimation of geogrid contribution to the fatigue performance of reinforced bituminous mixtures, mainly related to the specimen's geometry used to the characterization in this work.

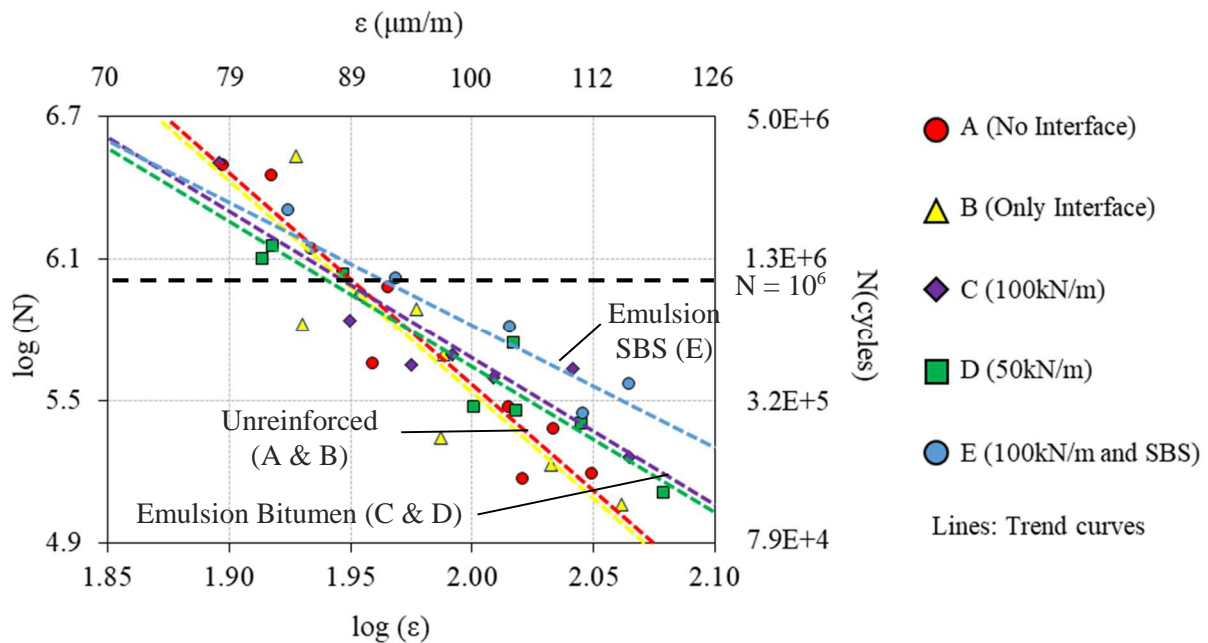


Figure 6-21. Fatigue test results in Wöhler curves for all analyzed configurations, reinforced and unreinforced specimens

Another important observation from Figure 6-21 is the  $\varepsilon_6$  comparison among configurations. This parameter is used to calculate the admissible strain ( $\varepsilon_{adm}$ ), used in the French design method of bituminous mixture pavement structures, standardized by NF P98-086 (2019). Configuration E presented the highest  $\varepsilon_6$  value, approximately 92 $\mu\text{m}/\text{m}$ , whereas the other four configurations presented similar  $\varepsilon_6$  values, between 87 and 89 $\mu\text{m}/\text{m}$ . However, due to the high scattered character of fatigue tests, the uncertainty of  $\varepsilon_6$  ( $\Delta\varepsilon_6$ ) can be estimated for each regression according to the following equations (NF P98-086 2019).

$$\Delta\varepsilon_6 = 0.5 \cdot \varepsilon_6(10^{-2bs_0} - 10^{2bs_0}) \tag{Eq. 6-3}$$

$$S_0 = S_N \cdot \sqrt{\left[ \frac{1}{N} + \frac{(\overline{\log\varepsilon} - \log\varepsilon)^2}{(n-1) \cdot S_{\log\varepsilon}^2} \right]} \tag{Eq. 6-4}$$

$$S_N = S_{\log N} \cdot \sqrt{\frac{(1-R) \cdot (n-1)}{n-2}} \tag{Eq. 6-5}$$

Where n is the number of tested specimens;  $\overline{\log\varepsilon}$  is the average of all  $\log\varepsilon$  values of tested specimens;  $S_{\log\varepsilon}$  is the standard deviation of  $\log\varepsilon$  values of tested specimens; and  $S_{\log N}$  is the standard deviation of  $\log N$  values of tested specimens. Figure 6-22(a) presents the comparison between the  $\varepsilon_6$  values with their uncertainty  $\Delta\varepsilon_6$  obtained for each configuration. Figure 6-22(b) presents the slopes from the Wöhler curves regressions ( $-1/b$ ). The parameter  $b$  is also used in the design method for the calculation of  $\varepsilon_{adm}$  in bituminous mixture layer.

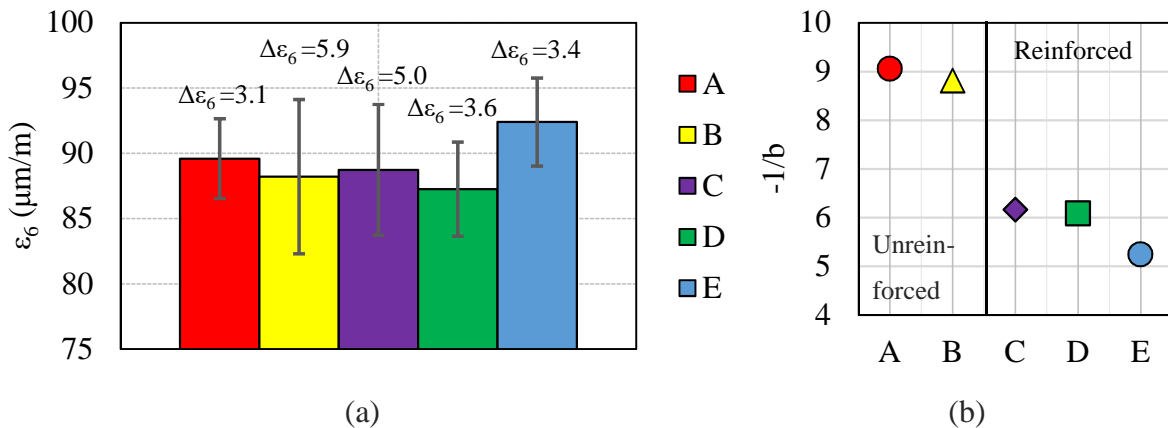


Figure 6-22. Analysis of parameter used in the French design methods of pavements: (a) strain amplitude corresponding to one million cycles loading fatigue life ( $\varepsilon_6$ ) with its uncertainty ( $\Delta\varepsilon_6$ ), and (b) slope of Wöhler curves ( $-1/b$ )

From the results is noticeable that, concerning  $\varepsilon_6$  and  $\Delta\varepsilon_6$  values obtained, the five different configurations did not present difference in relation to one another. This indicates that, for this parameter, no useful geogrid contribution to the French design method was observed. However, concerning  $-1/b$ , the increase in these parameters results in a decrease of  $\varepsilon_{adm}$  for bituminous mixtures. Thus, the reinforcement presented a positive contribution to the French design method.

## 6.7. Chapter conclusions

This chapter presented the fatigue experimental campaign of the five studied slab configurations. Sinusoidal tension-compression tests at different strain amplitudes were carried out in specimens type H. The geogrid contribution to the fatigue resistance was evaluated, as well as its influence on the French design method of pavements. Therefore, some conclusion can be drawn:

- As classically found in the literature, the tests at higher strain amplitudes supported less number of cycles before the deterioration of the specimen, regardless of geogrid presence.
- Regardless of the configuration, the earliest failure criterion was  $N_{f\_concavity}$  and it was the most accurate criterion to identify the transition between phases II to III. The classical  $N_{f\_slope\_phi}$  and  $N_{f\_50\%}$  criteria presented later failure, overestimating it.
- The different configurations presented distinct susceptibility to strain amplitude variation. Reinforced configurations (C, D, and E) were more resistant to fatigue at high strain amplitudes and less resistant to fatigue at low strain amplitudes in relation to the unreinforced ones (A and B).
- The configuration containing SBS presented the highest fatigue resistance at high strain amplitudes. The configurations with geogrid of 50 and 100kN/m and emulsion bitumen presented similar Wöhler curves. The same occurred with the unreinforced configurations (containing interface or not). It suggests that the increase of interface bond quality due to the presence of SBS was more significant on fatigue resistance than the maximum tensile strength of geogrid.



- The geogrid might not be entirely mobilized during the fatigue test that could lead to an underestimation of geogrid contribution to the fatigue performance of reinforced bituminous mixtures, mainly related to the specimen's geometry used to the characterization in this work.
- For the French design method for pavements, according to the parameter  $\varepsilon_6$  obtained in this work, the geogrid reinforcement effect was negligible. Wöhler curve slope ( $-1/b$ ) was smaller for reinforced specimens.

# Chapter 7: CRACK PROPAGATION TEST CAMPAIGN

7.1. Introduction .....	236
7.2. Objectives .....	237
7.3. Experimental procedures and devices .....	237
7.3.1. Hydraulic press and instrumentation.....	237
7.3.2. Specimens preparation .....	239
7.3.3. Four Points Bending Notched Fracture (FPBNF) test protocol .....	240
7.4. Digital Image Correlation (DIC) analysis .....	241
7.4.1. Procedure of analysis .....	242
7.4.2. Average strain vs beam's height: principle of calculation .....	245
7.5. Tested specimens .....	246
7.6. Example of crack propagation test result: B1-B2.....	247
7.7. Force evolution with beam's deflection analysis .....	249
7.8. Analysis of crack tip height (a).....	253
7.9. Energy restitution rate ( $G_f$ ) .....	256
7.10. Average and maximum strain images analysis .....	258
7.10.1. Example of specimen without interface: A2-B3.....	258
7.10.2. Example of unreinforced specimen with interface: B1-B2.....	260
7.10.3. Example of reinforced specimen: D1-B3.....	262
7.10.4. Comparison between analysed configurations.....	265
7.11. Chapter conclusions .....	267

## 7.1. Introduction

Recently, the use of geogrids has increased as a technical solution to rehabilitate pavements, extend its service life and reduce maintenance costs (de Bondt 2012). They could be used for both rehabilitation and construction of new bituminous pavements (GMA 2002; COST Action 2006). Many works in the literature evidences that the reinforcement by geogrid can be effective to reduce the cracking propagation in roadways. The geogrids have been proposed for controlling reflective cracking since the 1970s when the American Federal Highway Administration (FHWA) instituted a program to reduce reflective cracking in roadways (FHWA 1974, Carver and Sprague 2000). The reflective cracking is the cracks on pavement overlay formed by the propagation of those presented in the underlying pavement. Interlayer reinforcement by geogrids was indicated since it could work as a stress-relieving component and thus, effective to reflective cracking retardant (de Bondt 1999). In order to evaluate the cracking resistance and propagation for reinforced bituminous mixtures in a prismatic beam shape in the laboratory scale, some authors used different test configurations. Some used the three points bending (3Pb) test (Romeo et al. 2014; Canestrari et al. 2015; Graziani et al. 2016; Zofka et al. 2016). Others used the four points bending (4Pb) test (Virgili et al. 2009; Ferroti et al. 2011; Canestrari et al. 2015; Safavizadeh et al. 2015; Arsenie et al. 2016). Other different bending type of tests can be also found in the literature (Komatsu et al. 1998; Khodaii et al. 2009; Millien et al. 2012; Obando-Ante & Palmeira 2015; Gonzalez-Torre et al. 2015; Fallah & Khodaii 2015; Pasquini et al. 2014; Gonzalez-Torre et al. 2016; Nejad et al. 2016). Mentioned works indicated a noticeable improvement in the performance of the bituminous mixtures due to the reinforcement, retarding the cracks initiation and propagation. Moreover, Digital Image Correlation (DIC) technique was found to be an advantageous tool allowing the identification of different failure mechanisms during the crack propagation in reinforced beams and showing the stress-relieving capacity of geogrid reinforcements (Romeo et al. 2014; Canestrari et al. 2015).

The purpose of this chapter is to present the crack propagation test experimental campaign studied in this work. The four-point bending notched fracture (FPBNF) tests designed at the University of Lyon/ENTPE according to Nguyen et al. (2008) were carried out in three beams from each slab configuration. The testing procedure, as well as the hydraulic press, the cameras and the transducers used to measure the physical variations, temperature, and force during the test, are fully detailed in this chapter. To better analyze the tests, 3D Digital Image Correlation (DIC) device was used to calculate the strain field during the crack propagation as well as its tip. The influence of geogrid presence and type as well as the type of emulsion tack coat on the

crack propagation resistance of bituminous mixtures are evaluated. Lastly, an analysis from DIC results is performed to evaluate the stress-relieving capacity of the fiberglass geogrid reinforcing bituminous mixtures as well as the cracking behavior.

## 7.2. Objectives

For the investigation conducted in this chapter, some objectives can be listed:

- To evaluate the influence of the presence of fiberglass geogrid and its maximum tensile strength on crack propagation resistance of bituminous mixtures.
- To assess the influence of the type of emulsion tack used as tack coat to bond the bituminous mixture layers together, on crack propagation resistance of bituminous mixtures.
- To evaluate the influence of the fiberglass geogrid in the crack tip retarding during the tests.
- To verify the mobilization level of the geogrid during the bending tests.
- To verify the applicability of Digital Image Correlation (DIC) technique to analyze the crack propagation behavior of reinforced and unreinforced specimens.
- To evaluate the stress-relieving capacity of geogrid reinforcing bituminous mixtures using DIC analysis.

## 7.3. Experimental procedures and devices

### 7.3.1. Hydraulic press and instrumentation

The test were carried out using a servo-hydraulic press INSTRON<sup>®</sup> at LGCB/LTDS laboratory of the ENTPE at Vaulx-en-Velin, France. This press produces axial loading from its actuator, located in the machine bottom part. The actuator displacement was measured by an integrated transducer and used for controlling the loading performed during the tests. The press was equipped with a Dynacell<sup>®</sup> load cell with 50kN maximum capacity, which measures the axial stress response during the test. A thermal chamber type B.I.A. Climatic<sup>®</sup> MTH6-74 was used for temperature control during the tests. However, once the specimen was placed inside the thermal chamber, there was no space to place cameras in order to capture pictures from it during the test in order to perform DIC analysis. Moreover, the thermal chamber is a closed box

with only one window upfront, which makes it impossible to capture the pictures from outside it. Thus, the modification in the thermal chamber performed by Pedraza (2018) was used in this experimental campaign. It consisted of an extension of the thermal chamber with a polystyrene-made box coupled on it. This box was structured by its edges and two glass windows were constructed on its sides. The windows were located in the same height of the specimen making it visible to the cameras' range. In addition, around the window at the inner side of the box, LED lamps were installed oriented in the direction to the specimen in order to reach the necessary luminosity for DIC analysis. Figure 7-1 presents the hydraulic press, the thermal chamber with the extension coupled to it, and the cameras positioned to capture images during the test.

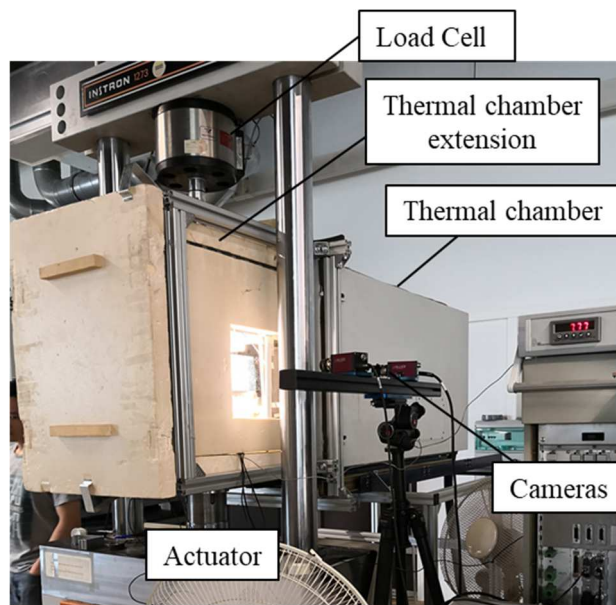


Figure 7-1. Hydraulic press, thermal chamber with extension and cameras used during FPBNF test

Three Linear Variable Differential Transducers (LVDT) were placed on supports (LVDT 1 and 3) and on beam center (LVDT 2) in order to measure the axial displacement in these three points. Beam's deflection was calculated by the LVDT2 measure corrected by the punching effect of the lower supports into the beam, obtained from LVDT1 and LVDT3 measures. Thus, the deflection was calculated according to the following equation.

$$Deflection = LVDT2 - \frac{LVDT1 + LVDT3}{2} \quad \text{Eq. 7-1}$$

Figure 7-2 presents a scheme containing all the devices used to conduct the four-point bending notched fracture (FPBNF) tests. In addition, a thermal gauge (PT100 temperature probe) fixed on the specimen surface was used to measure the specimen's temperature during the test. Furthermore, two cameras were positioned outside the thermal chamber in order to perform the DIC method.

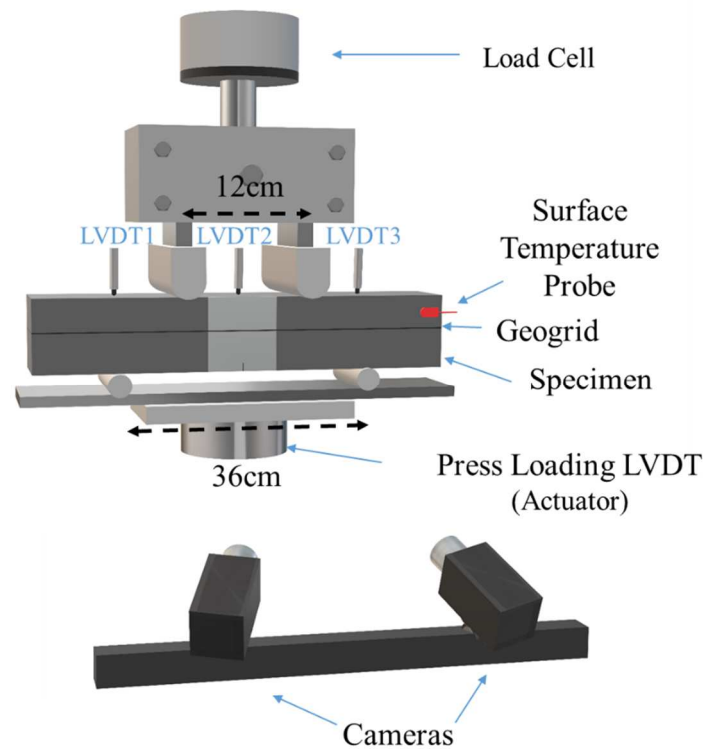


Figure 7-2. Experimental test device and procedure for FPBNF: scheme of specimen and measurement device location

### 7.3.2. Specimens preparation

As presented in Section 3.2.3, from each slab configuration, three prismatic bars, in a beam shape, with dimensions 550×70×110mm was sawed. The interface height, containing or not geogrid, was located at 65mm from the bottom and 45mm from the top of the beam. A 20mm pre-notch was sawed on its center-bottom resulting in an interface positioned in the middle of the remaining beam's height. Finally, to improve DIC accuracy, a speckle pattern was applied to the specimen rectangular central area with a thin layer of white acrylic paint and a spray of black paint on it. Figure 7-3(a) presents the illustration of the slabs composition and the final

beam used for the research development, whereas Figure 7-3(b) details the interface position in relation to the beam height.

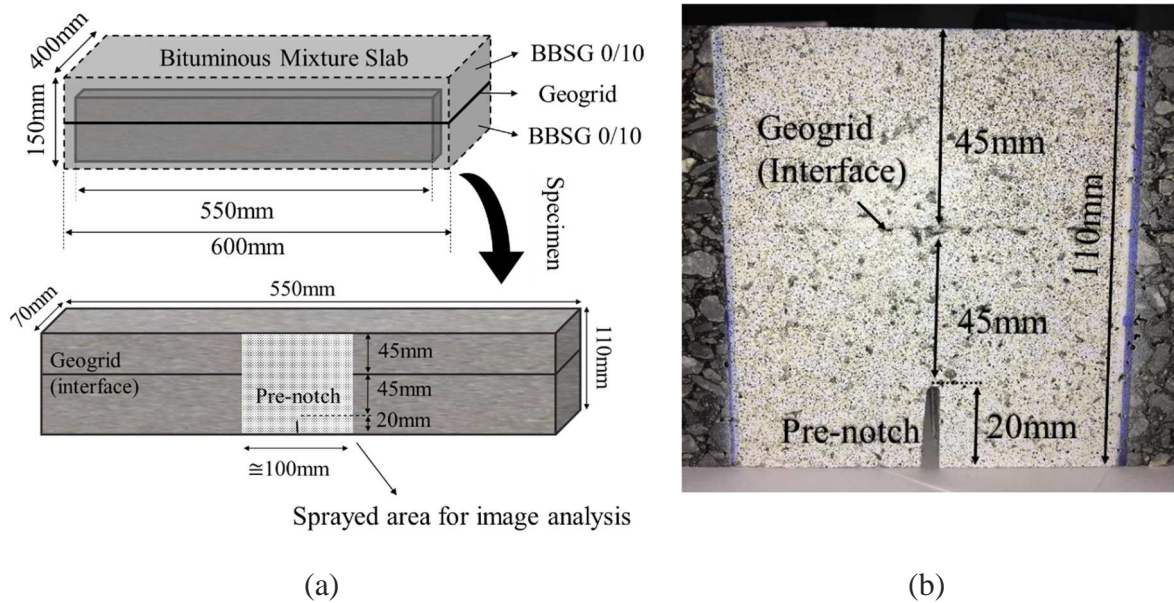


Figure 7-3. Detail of beam specimen obtained from sawing and prepared for testing: (a) position of specimen from the slab, and (b) pre-notch size and interface position in beam height

### 7.3.3. Four Points Bending Notched Fracture (FPBNF) test protocol

The specimens were conditioned at  $-5^{\circ}\text{C}$  overnight in a freezer and transferred to the press, where one additional hour of temperature conditioning at the same temperature was done. The FPBNF test was performed at a constant rate of actuator displacement: 0.2mm/min. The test was divided into two steps:

- 1) A preloading composed of two cycles of loading/unloading was performed to ensure the contact between specimen and supports. A maximum of 1kN and a minimum of 0.3kN of compression were used for these cycles.
- 2) Constant rate of actuator displacement loading was performed until the complete crack propagation throughout the specimen height.

Figure 3(b) presents a graph plotting the actuator displacement and the force (P) response measured during the test for the specimen A. At the same time, a couple of cameras was capturing high-resolution pictures of the sprayed area in a rate of 1 picture every 3 seconds, to be treated later using DIC technique discussed in the next section.

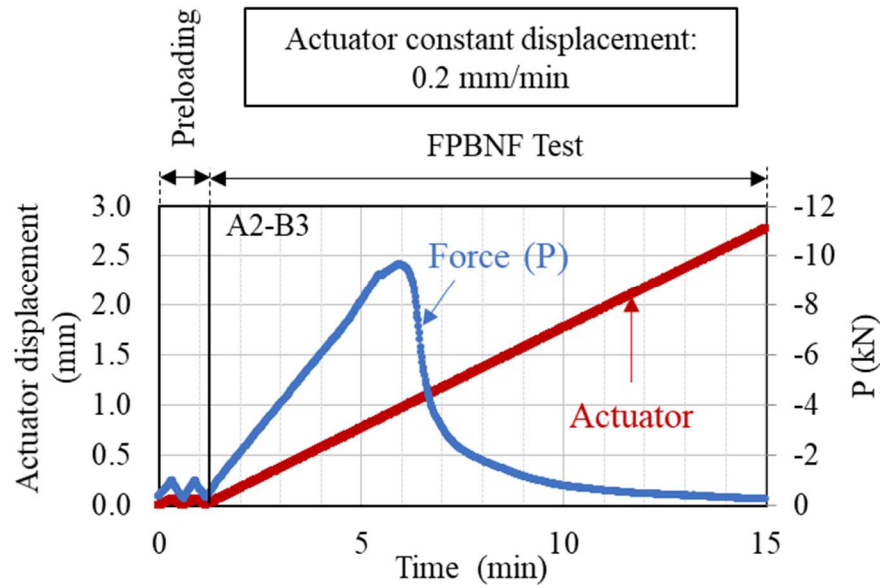


Figure 7-4. Actuator displacement and force versus time during the FPBNF test on specimen A2-B3

## 7.4. Digital Image Correlation (DIC) analysis

DIC is an optical and contactless measurement technique used to compute the displacement on a specific area of analysis (Sutton et al. 1983). From simultaneous monochromatic digital images acquired with the aid of two cameras, a 3D image was obtained by image correlation. Each picture is an arrangement of pixels in different shades of grey. The displacement is calculated by comparing subsets of virtual squares containing a small amount of pixel in original and deformed states. More details can be found at Pedraza (2018) and Attia (2020). This technique was used to compute the strain field of the beams' surface where the crack propagates during the test. The software Vic Snap (for data acquisition) and Vic 3D (for images correlation), both developed by Correlated Solutions, were employed to perform the DIC analysis conducted in this work.

The stereocorrelation is the tool used in the DIC analysis to transform two images 2D captured from two different cameras at different angles into a 3D image, similarly to the human vision operation. From these 3D images during the test, the displacements can be tracked and transformed in strain. Before each test, a stereocalibration needs to be done. This calibration consists in capturing pictures of a white target containing black dots disposed of in a mesh with known dimensions. Approximately 15 pictures of the grid on the target at different positions



are sufficient to perform the calibration. Figure 7-5 presents the pictures of the target used to this end.

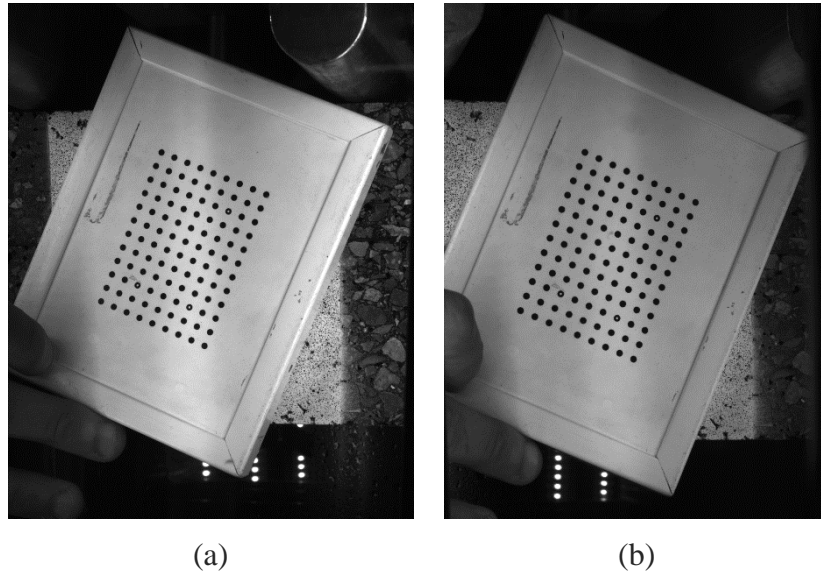


Figure 7-5. Pictures of the target with black dots for calibration of stereocorrelation taken at the same time by two different cameras: (a) camera on the left, and (b) camera on the right

#### **7.4.1. Procedure of analysis**

Using VIC-3D software, virtual gauge lines were created every 2mm of specimen height starting from notch tip. The initial height of the crack tip was the notch size ( $a_0$ ). Each virtual gauge line was composed of 200 virtual points. For each point, the horizontal strain ( $\epsilon_{xx}$ ) was calculated composing the strain field for the given area at instant  $t$ . The cracking appearance criteria, useful for crack tip identification, was the same used in previous work at University of Lyon/ENTPE and defined based on fracture mode I given by  $\epsilon_{xx} = 0.01\text{m/m}$  (Pedraza 2018). The origin of coordinates was virtually defined over the top of the notch as illustrated in Figure 7-7. Thus, the crack tip height is the coordinate  $y$  of the line presenting  $\epsilon_{xx} \geq 0.01\text{m/m}$  in any of his points for the first time since the beginning of the test. Then,  $a$  (crack tip height) =  $y + a_0$ .

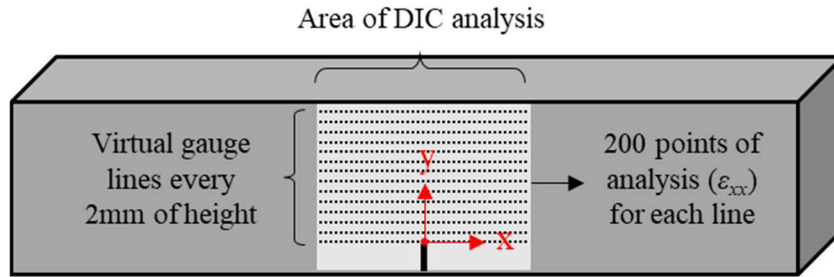


Figure 7-6. Virtual gauge lines and coordinates origin in the area of interest used in VIC-3D software for DIC analysis

From each virtual line, the  $\epsilon_{xx}$  was monitored at different instants of time during the test. Figure 7-6 presents an example concerning the specimen A2-B3, line 7 ( $y=14\text{mm}$ ), at 0s (Figure 7-6(a)), 342s (Figure 7-6(b)), and 390s (Figure 7-6(c)). The virtual gauge line was drawn on the figure by the white line. At the first figure, the specimen was not subjected to loading and, therefore, no strain was measured as indicated in the graphic below the DIC treated image. Along the course of the test, an increase of strain was measured with a concentration in the notch tip, as indicated in Figure 7-6(b). As the strain increases, the VIC-3D software defines a scale of color to indicate the strain level reached the analyzed point. In the latest point presented in Figure 7-6(c) (390s), a high strain concentration was measured around the crack and emphasized on DIC treated image by the red color. At this last point, the peak of strain ( $\epsilon_{xx} = 0.018\text{m/m}$ ) was higher than the value defined as cracking appearance criteria ( $\epsilon_{xx} = 0.01\text{m/m}$ ). However, as noticeable in the image, the crack was already passed from the analyzed line. Therefore, this criterion was validated and used to the definition of crack tip height, further presented in this chapter.

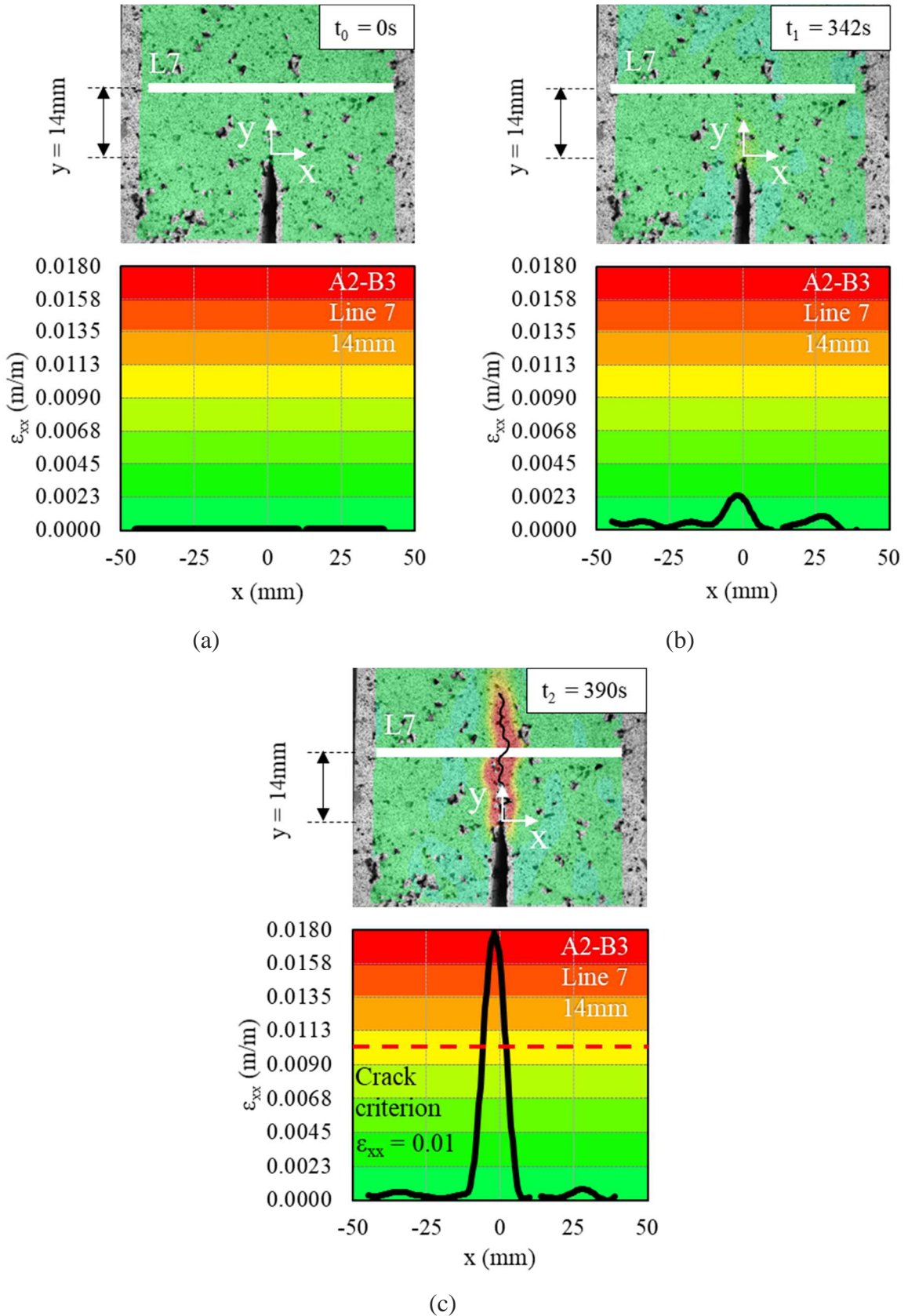


Figure 7-7. Horizontal strain curve with color scale obtained from virtual gauge line 7 (14mm of height) in DIC analysis of A2-B3 for: (a) at 0s, (b) at 342s, and (c) at 390s

### 7.4.2. Average strain vs beam's height: principle of calculation

In order to obtain the global strain in function of the beam's height, from each virtual gauge line, the strain average ( $\epsilon_{xx\text{ AVG}}$ ) of its points was calculated and plotted in function of  $Y = y$  (corresponding line coordinate) +  $a_0$ . This procedure was performed in order to obtain the classical curve of strain variation throughout the specimen's height as a result of a bending load. As the crack propagates through the central region in the analyzed area of the specimen, a reduction was applied and only the points within the central 60mm were considered in the analysis. Figure 7-8 presented the explanation of the adopted analysis methodology.

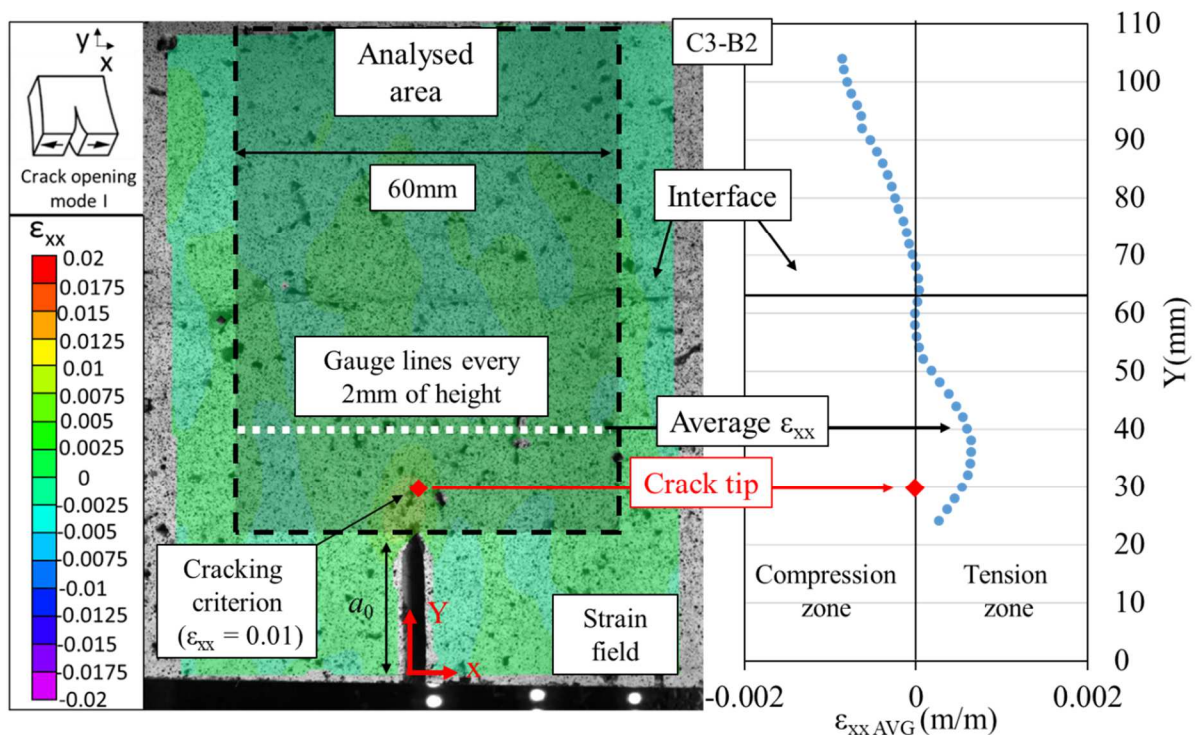


Figure 7-8. Explanation of analysis performed from data obtained with DIC using Vic-3D software

However, when the crack is open and its tip has already passed the analyzed line, the strain measured from DIC could be imprecise leading to errors in the analysis. Thus, a correction in the  $\epsilon_{xx\text{ AVG}}$  of the line in this situation was performed. It consists in disregard of the points placed at  $\pm 5\text{mm}$  from the crack in the average calculation performed for the corresponding line. To this end, the maximum strain measured on each line ( $\epsilon_{xx\text{ MAX}}$ ) is found for a given instant of time  $t$ . If  $\epsilon_{xx\text{ MAX}} \geq 0.01\text{m/m}$  (crack criterion), the coordinate  $x$  of this point is known and the points between the range of  $x \pm 5\text{mm}$  are removed from the average calculation. Moreover, if the line

just above the one lastly corrected did not present  $\epsilon_{xx\ MAX} \geq 0.01\text{m/m}$ , the same coordinate  $x$  of the previous line was used to perform the correction in this mentioned line and in all the other lines above until the top. Figure 7-9 illustrates the mentioned procedure.

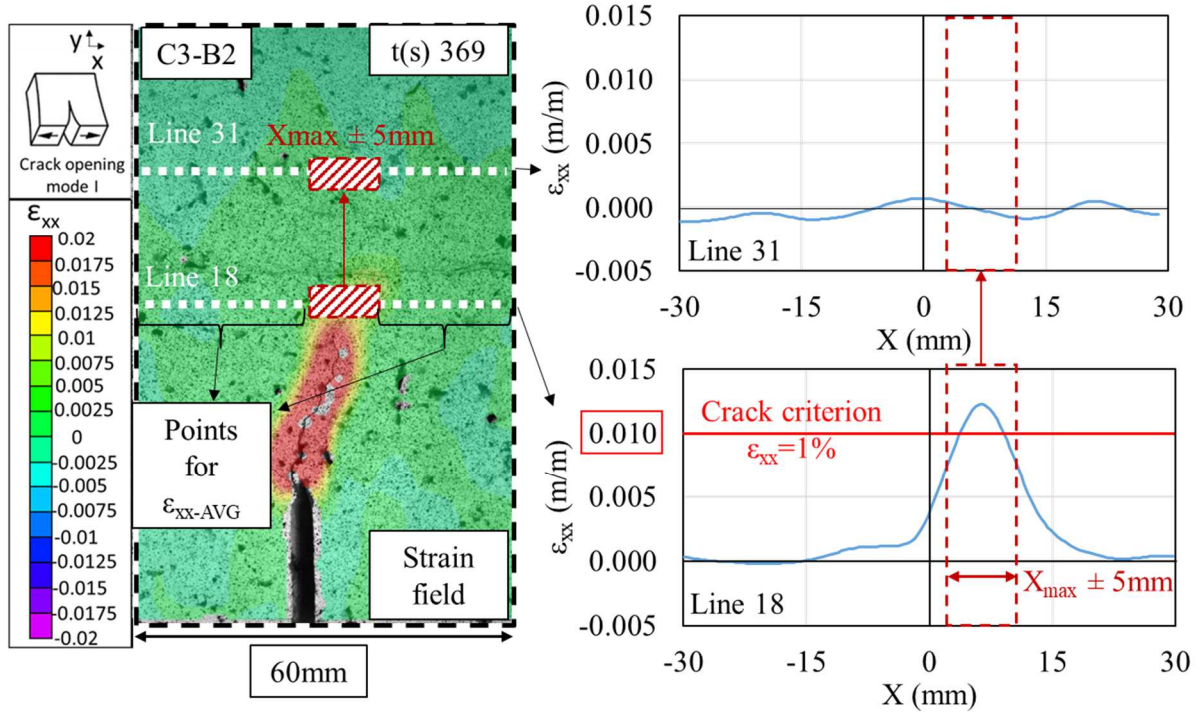


Figure 7-9. Explanation of correction performed in the calculation of average strain versus beam height

## 7.5. Tested specimens

For the crack propagation characterization held in this chapter, prismatic bars in beam shape were used. From the three beams sawed from each slab configuration, only for C all three beams were successfully tested. Concerning the other four configurations, only two specimens were successfully tested. Problems related to press calibration and handling, and temperature conditioning resulted in tests discard. Moreover, concerning the specimen B1-B3, an error in the camera data acquisition prevented to save the pictures captured during the test. Table 6-2 presents all the tested specimens with interface composition and tack coat rate, air voids calculated in the bituminous mixture, and strain amplitude of loading cycles.



Table 7-1. Tested specimens' composition, air voids in bituminous mixture and temperatures

Specimen	Interface		Air Voids (Mix) (%)	Temperature (°C)
	Composition	Tack coat rate		
A2-B2	Not applicable	Not applicable	6.3	2.3
A2-B3			7.8	-1.3
B1-B2	Emulsion Bitumen 160/220	292g/m <sup>2</sup>	5.4	-0.8
B1-B3			6.5	-1.0
C3-B1	Emulsion bitumen and GG 100kN/m	2×400g/m <sup>2</sup>	6.2	-0.4
C3-B2			4.1	2.3
C3-B3			4.7	-0.6
D1-B2	Emulsion bitumen and GG 50kN/m	2×400g/m <sup>2</sup>	6.1	-2.5
D1-B3			4.3	-1.0
E1-B1	Emulsion bitumen with SBS and GG 100kN/m	2×400g/m <sup>2</sup>	3.7	-2.3
E1-B2			3.9	-2.2

## 7.6. Example of crack propagation test result: B1-B2

In this section, an example of FPBNF test results is presented: specimen B1-H2, containing only interface with emulsion bitumen. Figure 7-10(a) presents the measured force evolution with time during the test. In this graphic, the preloading composed of the two cycles of loading/unloading performed before the test is presented. These cycles were removed from the data in further analysis since they do not represent the physical material response. Moreover, the peak of force ( $P_{max}$ ) corresponds to the beams' maximum resistance to bending load. Concerning specimen B1-H2,  $P_{max}$  was equal to 9.8kN. Figure 7-10(b) presents the measured force against the actuator displacement, which was the mode of loading input of the test. This graphic is important since the area underneath the curve corresponds to the mechanical work necessary to propagate the crack throughout the specimen's height. Thus, this parameter is used to calculate the energy restitution rate ( $G_f$ ) of fracture, further presented in this chapter. Lastly, Figure

7-10(b) presents the crack tip height ( $a$ ) vs time during the tests, obtained from DIC analysis. At the beginning of the test, the crack tip height measures the same size of the notch ( $a_0$ ) previously sawn in the center-bottom of the specimen, as explained in Section 7.3.

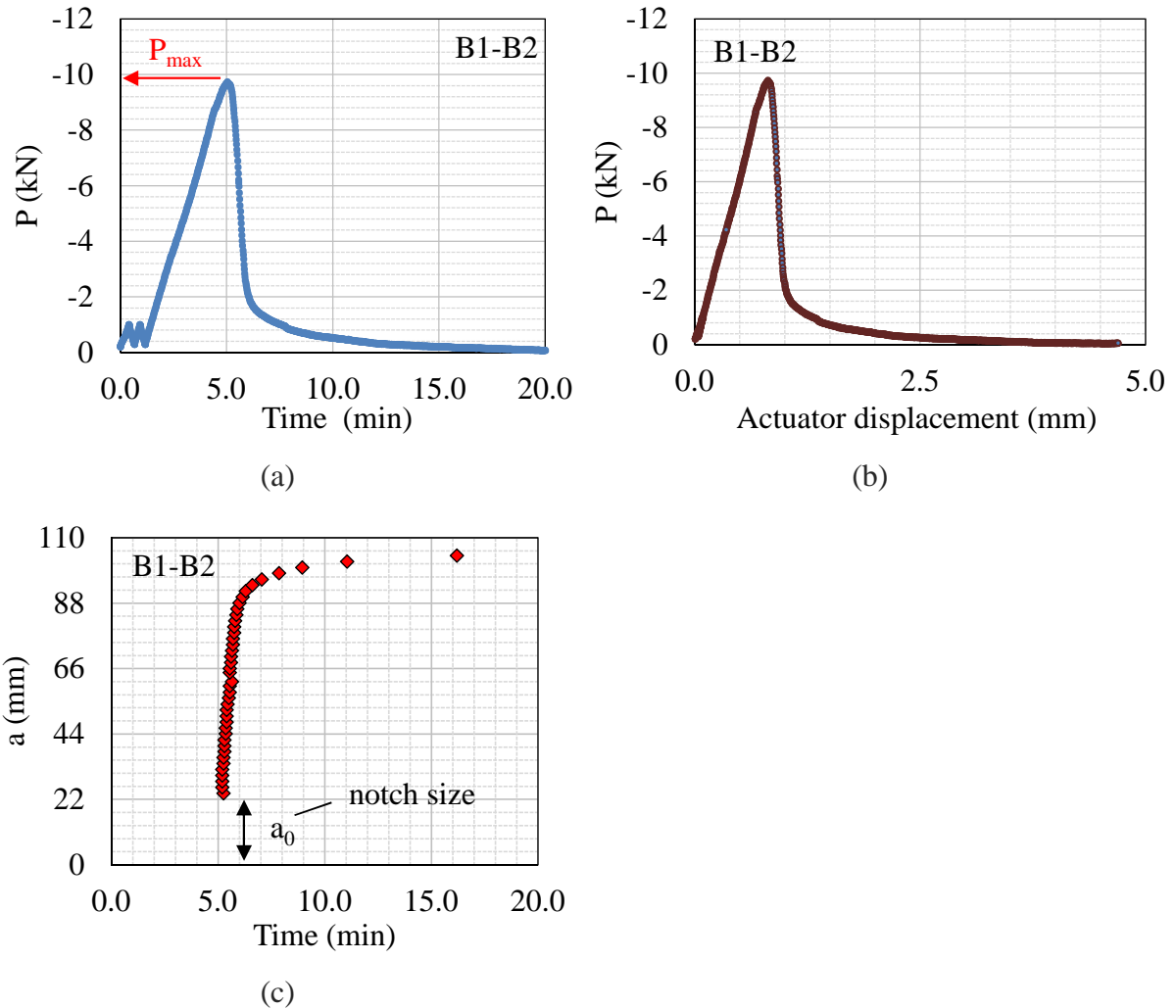


Figure 7-10. FPBNF test results example for specimen B1-B2: (a) force measured in the load cell, (b) force versus actuator displacement (test input), and (c) crack height tip evolution measured from DIC analysis

Figure 7-11 presents the graphic containing force and crack tip height in the ordinates against the beam's deflection in the abscissa. The beginning of the force curve until the peak corresponds to the stiffness of the bituminous mixture that composes the beam. Moreover, it is noticeable that, until the peak of the force curve, the crack does not propagate. The propagation initiates right after the peak of force and accelerates with the loss of beam capacity of loading support. Therefore, curve peak indicates the crack initiation and from this point, crack starts to propagate.

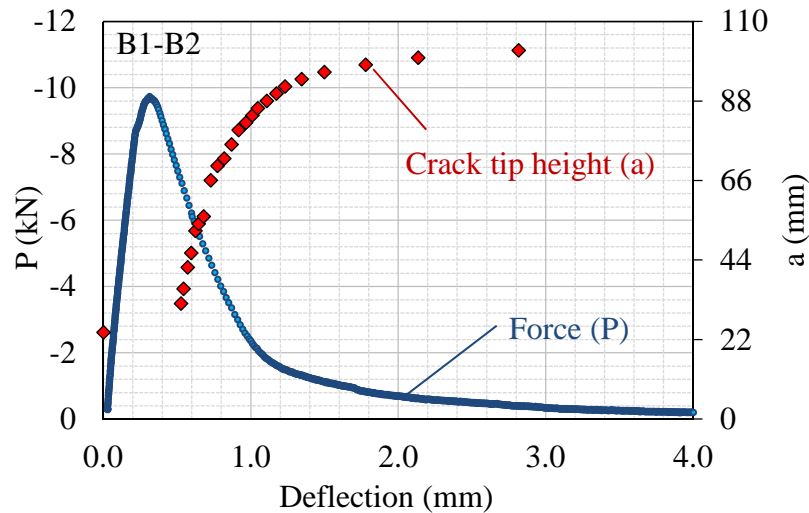


Figure 7-11. Force and crack tip height in function of beam deflection for specimen B1-B2

## 7.7. Force evolution with beam's deflection analysis

Figure 7-12(a) presents the curve  $P$  versus deflection for configuration A (no interface) and B (interface with emulsion bitumen). Similar curves and  $P_{max}$  were obtained, suggesting that the presence of an interface did not change the crack propagation resistance of the analyzed beams at the tested temperature (around  $-1^{\circ}\text{C}$ ).

Figure 7-12(b) presents the same mentioned curve for configuration C (100kN/m and emulsion bitumen). Similar curves and  $P_{max}$  were obtained suggesting good test repeatability. Unlike the last graphic containing the unreinforced specimens, the curves of configuration C did not lose rapidly its capacity of load support after 1mm of deflection. From this mentioned point, a force plateau was formed holding the force necessary to deflect the beam. At 2mm of deflection, this plateau was approximately 4kN concerning configuration C.

Figure 7-12(c) presents the curves concerning configuration D (50kN/m and emulsion bitumen). One more time the test presented good repeatability. The curves presented similar behavior even after the peak of force until 2mm of deflection. The same force plateau observed in the results of configuration C were again observed for configuration D, but with lower magnitude. At 2mm of deflection, the force plateau was approximately 2.5kN.

Figure 7-12(d) presents the curves concerning configuration E (100kN/m and emulsion bitumen modified by SBS). As the results obtained for the previous configurations, the good



test repeatability was obtained. Similarly to the obtained for the other reinforced configurations, the force plateau was again observed and measured 4kN of force at 2mm of deflection.

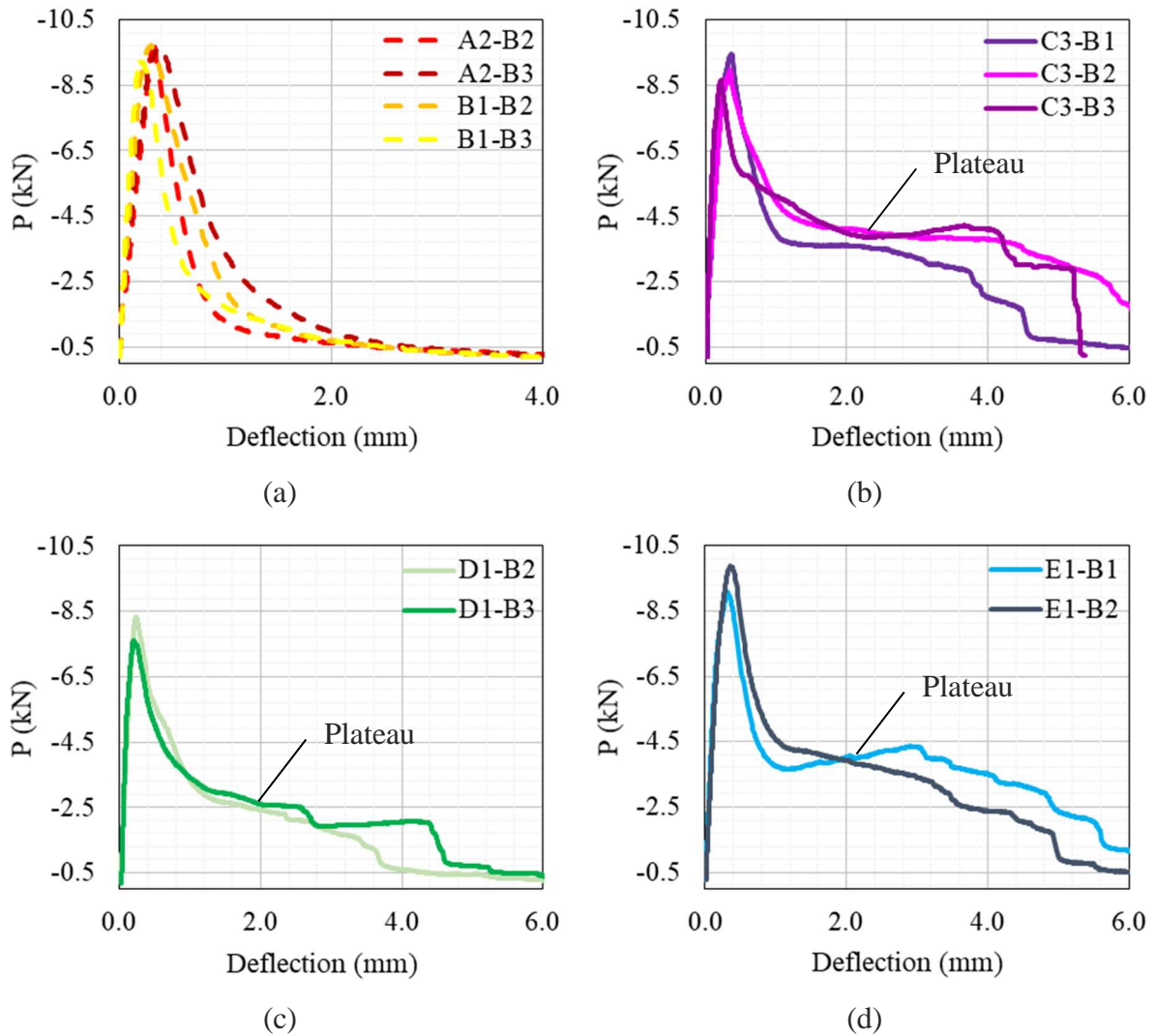


Figure 7-12. Force versus deflection curve results: (a) unreinforced configurations containing interface (B) and not (A), (b) configuration C (100kN/m), (c) configuration D (50kN/m), and (d) configuration E (100kN/m and SBS)

Figure 7-13 presents the  $P_{max}$  obtained for all tested specimens. Similar values were obtained regardless the configuration, with exception to configuration D that presented lowest  $P_{max}$  values (average of -7.9kN) in relation to the others.

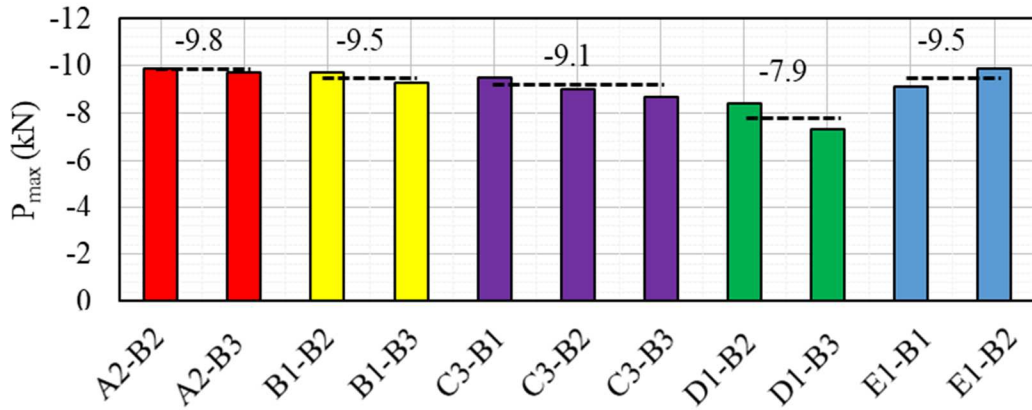


Figure 7-13. Force measured at peak of tested specimens

Figure 7-14 presents the graphic force versus deflection for all analyzed configurations. It is noticeable that the curves presented closed values at the beginning of the test until  $P_{max}$ . This result indicates that the presence of the geogrid does not noticeably influence the curve from the beginning until the load peak value, similarly to the found by Canestrari et al (2015). In addition, this figure highly evidences that the force plateau observed in the curve shapes was due to the geogrid presence. Moreover, the specimens containing the geogrid of 100kN/m maximum tensile resistance (C and E) presented the close values of force in the plateau, regardless of the type of emulsion used as the tack coat. This value was approximately the double of the force value obtained for the results of specimens containing the geogrid of 50kN/m maximum tensile resistance (D). This result indicates that the geogrid maximum tensile resistance directly influences the beam’s capacity of loading support during the crack propagation.

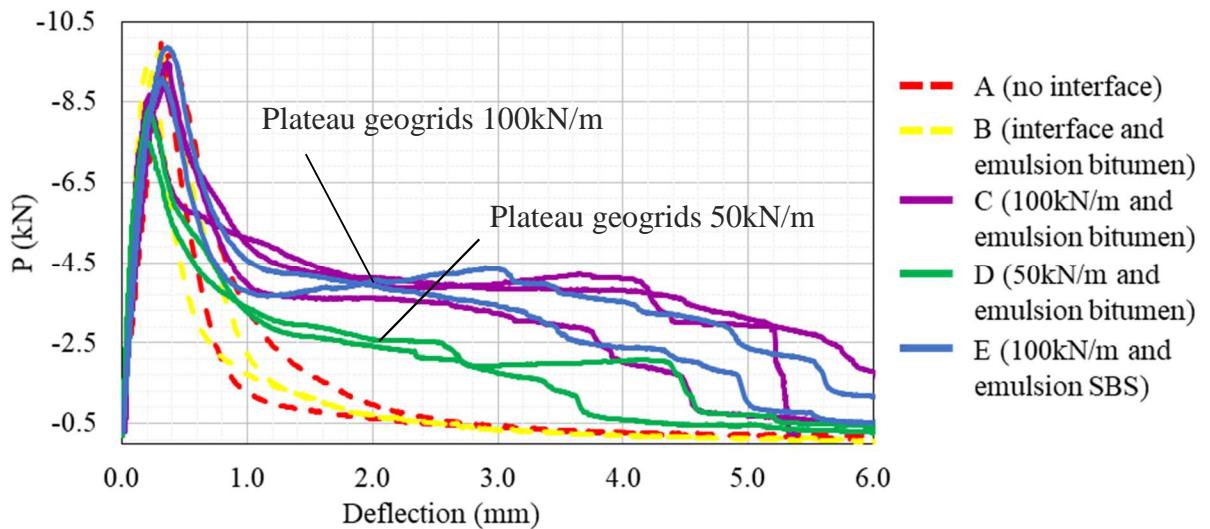


Figure 7-14. Force versus deflection curve results comparative between configurations

In order to evaluate the geogrid mobilization during the test, a verification calculation was conducted by assuming that only the geogrid supports loading from a certain point of the test. To perform the calculation, a beam according to the illustration presented in Figure 7-15 was considered, where the bituminous mixture in the central part was removed keeping the geogrid only. At the center-top, a hinge was inserted allowing the beam to pivot around this point simulating its strain due to the bending load. This hinge was located at a distance  $h$  from the geogrid, as illustrated in the figure. As a hypothesis, this distance of pivot  $h$  is higher than 3cm and slower than 4cm in order to have a high mobilization level of geogrid.  $F_{GG}$  is the force supported by the geogrid during the bending. Considering the maximum tensile resistance of the geogrids, 50 and 100kN/m, 3 yarns in the geogrid reinforcing the specimen, and 40 yarns/m,  $F_{GG}$  is 3.75kN for 50kN/m geogrid (configuration D) and 7.5kN for 100kN/m geogrid (configurations C and E).

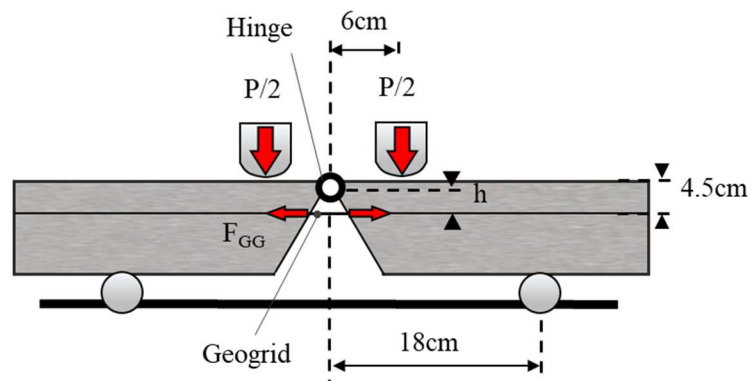


Figure 7-15. Illustration of four points bending beam pivoting around a hinge, supported only by the geogrid, used to calculate the pivot height ( $h$ ) of the hinge

Using the balance of moment around the hinge, Eq. 7-2 can be written. Using this equation with the  $P$  values obtained from the plateau considering 2mm of deflection, the  $h$  was obtained for each tested specimen. Table 7-2 presents the  $P$  considered and the corresponding  $h$ .

$$h = \frac{6 \cdot (P)}{F_{GG}} \quad \text{Eq. 7-2}$$

Table 7-2. Forces measured at 2mm of deflection on the tested specimens and corresponding pivot height ( $h$ )

Specimen	P (kN)	h (cm)
C3-B1	3.7	3.0
C3-B2	4.1	3.3
C3-B3	4.0	3.2
D1-B2	2.4	3.9
D1-B3	2.5	4.0
E1-B1	4.0	3.2
E1-B2	3.9	3.1

The results confirmed the hypothesis considered since all  $h$  values are contained within the range of 3 and 4cm. This result indicates that the force plateau observed in the results of reinforced specimens were a result of the geogrid mobilization during the test. Therefore, the tests in specimens in beam shape highly mobilized the geogrid in opposition to the results obtained from cylindrical specimens presented in the last three chapters.

## 7.8. Analysis of crack tip height (a)

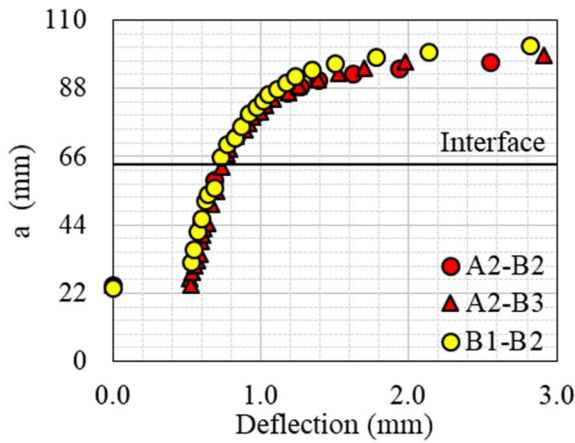
Figure 7-16(a) presents the crack tip height evolution in function of the beam's deflection for unreinforced specimens A (no interface) and B (interface emulsion). Continuum and overlapped curves were obtained for all the results, regardless of their constitution. Similarly to the results obtained in the last section (curve of force versus deflection), the presence of interface did not affect the evolution of crack tip height results and configuration B yields the same behavior of configuration A.

Figure 7-16(b) presents the same graphic, but including the results obtained for the test conducted with specimens of configuration C (100kN/m and emulsion bitumen). In this case, the three curves for the reinforced configuration presented distinct shapes. The curve for C3-B1 was similar to the curves for unreinforced specimens. However, C3-B2 and C3-B3 more deflection were observed to propagate the crack in the direction to the top of the beam. This increase in the deflection was initiated when the crack approximates the interface. At the interface level, the deflection measured for the unreinforced specimens measured approximately

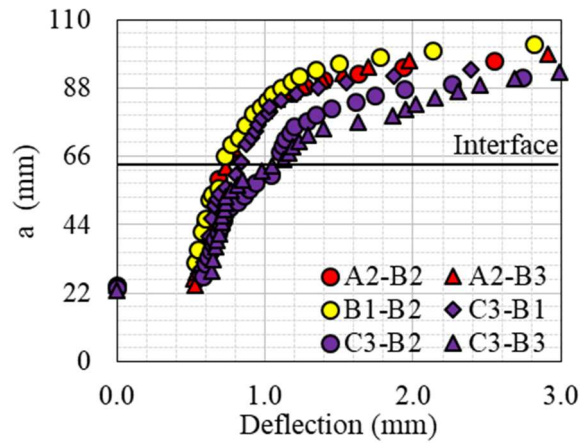
0.7mm, whereas C3-B2 and C3-B3 measured approximately 1.1mm, 1.6 times higher. This is indicative of crack retarding due to the presence of geogrid.

Figure 7-16(c) presents the same graphic, but including the results obtained for the test conducted with specimens of configuration D (50kN/m and emulsion bitumen) at this time. One more time, distinct curve shapes were observed. However, for both, D1-B2 and D1-B3, a discontinuity was observed when the crack propagates reaching the interface level. From this point, a cracking retard was noticeable. The deflection measured for configuration D results were approximately 1.05mm, 1.5 times higher.

Lastly, Figure 7-16(d) presents the same graphic but including the results obtained for the test conducted with specimens of configuration E (100kN/m and emulsion bitumen modified by SBS) at this time. In this case, the curves presented similar shape, but the configuration E was slightly higher in deflection than the unreinforced specimens. The deflection measured for configuration E results were approximately 0.85mm, 1.2 times higher.



(a)



(b)

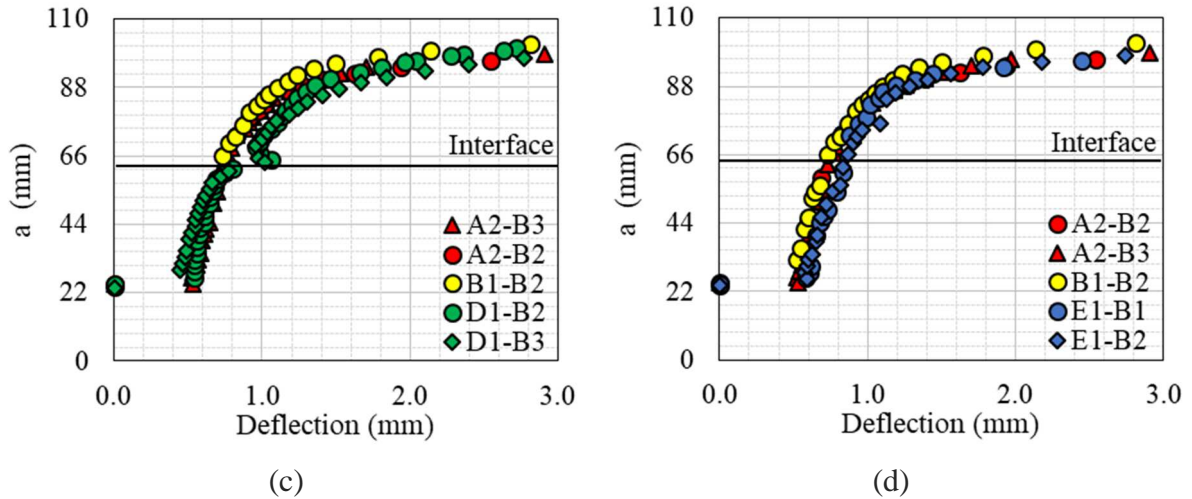
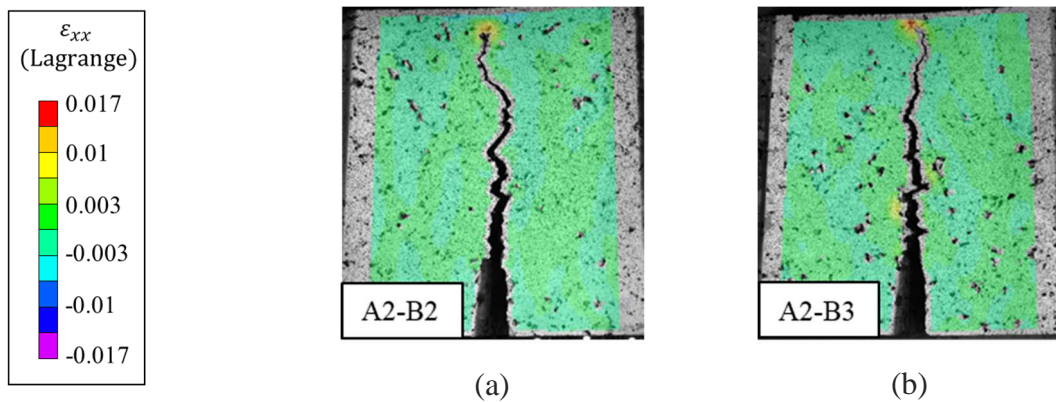


Figure 7-16. Crack tip height versus beam deflection results: (a) unreinforced configurations containing interface (B) and not (A), (b) configuration C (100kN/m) with unreinforced configurations, (c) configuration D (50kN/m) with unreinforced configurations, and (d) configuration E (100kN/m and SBS) with unreinforced configurations

Figure 7-17 presents images of all tested specimens at the end of their respective tests in order to observe the crack shape. Concerning unreinforced specimens (configurations A and B), it can be observed that the cracks presented a simple path from the bottom to the top. The same observation can be made concerning the specimens of configuration E and C3-B1, which can explain the continuous shape of those curves on graphic  $a$  versus deflection, previously observed. However, concerning the other two specimens of configuration C and the specimens of configuration D, the crack clearly had his path deviated by the geogrid. This result evidences the stress-relief property of the geogrid, regardless of its maximum tensile resistance.





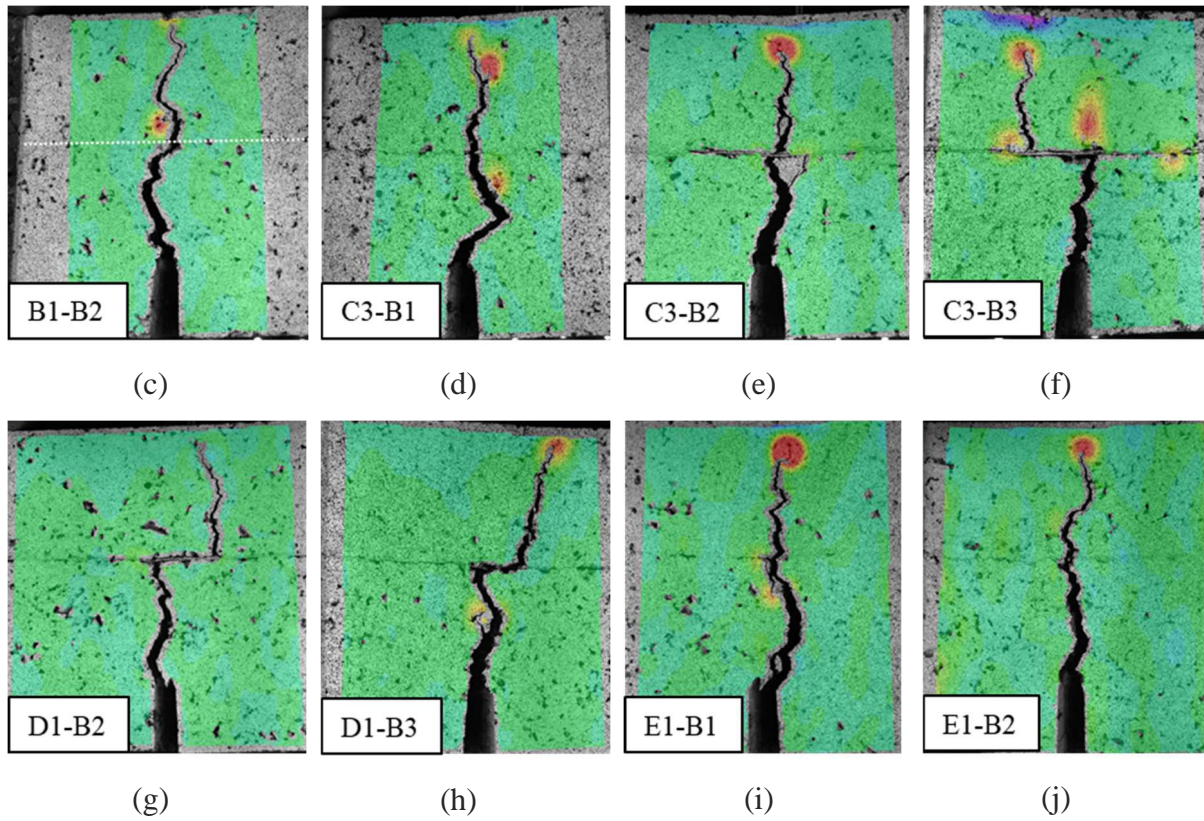


Figure 7-17. Treated images of tested specimens at the end of crack propagation: (a) A2-B2, (b) A2-B3, (c) B1-B2, (d) C3-B1, (e) C3-B2, (f) C3-B3, (g) D1-B2, (h) D1-B3, (i) E1-B1, and (j) E1-B2

## 7.9. Energy restitution rate ( $G_f$ )

An energy approach was used to evaluate crack propagation resistance of different configurations, reinforced and not. In this approach, the area underneath the curve  $P$  vs actuator displacement corresponds to the mechanical work necessary to propagate the crack throughout the specimen's height. Figure 7-18 illustrates the area used for this calculation. Thus, the energy restitution rate ( $G_f$ ) was obtained using Eq. 7-3.

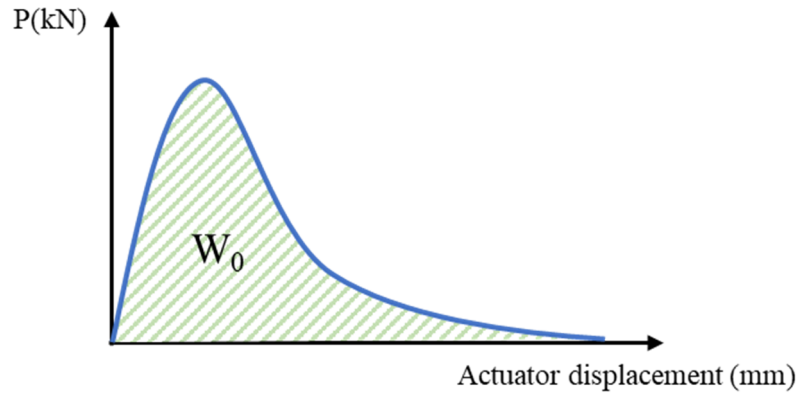


Figure 7-18. Illustration of area underneath the curve  $P$  versus actuator displacement used to the energy restitution rate ( $G_f$ ) calculation

$$G_F = \frac{W_0}{w(h - a_0)} \quad \text{Eq. 7-3}$$

Where  $W_0$  is the area of the curve illustrated in Figure 7-18,  $w$  is the beam width,  $h$  is the beam height (dimensions of beam's section), and  $a_0$  is the notch size. Figure 7-19 presents the  $G_f$  obtained for the results of the tested specimens, with the average of each slab configuration. The results obtained concerning unreinforced specimens (configurations A and B) presented much lower  $G_f$  than the reinforced specimens (configurations C, D, and E). Configuration C needed approximately 2.6 times more energy to propagate the crack in relation to A and 3.3 times more in relation to B. Configuration D needed approximately 1.5 times more energy in relation to A and 1.9 times in relation to B. Configuration E needed 2.5 times more in relation to A and 3.2 times more in relation to B. Comparing the reinforced specimens, configurations C and E needed similar amount of energy to propagate the crack and approximately 1.7 times more than D. This result indicates that the maximum tensile resistance of the geogrid influenced in the energy necessary to propagate the crack throughout the specimen height during the tests.



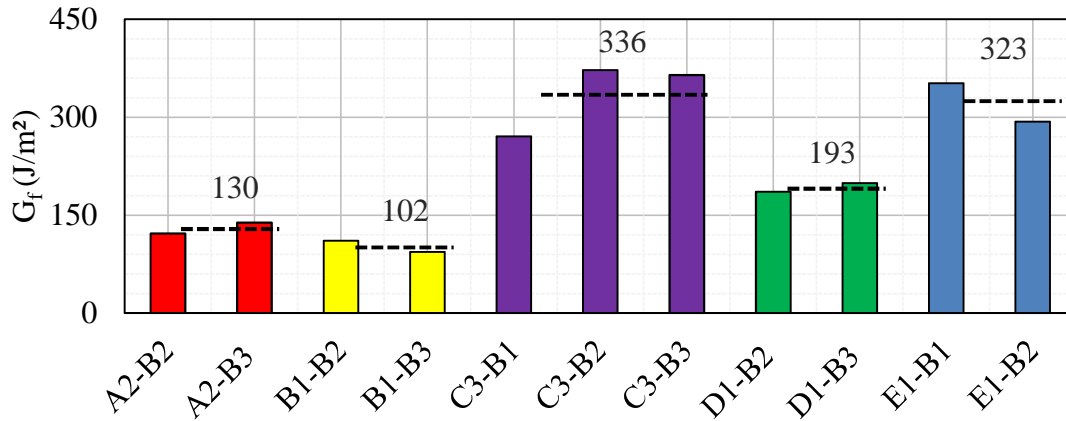


Figure 7-19. Energy restitution rate ( $G_f$ ) obtained for the tested specimens

## 7.10. Average and maximum strain images analysis

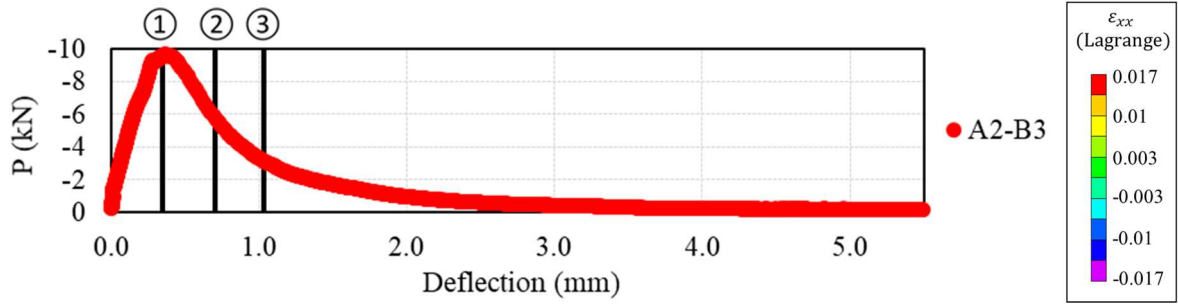
From the method described in section 7.4.2, it is possible to calculate the average strain in function of beam height during the test at different times  $t$ . This section is focused on presenting three examples of this mentioned analysis performed from the DIC results. Two examples of unreinforced configurations, containing interface (B1-B2) and not (A2-B3), and of reinforced specimen (D1-B3).

### 7.10.1. Example of specimen without interface: A2-B3

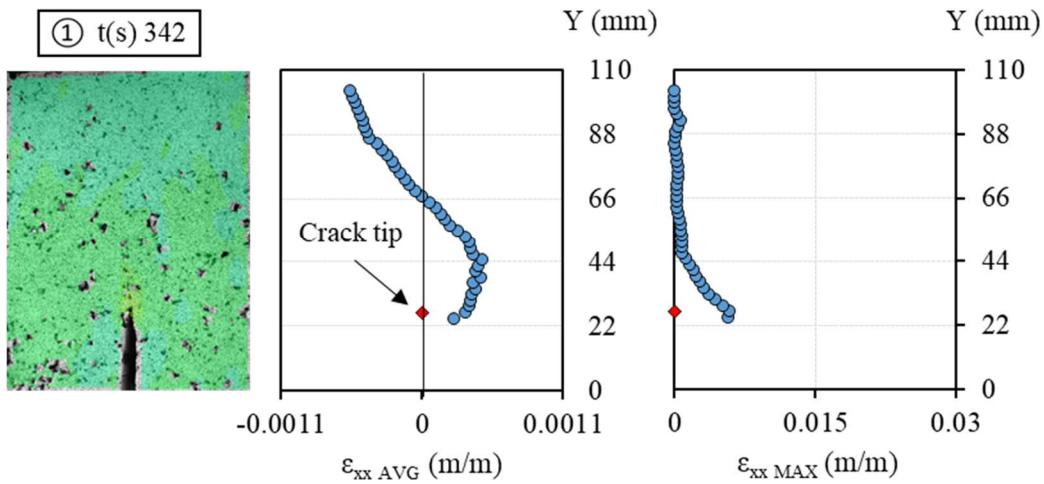
Figure 7-20(a) presents the graphic  $P$  versus deflection obtained for specimen A2-B3 in the FPBNF tests. In this graphic, three specific points were chosen for the analysis of average and maximum strains over the beam height: (1) peak point, deflection = 0.35mm,  $t = 342s$ , (2) deflection = 0.6mm,  $t = 390s$  and (3) deflection = 1mm,  $t = 420s$ . The first point represents the moment when the crack was about to start propagating, the last one represents the moment when the crack was almost at the end of propagation, and the second one is an intermediate point.

Figure 7-20(b) presents the analysis of point 1. From the treated image and the graphic of maximum strain, it is noticeable that there is a concentration of strain on the tip of the notch, indicating the beginning to crack propagation. At 66mm of height, the average strain was around zero indicating that it represents the neutral axis of the beam subjected bending. For  $Y$  values above the neutral axis, a linear-increasing compression was observed, and for  $Y$  values below the neutral axis, a linear-increasing compression was observed until 44mm. For this

range of  $Y$ , the analysis performed from the DIC data resulted in a strain behavior much similar to what is classically expect in the analysis of Portland concrete beams subjected to bending in the studies of civil engineering. Figure 7-20(c) presents the analysis of point 2. In this case, the crack propagated and his tip reached approximately 68mm of height. Figure 7-20(d) presents the analysis of point 3. In this last case, the crack propagated and his tip reached approximately 84mm of height.



(a)



(b)

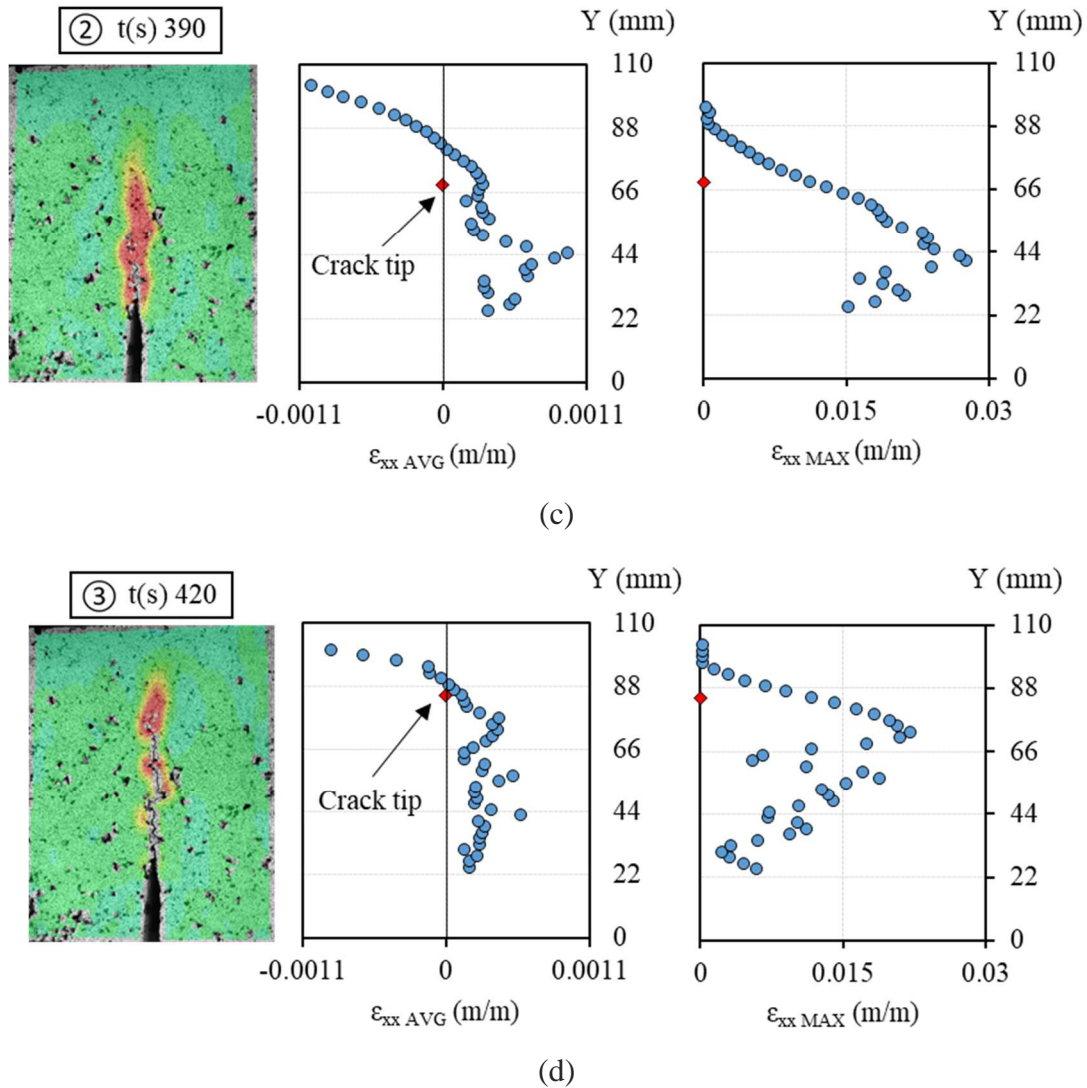
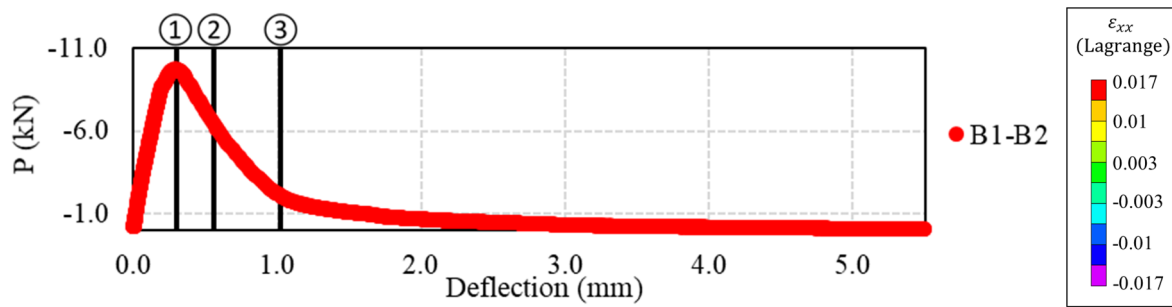


Figure 7-20. Analysis of average and maximum strain versus beam height concerning A2-B3: (a) three analyzed points emphasized in  $P$  versus deflection curve, (b) point 1,  $t = 342s$ , (c) point 2,  $t = 390s$ , and (d) point 3,  $t = 420s$

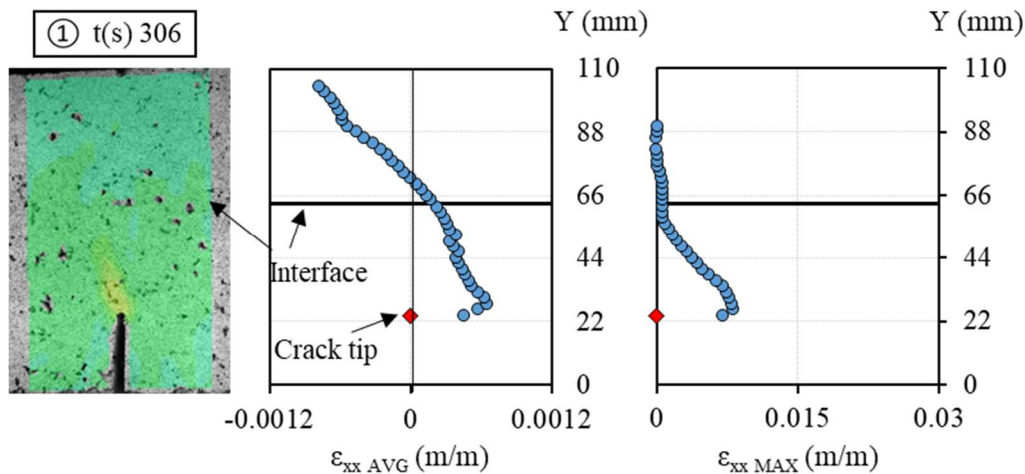
**7.10.2. Example of unreinforced specimen with interface: B1-B2**

Figure 7-21(a) presents the graphic  $P$  versus deflection obtained for specimen B1-B2 in the FPBNF tests. In this graphic, three specific points were again chosen for the analysis of average and maximum strains over the beam height: (1) peak point, deflection = 0.3mm,  $t = 306s$ , (2) deflection = 0.56mm,  $t = 333s$  and (3) deflection = 1mm,  $t = 360s$ . The first point represents the moment when the crack was about to start the propagation, the second one was the moment that the crack tip reaches the interface, and the last one represents the moment when the crack was almost at the end of propagation.

Figure 7-21(b) presents the analysis of point 1. Once again, from the treated image and the graphic of maximum strain, it is noticeable that there is a concentration of strain on the tip of the notch, indicating the beginning to crack propagation. In this case, the neutral axis was located at 70mm, and the classical strain behavior was, one more time, obtained using DIC data. Figure 7-21(c) presents the analysis of point 2. In this case, the crack propagated and his tip reached approximately 66mm of height. At this point, in both graphics, average strain, and maximum strain, a gap was observed between the points below and above the interface. This gap could indicate a slight slip on the interface between the bituminous mixture layers when the crack tip reaches it. Figure 7-21(d) presents the analysis of point 3. In this case, the crack propagated and his tip reached approximately 88mm of height. In this last point, the gap disappeared from the average strain graphic, possibly due to the correction performed (c.f. Section 7.4.2). However, in the maximum strain graphic, the gap was bigger.



(a)



(b)

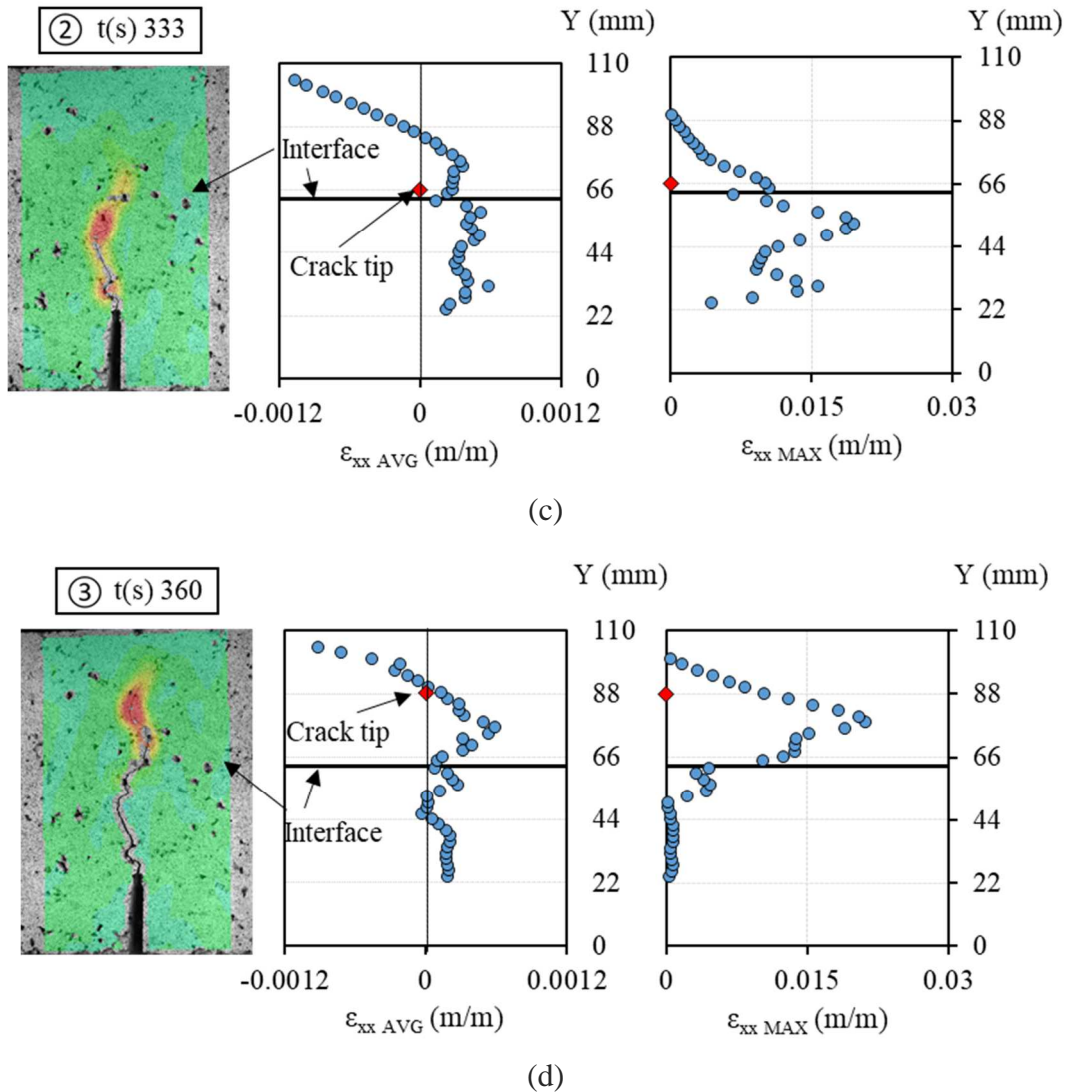


Figure 7-21. Analysis of average and maximum strain versus beam height concerning B1-B2: (a) three analyzed points emphasized in  $P$  versus deflection curve, (b) point 1,  $t = 306s$ , (c) point 2,  $t = 333s$ , and (d) point 3,  $t = 360s$

### 7.10.3. Example of reinforced specimen: D1-B3

As an example of the reinforced specimen, D1-H3 (50kN/m and emulsion bitumen) was chosen. Figure 7-22(a) presents the graphic  $P$  versus deflection obtained in the FPBNF tests. In this graphic, the four points were chosen for the analysis of average and maximum strains over the beam height: (1) peak point, deflection = 0.25mm,  $t = 306s$ , (2) deflection = 0.45mm,  $t = 348s$ , (3) deflection = 1mm,  $t = 456s$ , and (4) deflection = 2.6mm,  $t = 804s$ . The first point represents the moment when the crack was about to start the propagation, the second one was

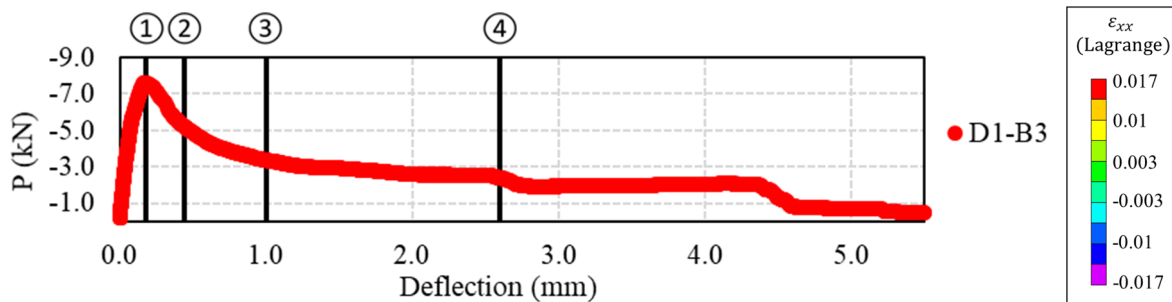
the moment that geogrid starts being mobilized, the third one was the beginning of force plateau, and the last one was the end of force plateau.

Figure 7-22(b) presents the analysis of point 1. The average strain at the interface level at this moment of the test was zero because the interface with geogrid was placed in the neutral axis of the beam. This result shows that the geogrid was not mobilized until the beginning of crack propagation. Moreover, it explained why the results obtained for all the specimens, regardless of its constitution were the same until the peak of force, as discussed in Section 7.7.

Figure 7-22(c) presents the analysis of point 2. In this case, the crack propagated and his tip reached approximately 29mm of height. Concerning the average strain graphic, the upper layer behaves as a beam subjected to bending alone. However, a high strain level at interface indicates that the geogrid was mobilized at this point. From the maximum strain graphic, it was noticeable that the strain was more concentrated in the lower layer than the upper layer. Moreover, there is no gap caused by interface suggesting that there was no slip in the interface. Thus, it evidenced the stress-relief property of the geogrid one more time.

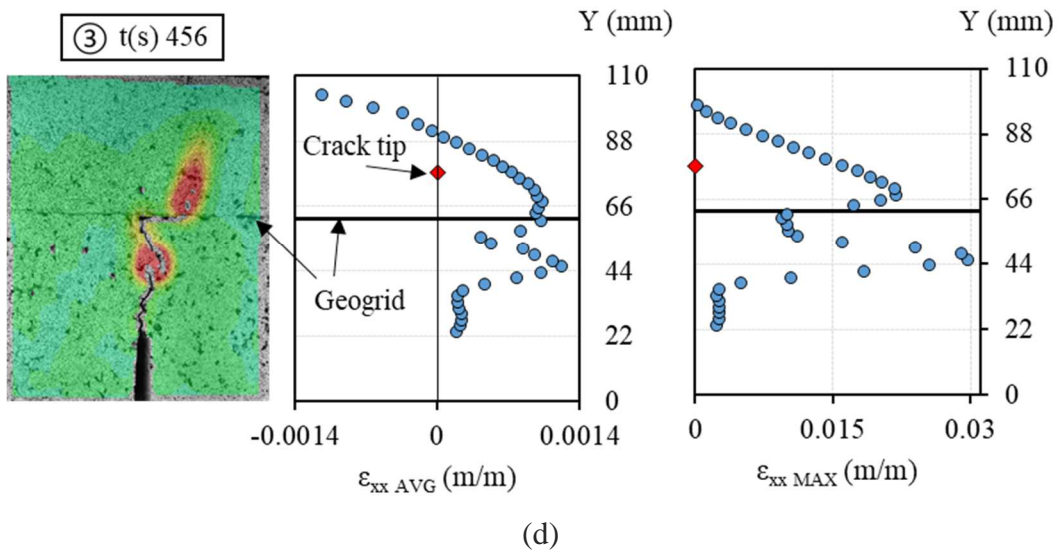
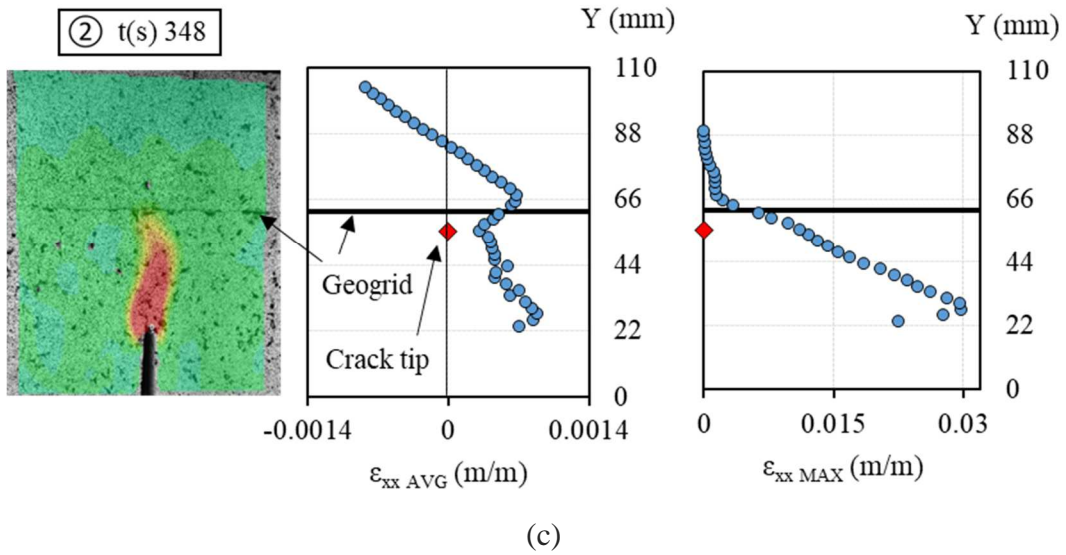
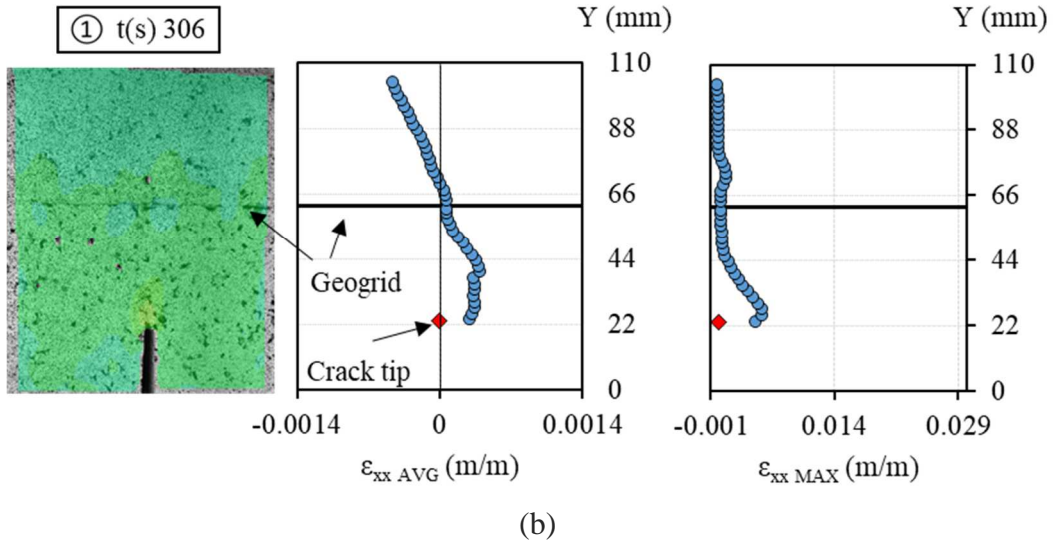
Figure 7-22(d) presents the analysis of point 3. At this point, the crack propagated and his tip reached approximately 77mm of height. When the crack tip reached the interface, it was deviated from its original path due to the geogrid presence. At this moment, it was noticeable that even when the crack tip passed through the geogrid, the tension strain is very high at the interface level, measuring approximately 0.001m/m average and 0.017m/m maximum. This result was another evidence that the geogrid was highly mobilized during the force plateau and, therefore, being responsible for it.

Finally, Figure 7-22(e) presents the analysis of point 4. At this point, the crack propagated and his tip reached approximately 97mm of height. At this moment, the geogrid was the only responsible for supporting the load since no more strain could be measure on the bituminous mixture. The decrease of loading support of the beam was related to the geogrid deterioration.



(a)





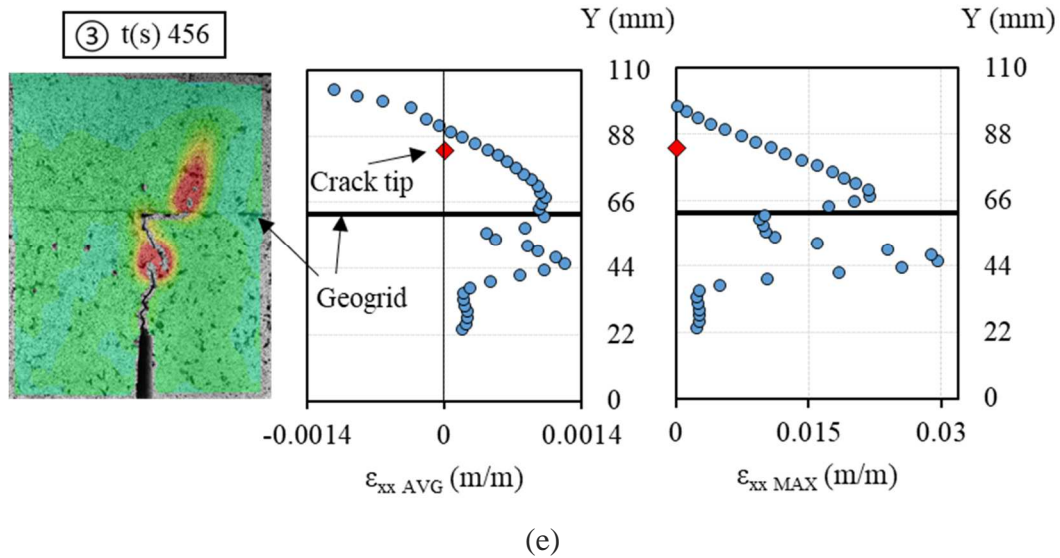


Figure 7-22. Analysis of average and maximum strain versus beam height concerning D1-B3: (a) four analyzed points emphasized in  $P$  versus deflection curve, (b) point 1,  $t = 306s$ , (c) point 2,  $t = 348s$ , (d) point 3,  $t = 456s$ , and (e) point 4,  $t = 904s$

#### 7.10.4. Comparison between analysed configurations

Figure 7-23 presents the curves of average strain versus beam height for all tested specimens at the point of force peak (point 1 from the last sections). Figure 7-23(a) presents the unreinforced specimens containing interface (configuration B) and not (configuration A). Figure 7-23(b) presents the three results obtaining from configuration C (100kN/m and emulsion bitumen) test results. Figure 7-23(c) presents the three results obtaining from configuration D (50kN/m and emulsion bitumen) test results. Figure 7-23(d) presents the three results obtaining from configuration E (100kN/m and emulsion bitumen modified by SBS) test results. From the results, it can be noticed that the specimens containing geogrid with 100kN/m maximum tensile resistance presented a non-linearity on the points closed to the interface, with exception to C3-B3. Moreover, most of the reinforced specimens presented strain close to zero at the interface on the peak of force, indicating that they were located at the neutral axis of the beam.



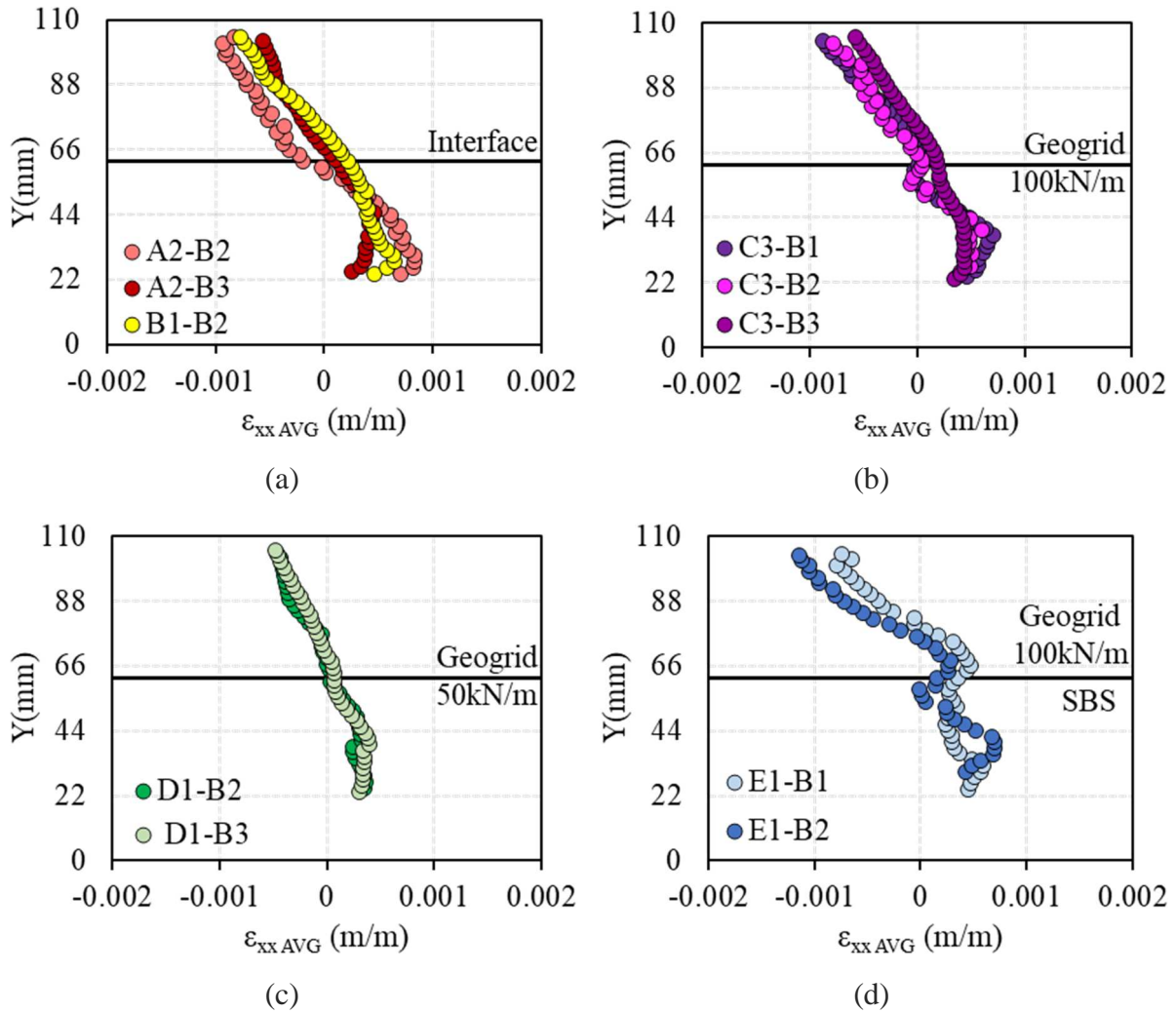


Figure 7-23. Average strain versus beam height at the point of force peak for all tested specimens: (a) unreinforced configurations containing interface (B) and not (A), (b) configuration C (100kN/m), (c) configuration D (50kN/m), and (d) configuration E (100kN/m and SBS)

Figure 7-24 presents the curves of average strain versus beam height for all tested specimens at 1mm of deflection (point 3 from last sections). Figure 7-24(a) presents the unreinforced specimens containing interface (configuration B) and not (configuration A). Figure 7-24(b) presents the results obtaining from configuration C (100kN/m and emulsion bitumen) specimens. Figure 7-24(c) presents the results obtaining from configuration D (50kN/m and emulsion bitumen) specimens. Figure 7-24(d) presents the results obtaining from configuration E (100kN/m and emulsion bitumen modified by SBS) specimens. At interface height, the reinforced specimens presented a high level of average strain, whereas the unreinforced specimens presented the average strain close to zero. Configurations C and D presented approximately

0.0018m/m of average strain closed to the geogrid, and configuration E presented approximately 0.001m/m. This result suggests that the geogrid was mobilized supporting part of the load at the analyzed point.

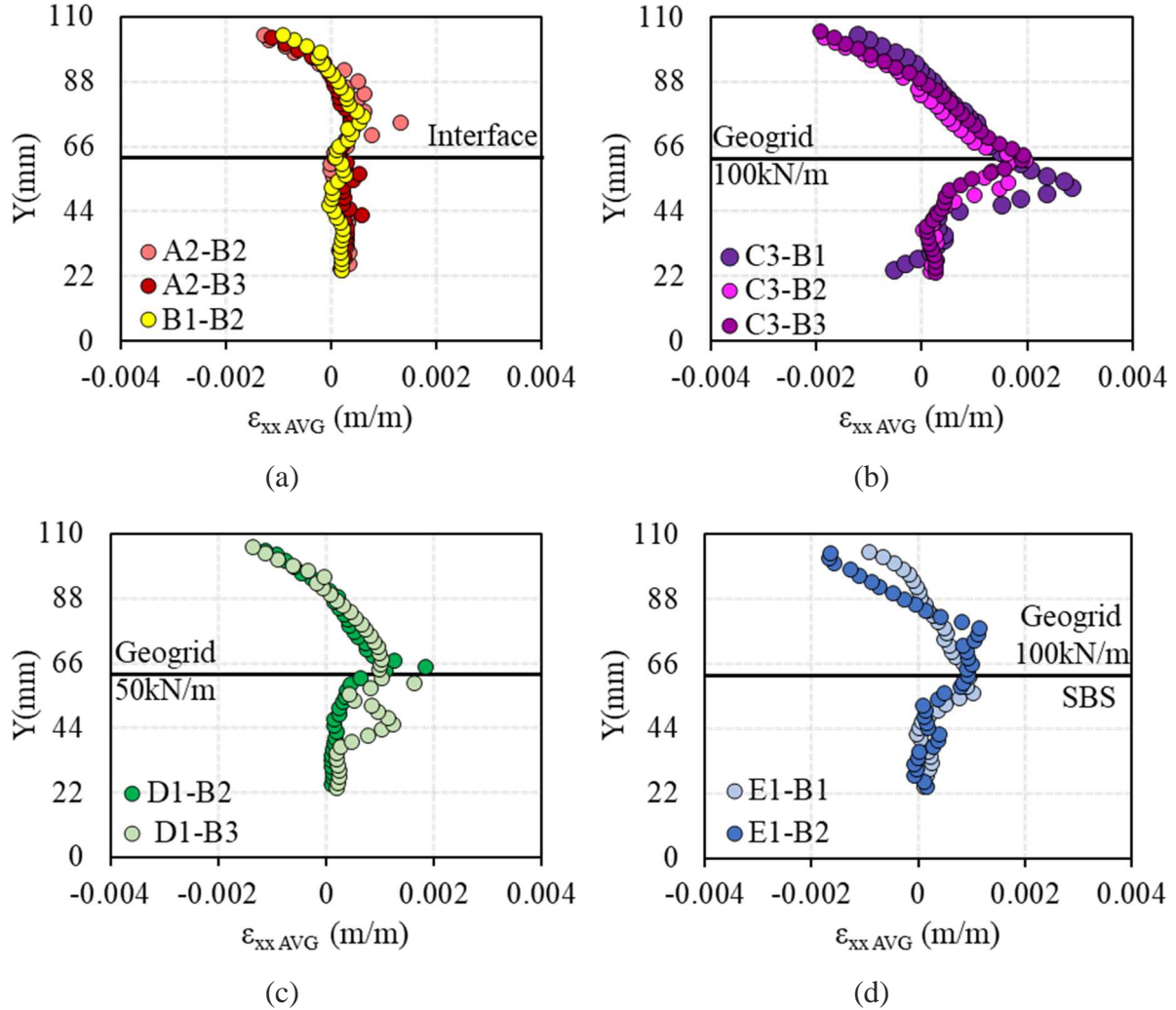


Figure 7-24. Average strain versus beam height at the point of 1mm of displacement for all tested specimens: (a) unreinforced configurations containing interface (B) and not (A), (b) configuration C (100kN/m), (c) configuration D (50kN/m), and (d) configuration E (100kN/m and SBS)

## 7.11. Chapter conclusions

This chapter presented the crack propagation experimental campaign of the five studied slab configurations. FPBNF tests were carried out in prismatic specimens in a beam shape. The

geogrid contribution to the crack propagation resistance was evaluated using DIC and energetic approach. Therefore, some conclusion can be drawn:

- The results presented good test repeatability.
- The presence of the interface with only emulsion bitumen did not change the crack propagation resistance compared to the unreinforced configuration without interface using the curve force versus displacement analysis.
- The same peak of load value was obtained regardless of the specimen constitution. Except for the configuration D, which presented the lowest  $P_{max}$ .
- The presence of the geogrid does not noticeably influence the curve from the beginning until the load peak value in the curve force versus displacement.
- Force plateau observed in reinforced results from 1mm of displacement with direct relation to the mobilization of the geogrid during the test.
- Geogrid maximum tensile resistance directly influences the beam's capacity of loading support to the crack propagation. However, the type of emulsion tack coat does not.
- The presence of geogrid could effectively retard the crack propagation in the reinforced beams.
- The reinforced specimens presents stress-relief property due to the geogrid presence. For most of the reinforced specimens, the crack deviated his path when reached the interface with geogrid. Whereas for unreinforced ones, the crack presented a simple propagation path.
- Considering the energy approach, the specimens containing interface bonded with emulsion (B) presented the lowest energy needed to crack propagation. Configuration D (50kN/m and emulsion bitumen) presented the lowest energy restitution rate from the reinforced specimens, but 1.9 times higher than B. Configuration C (100kN/m and emulsion bitumen) and E (100kN/m and emulsion bitumen modified by SBS) presented similar energy restitution rate, approximately 3.3 times higher than B and 1.7 times higher than D.
- A classical strain behavior of beams subjected to bending studied in civil engineering was measured using the analysis of average strain from DIC results versus beam height of unreinforced specimens.
- Until the peak of load, the geogrid is located at the neutral axis of the beam. Therefore, it is not mobilized until the beginning of crack propagation.

- Even after the passage of the crack from the interface, the geogrid is still highly capable of loading support.

# Chapter 8: CONCLUSION AND PERSPECTIVES

This thesis presented an experimental framework aiming at understanding the bituminous mixtures reinforced by fiberglass geogrid behavior, in order to use it as a solution to extend the pavements structures serviceability. From this point of view, the effect of maximum tensile resistance of the fiberglass geogrid and the bitumen-modification by SBS in the emulsion used as the tack coat had his effects evaluated. Thus, this doctoral work could contribute to the future development of new geosynthetics optimized to the reinforcement of bituminous mixtures. Moreover, it could provide useful information, which could allow the proposition of a new design method for reinforced pavement structures. From experimental observations and analysis, the conclusions can be summarised as follows.

- The newly proposed interface method of analysis was successfully applied in specimens with interface/geogrid oriented perpendicularly to the longitudinal direction of the cylindrical specimen (type V). It was able to measure separately the complex modulus of the interface ( $E_G^*$ ), as function of a chosen thickness ( $t$ ), and bituminous mixture ( $E_A^*$ ) that compose these specimens. Using this method, the  $E_A^*$  obtained in specimens containing interface, reinforced and not, presented the same LVE behavior obtained from the results of the unreinforced specimen without interface.  $E_G^*$  obtained experimentally were LVE and it could be modeled by 2S2PD. Interface bond quality (correct emulsion rate application and adhesion improvement by SBS modification) presented higher influence in the interface stiffness than the maximum tensile resistance of the geogrid. Moreover, this method was able to provide  $E_G^*$  of specimens containing only emulsion bitumen (configuration B) in the same order of magnitude of complex modulus classically obtained for bitumen, considering the  $t$  of a bitumen film. The proposed methodology could be a very useful tool for improving the design calculation of geogrid-reinforced pavement structures. Regarding the test results obtained for specimens with interface/geogrid oriented in the longitudinal direction of cylindrical specimen (type H), considerably low level of geogrid mobilization was obtained, especially for specimens with an interface containing bitumen modified by SBS. Slippage between the geogrid

and the bituminous mixture at high temperatures could be responsible for it. At low temperatures, the high stiffness of the bituminous mixture overcome the influence of the geogrid stiffness on measures. Results can be found in Chapter 4.

- The same interface analysis methodology used for complex modulus was successfully used to characterize the interface behavior to monotonic tension tests of specimen type V. The strain in the bituminous mixture was much smaller than the strain in the interface during the test. Thus, the failure of all these specimens was located in the interface level and the interface bond quality had a direct influence on the maximum tensile strength obtained. The variation on the diameter size presented no significant difference in the maximum tensile strength obtained for those specimens. However, these specimens were very sensible to the variation of bond quality and smaller differences encountered in the interface, mostly related to its position in the slab before coring. Specimens type V containing only emulsion bitumen in the interface (configuration B) presented the highest tensile strength among the specimens containing interface, reinforced and not. However, the interface strength should be influenced by its real thickness, and the reinforced specimens' interface is at least three times thicker. Moreover, a decrease in the effective bonding surface and the decrease in the indentation of the two granular layers due to the geogrid presence could result in lower maximum tensile strength. The validation of TTSP for these specimens was inconclusive since it was not possible to solicit the bituminous mixture and the interface of it correctly. Regarding the test results obtained for specimens type H, at the combination of high temperatures and/or low load rate, the geogrid was not mobilized, possibly due to the slippage in the interface caused by the high viscosity of the bitumen. At the combination of low temperature and/or high load rate, the geogrid mobilization does not have a significant influence on the tensile strength due to the elevated stiffness of the bituminous mixture. Lastly, the TTSP was successfully validated for plastic behavior and non-linear domains for these specimens. Results can be found in Chapter 5.
- The different configurations presented distinct susceptibility to strain amplitude variation according to the Wöhler curves obtained from fatigue experimental campaign. Reinforced configurations (C, D, and E) were more resistant to fatigue at high strain amplitudes and less resistant to fatigue at low strain amplitudes in relation to the unreinforced ones (A and B). This sensibility was even higher for configuration containing SBS in its interface (E). Almost identical fatigue resistance

curves were obtained for configurations with geogrid of 50 and 100kN/m, and emulsion bitumen. Therefore, the increase of interface bond quality due to the presence of SBS is more relevant to fatigue resistance than the maximum tensile strength of geogrid. However, the geogrid might not be entirely mobilized during the fatigue test on cylindrical specimens, as observed for complex modulus and tension experimental campaign. This could lead to an underestimation of geogrid contribution to the fatigue performance of reinforced bituminous mixtures. Lastly, the influence of the geogrid reinforcement on the fatigue parameter  $\varepsilon_6$ , used in the French design method, was negligible. Wöhler curve slope ( $-1/b$ ) was smaller for reinforced specimens. Results can be found in Chapter 6.

- The presence of interface in the specimen (configuration B) did not influence the resistance to the crack propagation compared to the specimen without an interface (configuration A). The presence of the geogrid does not noticeably influence the curve from until the load peak value, from where the crack starts the propagation since all the specimens presented the same behavior until the load peak. A force plateau was observed in reinforced results from 1mm of displacement related to the mobilization of the geogrid during the test. This plateau was proportional to the geogrid maximum tensile resistance and appears not to be influenced by the type of emulsion tack coat. At the end of the test, most of the reinforced specimens had the crack path deviated when reached the interface with geogrid, which could not occur for unreinforced specimens. It evidenced the stress-relief property due to the geogrid presence. From the energy approach, configuration B (only interface) presented the lowest energy needed to crack propagation. Configurations containing 100kN/m geogrid presented the highest (C and E), approximately 3.3 times higher than B and 1.7 times higher than D (50kN/m geogrid and emulsion bitumen). From DIC analysis, the monitoring of crack tip height evidenced the crack-retarding properties of the reinforcement by fiberglass geogrid. The strain average analysis in function of beam height showed that the geogrid is located at the neutral axis of the beam, and, therefore, it is not mobilized until the beginning of crack propagation. In addition, it showed that the bituminous mixture layer reinforced by geogrid is still highly capable of loading support, even after the crack passed through the interface. Finally, the FPBNF tests carried out in specimens with beam shape could successfully measure the geogrid reinforcement contributions to bituminous mixtures. Results can be found in Chapter 7.

Following these conclusions, some recommendations and perspectives for future research are presented hereafter.

- Different specimen geometries should be used as an alternative to the cylindrical ones, in order to obtain a higher mobilization level during the tests. Especially concerning the tests at high strain levels (tension tests) and tests with high material degradation levels (fatigue tests). The true contribution of geogrid reinforcement of bituminous mixtures can be obtained by combining such tests with a high mobilization geogrid level.
- Complementary characterization of permanent deformation at high temperatures, classically used for rutting characterization (around 60°C), should be carried out. At this temperature, bituminous mixture stiffness decreases and the geogrid could strongly contribute to the improvement of pavement performance.
- The proposition of a test that assesses the impact of the geogrids on enhancing the bituminous pavement structural capacity.
- The creation of a new design method of pavement structures, based on an adaptation of a pre-existent method that accounts for the contributory effects of the geogrid founds in this doctoral thesis. The geogrid contributions could be based in a combination of the fatigue results, concerning the fatigue Wöhler curve slope parameter ( $-1/b$ ), shown in Chapter 6, with the increase in the crack propagation resistance, shown in Chapter 7.
- Construction and monitoring of a field trial reinforced by the fiberglass geogrids and emulsions tack coat used in this study, in order to validate the results obtained in the laboratory characterization. In addition, the long-term performance of a reinforced roadway by fiberglass geogrid could be evaluated.



# REFERENCES

- AASHTO M320. (2009). Standard Specification for Performance-Graded Asphalt Binder. American Association of State Highway and Transportation officials.
- AASHTO PP6. (1994). Standard practice for grading or verifying the performance grade of an asphalt binder. American Association of State Highway and Transportation officials.
- Aldea, C. M., & Darling, J. R. (2004). "Effect of coating on fiberglass geogrid performance". Proceedings of the 5th international RILEM conference, Limoges.
- Al-Hedad A. S. A. and Hadi M. N. S. (2019). "Effect of geogrid reinforcement on the flexural behaviour of concrete pavements", *Road Materials and Pavement Design*, 20:5, 1005-1025, DOI: 10.1080/14680629.2018.1428217
- Al-Qadi, I. L., Brandon, T. L., Valentine, R. J., Lacina, B. A., and Smith, T. E. (1994). "Laboratory evaluation of geosynthetic-reinforced pavement sections." *Transportation Research Board* 1439, Transportation Research Board, Washington, D.C., 25-31.
- Al-Qadi, I. L., and Bhutta, S. A. (1999). "In Situ Measurements of Secondary Road Flexible Pavement Response to Vehicular Loading." *Transportation Research Record* 1652, Transportation Research Board, Washington, D.C., 206-216.
- Al-Qadi, I. L. Buttlar, W. G., Baek J., and Kim, M. (2008a). "Effectiveness Assessment of HMA Overlay Interlayer Systems Used to Retard Reflective Cracking." *ICT-RC58 Final Project Report*, ICT, UIUC, Urbana, Illinois.
- Al-Qadi I., Morian, D.A., Stoffels, S.M., Elseifi, M., Chehab, G., Stark, T. (2008b). "Synthesis on Use of Geosynthetics in Pavements and Development of a Roadmap to Geosynthetically-Modified Pavements." *Report*, Federal Highway Administration, Washington, D.C.
- Al Rousan, T.M. (2004). *Characterization of Aggregate Shape Properties Using a Computer Automated System*. Ph.D. Dissertation, Texas A&M University, College Station, TX.
- Anderson, D. A., Christensen, D. W., Bahia, H. U., Dongre, R., Sharma, M. G., Antle, C. E., Button, J. (1994). *Binder characterization and evaluation. Volume 3: Physical characterization (Strategic Highway Research Program A-369 Report)*. Washington, DC: National Research Council.
- ARA Inc. (2004), *Guide for mechanistic-empirical design of new and rehabilitated pavement structures*, Champaign, 2004

- Arrhenius, S. (1889). Über die Reaktionsgeschwindigkeit bei der Inversion von Rohrzucker durch Säuren (On the reaction velocity of the inversion of cane sugar by acids). *Zeitschrift für Physikalische Chemie*, 4, 226-248. (In German)
- Arsenie, I.M., Chazallon, C., Themeli, A., Duchez, J.L., and Doligez, D. (2012). "Measurements and predictions of fatigue behavior of glass fiber reinforced bituminous mixtures". Seventh International RILEM Conference on Cracking in Pavements. Volume 2 pp.653-664. DOI: 10.1007/978-94-007-4566-7\_64
- Arsenie, I.M., Chazallon, C., Duchez, J.L. and Hornych, P. (2016). "Laboratory characterisation of the fatigue behaviour of a glass fibre grid-reinforced asphalt concrete using 4PB tests." *Road Materials and Pavement Design*, 18:1, 168-180, DOI:10.1080/14680629.2016.1163280
- ASTM D1883 (2016). Standard Test Method for California Bearing Ratio (CBR) of Laboratory-Compacted Soils
- Attia, T., Di Benedetto, H., Sauzeat, C., Olard, F. and Pouget, S. (2017). "Hollow cylinder apparatus to characterize interfaces between pavement layers." 71st RILEM Annual Week & ICACMS, Chennai, India, Vol. 4, pp. 401-410.
- Attia, T. (2020). Interfaces between pavement layers in bituminous mixtures (Doctoral thesis). École Nationale des Travaux Publics de l'État (ENTPE) de l'Université de Lyon (UdL), Vaulx-en-Velin.
- Austin, R.A., and Gilchrist, A.J.T. (1997). "Enhanced performance of asphalt pavements using geocomposites." *Geotextile and Geomembranes*, Vol. 14, pp. 175-186.
- Babadopulos, L.F.A.L. (2017). Phenomena occurring during cyclic loading and fatigue tests on bituminous materials: Identification and quantification (Doctoral thesis). École Nationale des Travaux Publics de l'État (ENTPE) de l'Université de Lyon (UdL), Vaulx-en-Velin.
- Baaj, H. (2002). Comportement des matériaux granulaires traits aux liants hydrocarbonés. (Doctoral thesis). ENTPE-INSA Lyon, Lyon. (In French)
- Baaj, H., Di Benedetto, H., & Chaverot, P. (2003). Fatigue of mixes: an intrinsic damage approach. In M. N. Partl (Ed.), *Performance testing and evaluation of bituminous materials: Proceedings of the 6th International RILEM Symposium* (pp. 394-400). Zurich: RILEM.
- Barrett, P.J. (1980). The Shape of Rock Particles, a Critical Review. *Sedimentology*, Vol. 27.

- Barksdale, R. D., Brown, S. F., and Chan, F. (1989). "Potential benefits of geosynthetics in flexible pavements." NCHRP Report 315, Transportation Research Board, Washington, D.C.
- Barksdale, R. D. (1991). "Fabrics in asphalt overlays and pavement maintenance." NCHRP Report 171, Transportation Research Board, Washington, D.C.
- Bessa, I.S., Castelo Branco, V.T.F., Soares, J.B., Nogueira Neto, J.A., (2015). *Journal of Materials in Civil Engineering*, ASCE, Vol. 27, Issue 7. DOI:10.1061/(ASCE)MT.1943-5533.0001181
- Besson, J. (2004). "Local approach to fracture". Les Presses de l'Ecole des Mines, Paris, 428p.
- Beckham, W.K. and W.H. Mills (1935). "Cotton-Fabric-Reinforced Roads." *Engineering News Record*, Vol. 115, No. 13, pp. 453-455.
- Boltzmann L. (1876) *Pogg. Ann. Phys.*, 7, p. 624.
- Brown S.F., Brunton J.M., Hughes D.A.B. and Brodrick B.V. (1985) "Polymer grid reinforcement of asphalt", *Proceedings of the Association of Asphalt Paving Technologists*, Vol 54, pp 18-41.
- Brown S.F., Thom N.H. and Sanders P.J. (2001). "A study of grid reinforced asphalt to combat reflective cracking." *Journal of the Association of Asphalt Paving Technologies*, Vol.70, 543-571.
- Bui, H. D. (1978). "Mécanique de la rupture fragile". Masson, Paris, 215p. (In French)
- Burmister, D. M. (1943) "Theory of stresses and displacements in layered systems and application to the design of airport runways," *Proc. 23rd Annual Meeting of the Highway Research Board*.
- Button, J. W., and Lytton, R. L. (1987). "Evaluation of fabrics, fibers and grids in overlays." *Proc., 6th International Conference on Structural Design of Asphalt Pavements*, Vol. 1, Ann Arbor, MI, 925-934.
- Canestrari, F., Belogi, L., Ferrotti, G., Graziani, A. (2015). "Shear and flexural characterization of grid-reinforced asphalt pavements and relation with field distress evolution". *Materials and Structures*, 48:959–975. DOI: 10.1617/s11527-013-0207-1
- Cardona Ramirez, D. A. (2016). *Characterisation of thermomechanical properties of bituminous mixtures used for railway infrastructures (Doctoral thesis)*. École Nationale des Travaux Publics de l'État (ENTPE) de l'Université de Lyon (UdL), Vaulx-en-Velin.
- Carpenter, S., Ghuzlan, K., & Shen, S. (2003). *Fatigue Endurance Limit for Highway and Airport Pavements*. *Transportation Research Record: Journal of the Transportation Research Board*, 1832, 131–138. DOI: 10.3141/1832-16

- Carver, C. and Sprague, C.J. (2000). "Asphalt Overlay Reinforcement", Geotechnical Fabric Report Magazine, 2000, 30-33.
- Chantachot, T., Kongkitkul, W., Youwai, S., and Jongpradist P. (2016). "Behaviours of geosynthetic-reinforced asphalt pavements investigated by laboratory physical model tests on a pavement structure". Transportation Geotechnics, Technical Paper, In press. DOI: 10.1016/j.trgeo.2016.03.004
- Christopher, B.R. and Holtz, R.D. (1985), "Geotextile Engineering Manual", Report No. FHWA-TS- 86/203, Federal Highway Administration, Washington, D.C., 1044 p.
- Cho, S.H., Safavizadeh S.A. & Kim Y.R. (2016). Verification of the applicability of the time–temperature superposition principle to interface shear stiffness and strength of Glas-Grid-reinforced asphalt mixtures, Road Materials and Pavement Design, DOI: 10.1080/14680629.2016.1189350
- Correia, N.S., and Zornberg J.G. (2018). "Strain distribution along geogrid-reinforced asphalt overlays under traffic loading". Geotextiles and Geomembranes 46, pp. 111–120 DOI: 10.1016/j.geotexmem.2017.10.002
- Corté, J.-F., & Di Benedetto H. (2005). Matériaux routiers bitumineux 1: Description et propriétés des constituants [Bituminous paving materials 1: Description and constituent properties]. Paris: Hermes-Lavoisier. (In French)
- Cost Action 348 (2006). Reinforcement of pavements with steel meshes and Geosynthetics (REIPAS). Final report of a European Concerted Research Action Designated as COST Action 348.
- Coutinho, R. P., Babadopulos, L. F. A. L., Freire, R. A., Castelo Branco, V. T. F., & Soares, J. B. (2014). The use of stress sweep tests for asphalt mixtures nonlinear viscoelastic and fatigue damage responses identification. *Materials and Structures*, 47(5), 895–909. <https://doi.org/10.1617/s11527-013-0101-x>
- Darling, J. R., & Woolstencroft, J. H. (2004). "A study of fiberglass pavement reinforcement used in different climatic zones and their effectiveness in retarding reflective cracking in asphalt overlays". Proceedings of the 5th international RILEM conference on cracking in pavements, Limoges.
- Das, A. (2006) "A Revisit to Aggregate Shape Parameter. In Workshop on Aggregates". Flakiness and Elongation Indices. New Delhi, 2006.
- De Bondt, A. H. (1999). "Anti-reflective cracking design of reinforced asphaltic overlays", PhD thesis, Delft University of Technology, Netherland, 1999.

- De Bondt, A. H. (2012). 20 years of research on asphalt reinforcement – Achievements and future needs (pp. 327–335). In 7th international RILEM conference on cracking in pavements, Delft.
- De la Roche, C., Corté, J.-F., Gramsammer, J.-C., Odéon, H., Tiret, L., & Caroff, G. (1994). Étude de la fatigue des enrobés bitumineux à l'aide du manège de fatigue du LCPC. *Revue générale des routes et aérodromes*, 716, 62-74. (In French)
- Delaporte, B., Di Benedetto, H., Chaverot, P., & Gauthier, G. (2007). Linear Viscoelastic Properties of Bituminous Materials: from Binders to Mastics. *Journal of the Association of Asphalt Paving Technologists*, 76, 455–494.
- Delbono, H.L., & Giudice, C.A. (2014). “Adherence in a pavement rehabilitated with a polymeric grid used as interlayer”. *Construction and Building Materials*, 54, pp. 454–459. DOI: 10.1016/j.conbuildmat.2013.12.098
- Di Benedetto H. (1987) Modélisation du comportement des géomatériaux: application aux enrobés bitumineux et aux bitumes, Thèse d’Etat, Institut National Polytechnique de Grenoble. (In French)
- Di Benedetto, H. (1998). Modélisation: écart entre état des connaissances et applications. Paper presented at Journée technique LAVOC, Lausanne. (In French)
- Di Benedetto, H., Olard, F., Sauzéat, C., & Delaporte, B. (2004a). Linear viscoelastic behavior of bituminous materials: From binders to mixes. *Road Materials and Pavement Design*, 12, 129-158. DOI: 10.1080/14680629.2011.9690356
- Di Benedetto, H., de la Roche, C., Baaj, H., Pronk, A., & Lundström, R. (2004b). Fatigue of bituminous mixtures. *Materials and structures*, 37, 202-216. DOI: 10.1007/BF02481620
- Di Benedetto, H., & Corté, J.-F. (2005). *Matériaux routiers bitumeux 2: constitution et propriétés thermomécaniques des mélanges*. Paris: Hermès Science Publications.
- Di Benedetto, H., Delaporte, B., & Sauzéat, C. (2007). Three-dimensional linear behaviour of bituminous materials: Experiments and modeling. *International Journal of Geomechanics*, 7, 149-157. DOI: 10.1061/(ASCE)1532-3641(2007)7:2(149)
- Di Benedetto H, Nguyen H, Pouget S, Sauzéat C (2008) Time–temperature superposition principle for bituminous mixtures: three dimensional approach and extension in the non-linear domain. In: *Proceedings of International conference on transportation infrastructure (ICTI)*. Beijing, pp 178–188
- Di Benedetto, H.; Nguyen, Q. T.; Sauzéat, C. (2011). Nonlinearity, heating, fatigue and thixotropy during cyclic loading of asphalt mixtures. *Road Materials and Pavements Design*, Vol 12, Issue 1, pp. 129-158.

- Di Benedetto, H., Gabet, T., Grenfell, J., Perraton, D., Sauzéat, C., & Bodin, D. (2013). Mechanical Testing of Bituminous Mixtures. In M. N. Partl, H. U. Bahia, F. Canestrari, C. de la Roche, H. Di Benedetto, H. Piber, & D. Sybilski (Eds.), *Advances in Interlaboratory Testing and Evaluation of Bituminous Materials* (Vol. 9, pp. 143–256). Dordrecht: Springer Netherlands. [https://doi.org/10.1007/978-94-007-5104-0\\_4](https://doi.org/10.1007/978-94-007-5104-0_4)
- Donovan, E. P., Al-Qadi, I. L., and Loulizi, A. (2000). "Optimization of tack coat application rate for a geocomposite membrane used on bridge decks." *Transportation Research Record* 1740, Transportation Research Board, Washington, D.C., 143-150.
- Doubbaneh, E. (1995). Comportement mécanique des enrobés bitumineux des "petites" aux "grandes" déformations. ENTPE-INSA Lyon, Lyon. (In French)
- EN 13043 (2003) Granulats pour mélanges hydrocarbonés et pour enduits superficiels utilisés dans la construction des chaussées, aérodromes et d'autres zones de circulation. Association Française de Normalisation (AFNOR), Paris. (In French)
- EN 1426 (2007) Bitumes et liants bitumineux - Détermination de la pénétrabilité à l'aiguille. Association Française de Normalisation (AFNOR), Paris. (In French)
- EN 12597 (2014) Bitumes et liants bitumineux - Terminologie. Association Française de Normalisation (AFNOR), Paris. (In French)
- EN 12697-6 (2012) Mélanges bitumineux - Méthodes d'essai pour mélange hydrocarboné à chaud - Partie 6 : détermination de la masse volumique apparente des éprouvettes bitumineuses. Association Française de Normalisation (AFNOR), Paris. (In French)
- EN 12697-24. (2012). Bituminous mixtures. Test methods for hot mix asphalt. Part 24: Resistance to fatigue. Association Française de Normalisation (AFNOR), Paris. (In French)
- EN 12697-33 (2019) Bituminous mixtures - Test method - Part 33: Specimen prepared by roller compactor Association Française de Normalisation (AFNOR), Paris. (In French)
- EN 13043 (2015) Granulats pour mélanges hydrocarbonés et pour enduits superficiels utilisés dans la construction des chaussées, aérodromes et d'autres zones de circulation. Association Française de Normalisation (AFNOR), Paris. (In French)
- EN 13108-1 (2016) Mélanges bitumineux. Spécifications pour le matériau. Association Française de Normalisation (AFNOR), Paris. (In French)
- EN 13924-1 (2016) Bitumes et liants bitumineux - Cadre de spécifications pour les bitumes routiers spéciaux - Partie 1 : bitumes routiers de grade dur. Association Française de Normalisation (AFNOR), Paris. (In French)

- EN 13924-2 (2014) Bitumes et liants bitumineux - Cadre de spécifications pour les bitumes routiers spéciaux - Partie 2: Bitumes routiers multigrades. Association Française de Normalisation (AFNOR), Paris. (In French)
- EN ISO 10319 (2015) Géosynthétiques - Essai de traction des bandes larges. Association Française de Normalisation (AFNOR), Paris. (In French)
- Fallah S., Ali Khodaii, A. (2015). "Reinforcing overlay to reduce reflection cracking; an experimental investigation". *Geotextiles and Geomembranes*, 43, pp.216-227. DOI: 10.1016/j.geotexmem.2015.03.002
- Fantozzi, G., Orange G. and R'Mili M. (1988) "Rupture des matériaux". GEMPPM, INSA, Lyon.
- Ferrotti G, Canestrari F, Virgili A, Grilli A (2011). "A strategic laboratory approach for the performance investigation of geogrids in flexible pavements". *Construction and Building Materials*, 25(5):2343–2348.
- Ferry, J. D. (1980). *Viscoelastic properties of polymers* (3d ed). New York: Wiley.
- FHWA (1974). *Pavement Rehabilitation: Proceedings of a Workshop*. Publication No. FHWA-RD-74-60, June 1974.
- FHWA (2003). *Distress Identification Manual for the Long-Term Pavement Performance Program*, Publication No. FHWA-RD-03-031, June 2003.
- FHWA (2006). *Geotechnical Aspects of Pavements*, Publication No. FHWA NHI-05-037, May 2006.
- Freire, R.A., Babadopulos, L.F.A.L., Castelo Branco, V.T.F., Bhasin, A. (2017). Aggregate Maximum Nominal Sizes' Influence on Fatigue Damage Performance Using Different Scales. *Journal of Materials in Civil Engineering ASCE*. Vol 29, Issue 8. DOI 10.1061/(ASCE)MT.1943-5533.0001912.
- Freire, R.A., Di Benedetto, H., Sauzéat, C., Pouget, S., Lesueur, D. (2018) "Linear Viscoelastic Behaviour of Geogrids Interface within Bituminous Mixtures". *KSCE Journal of Civil Engineering* (2018) 22(6), p. 2082-2088. DOI 10.1007/s12205-018-1696-9
- Gayte, P., Di Benedetto, H., Sauzéat, C., & Nguyen, Q. T. (2016). Influence of transient effects for analysis of complex modulus tests on bituminous mixtures. *Road Materials and Pavement Design*, 17(2), 271–289. <https://doi.org/10.1080/14680629.2015.1067246>
- Gayte, P., (2016). *Modélisation du comportement thermo-viscoplastique des enrobés bitumineux* (Doctoral thesis). École Nationale des Travaux Publics de l'État (ENTPE) de l'Université de Lyon (UdL), Vaulx-en-Velin.
- Geosynthetic Material Association (2002). *Handbook of Geosynthetics*, USA.

- Graziani, A., Sangiorgi, C., and Canestrari, F. (2016). "Fracture characterization of grid-reinforced asphalt pavements". In: Chabot A., Buttlar W., Dave E., Petit C., Tebaldi G. (eds) 8th RILEM International Conference on Mechanisms of Cracking and Debonding in Pavements. RILEM Bookseries, vol 13. Springer, Dordrecht. DOI: 10.1007/978-94-024-0867-6\_9
- Graziani, A., Canestrari, F., Cardone, F. and Ferrotti, G. (2017). "Time–temperature superposition principle for interlayer shear strength of bituminous pavements." *Road Materials and Pavement Design*, 18:sup2, 12-25, DOI: 10.1080/14680629.2017.1304247
- Gilchrist A.J.T. and Brown S.F. (1988). "Polymer grid reinforced asphalt to limit cracking and rutting in pavements", 3rd International Road Fund Regional Meeting, Riyadh, Saudi Arabia.
- Giroud, J. P. and Noiray, L. (1981). "Geotextile-reinforced unpaved road design." *Journal of the Geotechnical Engineering Division, ASCE*, 107, No. GT9, 1231-54.
- Giroud J.P., (1987). "Tomorrow's Designs for Geostextile Applications. Geotextile Testing and the Design Engineer", ASTM STP 952, J.E. Fluett, Jr., Ed., American Society for Testing and Materials, Philadelphia, pp. 145-158.
- Godard, E., Van Rompu, J., Brissaud, L., Gileni, F. (2019). Renforcement des chaussées bitumineuses par grille de verre : bilan de 25 ans d'expérience, derniers développements reinforcement of bituminous pavements by glass grids: 25 years of experience, latest developments. In 12èmes Rencontres Géosynthétiques, pp. 85-94. Nancy. (In French)
- Gonzalez-Torre, I., Calzada-Perez, M.A., Vega-Zamanillo, A., Castro-Fresno D., (2015). "Evaluation of reflective cracking in pavements using a new procedure that combine loads with different frequencies". *Construction and Building Materials*, 75, pp.368–374. DOI: 10.1016/j.conbuildmat.2014.11.030
- Guler, E., and Atalay, I., "The Effects of Geosynthetics on Mitigation of Rutting in Flexible Pavements". 6th Eurasphalt & Eurobitume Congress, Berlin (2016). DOI dx.doi.org/10.14311/EE.2016.101
- Haas R., J. Walls, R.G. Carroll (1988). "Geogrid reinforcement of granular bases in flexible pavements". *Transportation Research Record*, 1188 pp. 19–27 Washington, DC
- Haliburton T.A. and J.V. Baron (1983) "Optimum-depth method for design of fabric-reinforced unsurfaced roads," *Transportation Research Record* 916, pp 26-32.
- Halim, A. O. A., Haas, R. C. G., and Phang, W. A. (1983). "Geogrid Reinforcement of Asphalt Pavements and Verification of Elastic Theory." *Transportation Research Record* 949, Transportation Research Board, Washington, D.C., 55-65.



- Hausmann, M.R. (1987). "Geotextiles for unpaved roads-A review of design procedures", *Journal of Geotextiles and Geomembranes*, 5, 201-233.
- Highway Research Board. (1961). *The AASHO road test: History and description of the project (Special Report 61A)*. Washington, DC: National Academy of Sciences, National Research Council.
- Holtz, R.D., Christopher, B.R., Berg, R.R. (1998). *Geosynthetic Design and Construction Guidelines*. FHWA Technical Report No. FHWA-HI-95-038, Federal Highway Administration, Washington, D.C., updated April 1998, 460pp.
- Hopman, P. C., Kunst, P. A. J., & Pronk, A. C. (1989). A renewed interpretation method for fatigue measurements: verification of Miner's rule. In *Proceedings of the 4th Eurobitume Symposium, Volume 1* (pp. 557-561).
- Hornych, P., Kerzrého, J. P., Sohm, J., Chabot, A., Trichet, S., Joutang, J. L., & Bastard, N. (2012). Full scale tests on grid reinforced flexible pavements on the French fatigue carousel. *Proceedings of the 7th international RILEM conference on cracking in pavements*, Delft.
- Huet, C. (1963). *Étude par une méthode d'impédance du comportement viscoélastique des matériaux hydrocarbonés* (Doctoral thesis). Université de Paris, Paris. (in French)
- Hughes D.A.B. (1986). "Polymer grid reinforcement of asphalt pavements", PhD Thesis, Department of Civil Engineering, University of Nottingham.
- Irwin, G. R. (1957) "Analysis of Stresses and Strains Near the End of a Crack Traversing a Plate". *Trans. ASME, J. Appl. Mech.*, Vol. E24, 1957, 361.
- Jamek M., Tschegg E. K., and Lugmayr R. (2012). "Mechanical and fracture-mechanical properties of geosynthetic reinforced asphalt systems" *Fatigue Fract Engng Mater Struct* 35, 648–657. DOI: 10.1111/j.1460-2695.2011.01659.x
- Janssen, M., Zuidema, J. and Wanhill, R.J.H, (2002). "Fracture mechanics". Taylor & Francis Group. 365p.
- Kachanov, L. M. (1958). Rupture time under creep conditions. *Izvestia Akademii Nauk SSSR, Otdelenie Tekhnicheskich Nauk*, (8), 26–31.
- Kachanov, L. M. (1986). *Introduction to continuum damage mechanics* (Vol. 10). Dordrecht: Springer Netherlands. <https://doi.org/10.1007/978-94-017-1957-5>
- Kennepohl, G., Kamel, N., Walls, J., and Hass, R. C. (1985). "Geogrid reinforcement of flexible pavements design basis and field trials." *Proc., Annual Meeting of the Association of Asphalt Paving Technologists*, Vol. 54, San Antonio, TX, 45-75.

- Khodaii, A., Fallah S., Fereidoon Moghadas Nejad, F.M. (2009). "Effects of geosynthetics on reduction of reflection cracking in asphalt overlays". *Geotextiles and Geomembranes* 27, pp.1–8. DOI:10.1016/j.geotexmem.2008.05.007
- Koerner, R.M. (2005). *Designing with Geosynthetics*. 5th Edition. Upper Saddle River, NJ: Prentice Hall.
- Komatsu, T., Kikuta, H., Yoshinobu, T., and Muramatsu, E. (1998). "Durability assessment of geogrid-reinforced asphalt concrete." *Geotextiles and Geomembranes*, Vol. 16, 257-271.
- Laurinavicius, A., & Oginskas, R. (2006). "Experimental research on the development of rutting in asphalt concrete pavements reinforced with geosynthetic materials". *J. Civ. Eng. Manag.* 12 (No. 4), 311–317.
- Leblond, J.-B. (2003) "*Mécanique de la rupture fragile et ductile*". Hermès – Lavoisier, 2003. 197p. (In French)
- LCPC (1998). "*Catalogue des dégradations de surface des chaussées*". Laboratoire Central des Ponts et Chaussées, Ministère de l'Équipement. (In French)
- Lemaître, J., & Chaboche, J.-L. (1990). *Mechanics of solid materials*. Cambridge: Cambridge University Press.
- Lesueur, D. (2009). The colloidal structure of bitumen: Consequences on the rheology and on the mechanisms of bitumen modification. *Advances in Colloid and Interface Science*, 145(1–2), 42–82. DOI:10.1016/j.cis.2008.08.011
- Leutner, R. (1979). Untersuchung des Schichtenverbundes beim bituminösen Oberbau. *Bitumen*, 41-3, 84–91. (In German)
- Li, X., Braham A. F., Marasteanu M. O., Buttlar W. G. and Williams R. C., (2008) "Effect of factors affecting fracture energy of asphalt concrete at low temperature". *Road Materials and Pavement Design - EATA 2008*, Vol. 9 (Special Issue), 2008, pp. 397-416.
- Li, P., Liu, J., Samueloff, M., and Jones, D. (2014). Performance of paving fabric reinforced asphalt mixture. *Climatic Effects on Pavement and Geotechnical Infrastructure*: pp. 126-138. DOI: 10.1061/9780784413326.013.
- Lytton R.L. (1988) "Reinforcing fiberglass grids for asphalt overlays". Texas Transportation Institute Report for Bay Mills Limited, Texas A&M University, College Station, Texas.
- Lytton, R. L. (1989). Use of geotextiles for reinforcement and strain relief in asphalt concrete. *Journal of Geotextiles and Geomembranes*, 8, 217–237.

- Mamatha K.H., Dinesh S.V. & Dattatreya J.K. (2019) Evaluation of flexural behaviour of geosynthetic-reinforced unbound granular material beams, *Road Materials and Pavement Design*, 20:4, 859-876, DOI: 10.1080/14680629.2017.1422790
- Mangiafico, S. (2014). Linear viscoelastic properties and fatigue of bituminous mixtures produced with Reclaimed Asphalt Pavement and corresponding binder blends (Doctoral thesis). École Nationale des Travaux Publics de l'État (ENTPE) de l'Université de Lyon (UdL), Vaulx-en-Velin.
- Mangiafico, S., Sauzéat C., Di Benedetto, H., Pouget S., Olard F., and Planque L. (2015) .Quantification of Biasing Effects During Fatigue Tests on Asphalt Mixes: Non-linearity, Self-heating and Thixotropy. Association of Asphalt Paving Technologists (AAPT), Portland, OR.
- Masad, E., and Button, J.W. (2000). Unified Imaging Approach for Measuring Aggregate Angularity and Texture. *Computer-Aided Civil and Infrastructure Engineering*, Vol. 15, pp. 273-280.
- Maxwell, J. C. (1867). On the dynamical theory of gases. *Philosophical Transactions of the Royal Society of London*, 157, 49-88. DOI: 10.1098/rstl.1867.0004
- Meyer, O. E. (1874). Theorie der elastischen Nachwirkung [Theory of the elastic aftereffect]. *Annalen der Physik und Chemie*, 227, 108-119. DOI: 10.1002/andp.18742270106 (In German)
- Meyer, O. E. (1878). Ueber die elastische Nachwirkung [Concerning the elastic aftereffect]. *Annalen der Physik und* (In German)
- Miannay, D. P. (1996). "Mécanique de la rupture". Les Editions de Physique, 1995. 287p.
- Millien, A., Dragomir, M. L., Wendling, L., Petit, C., & Iliescu, M. (2012). Geogrid interlayer performance in pavements: Tensile-bending test for crack propagation. In T. Scarpas, N. Kringos, I. L. Al-Qadi, & A. Loizos (Eds.), *7th RILEM International Conference on Cracking in Pavements* (Vol. 2, pp. 1209–1218). Dordrecht: Springer.
- Miner, M. A. (1945). Cumulative damage in fatigue. *Journal of Applied Mechanics*, 67, 159–164.
- Monismith, C. L., and Coetzee, N. F. (1980). "Reflection cracking: analysis, laboratory studies and design considerations." *Proc., Annual Meeting of the Association of Asphalt Paving Technologists*, Vol. 49, Louisville, KY, 268-313.
- Montepara, A., Romeo, E., and Tebaldi, G. (2012). Effectiveness of glasgrid® interlayer systems in preventing reflective cracking and extending pavement service life. Final Report, University of Parma, February, 2012.

- Mounes, S.M., Karim, M.R., Khodaii, A., Almasi, M.H. (2016). "Evaluation of permanent deformation of geogrid reinforced asphalt concrete using dynamic creep test". *Geotextiles and Geomembranes*, 44, pp. 109-116. DOI: 10.1016/j.geotexmem.2015.06.003
- MTAG (2009). Volume I - Flexible Pavement Preservation. 2nd Edition, Caltrans Division of Maintenance, January 27, 2009
- Nejad F. M., Asadi S., Fallah S., Vadood M., "Statistical-experimental study of geosynthetics performance on reflection cracking phenomenon", *Geotextiles and Geomembranes*, Volume 44, Issue 2, 2016, 178-187, DOI:10.1016/j.geotexmem.2015.09.002.
- NF P98-086 (2019) Dimensionnement structurel des chaussées routières - Application aux chaussées neuves. Association Française de Normalisation (AFNOR), Paris. (In French)
- Nguyen, H. M., Pouget, S., Di Benedetto, H., & Sauzéat, C. (2009). Time-temperature superposition principle for bituminous mixtures. *European Journal of Environmental and Civil Engineering*, 13(9), 1095–1107. <https://doi.org/10.1080/19648189.2009.9693176>
- Nguyen, M. L. & Sauzéat, C. & Di Benedetto, H. & Wendling, L. (2008). "Investigation of cracking in bituminous mixtures with a 4 points bending test. Pavement Cracking: Mechanisms, Modeling, Detection, Testing and Case Histories". 283-293. DOI:10.1201/9780203882191.ch28.
- Nguyen, M.L., Sauzéat, C., Di Benedetto, H., & Tapsoba, N. (2013a). Validation of the time–temperature superposition principle for crack propagation in bituminous mixtures. *Materials and Structures*, 46(7), 1075–1087. DOI: 10.1617/s11527-012-9954-7
- Nguyen, M.L., Blanca, J., Kerzréhoa, J.P. and Hornyh, P. (2013b). "Review of glass fibre grid use for pavement reinforcement and APT experiments at IFSTTAR." *Road Mater Pavement*. 14 (1): 287- 308. DOI: 10.1080/14680629.2013.774763
- Nguyen, Q. T.; Di Benedetto, H.; Sauzéat, C. (2012). Determination of thermal properties of asphalt mixtures as another output from cyclic tension-compression test. *Road Materials and Pavement Design*, 13:1, pp. 85-103.
- Noory A., Nejad F.M. & Ali Khodaii A. (2017). Effective parameters on interface failure in a geocomposite reinforced multilayered asphalt system, *Road Materials and Pavement Design*, DOI: 10.1080/14680629.2017.1305435
- Norambuena-Contreras, J., Gonzalez-Torre, I., Fernandez-Arnau, D., Lopez-Riveros, C. (2016). "Mechanical damage evaluation of geosynthetics fibres used as anti-reflective cracking systems in asphalt pavements". *Construction and Building Materials*, 109, pp. 47–54. DOI: 10.1016/j.conbuildmat.2016.01.057

- Obando-Ante, J. & Palmeira, E.M. (2015). "A Laboratory Study on the Performance of Geosynthetic Reinforced Asphalt Overlays". *Int. J. of Geosynth. and Ground Eng.*, 1:5. DOI: 10.1007/s40891-014-0007-x
- Olard, F., & Di Benedetto, H. (2003). General "2S2P1D" model and relation between the linear viscoelastic behaviours of bituminous binders and mixes. *Road Materials and Pavement Design*, 4, 185-224. DOI: 10.1080/14680629.2003.9689946
- Palmgreen, A. (1924). Die Lebensdauer von Kugellagem. *Zeitschrift des Vereins deutscher Ingenieure*, 68(339–341). (In German)
- Paris, P.C. and Erdogan, F. (1963) A Critical Analysis of Crack Propagation Laws, *Transactions of the ASME, Journal of Basic Engineering, Series D*, 85, No. 3.
- Pasquini, E., Pasetto, M., & Canestrari, F. (2015). Geocomposite against reflexive cracking in asphalt pavements: laboratory simulation of a field application. *Road Materials and Pavement Design*, 16:4, 815-835, DOI:10.1080/14680629.2015.1044558.
- Pedraza, A. (2018) "Propriétés thermomécaniques d'enrobés multi-recyclés", PhD thesis, University of Lyon/ENTPE, France. (In French)
- Pham, N.H., Sauzéat, C., Di Benedetto, H., Gonzalez-Leon, J.A., Barreto G., Nocolai, A. and Jajubowski, M. (2015). "RAP and additive influence on 3D linear behaviour of warm bituminous mixtures." *Road Materials and Pavement*, 16 (3), pp. 569-591, DOI:10.1080/14680629.2015.1021108
- Phan, C.V., Di Benedetto, H., Sauzéat, C., Lesueur, D., Pouget, S., Olard, F. and Dupriet, S. (2017). "Complex modulus and fatigue resistance of bituminous mixtures containing hydrated lime." *Construction and Building Materials*, Vol. 139, pp. 24-33, DOI:10.1016/j.conbuildmat.2017.02.042
- Piau, J.-M. (1989). "Modélisation thermomécanique du comportement des enrobés bitumineux". *Bulletin de liaison des laboratoires des ponts et chaussées*, Sept-Oct 1989, n°163, p41-54 (In French)
- Plug, C. P., & de Bondt, A. H. (2010). Adhesion of reinforcement grids in asphalt overlays. The 5th world congress on emulsion, Lyon. (In French)
- Poncelet, J. V. (1839). *Introduction à la mécanique industrielle, physique ou expérimentale: Deuxième édition, entièrement corrigée et contenant un grand nombre de considérations nouvelles*. Metz: Mme Thiel. (In French)
- Porter O. J. (1938). "The Preparation of Subgrades," *HRB Proc.*, pp. 324-331

- Pouget, S. (2011). Influence des propriétés élastiques ou viscoélastiques des revêtements sur le comportement des ponts à dalle orthotrope (Doctoral thesis). École Nationale des Travaux Publics de l'État (ENTPE) de l'Université de Lyon (UdL), Vaulx-en-Velin.
- Raab, C., Partl, M. N., and Abd El Halim, A. O. (2009). "Evaluation of interlayer shear bond devices for asphalt pavements." *Baltic Journal of Road and Bridge Engineering*, 4(4), 176–195.
- Read, J., Whiteoak, D., & Hunter, R. N. (2003). *The Shell Bitumen handbook* (5th ed). London: Thomas Telford.
- RILEM TC-50 FMC (1985). "Determination of the fracture energy of mortar and concrete by means of three-point bend tests on notched beams". *Materials and Structures*. Vol. 18, 1985, pp. 287-290.
- Roberts, F.L., Kandhal, P.S., Brown, E.R., Lee, D.Y., and Kennedy, T.W. (1996). *Hot Mix Asphalt Materials, Mixture Design, and Construction*. National Asphalt Paving Association Education Foundation. Lanham, MD.
- Romeo E., Freddi F. & Montepara A. (2014) Mechanical behaviour of surface layer fibreglass-reinforced flexible pavements, *International Journal of Pavement Engineering*, 15:2, 95-109, DOI: 10.1080/10298436.2013.828838
- Roschen, T.J. (1997). "A case study into the use of pavement reinforcing grid, mastic, and membrane interlayers on asphalt concrete overlays". *Geosynthetics 97 Conference Proceedings*, Vol. 2, pp. 66-71.
- Safavizadeh, A., & Kim, Y. R. (2014). Mode II fatigue and reflective cracking performance of glass grid reinforced asphalt concrete under repeated loading. *Proceedings of the 12th ISAP conference on asphalt pavements*, Raleigh, NC, pp. 1893–1902.
- Safavizadeh, S.A., Wargo, A., Guddati, M., & Kim, Y.R. (2015). "Investigation of reflexive cracking mechanisms in grid-reinforced asphalt specimens using four-point bending notched beam fatigue tests and digital image correlation". *Transportation Research Record*, (2507), pp.29-38.
- Sagnol L., Quezada J.C., Chazallon C. & Stöckner M. (2019) Effect of glass fibre grids on the bonding strength between two asphalt layers and its Contact Dynamics method modeling, *Road Materials and Pavement Design*, 20:5, 1164-1181, DOI: 10.1080/14680629.2018.1439764
- Salençon J. (1983) *Cours de calcul des structures anélastiques - Viscoélasticité*, Presses de l'École nationale des ponts et chaussées, Paris. (In French)

- Sanders, C.A., and Dukatz, E.L. (1992) Evaluation of Percent Fracture of Hot-Mix Asphalt Gravels in Indiana. Effect of Aggregate and Mineral Filler on Asphalt Mixture Performance. Philadelphia, PA.
- South Africa. (2008). Technical guideline: Asphalt reinforcement for road construction. Asphalt Academy.
- Sayegh, G. (1965). Variations des modules de quelques bitumes purs et enrobés bitumineux (Doctoral thesis). Université de Paris, Paris. (In French)
- SETRA-LCPC (1994) Guide Technique, conception et dimensionnement des structures de chaussée, SETRA-LCPC, décembre 1994. (In French)
- SETRA-LCPC (1997), “Systèmes limitant la remontée des fissures transversales de retrait hydraulique”, Note d’information n°93, avril 1997 (In French)
- Soares, J.B., Souza, F.V. (2002). Verificação do Comportamento Viscoelástico Linear em Misturas Asfálticas. 16o Encontro de Asfalto. Rio de Janeiro, RJ (In Portuguese)
- Sobhan K. & Tandon V. (2008) “Mitigating Reflection Cracking in Asphalt Overlays using Geosynthetic Reinforcements”. Road Materials and Pavement Design, 9:3, 367-387. DOI: 10.1080/14680629.2008.9690124
- Soltani, M.A.A. (1998). Comportement en fatigue des enrobes bitumineux (Doctoral thesis). Institut National des Sciences Appliquées (INSA) de Lyon, Lyon.
- Song, S. H., Paulino G. H. and Buttlar W. G. (2006). "A bilinear cohesive zone model tailored for fracture of asphalt concrete considering viscoelastic bulk material". Engineering Fracture Mechanics, Vol. 73 (N° 18), pp. 2829-2848.
- STBA (1999). “Techniques anti remontées des fissures - Guide d'emploi en chaussées aéronautiques ”, avril (In French)
- Sutton, M. A., W. J. Wolters, W. H. Peters, W. F. Ranson, and S. R. McNeill. (1983) “Determination of Displacements Using an Improved Digital Correlation Method.” Image and Vision Computing, 1 (3): 133-139
- Tang, X., Chehab, G. R., & Palomino, A. (2008). Evaluation of geogrids for stabilizing weak pavement subgrade. International Journal of Pavement Engineering, 9(6), 413–429.
- Tang, X., & Yang, M. (2013). Investigation of flexural behaviour of geocell reinforcement using three layered beam model testing. Geotechnical and Geological Engineering, 31(2), 753–765.
- Tapsoba, N.; Sauzéat, C.; Di Benedetto, H. (2011) Analysis of fatigue test for bituminous mixtures. Journal of Materials in Civil Engineering, v. 6, issue 2, pp. 701-710

- Tapsoba, N. (2012). Comportement des enrobés bitumineux à base de matériaux recyclés et/ou fabriqués à température réduite (Doctoral thesis). ENTPE, Lyon. (In French)
- Thomson W. (1856). Elements of a mathematical theory of elasticity. *Philosophical Transactions of the Royal Society of London*, 146, 481-498. DOI: 10.1098/rstl.1856.0022
- Thomson W. (1865). On the elasticity and viscosity of metals. *Proceedings of the Royal Society of London*, 14, 289-297. DOI: 10.1098/rspl.1865.0052
- Tsai, B. W.; Monismith, C. L. (2005). Influence of asphalt binder properties on the fatigue performance of asphalt concrete pavements. *Journal of the Association of Asphalt Paving Technologists*, 74, pp. 733-790.
- Tschegg E.K. (1986) Test method for the determination of fracture mechanics properties. Patent Specification No. A-233/86 390 328, Austrian Patent Office 1986, Prüfeinrichtung zur Ermittlung von bruchmechanischen Kennwerten sowie hierfür geeignete Prüfkörper, Österreichisches Patent AT- 390328. (In German)
- Tschegg E.K., Jamek M. & Lugmayr R. (2012) "Crack growth behaviour in geosynthetic asphalt interlayer systems". *Road Materials and Pavement Design*, 13:1, 156-170, DOI: 10.1080/14680629.2011.644414
- Voigt, W. (1892). Ueber innere Reibung fester Körper, insbesondere der Metalle (About internal friction of solid bodies, particularly the metals). *Annalen der Physik und Chemie*, 283, 671-693. (In German) DOI: 10.1002/andp.18922831210
- Vanelstraete, A., and Franken, L. (1997). Prevention-of-reflective-cracking-in-pavements (RILEM TC 157 PRC report).
- Virgili, A., Canestrari, F., Grilli, A., & Santagata, F. A. (2009). Repeated load test on bituminous systems reinforced by geosynthetics. *Geotextiles and Geomembranes*, 27, 187–195.
- Walubita, L. F., Faruk, A.N.M., Zhang J., and Hud, X. (2015). "Characterizing the cracking and fracture properties of geosynthetic interlayer reinforced HMA samples using the Overlay Tester (OT)". *Construction and Building Materials*, 93, pp. 695-702. DOI: 10.1016/j.conbuildmat.2015.06.028
- Webster, S.L. (1991) "Reinforced Base Courses for Light Aircraft: Literature review and Test Section Design Geotechnical Laboratory" Department of the Army, Waterways Experiment Station, U.S. Army Corps of Engineers, Mississippi.
- Williams, E. G. (1953) "Vibratory compaction of a macadam base" Kentucky dept. of highways, Highway Material Research Lab., Research report No. 1, University of Kentucky, Lexington



- Williams, M. L., Landel, R. F., & Ferry, J. D. (1955). The Temperature Dependence of Relaxation Mechanisms in Amorphous Polymers and Other Glass-forming Liquids. *Journal of the American Chemical Society*, 77(14), 3701–3707. <https://doi.org/10.1021/ja01619a008>
- Wöhler, A. (1870). Über die Festigkeitsversuche mit Eisen und Stahl. *Zeitschrift für Bauwesen*, 20, 73–106. (In German)
- Zamora-Barraza, D., Calzada-Peréz, M.A., Castro-Fresno, D., Vega-Zamanillo, A. (2010). “New procedure for measuring adherence between a geosynthetic material and a bituminous mixture”. *Geotextiles and Geomembranes*, 28, pp.483-489. DOI: 10.1016/j.geotexmem.2009.12.010.
- Zamora-Barraza, D., Calzada-Peréz, M.A., Castro-Fresno, D., Vega-Zamanillo, A. (2011). “Evaluation of anti-reflective cracking systems using geosynthetics in the interlayer zone”. *Geotextiles and Geomembranes*, 29, pp.130-136. DOI: 10.1016/j.geotexmem.2010.10.005
- Zornberg, J.G, and Thompson, N. (2010) “Application Guide and Specifications for Geotextiles in Roadway Applications.” FHWA Technical Report No. FHWA/TX-10/0-5812-1, Federal Highway Administration, Washington, D.C., February 2010, 128pp.
- Zofka A., Maliszewski, M. and Maliszewska, D. (2016). "Glass and carbon geogrid reinforcement of asphalt mixtures." *Road Materials and Pavement Design*, DOI:10.1080/14680629.2016.1266775